Experimental studies of the defect structure of the TiO2(110) surface before and after the exposure to oxygen, hydrogen and carbon monoxide
by Gerd Heinrich Rocker

A thesis submitted in partial fulfillment of the requirements for the degree of Doctor of Philosophy in Physics
Montana State University

Abstract:
The electronic defect structure of Ti02 (110) before and after exposure to O2, H2 and CO was studied by means of XPS, XAES., AES, EELS, ELS and conductivity as well as work function changes. Surface defects, created by high temperature treatment, ion bombardment and by evaporating submonolayer amounts of Ti, lead to an additional peak in the TiLMV Auger signal, changes in the valence band structure and broadening and/or additional peaks in the Ti2p, Ti3p and 01s core-levels. These effects result from the formation of Ti3+ in a Ti-V0-Ti complex at the surface and induce an increase in the surface conductivity as well as more (less) pronounced conductivity changes upon the adsorption of 02 (H2 and CO), if compared to the stoichiometric surface. In the presence of defects the adsorption of any of these gases also results in an increase of the work function whereas a decrease (increase) was observed during H2 and CO (02) exposure to ideal surfaces. The results are discussed quantitatively in terms of a modified charge transfer model.

EXPERIMENTAL STUDIES OF THE DEFECT STRUCTURE OF THE TiO_2(110) SURFACE BEFORE AND AFTER THE EXPOSURE TO OXYGEN, HYDROGEN AND CARBON MONOXIDE

by

Gerd Heinrich Rocker

A thesis submitted in partial fulfillment
of the requirements for the degree

of

Doctor of Philosophy

in

Physics

MONTANA STATE UNIVERSITY
Bozeman, Montana

August 1985

APPROVAL

of a thesis submitted by

Gerd Heinrich Rocker

This thesis has been read by each member of the thesis committee and has been found to be satisfactory regarding content, English usage, format, citations, bibliographic style, and consistency, and is ready for submission to the College of Graduate Studies.

8-5-85
Date

John Hermanson
Co-chairperson,
Graduate Committee

Approved for the Major Department

8-5-85
Date

Robert Stevens
Head, Major Department

Approved for the College of Graduate Studies

9-8-85
Date

M B Malone
Graduate Dean

STATEMENT OF PERMISSION TO USE

In presenting this thesis in partial fulfillment of the requirements for a doctoral degree at Montana State University, I agree that the Library shall make it available to borrowers under rules of the Library. I further agree that copying of this thesis is allowable only for scholarly purposes, consistent with "fair use" as prescribed in the U.S. Copyright Law. Requests for extensive copying or reproduction of this thesis should be referred to University Microfilms International, 300 North Zeeb Road, Ann Arbor, Michigan 48106, to whom I have granted "the exclusive right to reproduce and distribute copies of the dissertation in and from microfilm and the right to reproduce and distribute by abstract in any format."

Signature Gerd Rosse

Date 8/5/85

ACKNOWLEDGEMENTS

I would like to take this opportunity to thank my thesis advisor, Dr. Wolfgang Goepel, who suggested the research reported in this thesis. I am grateful to him for coming to Bozeman and giving valuable advice during numerous discussions. Also, I would like to express my sincere thanks to Dr. John Hermanson for his sustained support as the chairman of my Ph. D. committee during the absence of my thesis advisor. I deeply acknowlegde his helpful advice and the time he spent in reading the manuscript of this thesis. I am particularly grateful to Dr. James Anderson, who had the amazing ability to offer help and encouragement whenever physical problems arose and other advisors were unavailable. I greatly acknowlegde his valuable advice, his patience and his kind assistance during my measuring time in the CRISS lab. Special gratitude is extended to Dr. Gerald Lapeyre for awarding measuring time, and to Milton Jaehnig and Dr. David Frankel for their helpful support during numerous experiments. Furthermore, I deeply appreciate the technical assistance of Alfred Beldring. Without the electronic devices that he built, a major part of my experimental work would not have been possible. Finally, I gratefully acknowledge the generous financial support provided by an M. J. Murdock Charitable Trust Grant of Research Corporation.

TABLE OF CONTENTS

TABLE OF CONTENTS - CONTINUED

LIST OF TABLES

LIST OF FIGURES

LIST OF FIGURES - CONTINUED

LIST OF FIGURES - CONTINUED

LIST OF FIGURES - CONTINUED

Abstract

The electronic defect structure of TiO_2(110) before and after exposure to O_2, H_2 and CO was studied by means of XPS, XAES, AES, EELS, ELS and conductivity as well as work function changes. Surface defects, created by high temperature treatment, ion bombardment and by evaporating submonolayer amounts of Ti, lead to an additional peak in the TiLMV Auger signal, changes in the valence band structure and broadening and/or additional peaks in the Ti2p, Ti3p and O1s core-levels. These effects result from the formation of Ti^{3+} in a $Ti-V_O-Ti$ complex at the surface and induce an increase in the surface conductivity as well as more (less) pronounced conductivity changes upon the adsorption of O_2 (H_2 and CO), if compared to the stoichiometric surface. In the presence of defects the adsorption of any of these gases also results in an increase of the work function whereas a decrease (increase) was observed during H_2 and CO (O_2) exposure to ideal surfaces. The results are discussed quantitatively in terms of a modified charge transfer model.

CHAPTER 1

INTRODUCTION AND STATEMENT OF THE PROBLEM

Titanium dioxide is a transition-metal oxide and has proved its great practical importance in the field of gas sensors, catalysts, high-temperature-resistant semiconductors, masers, photodecomposition of water and the photo-oxidation of a number of organic and inorganic molecules (see chapter 2).

The underlying physical and chemical mechanisms, however, are not well understood yet. It is believed that surface point defects are responsible for the catalytic activity of titanium dioxide surfaces, in the sense that they provide adsorption sites for foreign gases and determine charge-transfer reaction rates (see chapter 2).

In this thesis, different methods for preparing stoichiometric and defective titanium dioxide surfaces will be presented. The interaction of various gases such as oxygen, hydrogen and carbon monoxide with these surfaces will be investigated by studying changes in the surface electronic structure. Measurements of changes in surface conductivity and work function as well as different electron spectroscopies will be applied as surface-sensitive experimental probes.

CHAPTER 2

LITERATURE SURVEY OF INVESTIGATIONS ON TITANIUM DIOXIDE

Bulk Properties and Bulk Defects

The three polymorphic structures of titanium dioxide (TiO_2) are known to be rutile, anatase and brookite [1,2,3]. The rutile structure to be investigated in this thesis is the most stable structure under atmospheric conditions at room temperature. It exhibits a tetragonal unit cell, which contains two titanium Ti^{4+} and four oxygen O^{2-} ions (Figure 1 and reference 4). Its coordination is 6:3 (oxygen-to-titanium neighbors).

The space group of the rutile structure is D_{4h}^{14}, whose irreducible representations, as well as those of its small groups, have been given by Dimmock and Wheeler and by Gay et al. [2,5,6].

Each titanium ion in the unit cell has two oxygen neighbors at a distance of 1.988 Å and four oxygen neighbors at a distance of 1.944 Å (Figure 1). Thus, each cation is surrounded by a nearly regular octahedron of six anions, and each anion is at the center of a nearly equilateral triangle of cations [2].

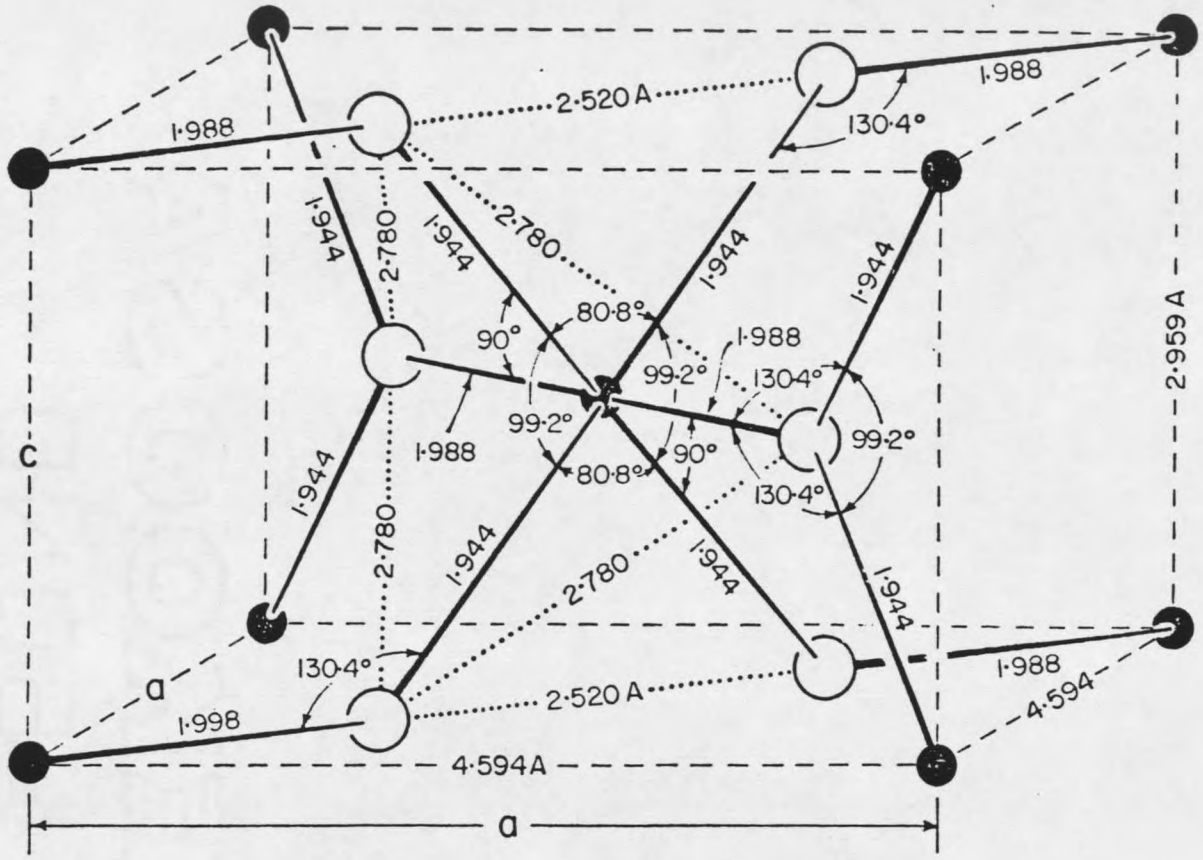

Figure 1. Unit cell of rutile TiO_2 (see reference 4). Black and white circles represent Ti^{4+} and O^{2-} ions, respectively.

From general group theoretical results [7] it is well-known that an octahedral ligand field causes the five degenerate Ti3d states to split into two states of e_g symmetry and three states of t_{2g} symmetry, but leaves the three O2p states unaffected. This effect is retrieved in the bulk electronic structure, since the octahedral environment is nearly preserved in the crystal, leading to two valence- and two conduction subbands of $e_g(3z^2-r^2,xy)$ and $t_{2g}(xz,yz,x^2-y^2)$ symmetry [2,8]. Due to the comparatively high ionicity of TiO_2 of 60-70 % [2] on Philip's ionicity scale, estimated from Raman Spectroscopy [9] and Positron Annihilation [10] studies, the valence and conduction bands are mainly derived from O2p and Ti3d orbitals, respectively. The fairly large optical band gap was determined to be 3.05 eV near room temperature [11]. The pure stoichiometric TiO_2 crystal is thus a transparent insulator showing a bulk conductivity of approximately $10^{-13}\,\Omega^{-1}cm^{-1}$ [12,13].

The phase diagram of the Ti-O system is complicated [14,15]. Below 2100 K (the melting point of TiO_2), there exists at least eight intermediate titanium oxides (Ti_nO_{2n-1}, n=3 to 10) between Ti_2O_3 (titanium sesquioxide) and TiO_2.

On reduction by heating in vacuum or hydrogen at 870 K for an hour, oxygen is partially lost from the TiO_2 lattice (the equilibrium oxygen partial pressure above TiO_2 at

870 K being about 10^{-18} mbar [15,16]), and the crystal becomes first yellow and then blue in color. In this case, transport measurements indicate that the crystal becomes an n-type semiconductor, and Paramagnetic Resonance studies show the presence of Ti^{3+} species [4,15]. The oxygen concentration can be restored by heating the reduced crystal in an oxygen atmosphere of about 250 mbar at 870 K for 1 hour, as shown by the color change of the crystal from blue to yellow [15].

In 1952, Cronemeyer [11] found that the blue color of the TiO_2 crystal arises from an optical absorption maximum at 0.73 eV and that further reduction of rutile leads to an opaque crystal. From weight losses and Hall coefficient data he calculated the bulk density of conduction-band electrons to be 10^{20} cm^{-3} in opaque crystals.

From further Infrared Absorption studies [17] Cronemeyer concluded that oxygen vacancies can be considered as doubly ionizable donors (two electrons are trapped at each oxygen vacancy), which are responsible for the conductivity of nonstoichiometric rutile. The existence of several donor levels in the band gap of defective rutile was mainly derived from the temperature dependence of the conductivity and Hall mobility [11,18,19]. Measurements of dielectric constants [20,21], Infared (IR) and Optical Absorption results [11,17] as well as studies of the dependence of the conductivity and Hall mobility on the

degree of reduction of rutile [16] led to the assumption that these donor levels can indeed be assigned to differently ionized bulk oxygen vacancies [22].

In this model, each bulk oxygen vacancy V_O is associated with two Ti^{3+} species ($2Ti^{3+}$ V_O) and can be ionized twice. The corresponding ionization potentials give rise to two different donor levels in the band gap, and were found 0.15 to 0.20 eV and 0.75 to 1.0 eV below the lower conduction-band edge E_C [13].

Ti^{3+} ions in the bulk of rutile may also be described as donors. They are assumed to be located at regular lattice sites [21,23] as well as interstitial sites [24,25]. Electron Spin Resonance (ESR) data [26,27] as well as studies of the internal friction [28,29] support both hypotheses.

Oxygen interstitials were only observed at oxygen partial pressures above 1 mbar [30] and lead to acceptor-type levels in the band gap, and even to p-type conduction at higher oxygen pressures [30].

The oxygen vacancy concentration obtained by a high temperature treatment (see above) with the help of reducing gases (H_2 or H_2O [11,31], CO or CO_2 [25,32]) is "frozen" by quenching down to temperatures below 800 K [33,34]. Although the thermodynamically stable oxygen vacancy concentration was determined to be less than 3.4×10^{12} cm^{-3} at temperatures below 600 K [35,36], no

changes in the bulk stoichiometry are observed below 800 K during the exposure of oxygen. Reversible uptake and removal of oxygen is only observed above 800 K [37].

The diffusion of titanium in the TiO_2 bulk was studied by Carnahan et al. [24], who derived a diffusion activation energy of 1.04 eV from changes in optical absorption.

Haul and Duembgen [38] studied the diffusion of oxygen in TiO_2 by means of gas/solid isotope-exchange experiments with ^{18}O-labelled oxygen. In the temperature range between 980 and 1570 K, they calculated a diffusion activation energy of 2.65 eV and a diffusion coefficient of $2.0 \times 10^{-3} \times \exp(-2.65\ eV/k_BT)\ cm^2/sec$ for oxygen diffusion (see also reference 1).

Many physical properties of rutile TiO_2 such as electrical conductivity, Hall mobility and dielectric constant are highly anisotropic [15] and have been investigated extensively during the last decades.

Different models such as the multiple-band model and the polaron hopping model have been suggested to explain the charge-carrier transport mechanism and thus the conductivity of rutile.

The scattering of electrons at ionic lattice defects and point defects is believed to be the dominant mechanism at temperatures below 50 K [21,39,40], whereas above 80 K

only scattering at acoustic and optical phonons has been considered, in terms of a multiple-band [16,18,40,41] as well as a polaron model [42-44,49].

Becker and Hosler [18] deduced the existence of multiple-band conduction in n-type rutile for temperatures above 40 K from studies of Hall coefficients and electrical conductivities from 2 to 600 K. They calculated the separation between the lowest conduction band and the bottom of the next higher one to be 0.05 eV, and showed that impurity and surface conductivity could be neglected.

Bogomolov and Zhuze [42] performed electrical conductivity and Hall mobility measurements on slightly reduced single-crystal rutile (parallel and perpendicular to the c-axis) in the range of 78 to 700 K. From their low Hall mobility values they concluded that the electrical conductivity of rutile can be described in terms of a hopping model of polarons with large effective masses rather than by a multiple-band model.

In 1968, Goto and Okada [44] presented results obtained from high-frequency conductivity measurements. Their results showed an increase in the bulk conductivity above 100 MHz and a saturation above 24 GHz. The magnitude of the dispersion turned out to be independent of temperature. They attributed the high-frequency conductivity in (reduced) rutile to the hopping conduction of small polarons localized around lattice defects.

Since 1970, both the multiple-band and the polaron model have been accepted as coexisting models [45], according to which free charge carriers are found in conduction bands and electrons trapped at defects are considered as polarons.

Whitehurst et al. [46] as well as Raalte [47] observed an instability in the electrical conductivity of nonstoichiometric ceramic and crystalline titanium dioxide. The conductivity was found to decrease slowly for as much as several hundred hours at constant measuring temperatures lying between 273 and 373 K, following quenching from temperatures between 470 and 670 K. Whitehurst's experimental curves showed that the conductivity varied with time at the measuring temperature according to:

$$\sigma = \sigma_e + B \times \frac{\sigma_0 - \sigma}{t} \qquad (1)$$

where σ, σ_0 and σ_e are, respectively, the conducivities at time t, at t=0 (immediately after quenching) and at equilibrium ($t \rightarrow \infty$). The factor B is a constant during a given isothermal experiment but, in general, depends on σ_0 and σ_e as well as temperature.

Whitehurst et al. interpreted their results in terms of the theory of reaction rates on the assumption that

electrons are trapped out of conduction states into empty traps. They calculated extremely small trapping cross sections of about 2×10^{-27} cm^2 [46].

Extensive studies on bulk Hall mobilities of TiO_2 have been presented in the literature during the last two decades. The Hall mobility μ strongly depends on the crystal temperature T, but does not show a dependence on the charge carrier concentration above 200 K [18,48]. The temperature dependence can be expressed as

$$\mu = a_1 \times T^{-a_2} \qquad (2)$$

where a_1, a_2 are constants [42,48].

In order to describe the mean mobility over a wider temperature range, a more complicated expression is favored:

$$\mu = a_1 \times T^{-a_2} \times [\exp(a_3/T) - a_4] \qquad (3)$$

where a_3 = const. and a_4 = 0 or 1 [16,49].

Due to comparable experimental conditions, the Hall mobilities used in this thesis (see chapter 5) were taken from reference 42, resulting in:

$a_1 = 10^{5.685}$ $cm^2K^{2.5}/Vsec$, $a_2 = 2.5$, $a_3 = a_4 = 0$ (4)

Dielectric constants of rutile TiO_2 were determined experimentally by Parker [50], Dominik et al. [21] as well as Hollander et al. [20]. Measurements were done parallel

and perpendicular to the c-axis, in temperature and frequency ranges from 1.2 to 1060 K and 10^2 to 10^5 Hz, respectively. The dielectric constants ϵ used in this thesis (see chapter 5) were derived from results given in reference 50. The following approximate temperature dependence was obtained in a temperature range from 300 to 420 K:

$$\epsilon \simeq \epsilon_1 x T + \epsilon_2 \qquad (5)$$

where $\epsilon_1 = -0.066\ K^{-1}$ and $\epsilon_2 = 140.7$.

From measurements of electrical and optical properties Frederikse [41] and Breckenridge et al. [16] determined effective masses of conduction band electrons. Using the expressions for the conductivity, Hall coefficient, and thermoelectric power of a nondegenerate electron gas [41], Frederikse calculated the effective electron mass m_{eff} at the bottom of the conduction band to be $25m_e$, where m_e is the rest mass of an electron. The above relationship will be used in the discussion in chapter 5.

Recalculations of Madelung potentials in stoichiometric rutile TiO_2 are reported by Iguchi et al. [51]. They determined Madelung potentials of 29.53 eV at the Ti^{4+} site and -41.20 eV at the O^{2-} site, leading to the value of 141.5 eV for the Madelung energy per TiO_2 "molecule" and also to the value of 4.810 for the Madelung constant.

Soffer [52] as well as von Hippel et al. [4] discovered during Infrared-Spectroscopic experiments that TiO_2 crystals grown by the Verneuil method always contain residual hydrogen, indicated by a narrow double band near 3300 cm^{-1}, the typical OH stretching vibration. Various reactions in hydrogen and oxygen and the effects of reduction on electron mobilization and the Optical Absorption spectrum were studied subsequently. Theoretical studies [53] on the solubility of hydrogen and deuterium, as well as diffusion experiments [54,55] involving hydrogen and deuterium, have also been reported during the last few years. Johnson et al. [54] have measured diffusion coefficients D for hydrogen both parallel and perpendicular to the c-axis; their results are:

$$D_{\parallel} = 1.8 \times 10^{-3} \times \exp(-0.59\ eV/k_B T)\ cm^2/sec \quad \text{and}$$

$$D_{\perp} = 0.38 \times \exp(-1.28\ eV/k_B T)\ cm^2/sec.$$

Surface Structure Including Surface Defects

Titanium dioxide surfaces have been studied by several surface science groups in the past [2,15,56-97]. From the basic science point of view, studies at (110) single-crystal TiO_2 surfaces are of particular interest (geometric model in Figure 2, and reference 80). First, this surface is the thermodynamically most stable surface of TiO_2 [65,79,86,94] and is expected to make possible the study of reversible solid-gas interactions. Secondly, ideal TiO_2 surfaces show no intrinsic surface states in the band gap [65,79,86].

States may, however, be induced by the formation of either point defects of the ideal TiO_2 lattice, such as vacancies or interstitial atoms, or of extrinsic defects associated with foreign atoms [45,57,59,62,63,65,79]. Electronic states in the gap have been associated with the existence of intrinsic, paramagnetic defects [65,79,80], and earlier studies on the defect formation at $TiO_2(110)$ [56,79] indicated that filled band-gap defect surface states correspond to $2Ti^{3+}$ V_{Os} vacancy complexes, although the detailed geometry of those complexes is not precisely known.

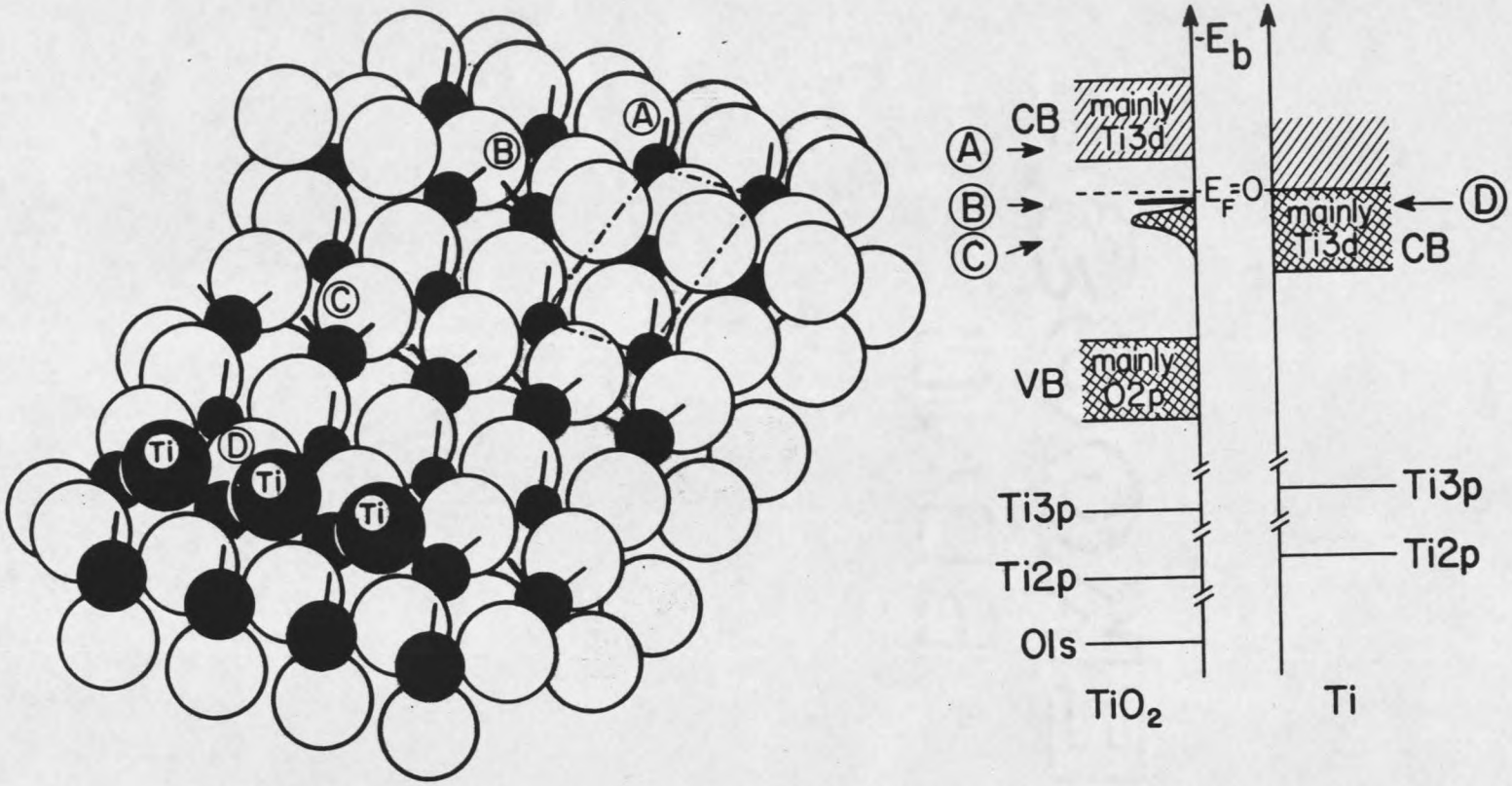

Figure 2. Left: geometric representation of the $TiO_2(110)$ surface with different types of intrinsic defects (see text). White circles represent oxygen, black circles titanium species.
Right: schematic energy diagram for TiO_2 and Ti, indicating the expected energetic positions of the different defects (see reference 80).

The most probable type of surface point defect at TiO_2(110) is shown in Figure 2 (black circles: Ti ions, white circles: O ions) by the missing O ion (labelled B) that bridges two sixfold-coordinated Ti ions. When a bridging O ion is removed, the two neighboring Ti ions become fivefold-coordinated.

However, observations on nearly perfect TiO_2(110) and (100) surfaces [79] show that fivefold coordination may not be sufficient to completely populate band-gap surface states in n-type material resulting in only partially filled donor levels (see reference 79 and chapter 5). For this defect the two Ti ions are very poorly screened from each other, which is somewhat analogous to the situation in bulk Ti_2O_3. This poorly screened pair of Ti ions at the defect site may well share an electron in a similar manner, giving rise to a band-gap surface state. This situation is illustrated in Figure 2, which also presents schematic energy diagrams of TiO_2 as well as Ti. The thick solid line labelled B represents the point-defect (see geometric model) induced donor level in the TiO_2 band gap between the O2p-derived valence band (VB) and the Ti3d-derived conduction band (CB, corresponds to A for the stoichiometric surface). The Fermi level, E_F, indicated by the dashed line, was found to be close to the donor level and changes its relative position to the latter one as a

function of temperature [79]. Thus both partially and completely filled donor levels are possible.

Point defects at TiO_2(110) as indicated by B in Figure 2 can easily be created by high temperature treatments (see references 79-81 and chapter 4) and lead to discrete energy (donor) levels in the band gap. Heavy ion bombardment, however, may result in the formation of line defects accompanied by defect energy bands in the band gap. This phenomenon is illustrated by C in Figure 2 and has been observed during UPS (Ultraviolet Photoemission Spectroscopy) experiments by Henrich et al. [56] as well as Chung et al. [15]. Argon-ion bombardment led to an additional band-gap emission 0.7 eV below the TiO_2 conduction band [56] and was attributed to disorder-induced Ti^{3+}-oxygen-vacancy complexes at the surface.

ELS (Electron Loss Spectroscopy) studies done on ion-bombarded TiO_2(110) surfaces [56] (to be discussed in more detail in chapters 4 and 5) also showed an additional electronic loss feature at a loss energy of 1.9 eV. This feature was assigned to a d-to-d transition involving defect-induced occupied Ti3d states in the band gap as well as empty Ti3d states in the conduction band (see also chapter 5) and has also been detected by Goepel et al. [80,81].

Still further ion bombardment produced ordering of Ti^{3+} pairs into a Ti_2O_3-like surface structure according to

UPS and ELS spectra [56]. The intensities of the defect-induced UPS and ELS features dropped significantly during the exposure to 10^8 L [Langmuir (1L = 1.33×10^{-6} mbar sec)] of oxygen at room temperature as was shown by Henrich et al. [56].

The formation of surface defects at $TiO_2(110)$ apparently results in less positively (compared to the Ti^{4+} ions in the bulk) charged titanium species at the surface due to the occupation of originally empty Ti3d states indicated by B and C in Figure 2.

In a further step of surface chemical reduction, the presence of neutral titanium atoms at the surface will be of interest and is emphasized by big dark circles (labelled D) and a schematic titanium energy diagram in Figure 2. The situation encountered after the deposition of titanium atoms on $TiO_2(110)$ will be discussed extensively in chapters 4 and 5.

Low Energy Electron Diffraction (LEED) studies have been reported, e.g., by Henrich et al. [56], Chung et al. [15], Kao et al. [87] as well as Firment [72]. The stoichiometric $TiO_2(110)$ surface showed a stable (1x1) unreconstructed structure after annealing at 670 K for 15 minutes [15,87] and a (1x2) pattern after an extended annealing at 885 K for 14 hours [87]. A $TiO_2(110)$ surface

sputtered for a dose of $3x10^{15}$ argon ions/cm^2 at an ion energy of 2 KeV exhibited a very diffuse LEED pattern [87].

With the help of UPS measurements, Chung et al. [15] found that the work function increased from 4.6 eV for the TiO_2(110) argon-bombarded surface to 5.5 eV for the well-annealed (110) surface. This result is consistent with that of Henrich et al. [56] reported for the (110) surface. On the other hand, the work function of an initially well-ordered TiO_2(110) surface was unaffected by oxygen-ion bombardment up to $7.2x10^{15}$ ions/cm^2 [15]. Together with the work function measurements and the known values of electron affinity and band gap for TiO_2 (4 and 3 eV respectively), Chung et al. also calculated a surface band bending of 1.7 ± 0.2 eV for both the annealed or oxygen-ion-bombarded (110) surface and 0.9 ± 0.2 eV for the argon-ion-bombarded surface.

Auger Electron Spectroscopy (AES) studies on TiO_2(110) surfaces have been reported, e.g., by Chung et al. [15], Davis et al. [77], Knotek et al. [60] as well as Nishigaki [76]. Chung et al. found an increase in the OKVV/TiLMM ratio from ~1.3 on the argon-ion-bombarded surface to ~1.7 on the annealed TiO_2(110) surface. This ratio turned out to be fairly reproducible over many sputtering-annealing cycles, indicating oxygen deficiency at argon-ion-bombarded surfaces.

During his AES experiments on TiO_2(110) surfaces Nishigaki discovered that the line shape of the Auger transition TiLMV changed upon argon-ion bombardment. He interpreted this phenomenon in terms of Ti^{3+} species at sputtered surfaces, inducing an additional intra-atomic Auger process involving occupied Ti3d states. Similar features have been observed in the course of X-ray-induced Auger Electron Spectroscopy (XAES) studies performed on TiO_2(110) samples by Goepel et al. [80].

The origin of the TiLMV Auger line on stoichiometric and defective TiO_2(110) surfaces is explained in Figure 3 (see also reference 80). A $Ti2p_{3/2}$ (=L) core-hole level is reoccupied by a Ti3p (=M) electron. The de-excitation energy gained in this process causes the emission of a valence-band (V) electron and thus the Auger line TiLMV. Due to the fact that the valence band of TiO_2 is mainly oxygen-derived, the TiLMV Auger transition in TiO_2 is interatomic, involving both titanium and oxygen ions. In the presence of surface defects, however, Ti3d-derived states are found in the band gap (see above) and make possible an additional intra-atomic TiLMV Auger transition (see arrows in Figure 3) involving titanium energy levels only. Owing to the higher cross section for intra-atomic Auger transitions, even very low concentrations of surface defects, i.e. Ti^{3+} ions, cause an additional peak of higher kinetic energy in the TiLMV line.

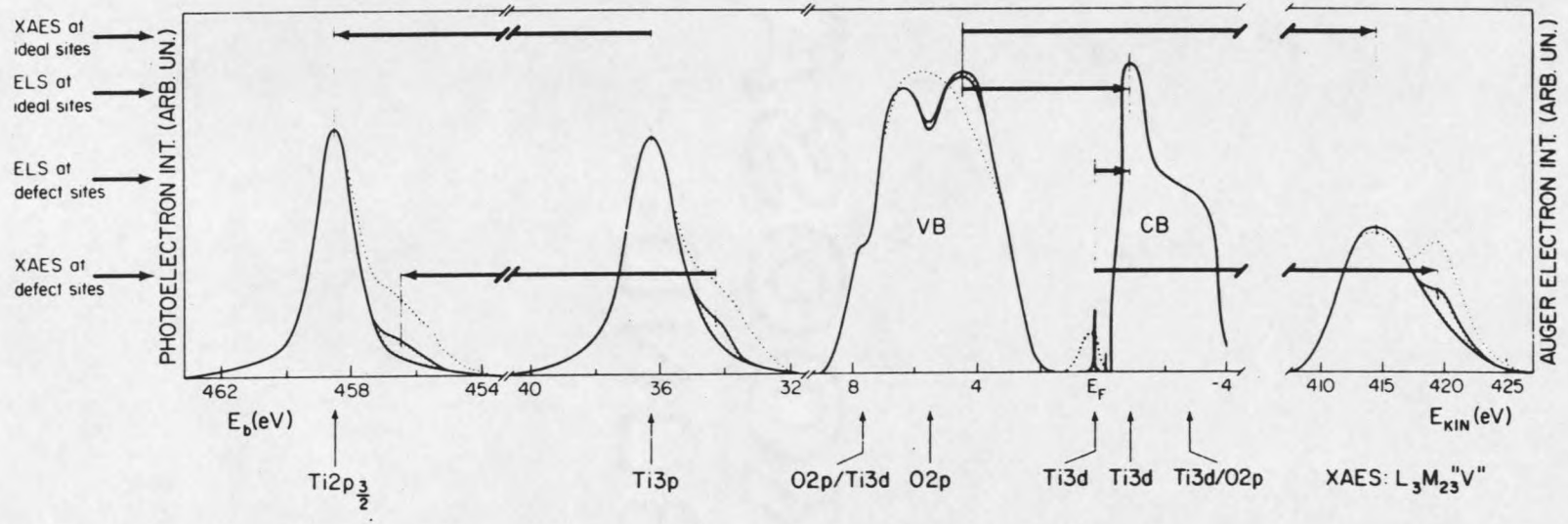

Figure 3. Schematic representation of XPS, XAES and EELS transitions at ideal and defective surfaces (see text and reference 80).

The results obtained by Nishigaki and Goepel et al. present evidence from Auger Spectroscopy to support the proposal by Knotek and Feibelman [61,76], who, suggesting the core-hole Auger decay model for O^+ desorption from TiO_2, found a large drop in desorption yield from surfaces upon sputtering. Their model assumes that a negatively charged surface oxygen loses two electrons through the interatomic Auger transition, filling a M-core hole level of a neighboring titanium atom produced by electron stimulation [in Electron Stimulated Desorption (ESD) Spectroscopy, see reference 61]. The sputtering produces Ti^{3+} ions, and the titanium core-hole in the sputtered layer is then de-excited through the dominant intra-atomic Auger decay without accompanying the removal of the adjacent oxygen charge. This process does not induce oxygen desorption, causing a large drop in the yield [76].

TiLMV Auger line-shape studies on various titanium oxides, such as TiO, Ti_2O_3 and TiO_2 (anatase and rutile) have been reported by Davis et al. [77]. Again, it could be shown that this Auger transition is a sensitive indicator of the average stoichiometry of the surface being studied.

Photon-and Electron-Stimulated Desorption experiments (PSD and ESD) have been performed on clean and oxidized Ti(0001) surfaces by Bertel et al. [66-68], who studied the decay channels of the 3p resonances in 3d transition metals and also discovered that clean Ti(0001)

surfaces can easily be oxidized at room temperature during 4 to 100 L exposures of oxygen. Subsequent UPS and ELS measurements demonstrated the presence of a protective TiO_2 overlayer, which turned out to be stable up to 520 K [68].

X-ray Photoelectron Spectroscopy (XPS) studies on titanium dioxide have been reported e.g. by Scrocco [97], Sham et al. [88], Murata et al. [78], Kao et al. [87] as well as Goepel et al. [79,80].

Sham et al. performed angle-resolved XPS studies on clean and hydrated TiO_2 (rutile) surfaces and observed one set of Ti2p peaks and more than one O1s for the clean TiO_2 sample, suggesting that oxygen ions terminate at the surface. These ions are strongly polarized by the surface cations which are believed to be half-buried under the very first layer of oxygens. Thus the Ti ions experience a smaller change of potential than surface oxygen ions and the binding-energy shift for surface Ti^{4+} ions cannot be resolved [88].

Goepel et al. discovered that high temperature low-oxygen-pressure treatments or moderate ion bombardment of TiO_2(110) samples lead to the formation of surface defects with characteristic shifts in the cation (Ti2p and Ti3p) core-levels of 1.7 eV towards lower binding energies and in the anion (O1s) core-level towards higher binding energy. Simultaneously, attenuation of nonbonding O2p valence band states was observed [79,80].

High-resolution Electron-Energy-Loss Spectroscopy (EELS) experiments on TiO_2(100) and TiO_2(110) surfaces have been carried out by Kesmodel et al. [82] and Rocker et al. [81], respectively. The existence of highly intense surface optical (Fuchs-Kliewer) phonons (see references 98,99 and Appendix B) could be shown on both surfaces. Rocker et al. were able to detect three different vibrational modes at 46, 54 and 95 meV loss energy as well as the OH stretch vibration at 455 meV loss energy on surfaces that had been exposed to atomic hydrogen [81]. They also observed small primary-energy dependent shifts of the Fuchs-Kliewer phonons towards lower loss energies upon defect formation. An attempt was made to explain the physical origin of these peaks in terms of damped harmonic oscillators (see chapter 5).

The surface electronic structure of TiO_2(110), TiO_2(100) and TiO_2(001) surfaces have been investigated theoretically by Kasowski et al. [86] as well as Munnix et al. [2,83-85]. Linear combination of Muffin-Tin Orbitals (LCMTO) energy-band methods [86] as well as scattering theoretic methods [83-85] have been applied to study stoichiometric TiO_2 surfaces.

A recent theoretical study on defective TiO_2(110) sufaces has been performed by Munnix and Schmeits [85], showing that the experimentally observed gap state (see above) on defective surfaces is indeed due to an oxygen

vacancy. This state, however, is not due to the removal of an O atom from a surface bridging site, as frequently proposed, but results from a subsurface oxygen vacancy [85].

In general, the surface conductivity of a semiconductor is given by contributions from conduction in intrinsic and extrinsic (e.g. adsorbate-induced) surface states as well as conduction in space-charge layers [13,79,100,101]. Theoretical [102] and experimental [65,103] investigations showed no evidence for the presence of intrinsic surface states in the band gap of rutile, due to surface-atom reconstruction immediately following the creation of the surface. Conduction in intrinsic surface states can thus be neglected.

Due to extremely low coverages obtained during gas exposures, conductivity in extrinsic (adsorption-induced) surface states at TiO_2 surfaces has not been observed yet, either [104].

Surface Hall mobilities can be estimated within the frame of a space-charge model (see references 100,104 and chapter 5) and are usually determined to be smaller than the bulk Hall mobilities, because of additional scattering processes at the surface [100,104].

Adsorption on Stoichiometric Surfaces

Oxygen Adsorption

The first UPS studies of adsorption of oxygen on TiO_2 surfaces were performed by Henrich et al. [56,58,105]. Subsequently, Lo et al. [59] studied the interaction of O_2 and other gases with the TiO_2(100)-(1x3) surface.

Henrich et al. [56,58,105] found complex adsorption features on TiO_2(110) surfaces after the exposure to oxygen. Up to exposures of 100 L, the UPS spectra showed an additional emission attributed to a specific adsorbed phase. Exposures greater than 100 L gave complicated spectra, indicating the presence of several adsorbed phases. The similarity of calculated difference spectra to the TiO_2 valence-band emission suggested that oxygen adsorption leads to O^{2-} species at the surface, since the bulk valence band is derived predominately from O^{2-} ions [58].

Lo et al. [59] found that the UPS spectrum of a TiO_2(100)-(1x3) surface after oxygen adsorption showed three new emissions with energies of -5.2, -6.8 and -10.3 eV (referred to the Fermi level). Their previous studies [15] had shown that the -10.3 eV emission peak only occurs for a disordered TiO_2 surface, and thus they concluded that adsorbed oxygen forms a disordered overlayer, consistent

with their LEED observations which showed that the (1x3) pattern degraded after oxygen adsorption [59].

The adsorption of oxygen on TiO_2(110) surfaces was also studied by Feierabend [13] and Goepel et al. [79] who measured pronounced decreases $\Delta\sigma_s$ in the surface conductivity as well as increases $\Delta\phi$ in the work function during oxygen exposure. The strong temperature dependence of the conductivity changes indicated that the changes above T = 350 K were mainly determined by bulk diffusion of oxygen due to the small activation barriers of diffusion which result from a strong electrochemical potential gradient near the TiO_2 surface. With the help of a charge-transfer model, attempts were made to separate surface and bulk contributions of the $\Delta\sigma_s$ effects [79].

Separate Thermal-Desorption-Spectroscopic (TDS) studies yielded relative oxygen coverages of up to Θ = 0.015 after 3000-sec exposures (P_{O2} = 6.7x10^{-6} mbar, T = 303 K). The activation energy of desorption was determined to be E^{des} = 0.97 eV.

The partial charge (see chapter 5) transferred from the TiO_2 substrate to each chemisorbed oxygen molecule was assumed to be δ = -1, according to studies performed by Hupfeld [106] as well as Goepel et al. [101,107,108]. From this point of view, oxygen is believed to adsorb as O_2^{-1},chem.

From the initial time derivative of $\Delta\sigma_s(t)$ an initial sticking coefficient of $S_{O2} = 8x10^{-5}$ (T = 303 K) was estimated (see also chapter 5) for oxygen adsorption. By analogy to results obtained on ZnO($10\bar{1}0$) surfaces [101,107,108], it was furthermore assumed that no changes in the electron affinity (and thus no changes in the normal component of the surface dipole moment) occur upon the adsorption of oxygen on TiO_2(110).

Hydrogen Adsorption

The nature and extent of the interaction of hydrogen with transition-metal-oxide surfaces are still largely unknown [65]. The interaction of hydrogen with different TiO_2 surfaces was first investigated by Henrich et al. [58,65], Lo et al. [59] as well as Knotek et al. [62-64].

Lo et al. [59] observed that a 10^5 L exposure of molecular hydrogen to a TiO_2(100)-(1x3) surface at 300 K induced three UPS emission peaks at -5.5, -7.7 and -10.8 eV respectively. The work-function change was measured to be -0.4 eV, indicating donor-type adsorption of hydrogen on stoichiometric TiO_2(100)-(1x3).

During Electron-Stimulated Desorption (ESD) experiments on TiO_2 surfaces Knotek [63] found evidence that an annealed TiO_2 surface, which has no adsorbed hydroxyl species, is compensated by H-atoms, bonded in both hydride-type bonds with Ti ions, as well as hydroxyl-type

bonds with subsurface or bridgebonded oxygens. Such a "compensated" surface turned out to be very unreactive with adsorbates. Furthermore, hydrogen was found at high levels in the near-surface region as a contaminant [63].

Feierabend [13] and Goepel et al. [79] have reported measurements of surface conductivity and work function changes upon the exposure of a TiO_2(110) sample to molecular hydrogen. Surface conductivity increases indicated donor-type adsorption of hydrogen species. Separate Thermal-Desorption-Spectroscopic (TDS) studies yielded an isosteric heat of q_{st} = 0.86 eV and an activation energy of desorption of E^{des} = 1.06 eV. The partial charge residing on each adsorbed hydrogen species was calculated to be δ = 0.01. From both surface conductivity and work function changes, an adsorbate-induced dipole moment (normal component) of μ_{ad}/ϵ_s = -12 Debye was calculated (ϵ_s = unknown surface dielectric constant). An initial sticking coefficient of $S_{H2} = 1 \times 10^{-6}$ was estimated for hydrogen adsorbed on TiO_2(110) at room temperature.

Water Adsorption

The adsorption of water on TiO_2 surfaces was studied by Henrich et al. [57,58], Lo et al. [59] as well as Bermudez et al. [92].

At low water exposures (1-10 L, at room temperature), Henrich et al. [57] found evidence for the presence of OH free radicals on stoichiometric $TiO_2(110)$. At high exposures (up to 10^8 L, at room temperature), a spectrum of slightly perturbed adsorbed H_2O was observed, with the a_1 molecular orbital shifted 0.7 eV towards tighter binding. This suggested that H_2O binds to the surface of TiO_2 via its a_1, in-plane O lone-pair orbital.

Lo et al. [59] detected three distinct new UPS emissions after exposing a stoichiometric $TiO_2(100)$-(1x3) surface to 10^5 L of water. These peaks were located at -6.1, -7.8 and -11.2 eV binding energy (referred to the Fermi level). The calculated UPS difference spectrum was very similar to the photoemission spectrum of gas phase molecular water, suggesting that water adsorbs as an intact molecule on the stoichiometric $TiO_2(100)$-(1x3) surface.

Sham et al. [88] performed XPS studies on clean (scraped) and hydrated (exposed to H_2O, e.g. 1 min. at 1.3×10^{-3} mbar H_2O) TiO_2 (rutile) surfaces and detected several oxygen sites that were attributed to surface oxygen ions as well as chemisorbed and physisorbed H_2O. Besides molecular H_2O overlayers, two types of surface OH species, namely Ti-OH and acidic OH(s), were discussed.

Adsorption on Defective Surfaces

Oxygen Adsorption

The adsorption of oxygen on defective TiO_2 surfaces was studied by Henrich et al. [56,58,105] and Lo et al. [59]. Apart from a decrease in the intensity of the defect-induced band-gap peak (see above), neither Henrich et al. nor Lo et al. found essential differences between the UPS spectra obtained on stoichiometric and defective (argon-ion-bombarded), Ti3+-rich TiO_2 surfaces. Lo et al. [59] observed that the work function change upon oxygen adsorption increased from 0.2 eV on a stoichiometric TiO_2(100)-(1x3) to 0.3 eV on a defective TiO_2(100)-(1x3) surface.

Hydrogen Adsorption

The adsorption of hydrogen on defective TiO_2 surfaces was studied by Henrich et al. [58,65], Lo et al. [59] as well as Knotek et al. [62-64] and Rocker et al. [81].

Lo et al. [59] again observed three new UPS emissions after a 10^5 L hydrogen exposure to an argon-ion-bombarded TiO_2(100)-(1x3) surface, but the energetic positions of these peaks were shifted relative to the peak positions obtained on a stoichiometric surface. The new binding energies turned out to be -4.3, -7.6 and -10.0 eV. In addition, the work function had increased by 0.1 eV during hydrogen exposure (compared to a decrease of -0.4 eV on a

stoichiometric surface, see above). These phenomena were interpreted as indicating the presence of Ti^{3+} species at the surface which lead to acceptor-type chemisorption of hydrogen by forming Ti^{4+}-H^- complexes at the surface [59].

The results obtained by Lo et al. are strongly supported by ESD and electron-excited Auger Stimulated Desorption (ASD) experiments carried out by Knotek [62,63].

Rocker et al. [81] observed O-H stretch vibrations in EELS spectra obtained on hydrogen-exposed (1000 L, at room temperature) TiO_2(110) surfaces with point defects.

Water Adsorption

The interaction of water with defective TiO_2 surfaces was investigated by Henrich et al. [57,58], Lo et al. [59] as well as Bermudez et al. [92].

On argon-ion-bombarded TiO_2(110) surfaces, Henrich et al. observed the same UPS features that they had already found on stoichiometric surfaces (see above), but on defective surfaces the binding energy shift of the a_1 orbital was determined to be 1.0 eV, compared to 0.7 eV on the stoichiometric surface (see above). This indicates that the bonding between a water molecule and the TiO_2(110) surface is stronger if the surface has defects.

Lo et al. [59] observed significant binding energy shifts of the three water-induced UPS emissions when comparing the stoichiometric to the Ti^{3+}-rich TiO_2(100)

surface. The peaks were found at binding energies of -4.2, -7.5 and -10.1 eV, close to the peak positions obtained after exposing defective surfaces to hydrogen (see above). The similarities of the photoemission spectra obtained on hydrogen-exposed defective surfaces to those obtained on water-exposed defective surfaces were explained in terms of the presence of OH groups on defective surfaces following exposure to water. It was also assumed that hydrogen adsorbs dissociatively on Ti^{3+} rich surfaces and forms surface hydroxyl groups which give characteristic UPS spectra [59].

Furthermore, the TDS spectra obtained by Lo et al. [59] show that adsorbed water is bound more strongly on Ti^{3+} rich surfaces, in agreement with results obtained by Henrich et al. (see above).

In additional ELS studies performed during band-gap (3.05 eV) UV-light illuminations of a clean $TiO_2(100)$-(1x3) surface, Lo et al. [59] also demonstrated that one possible effect of light in photoassisted decomposition of water is to regenerate the Ti^{3+} active sites after water adsorption.

Adsorption of Other Gases

Feierabend [13] and Goepel et al. [79] also studied CO and CO_2 adsorption on $TiO_2(110)$ surfaces by means of $\Delta\sigma_S$, $\Delta\phi$ and TDS measurements. It was believed that during CO exposure at low temperatures (~ room temperature),

additional oxygen vacancies due to CO_2 formation can be formed only in the vicinity of an already existing oxygen vacancy. As a result of repulsion between the remaining adjacent oxygen vacancies after this surface reaction, one of these point defects diffuses into subsurface layers. This explained the experimentally observed increase in $\Delta\sigma_s$ with increasing temperature at almost constant $\Delta\phi$ [79].

No changes in the surface conductivity and work function were observed during the exposure of CO_2.

Furthermore, rutile (defective) surfaces act as catalysts for the decomposition of alcohol [109] and the oxidation of isobutane [110] and carbon monoxide [109,111,112].

The palladium/rutile system is being discussed as a gas sensor for hydrogen [113].

Futher applications of TiO_2 in the fields of photodecomposition of water, photo-oxidation of organic and inorganic compounds as well as gas sensors and catalysts are discussed in references 114-119.

Deposition of Nickel on $TiO_2(110)$

Kao et al. [87] studied $TiO_2(110)$-(1x1) and $TiO_2(110)$-(1x2) surfaces (see above) as well as the $Ni/TiO_2(110)$ interface by means of XPS, UPS, AES and LEED. From binding energy shifts of the $Ni2p_{3/2}$ peak and kinetic energy shifts of the $NiL_3M_{23}M_{23}$ Auger peak as a function of

Ni coverage, they estimated the partial charges transferred to each Ni atom, at a Ni coverage of half a monolayer, to be $\delta = -0.13$ on the $TiO_2(110)$-(1x1) and $\delta = -0.07$ on the $TiO_2(110)$-(1x2) surface. Nickel was found to diffuse into the TiO_2 bulk above 570 K.

CHAPTER 3

EXPERIMENTAL TECHNIQUES AND SET-UPS

The defect structure of the $TiO_2(110)$ surface and its interaction with gases was studied using measurements of conductivity ($\Delta\sigma$) and work function ($\Delta\phi$) changes as well as different electron spectroscopies such as X-ray Photoelectron Spectroscopy (XPS), X-ray-induced (XAES) and electron-induced (AES) Auger Electron Spectroscopy,, high resolution Electron Energy Loss Spectroscopy (EELS) and Electron Loss Spectroscopy (ELS). The surface geometric structure was probed by Low Energy Electron Diffraction (LEED). These techniques will be described in the following sub-chapters. Further details concerning the theoretical background of data evaluation are given in the appendices.

Electron Spectroscopies: XPS/XAES, AES, EELS/ELS, LEED

XPS/XAES and AES

When high-energy (e.g. 10 keV) electrons strike a target such as aluminum, magnesium, copper etc., X-rays with a characteristic energy distribution are emitted due to the reoccupation of ionized core-levels. In addition, bremsstrahlung is observed. Depending on the core levels involved these so-called X-ray lines are labelled, e.g., by $K\alpha_{1,2}$ (main peak) and $K\alpha_{3,4,5,6}$, K_β (satellites) for Mg and Al, and $L\alpha_i$ for Cu (see e.g. reference 120).

X-rays can be used to probe the electronic structure of solids. These are illuminated with X-rays of energy $h\nu$ and emit so-called photoelectrons of kinetic energy E_{kin} according to the Einstein relation:

$$E_{kin} = h\nu - E_b - \phi \qquad (6)$$

Here, E_b is the binding energy of an (ionized) core level, referred to the Fermi level, and ϕ is the work function of the sample.

The measured kinetic energies E_{kin}^{exp}, however, are determined by the work function ϕ_A of the analyzer due to matching Fermi level positions of sample (grounded) and analyzer. This requires a correction term $-(\phi_A-\phi)$ on both

sides of Equation 6, leading to:

$$E_{kin}^{exp} = h\nu - E_b - \phi_A \qquad (7)$$

Further details are discussed in references 120, 153-155.

The intensity analysis of photoelectrons as a function of their kinetic energy is accomplished in electron energy analyzers and yields characteristic core-level spectra that allow the identification of the sample and the estimation of the concentrations of its constituents (see Appendix A).

In addition to the core-level lines mentioned above, we may also observe so-called Auger lines. An Auger line is produced when a X-ray-induced core hole of binding energy $E_{b1}(Z)$ is reoccupied by an electron of lower binding energy $E_{b2}(Z)$. The de-excitation energy gained in this process may be high enough to remove an electron of binding energy $E_{b3}(Z+\Delta)$. This leads to the emission of a so-called Auger electron with kinetic energy

$$E_{kin}(Z) = E_{b1}(Z) - E_{b2}(Z) - E_{b3}(Z+\Delta) - \phi \qquad (8)$$

Here, Z is the atomic number and $0.5 < \Delta < 3.5$ accounts for the extra (positive) charge [156]. Again, the correction term $-(\phi_A-\phi)$ has to be added in order to obtain the measured kinetic energy. Thus the Auger line position in the XPS/XAES spectra is independent of the X-ray energy.

Another commonly used method (Auger Electron Spectroscopy, AES) of producing Auger electrons is achieved by bombarding the sample with electrons of energies up to 3 keV. The resulting AES intensities are higher compared to the XAES intensities. Further details are given in references 120, 156-158.

The X-ray Photo (XPS)- and X-ray-induced Auger Electron (XAES)-Spectroscopic measurements presented in this thesis were carried out in a LEYBOLD-HERAEUS (L-H) ultrahigh vacuum chamber by using X-rays emitted from a magnesium anode in a commercial X-ray gun (L-H RQ10/63). The X-ray energy of the dominant $MgK_{\alpha_{1,2}}$ line is 1253.6 eV. Due to the unavailability of a monochromator weak MgK_{α_3} X-ray satellites were also observed in the core-level spectra (see chapter 4), and the resolution was strongly limited because of the fairly large line width of the X-ray source of 0.8 eV. The photoelectrons were analyzed in a hemispherical capacitor-type energy analyzer (L-H EA11) with an input lens column for variable retardation and variable angle of acceptance. It was usually run at a constant pass energy of ΔE = 100 eV, but could also be operated in a $\Delta E/E_{kin}$ = const. mode. The XPS-spectrometer was controlled by a TEKTRONIX 4052 microcomputer.

The sample was mounted on a directly heated piece of tantalum foil and then attached to a sample rod which could be introduced into the ultrahigh vacuum chamber through a

separately pumped prep-chamber. For sample adjustment the rod could also be rotated about an axis. In addition, the influence of the tantalum holder on the core-level spectra could be minimized by varying the analyzer slit width. Sample temperatures were measured with a chromel-alumel thermocouple, spot-welded to the sample holder.

The L-H vacuum chamber was equipped with a gas inlet system and high purity gases (MATHESON). It was pumped by two water-cooled turbo pumps (L-H TURBOVAC 360), an ion pump (L-H IZ 270) and a titanium sublimation pump (L-H V 150). The ultimate chamber pressure was 4×10^{-11} mbar, the working pressure between 1 and 2×10^{-10} mbar.
A differentially pumped ion gun (L-H IQE 12/38) with xy-raster was installed for sputter-cleaning samples in UHV.

AES and ELS (see below) measurements were carried out in a high resolution, computer-controlled (PDP11: Digital Equipment Corporation) Scanning Auger Microprobe (SAM, model PHI 595 from PHYSICAL ELECTRONICS) whose minimum beam size was about 500 Å. The resolution of its cylindrical mirror analyzer (CMA) was given as $\Delta E/E_{kin} = 0.1$ %. The UHV chamber was pumped by a turbo pump (BALZERS TSU 110), an ULTEK D-I ion pump (eight 25 l/s differential ion pump elements) and an ULTEK titanium sublimation pump. The

ultimate pressure in the PHI 595 chamber was less than 10^{-10} mbar, the working pressure less than 5×10^{-10} mbar.

The sample was directly heated and held by two tantalum clips which were attached to the carousel of a x,y,z,Θ sample manipulator. The sample temperature (above 450 K) was determined from outside the vacuum chamber with the use of an infrared thermometer. A high-powered, differentially pumped sputter gun (PHI model 04-303) with xy-raster was available for surface treatments of the samples.

EELS/ELS

If a low-energy (several eV) electron is scattered from a target surface it may lose (gain) energy nh_s due to surface or adsorbate phonon creation (annihilation):

$$E_{s,n} = E_0 \pm nh\nu_s \qquad (9)$$

E_0 is the incident electron energy and $E_{s,n}$ the energy of the scattered electron to be analyzed, whereas the vibrational quantum number n indicates single ($n = 1$) or multiple ($n > 1$) losses (gains) [- or + sign] of frequency ν_s. Hence the high-resolution intensity analysis of the scattered electrons as a function of their energy $E_{s,n}$ (high resolution Electron Energy Loss Spectroscopy: EELS) probes the surface or adsorbate vibrational structure. In addition, the elastically scattered electrons ($n = 0$) give

information about surface conditions (roughness or smoothness, e.g.) as well as the density of conduction-band electrons (see references 121, 122). Further details concerning surface optical phonons are given in Appendix B.

Incident electrons of higher energy (e.g. 50, 100 or more eV) are also capable of exciting plasmons in metals or of inducing electronic transitions from occupied to unoccupied levels. Hence this spectroscopy, simply called Electron Loss Spectroscopy (ELS), gives insight into the electronic structure of the material being studied. Further details are discussed in references 121 and 155.

All the EELS and some ELS measurements presented in this thesis were carried out in the L-H ultrahigh vacuum chamber briefly described above. For these measurements the sample was mounted on a x,y,z,Θ (plus flip for ϕ-motion) hot/cold manipulator allowing fine adjustments. The sample was directly heated and held by two tantalum clips. A platinum/platinum-10%-rhodium thermocouple was spot-welded to one of the clips to assure reproducible temperatures (450 K < T < 900 K), which were calibrated with an infrared thermometer from outside the UHV chamber.

The EELS spectrometer used (L-H 22) was capable of working at resolutions of about 5 meV with a high counting rate and low background. Its electron optics basically consisted of four cylindrical 127° capacitors, two of which served as pre- and main monochromators that produced an

electron beam of defined energy. After being scattered from the target this electron beam was then directed into the analyzer, consisting of the remaining two capacitors. This so-called tandem system minimized the effect of the angular divergence of the entering electrons on the relative band width of the cylindrical capacitors.

The EELS spectrometer was operated in the ΔE = const. mode which corresponds to sweeping the analyzer slit voltage at a constant voltage between the analyzer capacitor plates. The counts from the channeltron as well as the ramp voltage were read with the TEKTRONIX-4052 computer mentioned above.

Most of the higher loss ELS measurements were carried out in the PHI 595 ultrahigh vacuum chamber. For primary energies between 300 and 1000 eV, resolutions ranging from 0.3 to 1.0 eV could be achieved (see above), and loss features of up to 100 eV were observed (see chapter 4).

LEED

Low energy electrons (100 eV or less) whose wavelengths are of the order of magnitude of lattice constants produce diffraction patterns according to Bragg's diffraction condition for constructive interference:

$$n \cdot \vec{G} = \vec{K}' - \vec{K} \qquad (10)$$

Here, $\vec{K}$ and $\vec{K}'$ are the wavevectors of incident and scattered electrons of wavelength λ, n is an integer and $\vec{G}$ a reciprocal lattice vector whose magnitude is inversely proportional to the pertinent interplanar spacing. For the two-dimensional direct and reciprocal surface lattices we hence find:

$$n_{\parallel}\vec{G}_{\parallel} = \vec{K}'_{\parallel} - \vec{K}_{\parallel} \qquad (11)$$

In one dimension, this equation is equivalent to

$$n_{\parallel}\lambda = a \cdot \sin\Theta_f - a \cdot \sin\Theta_i \qquad (12)$$

because $|\vec{G}_{\parallel}| = 2\pi/a$ and $|\vec{K}| = |\vec{K}'| = 2\pi/\lambda$ for elastic scattering, a is the distance between two surface atoms and Θ_i and Θ_f are the incident and scattering angle measured with respect to the surface normal. In two dimensions $\vec{G}_{\parallel}$ is given as a linear combination of reciprocal base vectors determined by inter-row spacings (in general not equal to the lattice constants). The coefficients in this linear expansion are used to label the diffraction spots [(00), (01), (02), (10), ...] which can be observed, e.g., on a fluorescent screen. Due to the fact that only vectors in K-space are considered in the diffraction condition, the observed pattern is virtually a "magnification" of the two-dimensional reciprocal lattice.

This technique, called Low Energy Electron Diffraction (LEED), thus gives information about the

surface geometric structure and makes possible the determination of surface lattice constants.

The inelastic mean free path of LEED electrons is fairly small (see below), but, due to their finite penetration depth, scattering also occurs at lower-lying sub-surface planes. Constructive interference can be observed whenever the third component of Equation 10 is fullfilled:

$$n_{\perp} \vec{G}_{\perp} = \vec{K}'_{\perp} - \vec{K}_{\perp} \qquad (13)$$

which is equivalent to:

$$2\, d \cos\Theta = n_{\perp} \lambda \qquad (14)$$

Here, d is the (vertical) spacing between two planes and $\Theta = \Theta_i = \Theta_f$ (i.e. the (00)-beam).
If now the primary electron energy (corresponding to a defined λ) is plotted versus the (00)-spot intensity, the resulting maxima in this so-called I-V curve determine the integers $n_{\perp}$ and hence the interplanar (vertical) distance.

A more quantitative, theoretical analysis involving anisotropic and multiple scattering (dynamic theory) also provides information about atomic positions within the unit cell as well as LEED intensities. More detailed information is given in references 123-127.

In common experimental LEED set-ups electrons are produced in electron guns, whereas the scattered electrons

are detected with the use of fluorescent screens, multichannel analyzers or Faraday cups. The LEED pictures shown in the following chapter were obtained with a commercial 4-grid VARIAN LEED optics (model 981-0127) which displays the LEED pattern on a fluorescent screen for further photograhic analysis (radius of fluorescent screen: 6.35 cm, angle of acceptance from the target: 120° at the collector screen).

Conductivity Measurements

The conductivity and the Hall mobility of semiconductors are often determined by applying the 4-point van-der-Pauw method [128,129]. This method makes possible the elimination of influences from electrical contacts during conductivity measurements. The method holds for flat samples of arbitrary shape, if the following conditions are fullfilled:

a) The four contacts are at the circumference of the sample.
b) The contacts are sufficiently small.
c) The sample thickness is homogeneous.
d) The surface of the sample is singly connected, i.e. the sample must not have isolated holes.

Let the four contacts be labelled by A, B, C, D. A current I_{AB} enters the sample through the contacts A and leaves it through the contact B. A potential difference $V_D - V_C$ is measured between contacts D and C. We then define the resistance $R_{AB,CD}$ as follows:

$$R_{AB,CD} = \frac{V_D - V_C}{I_{AB}} \qquad (15)$$

The resistance $R_{BC,DA}$ can be determined in a similar way. It was shown in [128,129], that in this case the

conductivity of the sample is given by:

$$\mathrm{EXP}(-\pi R_{AB,CD}\, d\, \sigma) + \mathrm{EXP}(-\pi R_{BC,DA}\, d\, \sigma) = 1 \qquad (16)$$

Here, d is the thickness of the sample. The above equation is equivalent to:

$$\frac{1}{\sigma} = \frac{d}{\ln 2}\, \frac{R_{AB,CD} + R_{BC,DA}}{2}\, f\left(\frac{R_{AB,CD}}{R_{BC,DA}} \right) \qquad (17)$$

The function f is given via the following transcendental equation:

$$\ln 2\, \frac{R_{AB,CD} - R_{BC,DA}}{R_{AB,CD} + R_{BC,DA}} = f\, \mathrm{arccosh}\left[\frac{\mathrm{EXP}(\ln 2/f)}{2} \right] \qquad (18)$$

The Hall mobility μ_H is calculated from:

$$\mu_H = (d/B)\, \sigma \cdot \Delta R_{BD,AC} \qquad (19)$$

$\Delta R_{BD,AC}$ is the change of the resistance $R_{BD,AC}$ due to the magnetic induction B perpendicular to the sample.

In order to estimate the order of magnitude of the errors introduced if the contacts are of finite size and/or not at the circumference of the sample, van der Pauw derived approximation formulas for a few special cases which are discussed in references 128,129.

In addition to $R_{AB,CD}$ and $R_{BC,DA}$ the resistances $R_{CD,AB}$ and $R_{DA,BC}$ were measured, too, resulting in four conductivity values, which were then averaged to give a more accurate result for the sample conductivity.

The conductivity measurements presented in this thesis were carried out in a PHI 545A ultrahigh-vacuum chamber from PHYSICAL ELECTRONICS, pumped by an ULTEK D-I ion pump, model 7-8957 (eight 25 l/s differential ion pump elements), as well as a titanium sublimation pump. The ultimate pressure after a twenty-hour bakeout was about 2×10^{-10} mbar whereas the working pressure was comparatively high ($\sim2\times10^{-9}$ mbar) due to the cleaning and annealing procedures (see next chapter) required for the UHV sample preparation. Four different high-purity gases (MATHESON), namely oxygen, hydrogen, carbon monoxide and argon could be introduced into the vacuum chamber through VARIAN leak valves (model 951-5106). An ion gun (PHI model 04-161) was used for sputter-cleaning the samples. A 4-grid VARIAN LEED optics (model 981-0127) in connection with a high voltage power supply (KEPCO OPS 2000B) and a lock-in amplifier (ORTEC BROOKDEAL 9503) with built-in oscillator made possible Auger-electron-spectroscopic measurements to check the cleanliness of the samples to be studied.

In order to carry out van-der-Pauw conductivity measurements, two different sample holders were used for two different samples.

Holder 1

A yellowish TiO_2(110) single crystal wafer (1.15 cm x 1.30 cm, thickness: 0.65 mm) had four tiny cavities on one side, close to the edges. These cavities contained small amounts of gold so as to assure good electrical contacts. The contacts became ohmic only after heating the sample to above 700 K, but remained ohmic after subsequent cooling. The sample was fixed to a sapphire oven by four molybdenum wires (diameter: 1 mm), whose tiny tips just fit into the cavities. Insulated stainless steel leads (diameter: 0.25 mm) were spot-welded to these molybdenum wires to carry out four-point van-der-Pauw conductivity measurements. The sapphire oven consisted of two polished sapphire wafers (1.5 cm x 1.5 cm, thickness: 1.5 mm), which were held together by two M1 srews. Tungsten wire (diameter: 0.1 mm) was wound around the bottom wafer, whereas the top wafer served mainly as an electrical insulator with high thermal conductivity.

In addition, four notches were sawed into the sapphire wafers to hold the molybdenum wires and to insulate them from the heater. A chromel-alumel thermocouple was fixed between sample and top sapphire wafer in order to measure the sample temperature. Two stainless steel wires (diameter: 1 mm) were spot-welded to small pieces of tantalum foil which were also held by the M1 srews mentioned above. They served as electrical leads for the

tungsten filament and were directly attached to an electrically insulating piece of machinable ceramic. The latter was screwed to the shaft of a home-made x,y,z,Θ sample manipulator.

Holder 2

Conductivity measurements on an opaque TiO_2 single crystal wafer (1 cm x 1.5 cm, thickness: 0.57 mm) were done with the use of a different, electrically insulating holder (see Figure 4). This holder consisted of three sapphire wafers (2 cm x 2 cm, thickness: 1 mm) forming a "sandwich", which was held together by six screws (diameter: 0.864 mm). The sample was placed on the bottom one and just fit into a rectangular (centered) hole (~1 cm x1.5 cm) that had been etched into the middle wafer, i.e. this wafer served as an insulating frame for the sample. The top wafer was used as a protective cover and contained a sawed-in notch (~0.9 cm x 1.5 cm), which made it possible to reach the surface of the sample with a Kelvin probe (see below). Four tiny pieces of tantalum foil (thickness: 0.025 mm) were pushed down onto the surface of the sample by the top sapphire wafer and served as electrical contacts for van-der-Pauw conductivity measurements. Previous experiments on blue and opaque samples (high conductivity) had shown that these contacts were ohmic.

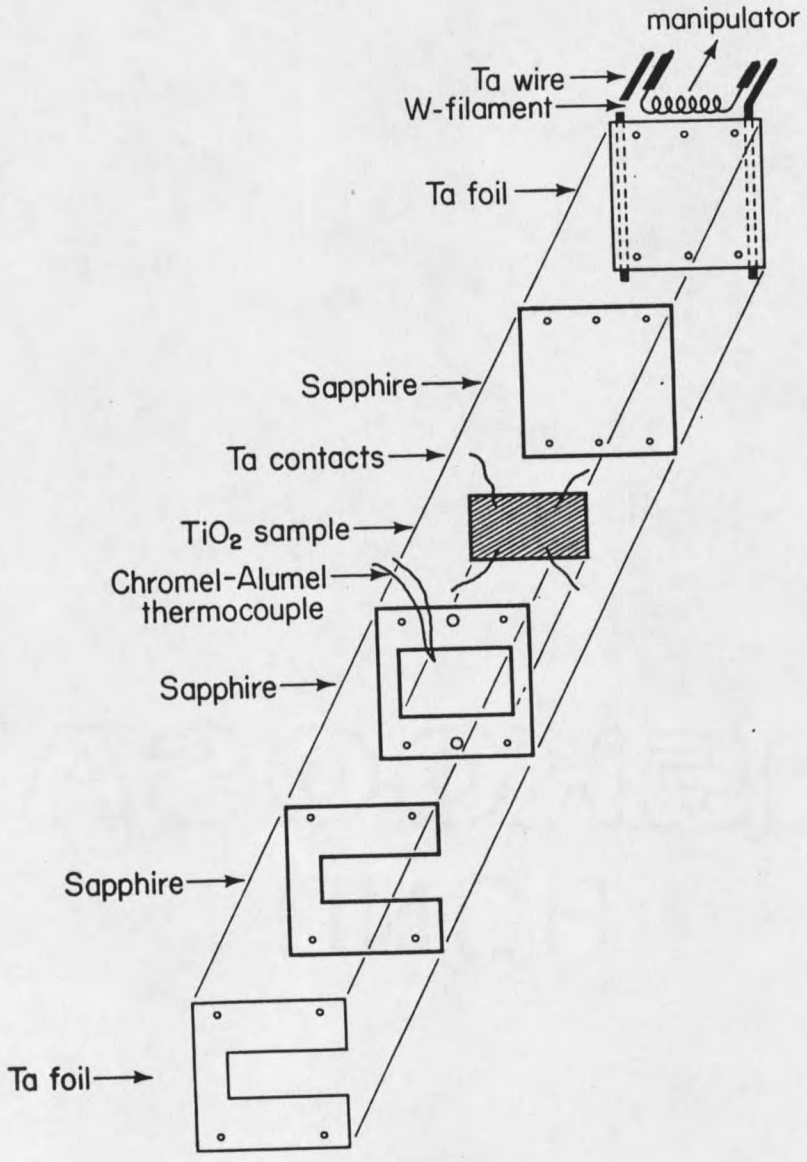

Figure 4. TiO_2 sample holder (see text: "Holder 2) for and measurements.

Insulated stainless steel leads (diameter: 0.25 mm) were spot-welded to the tantalum contacts in order to be able to carry out conductivity measurements. A thermocouple (chromel-alumel) was pushed between the sample and the top sapphire wafer to guarantee reproducible sample temperatures.

The bottom side of the bottom sapphire wafer as well as the top side of the top sapphire wafer were covered with thin tantalum foil (thickness: 0.025 mm), in order to avoid charging problems during AES measurements, on the one hand, and to be able to heat the holder by electron bombardment. Two tantalum wires (diameter: 1.25 mm) were spot-welded to the bottom piece of tantalum foil and were directly attached to the insulating piece of ceramic mentioned above. The latter also held the tungsten filament used for electron bombardment.

The van-der-Pauw resistances defined above were directly measured with a 6.5-digit-multimeter (KEITHLEY 192) - capable of performing 4-wire-resistance measurements - and transferred into a microcomputer (TEKTRONIX 4051) through an IEEE-488 interface bus.

A home-made Rheed-relais unit - also controlled by the microcomputer via a RS-232 interface bus - was capable of switching the four electrical contacts (see above) in a cyclic manner, so that each of the four van-der-Pauw resistances could be measured and stored on magnetic tape.

In addition to these four resistances the multimeter also measured either the thermocouple or the ion gauge voltage. Hence, each van-der-Pauw measurement consisted of taking five readings within 4 to 5 seconds.

In earlier experiments [13,79] it was found that the conductivity of TiO_2 samples varies sensitively with temperature. Thus the sample temperature had to be kept extremely stable during the conductivity measurements. This problem was solved by using a home-made, triac-driven AC-temperature controller which kept the temperature fluctuations below ± 0.01 K. Its input signal was given by the thermocouple voltage and its AC-output terminals were connected to the sample heater.

The sample was first heated with another AC-power supply in such a way that the final equilibrium temperature reached was just below the desired value. Then the temperature controller was turned on and stabilized the temperature within a short period of time.

Measurement of Work Function Changes

The minimum energy required to remove an electron from the interior of a solid to a point just outside the solid is called the work function ϕ of the solid. In the thermodynamical average it is essentially given by the Fermi enery measured with respect to the vacuum level of the solid, but is also influenced by the electric field accompanying the redistribution of surface charge (often referred to as the double layer [130]). as well as adsorbate dipole layers, and band bending in semiconductors.

The work function of a material can be determined by various techniques, such as thermionic, photo- or field emission (see e.g. [131]). With the use of other methods, such as the diode method or the Kelvin method (see e.g. [132-134]), shifts $\Delta\phi$ in the work function - e.g. upon gas adsorption - can be determined by exploiting the fact that a contact potential difference (CPD) is built up between the sample and a reference electrode.

The measurements of work function changes presented in the next chapter were obtained by applying the Kelvin method. In this method, a vibrating reference electrode (amplitude ~0.5 mm) of a so-called Kelvin probe is moved close to the sample (distance <1 mm). This arrangement corresponds to a capacitor with varying distance d between

its parallel faces and hence varying capacitance C(t). The current induced is thus given by:

$$I(t) = V_{CP} \frac{dC(t)}{dt} \qquad (20)$$

V_{CP} is the contact potential difference.
This current provides the input signal of a lock-in amplifier. An external potential bias is then added to the circuit in such a way that no net current flows, when the distance d is variied. When this is achieved, the bias will be equal in absolute value and opposite in sign to the contact potential.

The $\Delta\phi$ measurements were carried out with commercial, piezoelectric Kelvin probes (molybdenum, or gold-plated; resonance frequency: 160 Hz in the first mode, 800 Hz in the second mode) driven by a Kelvin control unit (BESOCKE, DELTA-PHI ELEKTRONIK model 05). An experimental Kelvin-probe set-up is shown in Figure 5.

With this set-up, low noise measurements with a CPD sensitivity of less than 1 mV were possible. In order to guarantee low noise CPD and reference signals (checked with an oscilloscope), a doubly shielded coaxial cable with silver-coated center lead and silver-coated shielding (RG223/U, MIL-C-17F) was used to carry the signal from the floating sample (i.e. the electrical feedthroughs of the manipulator) to the lock-in amplifier in the control unit.

Set up proposal for Kelvin probe

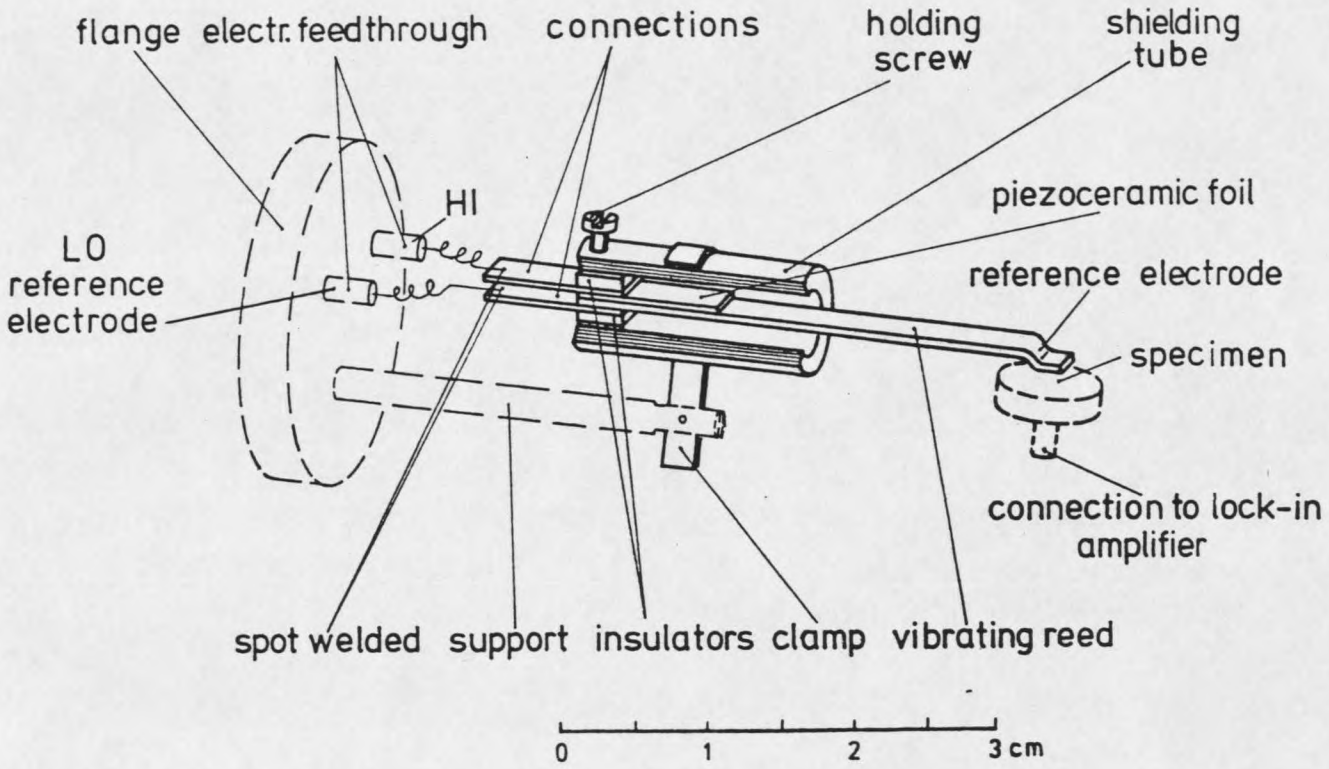

Figure 5. Experimental Kelvin-probe set-up for $\Delta\phi$ measurements.

The input signal was automatically biased, and the bias voltage was read by a 6.5-digit-multimeter (KEITHLEY 192), then transferred into a microcomputer (TEKTRONIX 4051) for further analysis.

One important problem encountered was the sensitivity of the $\Delta\phi$ measurements to mechanical and electrical noise in the laboratory. For this reason, the experiments were carried out during the night. In addition, the use of Turbo pumps was avoided.

Titanium Evaporators and Thickness Monitors

Titanium Evaporators

Two different kinds of titanium evaporators were used to deposit thin layers of titanium on TiO_2(110) crystals.

The first kind of evaporator consisted simply of a short piece of titanium foil (6.5 mm x 0.8 mm, thickness: 0.127 mm) which was mounted on an electrical ultrahigh-vacuum feedthrough and could be heated directly by an AC-power supply. This evaporator was used in the PHI 545A system for a few conductivity measurements only. The distance between the titanium foil and the TiO_2(110) sample - mounted on the sample manipulator mentioned above - was measured to be approximately 6.5 cm.

The advantage of this evaporator was that the current needed for the titanium evaporation could be kept fairly low, i.e. sample and thickness monitor (see below) didn't heat up due to radiation. If, e.g., a current between 4 and 5 A was run through the titanium foil for about 30 seconds, roughly a fifth of a monolayer of titanium was deposited on the TiO_2(110) wafer.

The disadvantage of this evaporator turned out to be the fact that the small piece of titanium foil was quickly used up (the evaporation current had to be adjusted continually) and burnt out very easily. Mainly for these reasons a different, more reliable kind of evaporator was

used for most of the conductivity measurements and for all the $\Delta\phi$ and electron-spectroscopic experiments.

This evaporator consisted essentially of a commercial, cone-shaped tungsten wire basket (TED PELLA INC., maximum diameter: 5.5 mm, height: 7 mm, 9 turns, wire diameter: 0.5 mm, length of wire lead: 4 cm) which had been mounted on an electrical ultrahigh-vacuum feedthrough. The distance between the top of the tungsten basket and the sample was approximately 6.5 cm in the PHI 545A chamber and between 5 and 7 cm in the L-H chamber (note: one sample was introduced on a sample rod, another one on a manipulator).

Small amounts of titanium were filled into the tungsten basket up to a height corresponding to approximately four wire turns. It was found that if a lot more titanium was put into the basket, an unreasonably high current had to be run through the evaporator in order to start the evaporation. Furthermore, the bottom tip of the basket would get very hot and melt the titanium evaporant (melting point of titanium: 1941 K).

A tungsten/tungsten-26%-rhenium thermocouple was spot-welded to the top of the tungsten basket in order to reproduce the evaporation temperature. Calibrations with the use of a thickness monitor (see below) showed that the evaporation rate of titanium was constant for many evaporation cycles (for the same evaporation current and the same thermocouple reading).

If, e.g., a current of 12 A was run through the basket for about one minute (corresponding to a thermocouple reading of 1070 K), roughly half a monolayer of titanium was deposited on the sample mounted on the manipulator of the PHI 545A chamber.

Thickness Monitors

The resonant frequencies of a vibrational system are determined by the total mass of the vibrating body, along with some other physical parameters. Thus, when materials are added to, or removed from the vibrating system, a change in its resonant frequencies occurs. This phenomenon can therefore be used for mass determination [135].

Most of the requirements [135] for these systems are met by high frequency resonators made of thin piezoelectric quartz crystal plates with a specific crystallographic orientation.

A piezoelectric quartz crystal resonator is a precisely cut slab from a natural or synthetic crystal of quartz. The mode of vibration which is most sensitive to the addition or removal of mass, is the high frequency thickness-shear mode [135], whose wavelength is given by

twice the thickness of the plate. This means that the relative resonant frequency shift is given by:

$$\frac{df_q}{f_q} = - \frac{dM_q}{M_q} \sim - \frac{dM_f}{M_q} \qquad (21)$$

Here, M_q is the mass of the quartz crystal and dM_f an infinitesimal amount of foreign mass uniformly distributed over the crystal surface. Here it was assumed that for small mass changes the addition of foreign mass can be treated as an equivalent mass change dM_q of the quartz crystal itself [135]. This assumption allows us to calculate the film thickness d of the added material of density ρ_f:

$$d = - \frac{\Delta f_q}{C_q} \frac{1}{\rho_f} \qquad (22)$$

C_q is the sensitivity or calibration constant of the quartz crystal.

The film thickness d is often given in monolayers of the added material, whose monolayer thickness a_f can be determined with the help of the following equation [136]:

$$a_f = \left(\frac{A_f}{\rho_f \; n_f \; N_A}\right)^{1/3} \qquad (23)$$

A_f = molecular or atomic weight of the material

n_f = number of atoms in one molecule of the material

ρ_f = density of the material

N_A = Avogadro's number

For this thesis the thicknesses of evaporated titanium films were calibrated by using a 10 MHz quartz crystal (CATHODEON T17231, TTC-cut, diameter: 1.27 cm, thickness: 0.185 mm, $C_q = 2.17 \times 10^8$ $sec^{-1}g^{-1}cm^2$) in the PHI 545A system and a water-cooled 5 MHz quartz resonator (SLOAN, $C_q = 5.65 \times 10^7 sec^{-1}g^{-1}cm^2$) in the L-H vacuum chamber.

The 10 MHz crystal was operated by a home-made oscillator. Its frequency was read by a KONTRON frequency counter (model 6006), which was connected to a microcomputer (TEKTRONIX 4051) via an IEEE-488 interface bus.

The 10 MHz crystal turned out to be a lot more sensitive to mass as well as temperature changes than the 5 MHz crystal and was mainly used for depositing sub-monolayer amounts of titanium on $TiO_2(110)$ samples. Its least temperature-sensitive range was measured to be around 340 K. The frequency variation between 328 and 363 K was only ± 2 ppm.

The frequency behavior of this TTC crystal before, during and after the evaporation of titanium is shown in Figure 6.

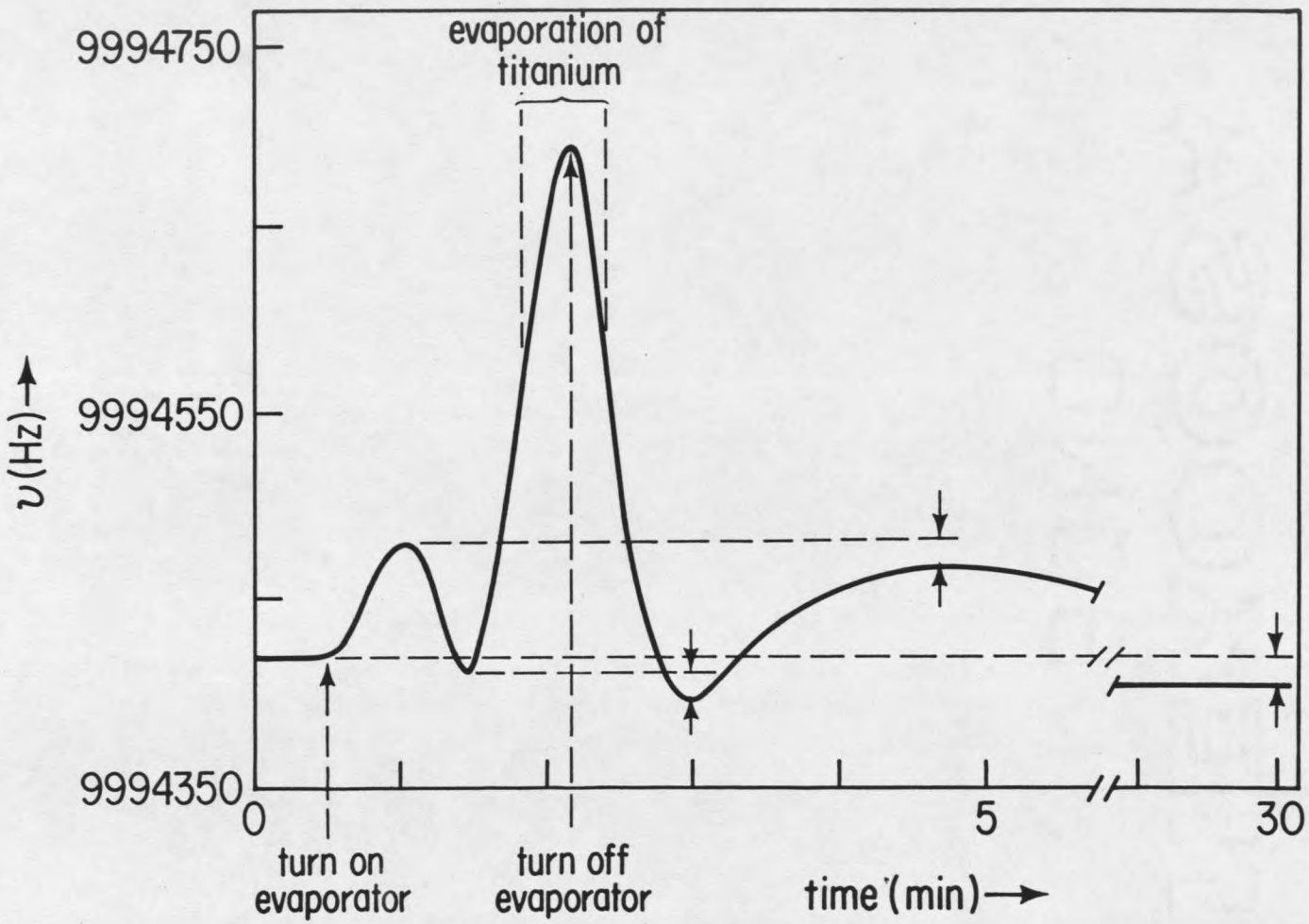

Figure 6. Frequency behavior of a 10 MHz TTC quartz crystal upon evaporation of titanium (see text).

The quartz crystal was mounted on the other side of the electrically insulating block of ceramic mentioned above, i.e. by rotating the manipulator, the quartz crystal could be moved in front of the evaporator in order to determine evaporation rates for the deposition of titanium on the TiO_2(110) sample. The distance between the top of the tungsten basket and the quartz crystal was approximately 8 cm, roughly 1.5 cm greater than the distance between the basket and the TiO_2 sample (see above). Therefore the titanium deposition rate had to be calculated for the TiO_2 sample.

When the evaporator current was increased to its desired value, the frequency of the quartz resonator first increased also, due to radiation. After passing a maximum (see Figure 6) - which was determined to be around 340 K (see above) - the frequency dropped, passed through a minimum (below its former equilibrium value) and then rapidly increased. After the evaporator was turned off, the frequency dropped quickly, and again passed through a minimum and a maximum and, finally, reached its new (smaller) equilibrium value.

But in addition to a lower equilibrium value, downward shifts in the frequencies at the minimum and the maximum were observed (see Figure 6) and this phenomenon facilitated the procedure of finding the resonant frequency shift, because instead of waiting for the new equilibrium

frequency to be reached, the new minimum and maximum values were recorded and compared to the old values (before the evaporation). Separate experiments showed that the average frequency shift determined from the changes in the maximum and minimum values was in good agreement with the change in the equilibrium frequency.

With the help of Equations 22 and 23 it was found that one monolayer of evaporated titanium (2.6 Å) corresponds to a frequency decrease of approximately 25 Hz.

The frequency of the water-cooled 5 MHz crystal used in the L-H vacuum chamber was not very sensitive to temperature changes. While the evaporator was reaching its equilibrium temperature, the frequency of the quartz crystal first increased to a maximum value and then slowly dropped during the deposition of titanium. Due to the water cooling, the new equilibrium frequency was reached very rapidly, after the evaporator had been turned off. In this case, one monolayer of titanium corresponded to a frequency decrease between 6 and 7 Hz.

The sample mounted on the manipulator mentioned above could be moved close to the quartz crystal. Hence titanium was deposited on the sample and quartz crystal at the same time, whereas the sample in the sample rod described above had to be shoved in between the evaporator and quartz crystal, so that no titanium was deposited on the latter.

This made necessary the determination of an evaporation rate before depositing titanium on the TiO_2 sample.

The thickness of evaporated titanium layers was also calibrated by XPS. When small amounts of titanium were evaporated onto a TiO_2 sample, the intensity of the oxygen 01s core-level as well as the oxygen KVV Auger line decreased. By assuming an exponential decrease we found:

$$I(d) = I_0 \, EXP(-d/\lambda) \qquad (24)$$

$I_0/I(d)$ = intensity of the oxygen core-level or Auger lines from a clean/titanium-covered $TiO_2(110)$ surface.

d = thickness of the evaporated titanium layer.

λ = inelastic mean free path (IMFP) of the photo- or Auger electrons emitted.

The kinetic-energy-dependent IMFP's were determined from the "universal" curves published in reference 136. For 01s photoelectrons (E_{kin} = 720 eV) we found λ = 14.6 Å in titanium and λ = 19.7 Å in titanium dioxide. In the case of OKVV Auger electrons (E_{kin} = 510 eV), we calculated λ to be 12.3 Å in titanium and 16.6 Å in TiO_2.

With the knowledge of these values, Equation 24 and the measured intensities I(d) and I_0, we determined the layer thickness d.

CHAPTER 4

EXPERIMENTAL RESULTS

In the first part of this chapter, a method for preparing clean and defect-free TiO_2(110) surfaces will be discussed.

In the second part, electron-spectroscopic results on TiO_2(110) samples obtained by XPS/XAES, AES, EELS/ELS and LEED will be presented.

The third part of this chapter shows results from a representative selection of measurements of conductivity and work function changes.

The experimental results of this chapter will be discussed in chapter 5.

Preparation of Clean Samples

Before introducing the polished titanium dioxide wafers into the ultrahigh vacuum (UHV) chambers, they were cleaned in an ultrasonic acetone bath for about 15 minutes.

In the UHV chamber, most of the carbon contaminants were removed by argon-ion bombardment for about 15 minutes at a primary-ion energy and an emission current of 1000 eV and 3 mA, respectively. In the L-H vacuum chamber, e.g., a target current of approximately 5×10^{-7} A could be achieved by adjusting the argon pressure in the differentially pumped sputter chamber, resulting in a pressure of the main chamber of about 4×10^{-7} mbar.

Subsequently, the samples were annealed in oxygen at 870 K and 6.7×10^{-6} mbar for about 15 minutes in order to remove the residual amounts of carbon.

In a further step, surface defects produced during ion bombardment were annealed in a 6.7×10^{-6}-mbar oxygen atmosphere at 570 K for 30 minutes in order to produce a stoichiometric surface. The annealing process was controlled by monitoring the surface-sensitive TiLMV Auger line (see below). It was found, however, that surface defect annealing could be improved by exposing the samples to higher oxygen pressures at some elevated temperature ($<<$ TiO_2 decomposition temperature under UHV conditions) for longer exposure times, e.g., for 1 hour at 570 K and

5.3×10^{-5} mbar O_2. This procedure was usually adhered to in the PHI 545A vacuum chamber, because a poppet valve made it possible to valve off the ion pump resulting in low working pressures.

After the cleaning procedures described above, small amounts of potassium were still detected in the XPS spectra. Attempts to remove these residual contaminations were not very successful, because the potassium $K2p_{3/2}$ core-level peak reappeared after the temperature treatments necessary for surface defect annealing. This observation led to the assumption that potassium probably diffuses from the bulk to the surface upon heating.

Electron-Spectroscopic Results

The figures presented in this subchapter show results obtained from XPS/XAES (Figures 7-13), EELS/ELS (Figures 14-20) and AES/ELS (Figures 21-24) measurements on $TiO_2(110)$ surfaces. The reciprocal lattice structures of clean and titanium-covered $TiO_2(110)$ surfaces are reflected in the LEED patterns shown in Figure 25.

The lower part of Figure 7 demonstrates the effect of thin evaporated titanium layers on the $Ti2p_{1/2}$ (left peak) and $Ti2p_{3/2}$ (right peak) core-level intensities. Curve a represents the stoichiometric $TiO_2(110)$ surface of a yellowish sample, which was introduced into the L-H vacuum chamber via a sample rod (see chapter 3). The clean stoichiometric surface was obtained by applying the sample preparation methods described above. The small peak to the very right in curve a (E_{kin} = 803.8 eV) is due to the X-ray satellite MgK_3 (see chapter 3) produced by the $Ti2p_{3/2}$ core-level.

The peaks in curve a correspond to Ti^{4+} ions predominantly found in stoichiometric TiO_2 (indicated by the solid vertical line) and therefore appear at comparatively high binding energies (referred to the upper valence band edge E_V) or low photoelectron kinetic energies, respectively.

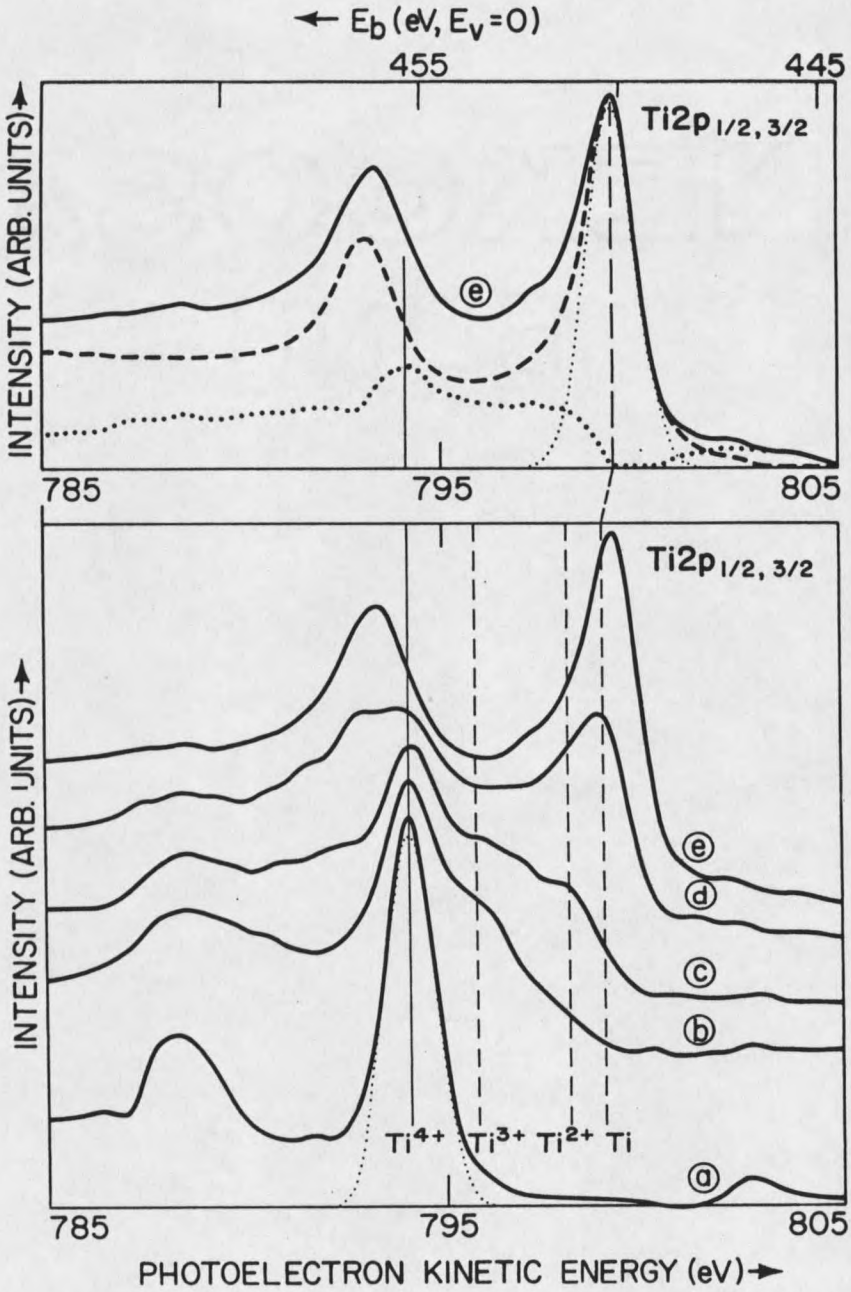

Figure 7. Lower part: Ti2p core-level spectra before (a) and after evaporation of 0.7 (b), 1.1 (c), 2.0 (d) and 4.5 (e) monolayers of Ti.
Upper part: comparison between curve e and the experimentally observed Ti2p spectrum of metallic Ti. Further details are given in the text.

These peak positions could be reproduced on blue TiO_2(110) samples that had been introduced into the L-H vacuum chamber via a sample manipulator (see chapter 3). These interesting results indicate that the (110) surface - and a subsurface region down to at least the XPS sampling depth (~20 Å for the Ti2p photoelectron kinetic energies) - of the blue TiO_2 samples with high defect concentrations can be almost perfectly annealed by the UHV sample treatments described above. The diffusion of oxygen vacancies from the bulk to the surface, however, turned out to be much more pronounced on these samples (see chapter 5), resulting in non-stoichiometries at the surface after a certain period of time.

Curve b was obtained, after 0.7 monolayers of titanium had been deposited on the yellowish TiO_2(110) sample according to the evaporation procedure described in the previous chapter. Both core-level lines are broadened and show additional emissions on their low binding energy side. This phenomenon will be discussed in the next chapter.

Curves c, d and e were recorded for titanium coverages of 1.1, 2.0 and 4.5 monolayers and demonstrate the growth of the $Ti2p_{1/2}$ and $Ti2p_{3/2}$ core-levels of metallic titanium, because the $Ti2p_{3/2}$ line in curve e is found - apart from a small work function change of 0.31 eV - at the peak position expected in titanium (see dashed vertical line "Ti").

In the upper part of Figure 7, curve e is compared to the experimentally obtained [120] Ti2p spectrum of metallic titanium represented by the dashed curve. The difference spectrum calculated by subtracting the dashed curve from curve e is shown as a dotted line and yields the attenuated Ti2p core-level emission from the TiO_2 substrate, covered with a 4.5-monolayer titanium film.

The thin dotted lines under curves a (lower part of Figure 7) and e (upper part of Figure 7) schematically indicate Gaussian line shapes of $Ti2p_{3/2}$ contributions. These curves are found theoretically by fitting Gaussians to the experimentally obtained spectra (see chapter 5).

When the titanium-covered TiO_2 surface represented by curve e was annealed in a 6.7×10^{-6}-mbar oxygen atmosphere at approximately 920 K for at least 15 minutes, the stoichiometric surface and hence curve a could be reproduced. This indicates that either titanium diffuses into the TiO_2 bulk, or titanium overlayers are oxidized to titanium dioxide overlayers .

In Figure 8, curve a again represents the stoichiometric surface, whereas curve b' was obtained after 30 minutes of argon-ion bombardment at a primary ion energy of E_p = 1500 eV and an emission current of I_{em} = 3 mA, resulting in a target current of I_{targ} = 1.1 μA. As in Figure 7, we observe additional emissions on the low binding energy sides of the Ti2p core levels.

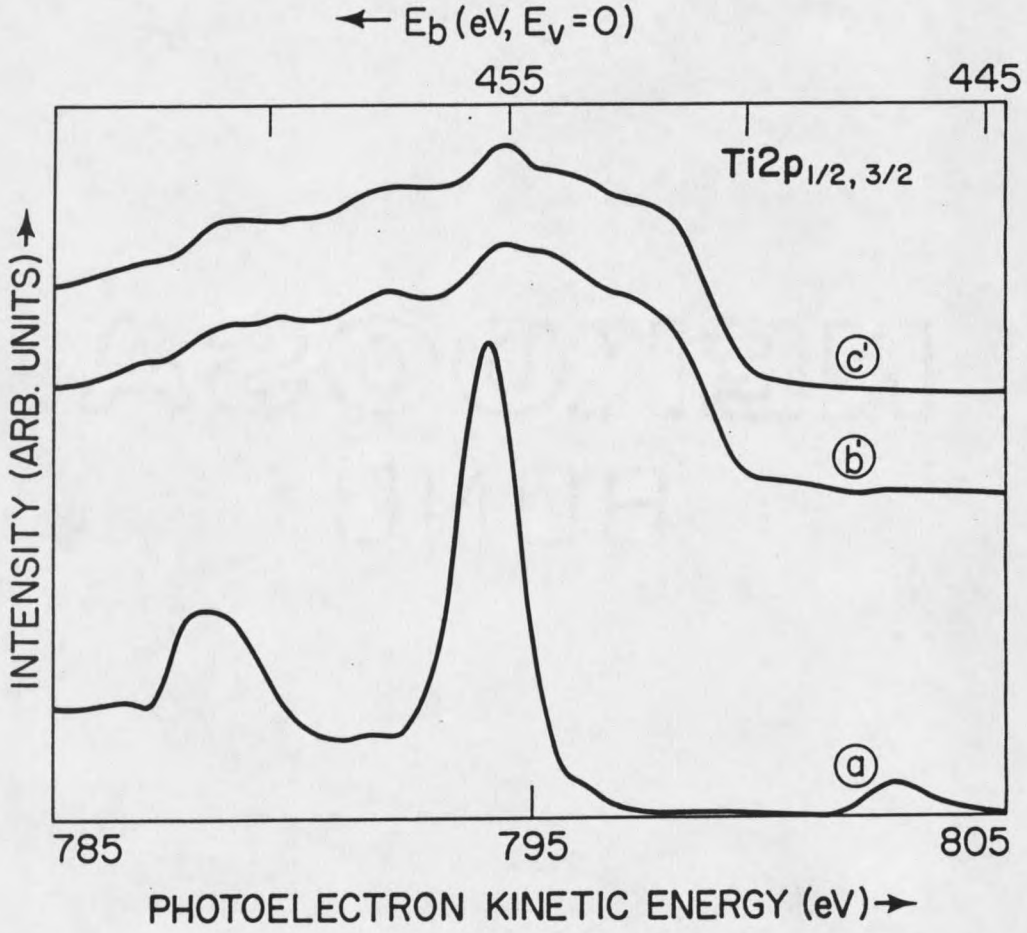

Figure 8. Ti2p core-level spectra before (a) and after argon-ion bombardment for 30 (b') and 60 (c') minutes at primary energies of E_p = 1500 and 2000 eV.

Further ion bombardment at a primary energy of E_p = 2000 eV and an emission current of I_{em} = 3 mA (I_{targ} = 1.6 μA) for about 30 minutes did not enhance these features significantly.

The similarities of the results found on titanium-covered and sputtered surfaces will be discussed in the next chapter.

The spectra in Figure 9 illustrate the shift and the attenuation of the O1s core-level peak of the TiO_2(110) crystal upon evaporation of small amounts of titanium. The curves a to e correspond to the curves a to e in Figure 7, i.e. they were obtained after the same surface treatments and could thus be used to calibrate the titanium layer thicknesses, as was explained in the previous chapter.

The vertical solid line indicates the O1s core-level position in stoichiometric TiO_2, which is composed of Ti^{4+} and O^{2-} ions, i.e. the O1s core-level binding energy arises from doubly negatively charged oxygen ions. A distinct shift in the peak maximum of up to 0.4 eV towards higher binding energies was observed after submonolayer-to-monolayer amounts of titanium had been deposited on the sample. A possible explanation for this phenomenon will be given in chapter 5.

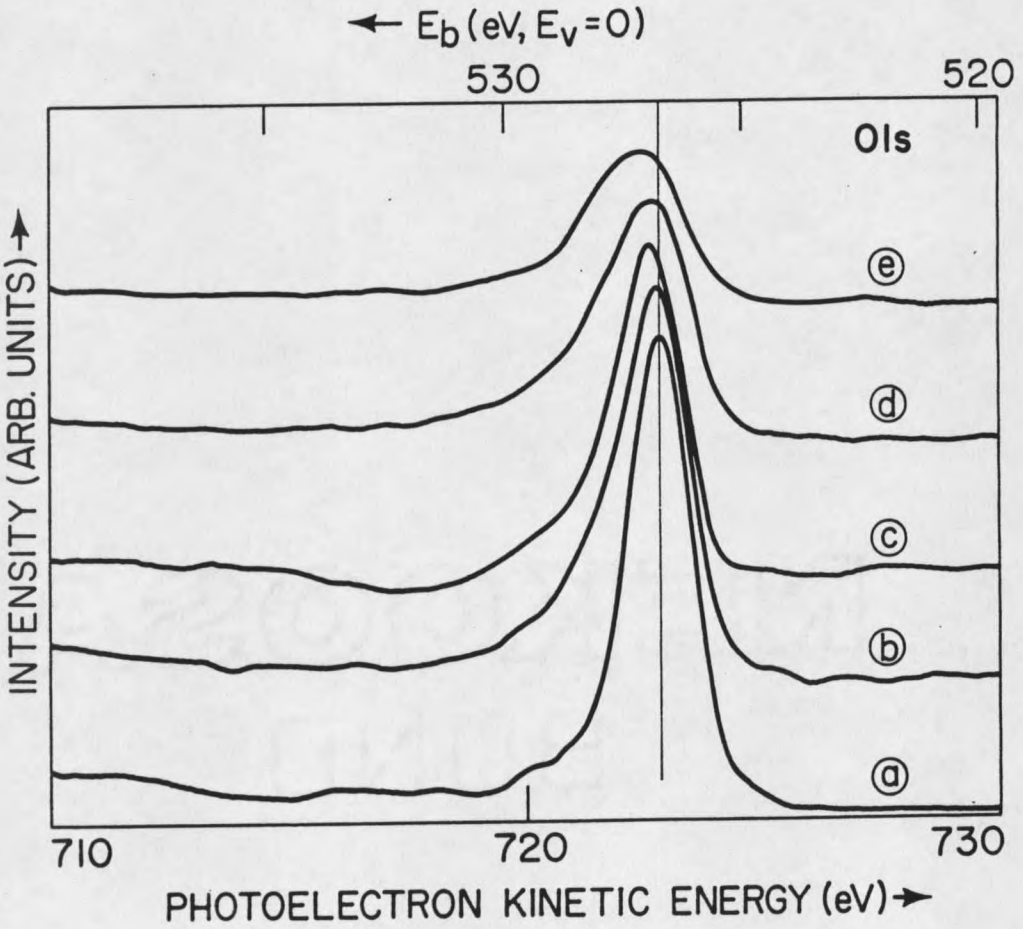

Figure 9. O1s core-level spectra before (a) and after (b-e) evaporation of Ti. The evaporated amounts are the same as in Figure 7.

Figure 10 presents Ti3p core-level spectra a to e that were recorded after the surface treatments explained above. The curves were smoothed, since the signal-to-noise ratio was low in these spectra because of the comparatively low $Ti3p_{3/2}$ cross-section (factor of ~1/10 if compared to the $Ti2p_{3/2}$ cross-section [145]). Due to the limited resolution of the XPS spectrometer (see chapter 3) the expectedly small spin-orbit splitting between the $Ti3p_{1/2}$ and $Ti3p_{3/2}$ levels was not resolved. Similar to Figure 7, we observe the growth of a second peak of lower binding energy upon evaporation of titanium.

The change in the mainly O2p-derived valence band structure after corresponding surface treatments is shown in Figure 11. Due to the small valence band cross-section (factor of ~1/400 if compared to the $Ti2p_{3/2}$ line [145]) the background noise level was fairly high, which again required curve smoothing.

The two maxima in the valence-band structure of curve a indicate the existence of two valence sub-bands in stoichiometric samples (see chapter 5). The intensity of the maximum of lower binding energy drops drastically after the deposition of titanium, as shown in curves d and e, but now an additional band is found several electron volts above the upper valence band edge E_V.

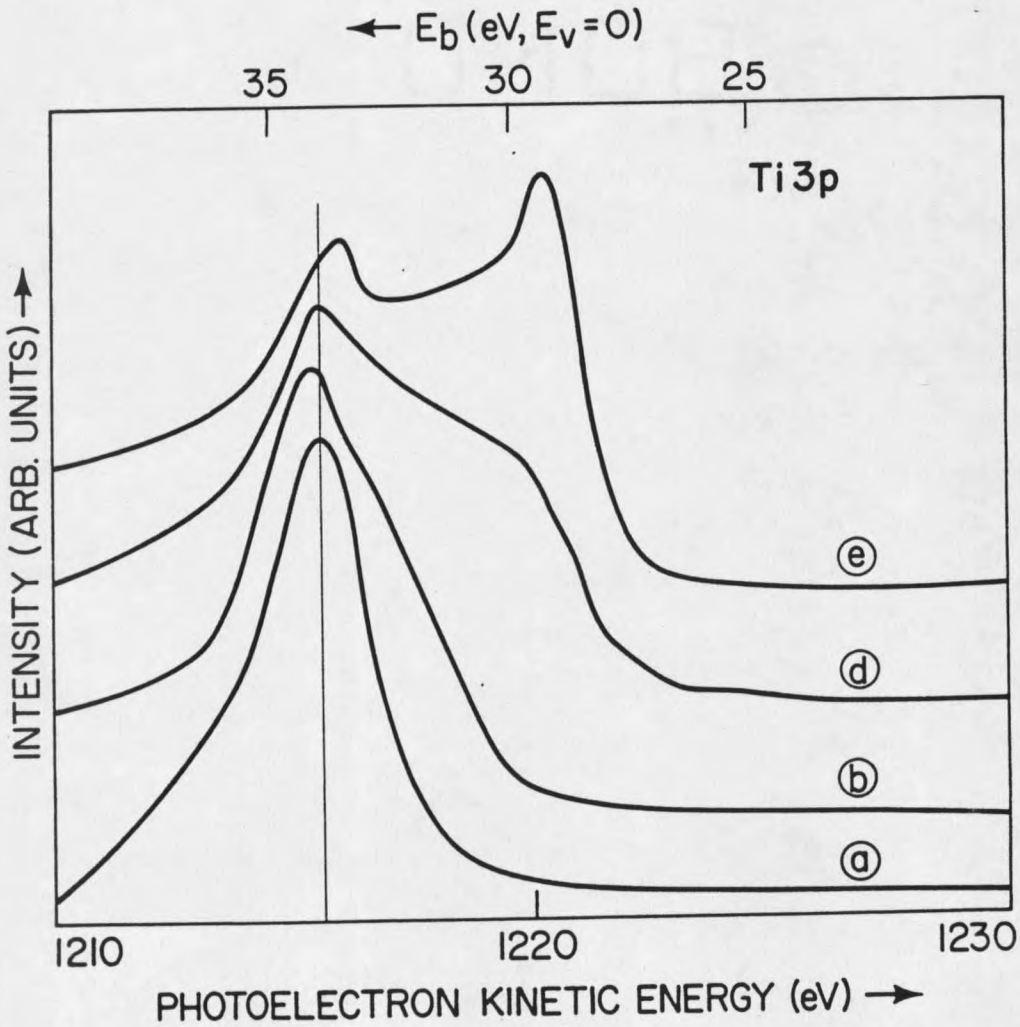

Figure 10. Ti3p core-level spectra before (a) and after (b,d,e) evaporation of Ti. The evaporated amounts are the same as in Figure 7.

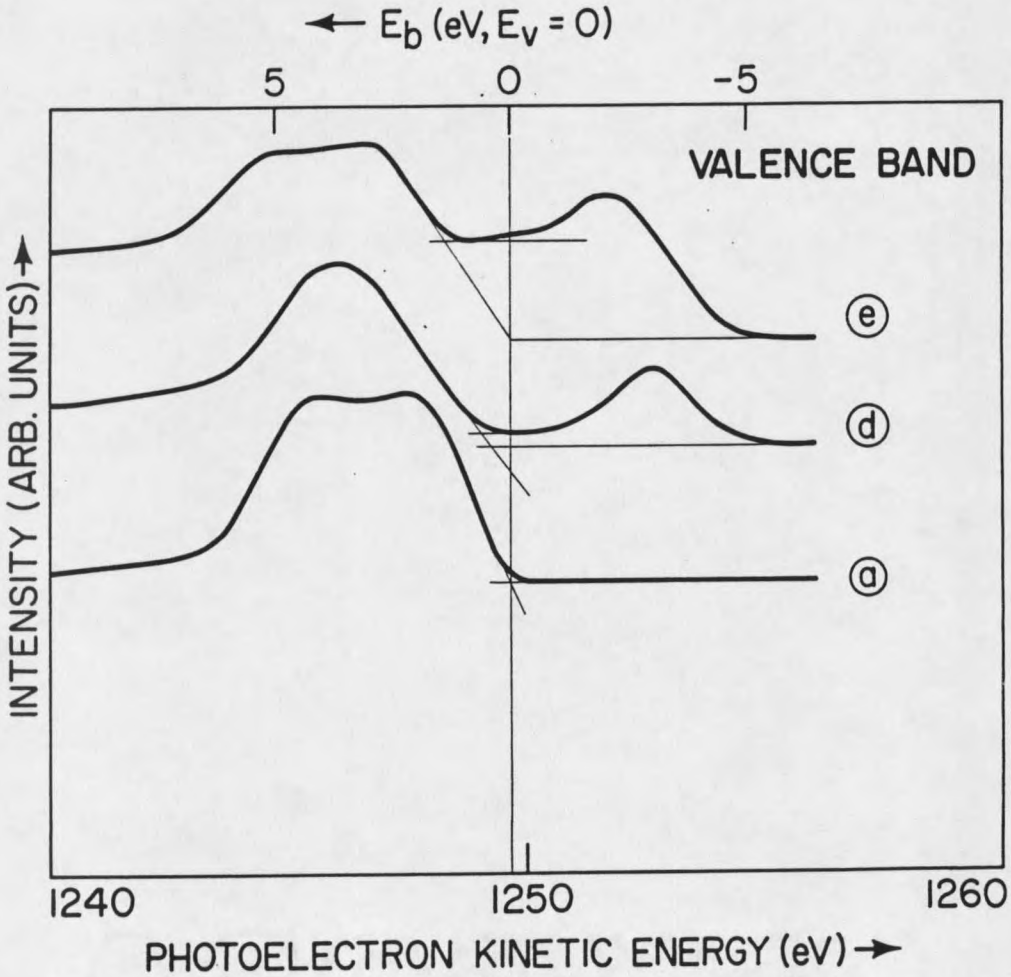

Figure 11. TiO_2 valence-band structure and XPS band-gap emission before (a) and after (d,e) evaporation of Ti. The evaporated amounts are the same as in Figure 7. Further details are given in the text.

The higher the titanium coverage, the more this band smears out towards the original valence band, as can be verified by comparing curves d and e, which correspond to the curves d and e in Figure 7. The horizontal and sloping lines will be explained in chapter 5.

In Figure 12, the changes in the X-ray-induced $TiL_3M_{23}V$ Auger line upon evaporation of titanium are illustrated in curves a to e which were obtained after the surface treatments described above. This Auger line is due to an electronic transition from a $Ti3p_{1/2,3/2}$ (i.e., the M_{23}) level to a $Ti2p_{3/2}$ (i.e., the L_3) core hole with subsequent emission of a valence band (V) electron. It appears to be extemely sensitive to small additions of titanium atoms, because even submonolayer amounts of evaporated titanium cause a second peak in the Auger line, as shown in curve b. This peak grows rapidly with increasing titanium coverage, and is apparently the result of a corresponding Auger transition in metallic titanium. This can be verified by comparing the Auger electron kinetic energy to corresponding experimental data obtained on titanium samples [120].

The following Figure 13 demonstrates the effect of heavy argon-ion bombardment on the $TiL_3M_{23}V$ Auger line shape. Curve a again represents the stoichiometric surface, whereas curve c' was recorded for the same surface conditions that led to curve c' in Figure 8.

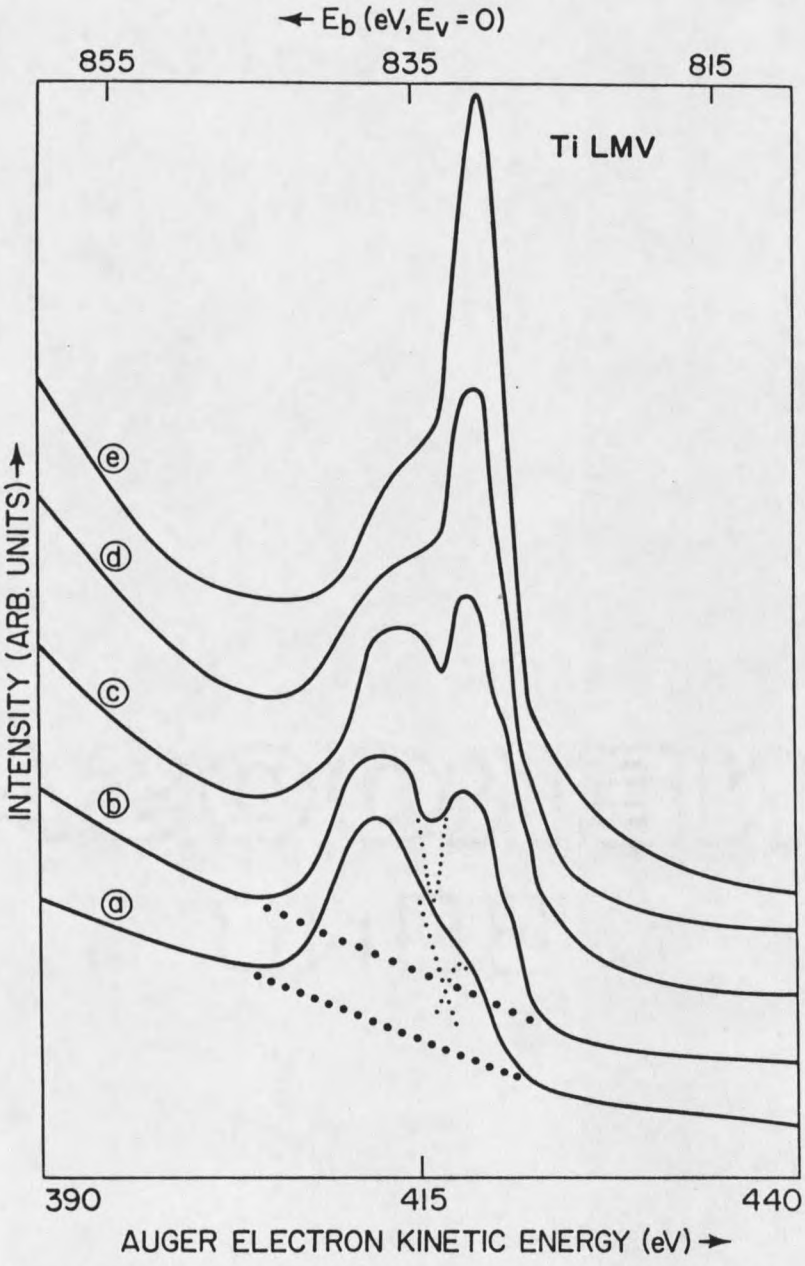

Figure 12. $TiL_3M_{23}V$ Auger transition before (a) and after (b-e) evaporation of Ti, indicating the growth of an additional intra-atomic Auger peak (see text). The evaporated amounts are the same as in Figure 7.

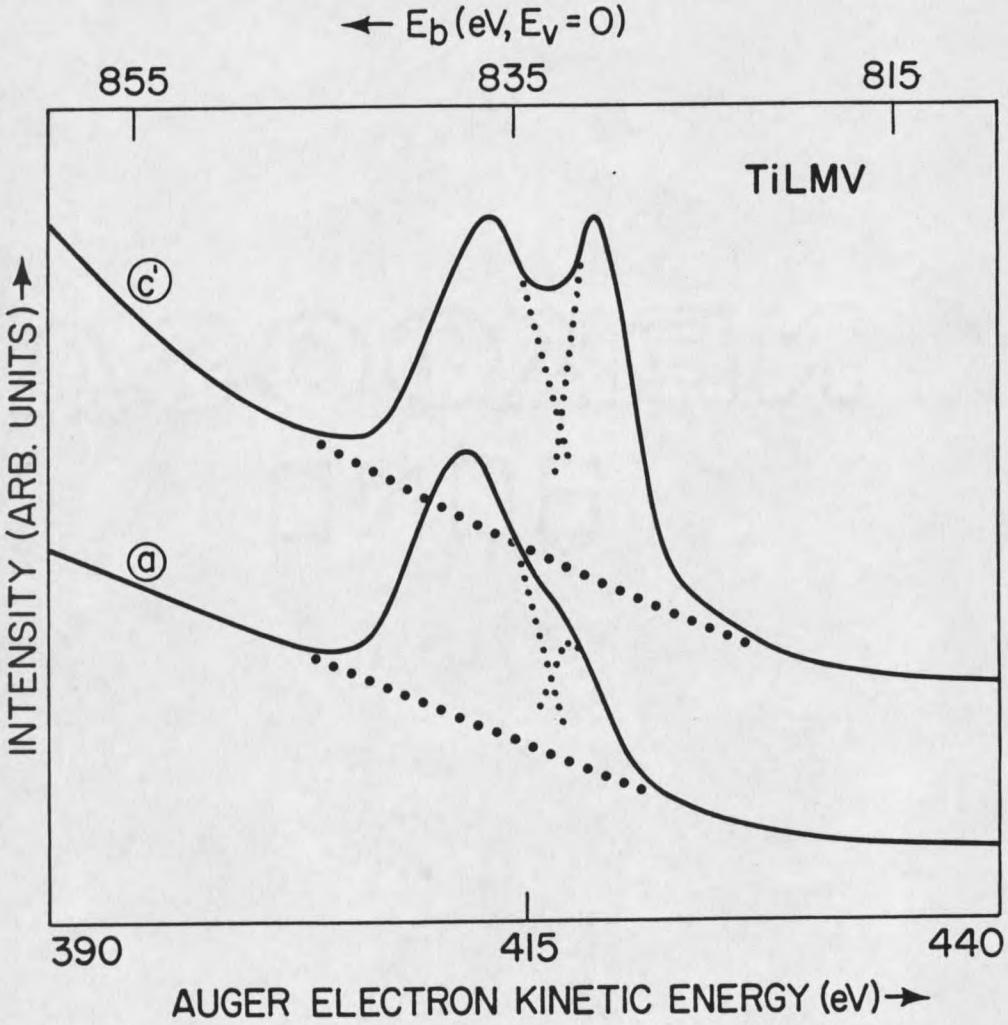

Figure 13. $TiL_3M_{23}V$ Auger transition before (a) and after (c') argon-ion bombardment. The sample pretreatments are the same as in Figure 8.

Again, the similarities in the results obtained on titanium-covered and sputtered surfaces are striking. An explanation for these features will be given in chapter 5.

The dotted lines in Figures 12 and 13 schematically indicate background levels as well as the two (TiO_2- and Ti-derived) contributions to the TiLMV Auger transition.

The following Figures 14-20 show results obtained from EELS/ELS experiments that were carried out on a bluish $TiO_2(110)$ sample in the L-H vacuum chamber described in chapter 3.

Figure 14 presents a survey spectrum (see also reference 81) of the delocalized surface optical (Fuchs-Kliewer) phonons. These are usually found on ionic semiconductor surfaces and were first detected on a $TiO_2(100)$ surface by Kesmodel and Gates [82]. The origin of these phonons will be discussed in more detail in chapter 5 and in Appendix B. Three different vibrational modes at 54, 95 and 46 meV denoted by $\tilde{\nu}_1$, $\tilde{\nu}_2$, $\tilde{\nu}_3$ were observed for a primary electron energy of $E_p = 6.4$ eV in the specular beam direction with $\Theta_i = \Theta_e = 45°$. For the first time, the third mode $\tilde{\nu}_3$ could be resolved, because of an excellent spectrometer resolution of $\Delta E = 6.5$ meV. Due to an extremely high counting rate ($\sim 1.5 \times 10^5$ cps in the elastic peak), multiple and combined losses up to loss energies of approximately 300 meV were recorded.

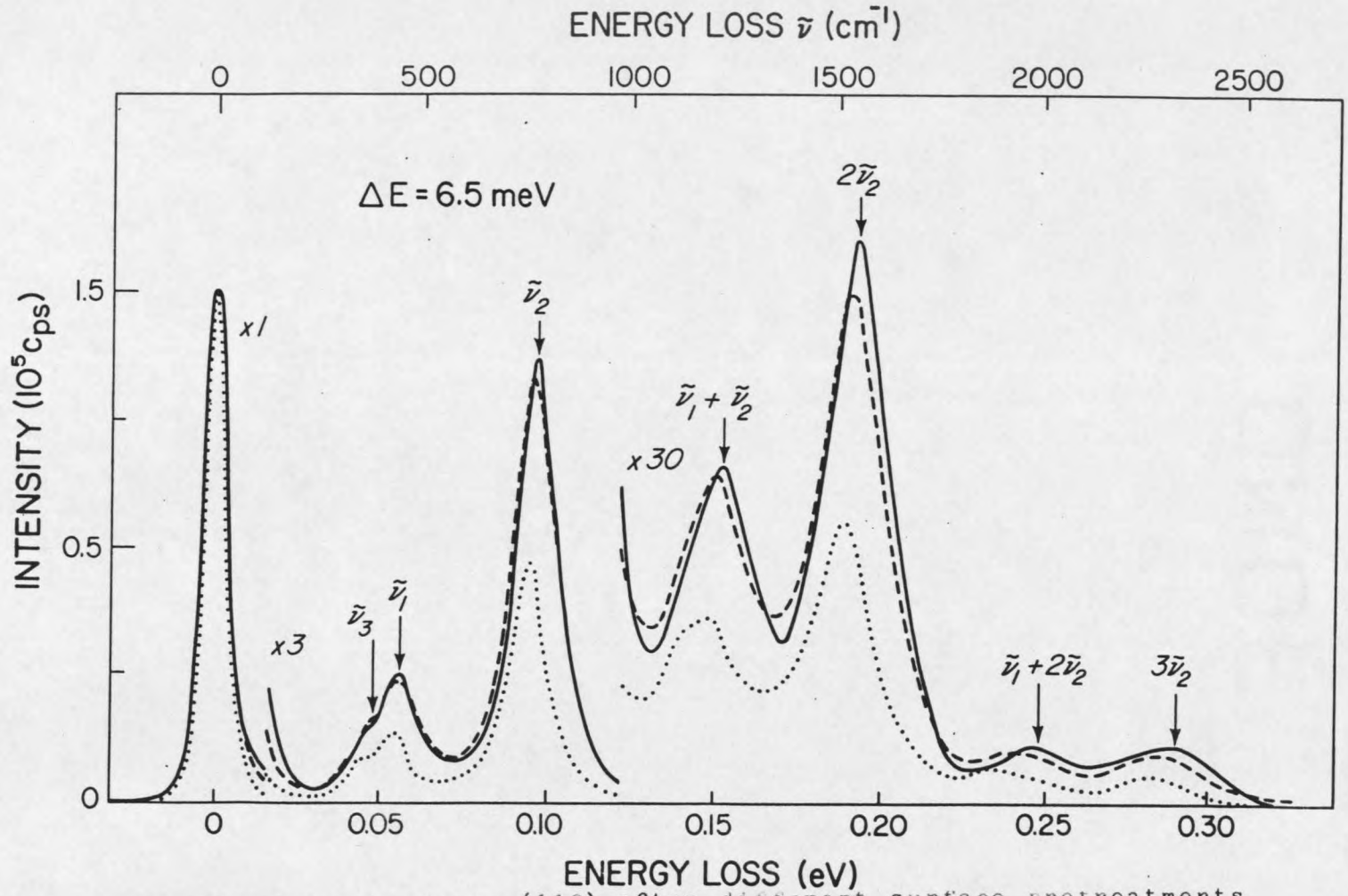

Figure 14. EELS spectra of TiO_2(110) after different surface pretreatments (see text), showing single, multiple and combined losses of surface optical phonons $\tilde{\nu}_1$, $\tilde{\nu}_2$ and $\tilde{\nu}_3$. The spectra were taken at a primary energy of E_p = 6.4 eV with a FWHM of ΔE = 6.5 meV.

These show the expected Poissson distribution of intensities as can be verified with the help of Figure 5 in reference 81 (see also chapter 5 and Appendix B).

The solid curves in Figure 14 represent the stoichiometric surface in the absence of point defects. The dashed lines show results obtained on surfaces with thermally produced defects, i.e. after heating the sample to 1310 K for 10 minutes at an oxygen partial pressure of about $1x10^{-10}$ mbar. The dotted lines indicate results obtained after 10 minutes of argon-ion bombardment at a primary ion energy of E_p = 500 eV and an emission current of I_{em} = 3 mA, resulting in a target current of $I_{targ} = 3x10^{-7}$ A. This sample treatment apparently led to pronounced surface-atom disorders accompanied by an attenuation of the Fuchs-Kliewer phonons.

The EELS spectra in Figure 15 were recorded for the same experimental conditions as in part a and also include the corresponding gain peaks as well as the effect of hydrogen exposure. The ratios of the gain-to-loss intensities show the expected Boltzmann behavior to be discussed later. The dashed curves were obtained after exposing the stoichiometric TiO_2(110) surface to 1000 L [1 L(Langmuir) = $1.33x10^{-6}$ mbar sec] of atomic hydrogen at a molecular hydrogen pressure of $6.7x10^{-6}$ mbar and a sample temperature of 300 K.

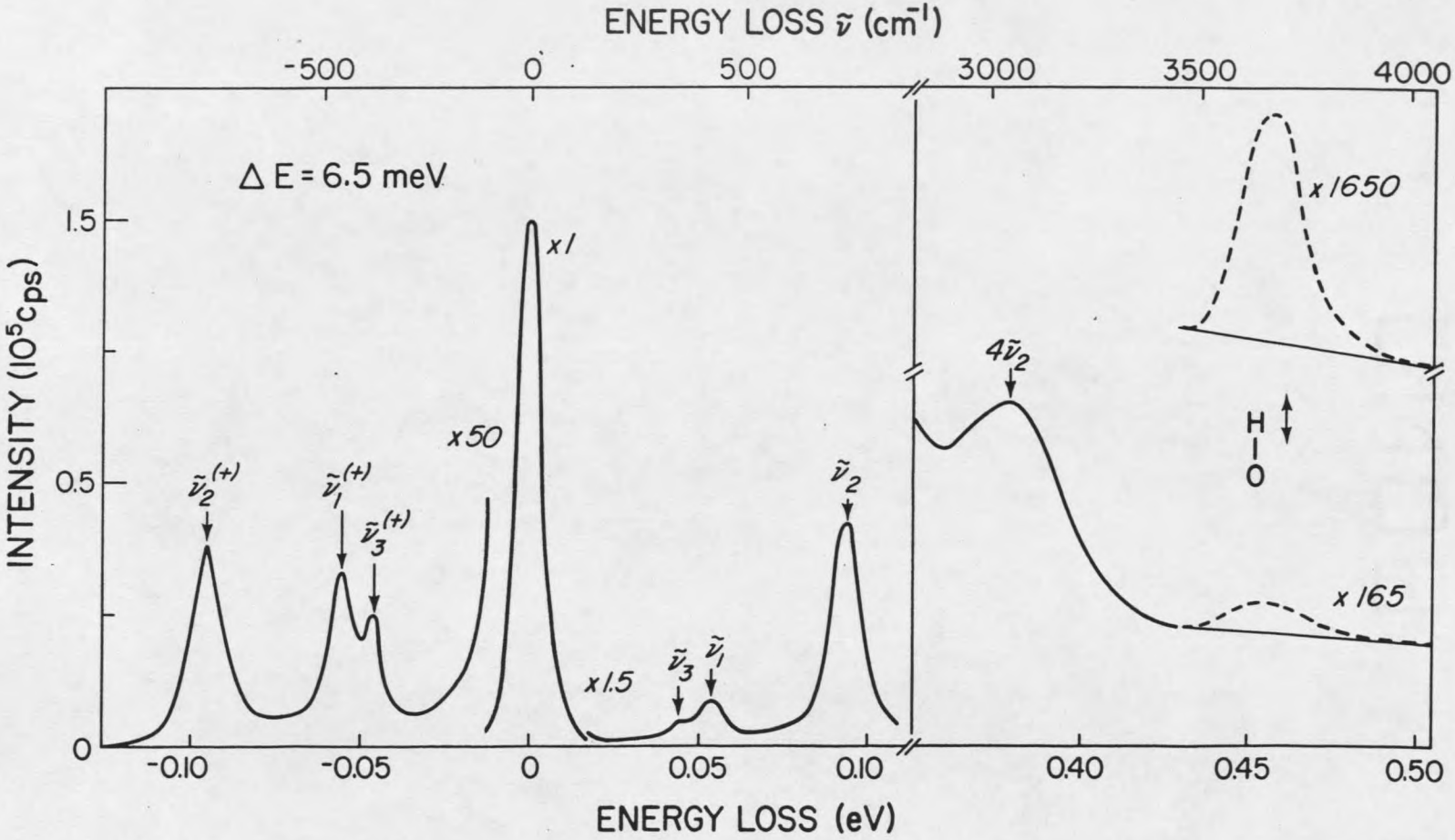

Figure 15. EELS spectra (obtained for the same experimental conditions as in Figure 14) shown over a wider energy range which also includes characteristic gain peaks and the effect of hydrogen exposure.

Hydrogen molecules were dissociated with a hot tungsten filament mounted in close proximity of the sample. The resulting loss feature at 455 meV is apparently due to the formation of surface OH groups, leading to the well-known O-H stretch vibration.

The EELS spectra shown in the following Figure 16 were obtained at a primary electron energy of E_p = 27.1 eV, in the specular beam direction with $\Theta_i = \Theta_e = 60^o$, and demonstrate the screening of Fuchs-Kliewer phonons by an overlayer of titanium. The solid curves represent results obtained on the clean stoichiometric surface and were recorded at a spectrometer resolution of ΔE = 30 meV. The first peak to the right of the elastic peak is due to the most intense vibrational mode $\tilde{\nu}_2$, whereas the modes $\tilde{\nu}_1$ and $\tilde{\nu}_3$ are responsible for the shoulder on the left side of this peak. The second peak in the spectrum includes both the second loss of the mode $\tilde{\nu}_2$ and a combination loss of modes $\tilde{\nu}_1$ and $\tilde{\nu}_2$ (see previous figures). The dashed curves were obtained at a resolution of ΔE = 32 meV after 4.5 monolayers of titanium had been deposited on the $TiO_2(110)$ surface. They clearly demonstrate that very thin (several Å) overlayers of a conducting material almost completely quench highly intense surface optical phonons of the ionic substrate. This phenomenon was also observed on silver-covered gallium arsenide surfaces by Dubois et al. [137]. and will be discussed in Appendix B.

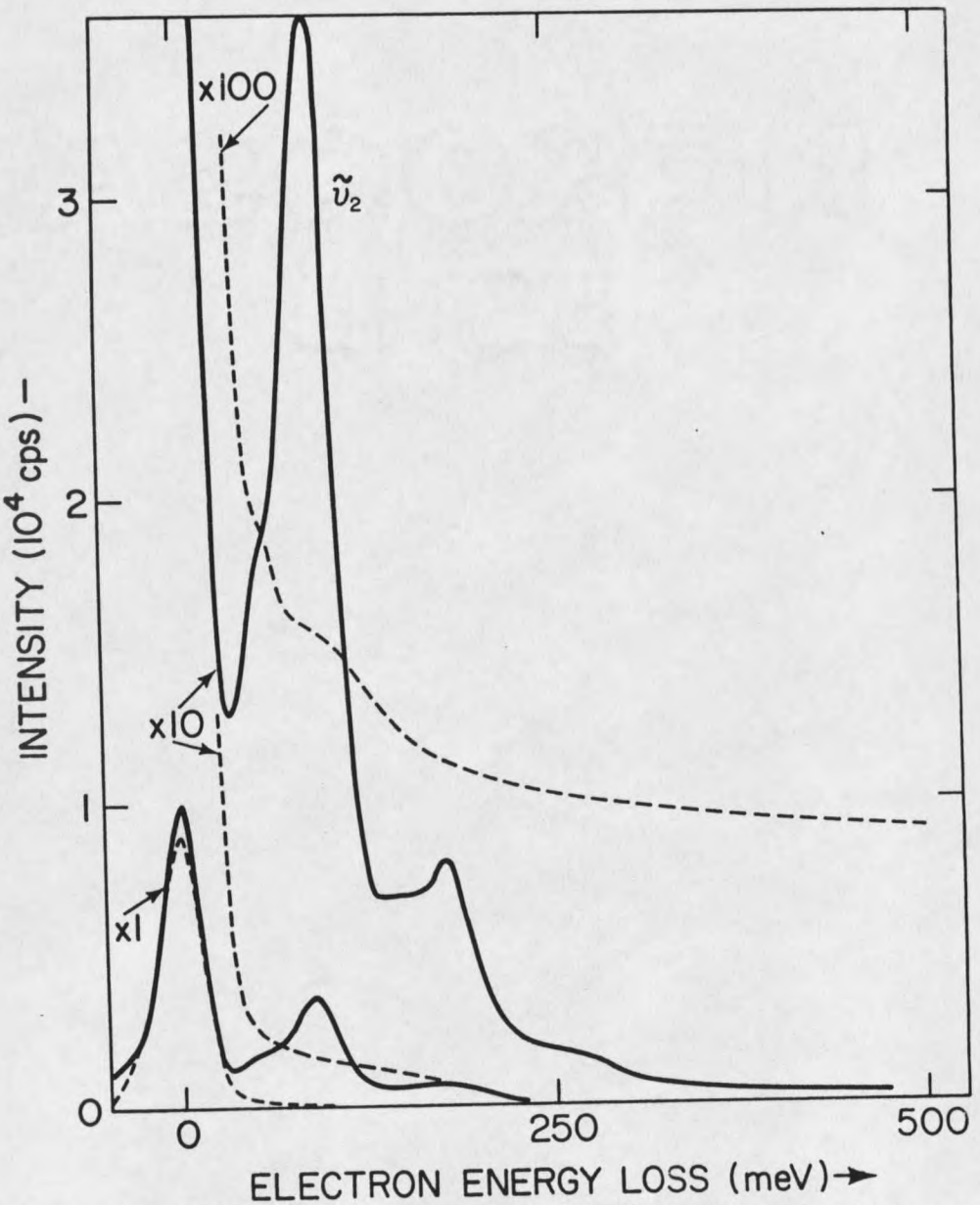

Figure 16. EELS spectra of TiO_2(110) before (solid curves) and after (dashed curves) evaporation of 4.5 monolayers of Ti (E_p = 27.1 eV, ΔE = 30 and 32 meV).

The curves in the following Figure 17 show the effect of heating and argon-ion bombardment on the elastic peak and the Fuchs-Kliewer phonons. The experiments were run at a primary electron energy of E_p = 27.1 eV in the specular beam direction with $\Theta_i = \Theta_e = 60^\circ$. The solid line represents results obtained on the stoichiometric TiO_2(110) surface and was recorded at a spectrometer resolution of ΔE = 30 meV. The dotted spectrum was taken immediately after argon-ion bombardment (t = 15 min., E_p = 2000 eV, I_{em} = 3 mA, I_{targ} = 1-1.5 μA) and shows slightly attenuated Fuchs-Kliewer phonons at a higher background level. The broadening in the elastic peak led to a resolution of ΔE = 45 meV. The dashed curve was recorded right after heating the ion-bombarded sample to 820 K for about 2 minutes and demonstrates that a short, moderate temperature treatment restores the stoichiometric surface.

The spectra of Figure 17 are shown over a wider energy range in Figure 18 and now also include a broad loss feature between 0.5 and 2 eV that appeared after the ion bombardment and was attenuated during the temperature treatment. This loss feature was also observed in earlier experiments [80,81].

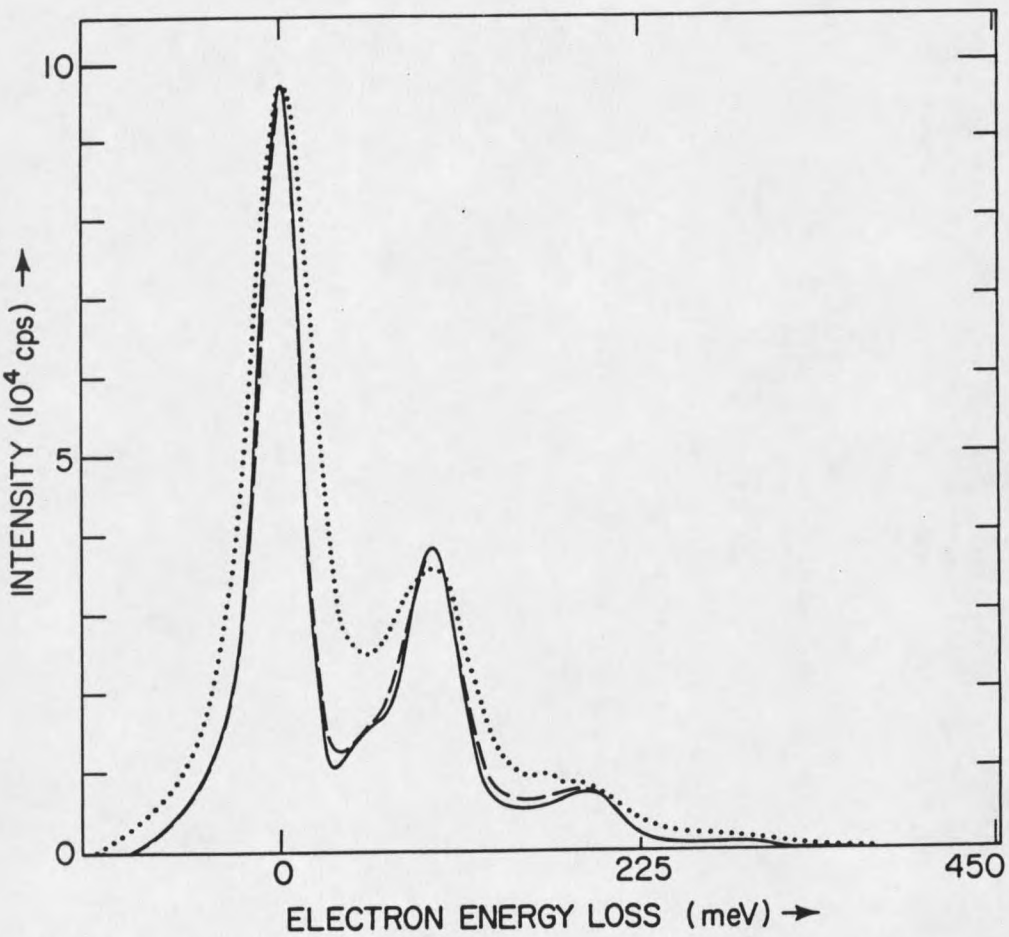

Figure 17. EELS spectra of differently treated TiO_2(110) surfaces, taken at a primary energy of E_p = 27.1 eV. The solid curve (ΔE = 30 meV) represents the stoichiometric surface, the dotted curve (ΔE = 45 meV) was recorded after argon-ion bombardment (15 minutes, 2000 eV). The dashed curve (ΔE = 30 meV) was obtained after heating (2 minutes at 820 K) the ion-bombarded surface represented by the dotted line.

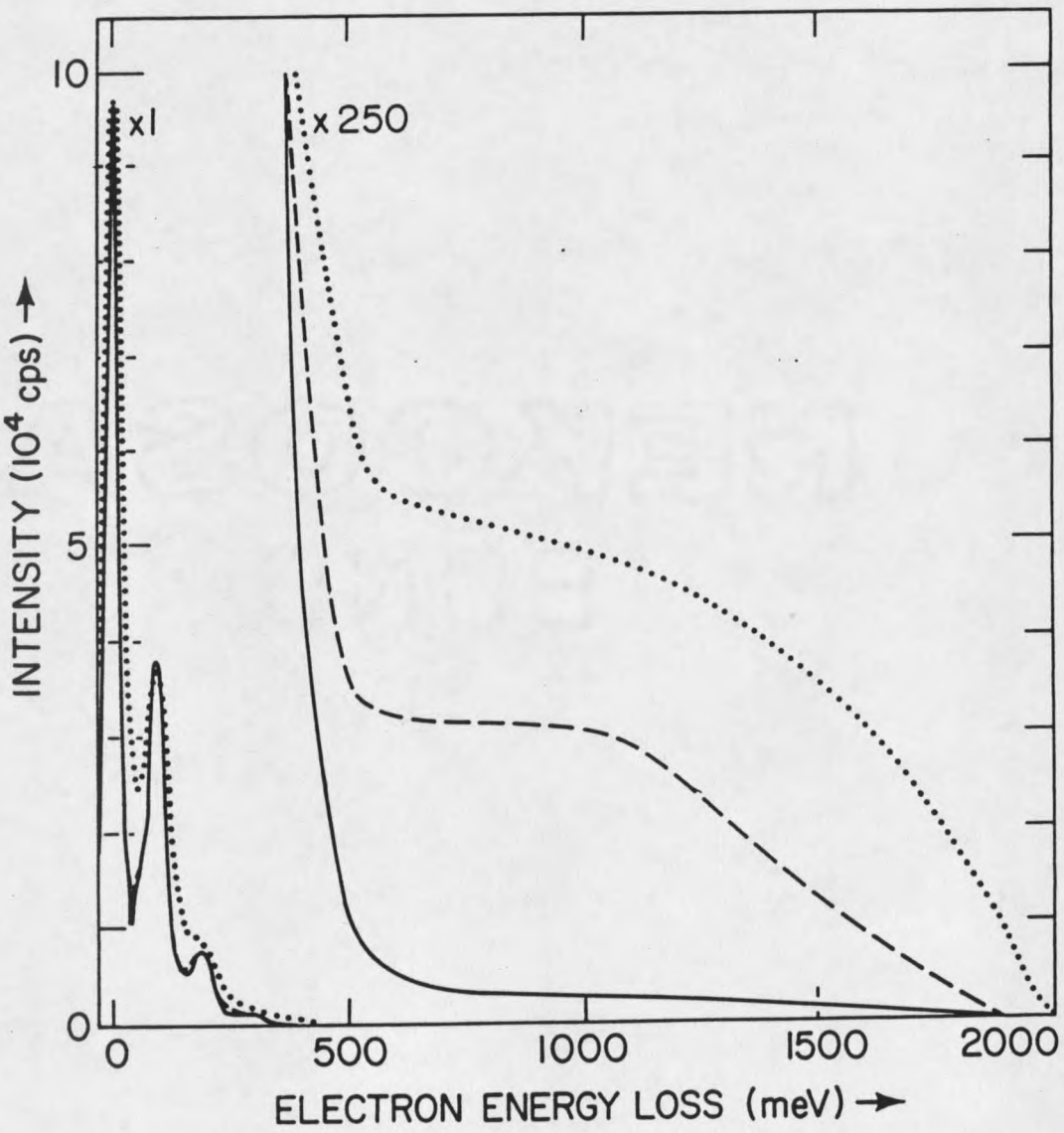

Figure 18. EELS spectra of Figure 17 shown over a wider energy range which also includes a broad electronic loss feature between 0.5 and 2 eV.

The effects of a thin titanium overlayer are shown in the following Figures 19 and 20. The solid curves again represent results obtained on a stoichiometric surface, whereas the dotted lines were recorded immediately after the evaporation of 0.5 monolayers of titanium. The dashed curves were obtained after the same temperature treatment as in Figures 17 and 18. The dot-dashed line shown in Figure 19 corresponds to the dashed curves in Figure 16 and thus represents the situation after the evaporation of 4.5 monolayers of titanium.

The dotted lines clearly demonstrate that even submonolayer amounts of titanium attenuate the strong Fuchs-Kliewer phonons and cause the same broad loss feature that was observed after ion bombardment. A short temperature treatment restores the original surface phonon intensities, but does not completely quench the loss feature between 0.5 and 2 eV.

The following four figures show results obtained from AES and ELS experiments carried out in the PHI 595 vacuum chamber described in chapter 3.

Figure 21 presents a numerically differentiated Auger survey spectrum taken at a TiO_2(110) surface after 5 minutes of argon ion bombardment (E_p = 2500 eV, I_{em} = 25 mA) and 1 minute of heating (up to 800 K). The primary electron energy was chosen to be 3000 eV.

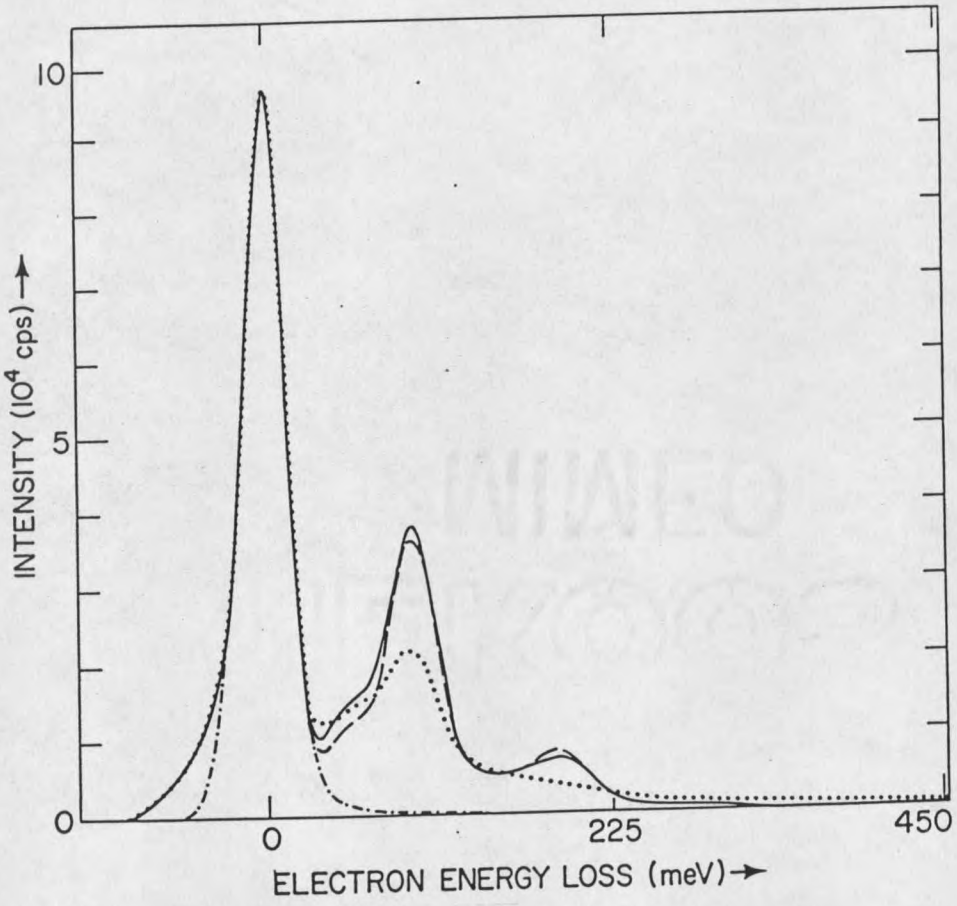

Figure 19. EELS spectra of clean and Ti-covered TiO_2(110) surfaces. The solid curve is identical to the solid curve in Figure 17, the dotted and dot-dashed spectra were obtained after evaporation of 0.5 and 4.5 monolayers of Ti, respectively. The dashed curve was recorded after heating (2 minutes at 820 K) the Ti-covered surface represented by the dotted line.

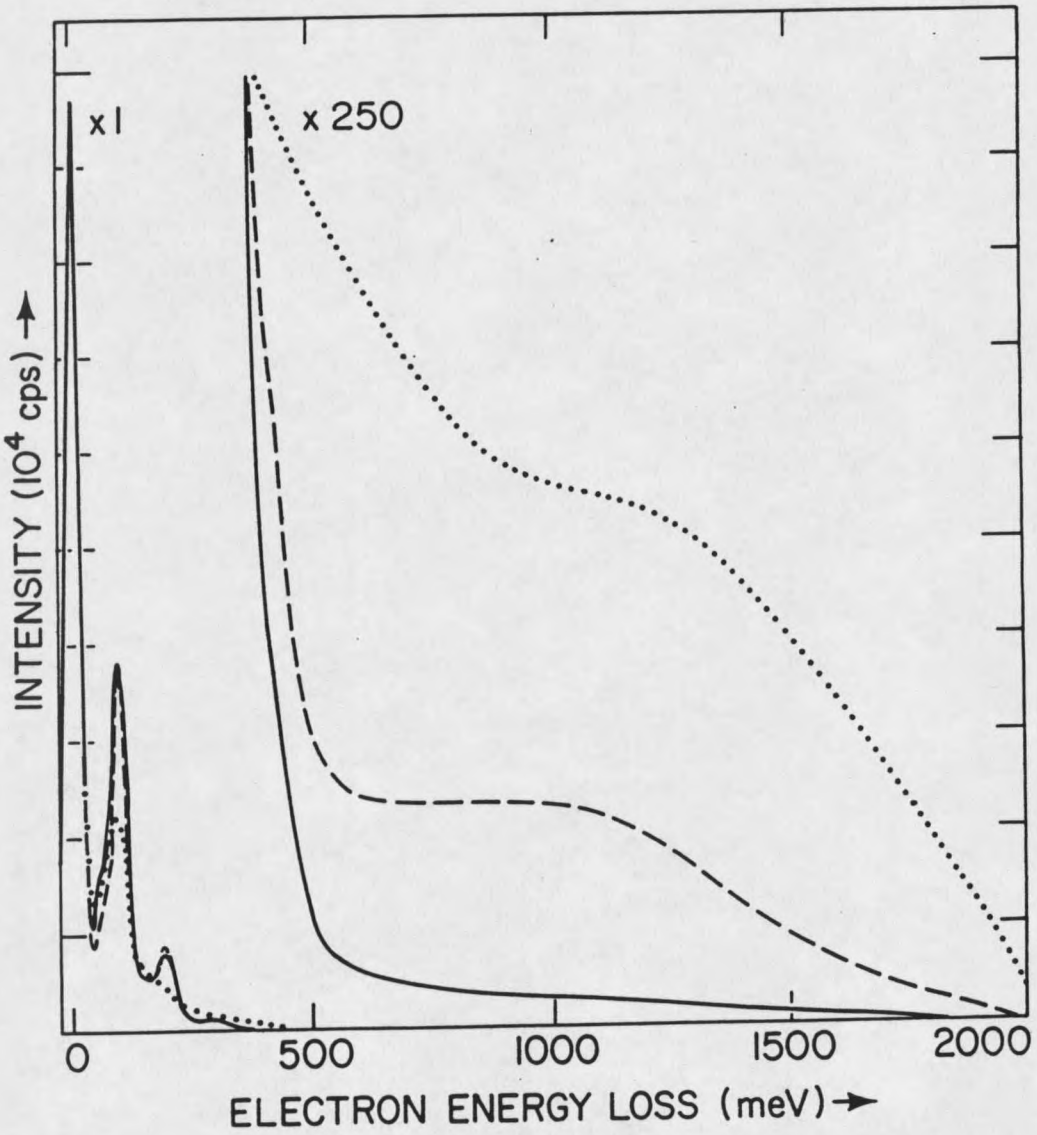

Figure 20. EELS spectra of Figure 19 shown over a wider energy range which also includes the broad loss feature observed in Figure 18.

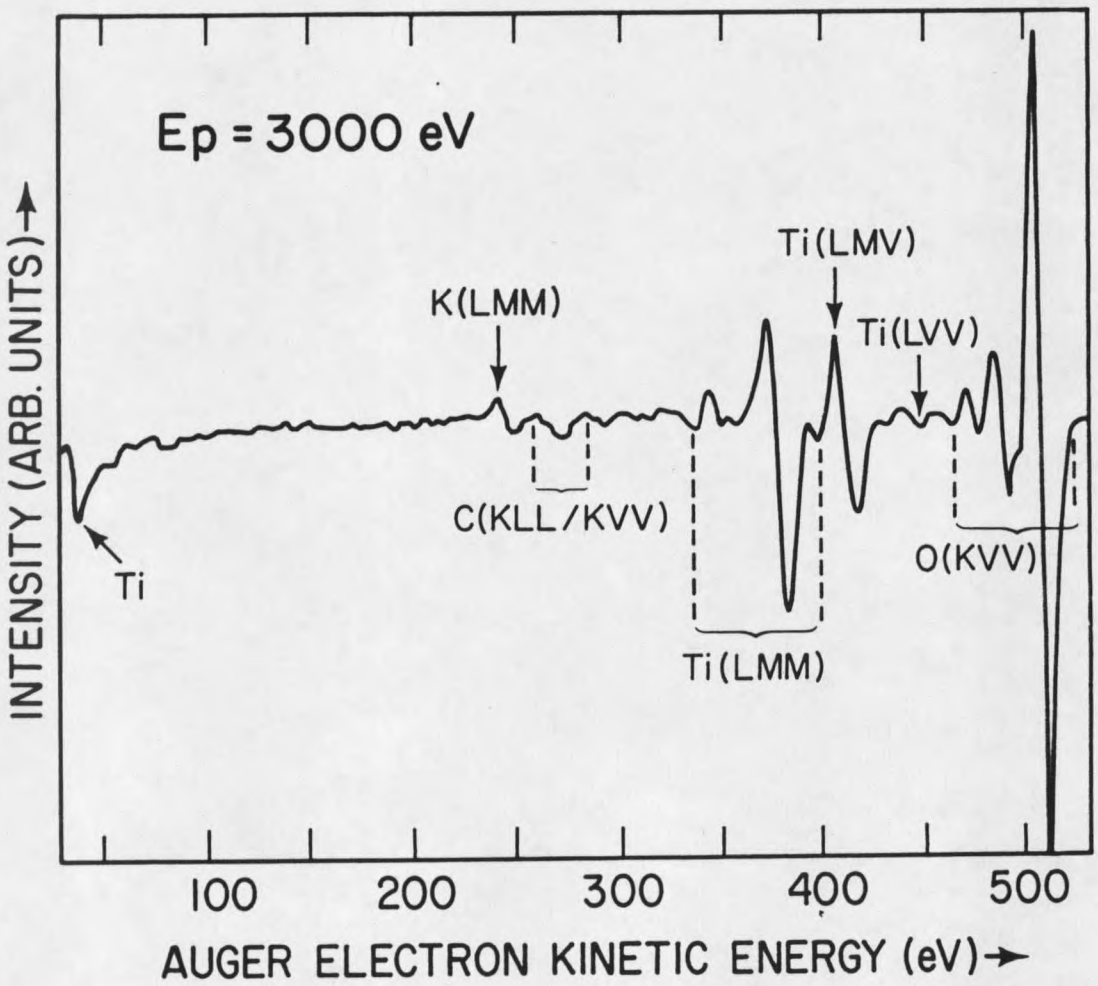

Figure 21. AES spectrum of a TiO_2(110) surface with residual carbon and potassium contaminants (the sample pretreatments are described in the text).

Besides the principal titanium and oxygen Auger lines $TiL_3M_{23}M_{23}$, $TiL_3M_{23}V$, TiL_3VV and OKVV ($K = 1s_{1/2}$) weak carbon and potassium Auger transitions CKLL/CKVV and KLMM were also detected. The carbon and most of the potassium contaminants could be removed by further annealing in oxygen, as mentioned earlier in this chapter.

Due to inhomogeneous heating of the sample (see chapter 3), one part of the TiO_2 wafer remained yellowish/transparent, whereas another part turned black/opaque.

Figure 22 shows results obtained from ELS measurements done on the transparent part of the sample at a primary electron energy of $E_p = 300$ eV. The solid line represents a spectrum taken at a clean stoichiometric surface (obtained after additional annealing in an oxygen atmosphere of $4x10^{-5}$ mbar at 800 K) and exhibits the loss features b, c, d and e at loss energies of 5.5, 10.2, 13.7 and 25.0 eV. The loss features b, c and d had already been detected in earlier experiments carried out in the L-H vacuum chamber [80,81]. The broad feature (a) between 0.5 and 2 eV presented in Figures 18 and 20 could not be observed due to a low resolution of $\Delta E = 0.3$ eV (see chapter 3). The dashed curve was recorded immediately after 15 minutes of argon-ion bombardment ($E_p = 2500$ eV, $I_{em} = 25$ mA) and shows lower intensities, especially for the features b and c. This result was also found in earlier experiments [80,81].

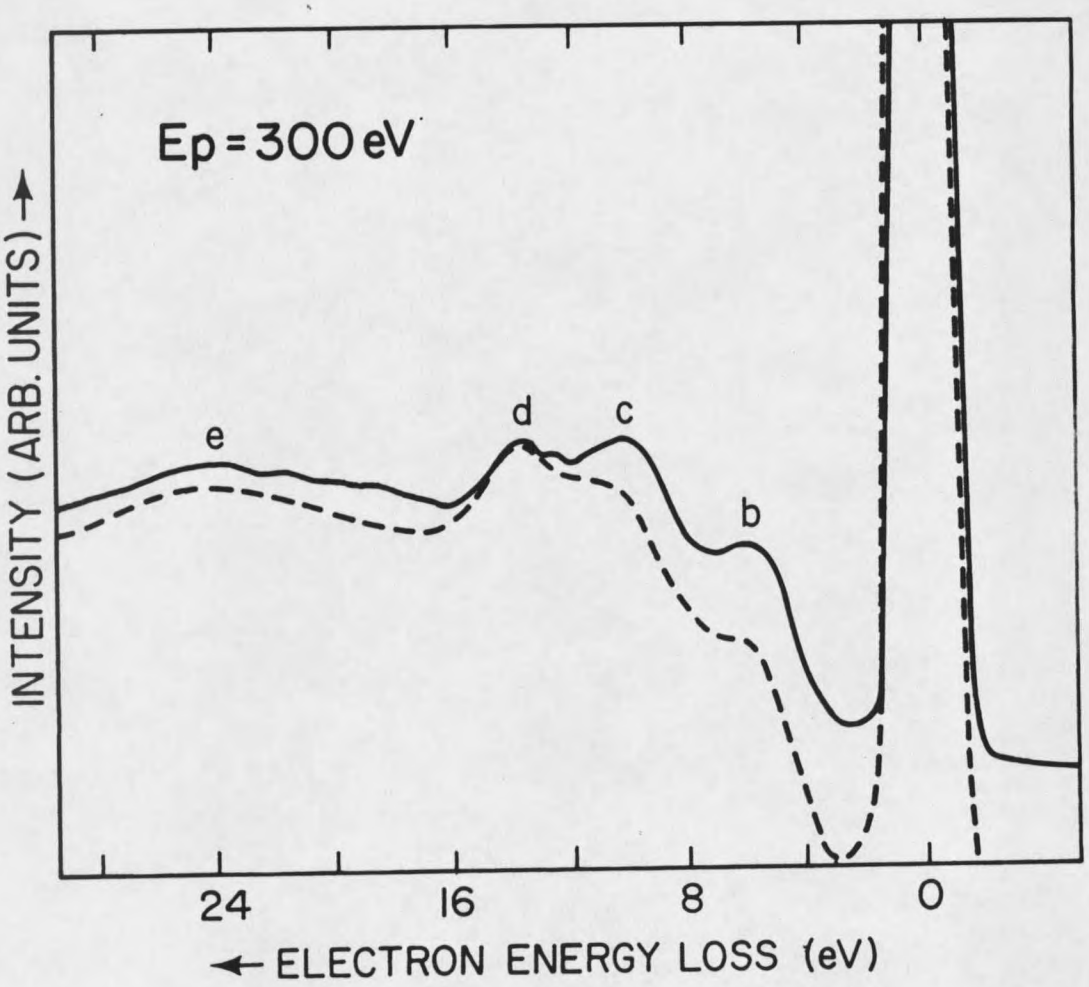

Figure 22. ELS spectra of a transparent TiO_2(110) sample before (solid curve) and after (dashed curve) argon-ion bombardment, showing electronic loss features b, c, d and e (see text).

The spectra presented in Figure 23 were taken on the opaque part of the sample after the same surface treatments as in Figure 22, and exhibit significant increases in the intensity of the loss feature c. Argon ion bombardment again reduces the intensities of the features b and c.

The ELS spectrum presented in Figure 24 was obtained on the transparent part of the annealed sample and also shows the higher losses f, g, h, i and j at loss energies of 39.3, 47.6, 63.5, 79.5 and 104.0 eV. These results were recorded at a primary electron energy of E_p = 1000 eV and a resolution of ΔE = 1 eV.

Figure 25 presents two LEED patterns a and b that were obtained in the L-H vacuum chamber.

Picture a was taken from a blue TiO_2 sample that had been mounted on a sample manipulator (see previous chapter) and reflects the (1x1)-structure of a clean stoichiometric TiO_2(110) surface which had been heated at about 1120 K for 1 minute. The primary electron energy was chosen to be E_p = 52 eV (exposure time: 5 secs., aperture: 2.8).

A yellowish TiO_2(110) sample in a sample rod (see chapter 3) was used to study the infuence of titanium overlayers on the LEED pattern, because heating and temperature measurement had turned out to be more homogeneous and accurate on this sample.

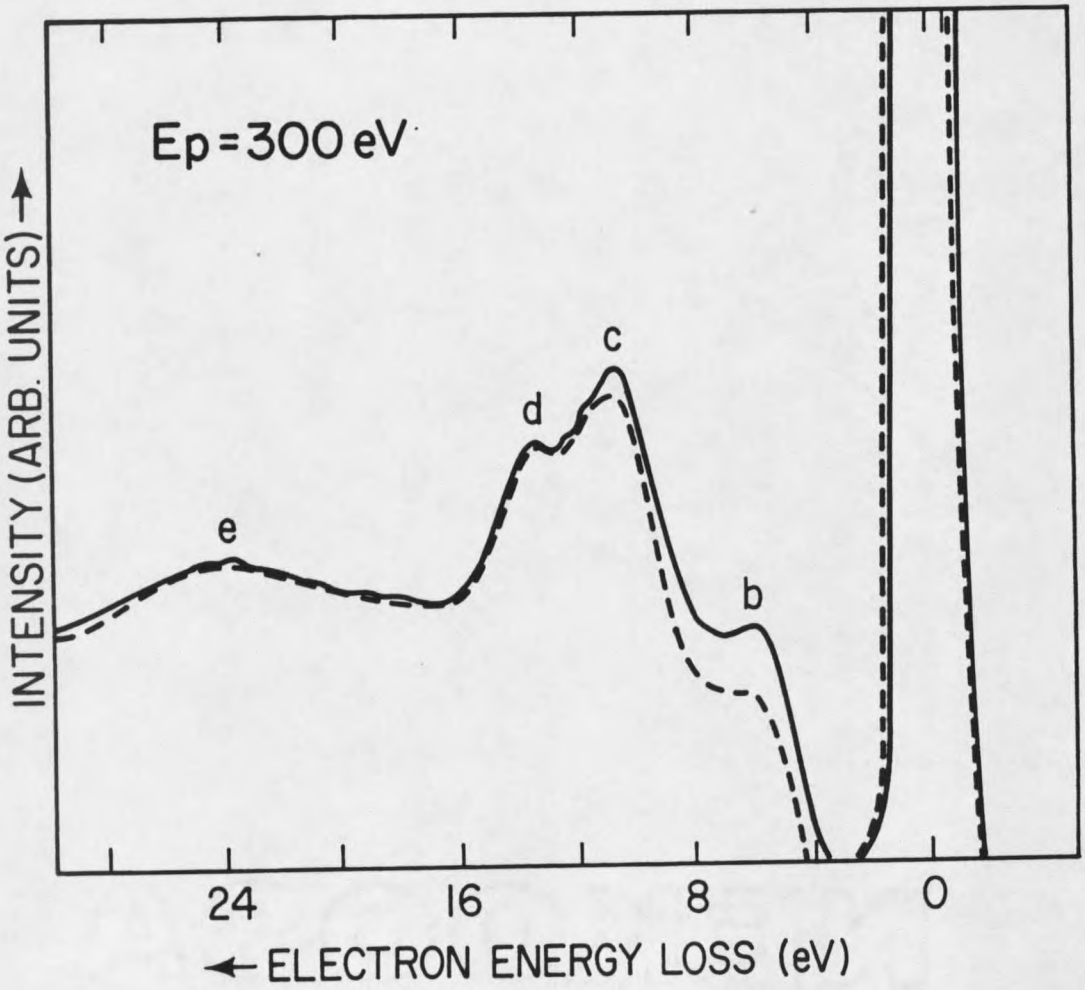

Figure 23. ELS spectra of an opaque TiO_2(110) sample, taken after the same sample pretreatments as in Figure 22.

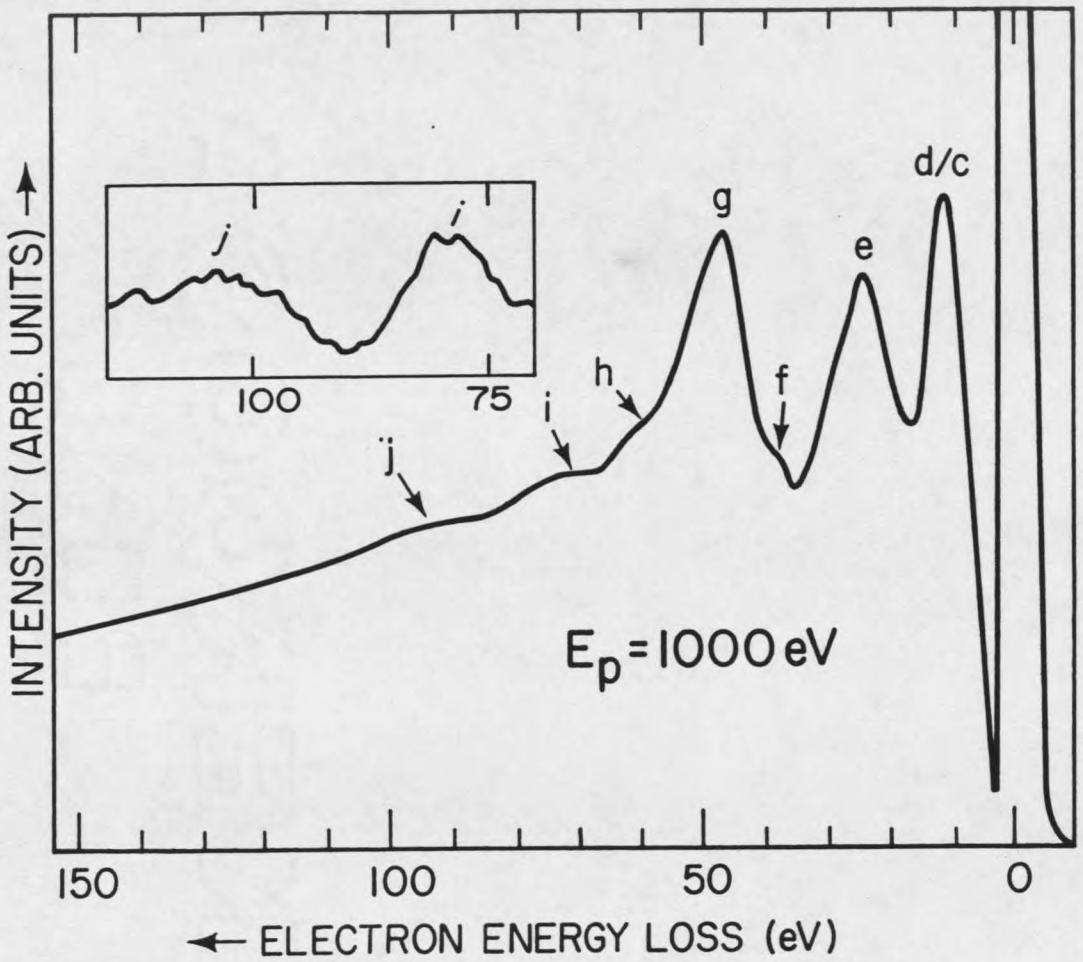

Figure 24. ELS spectrum of a transparent (annealed) TiO_2(110) sample, taken at a higher primary energy (E_p = 1000 eV). High-energy loss features f, g, h, i and j are also shown in the spectrum.

a

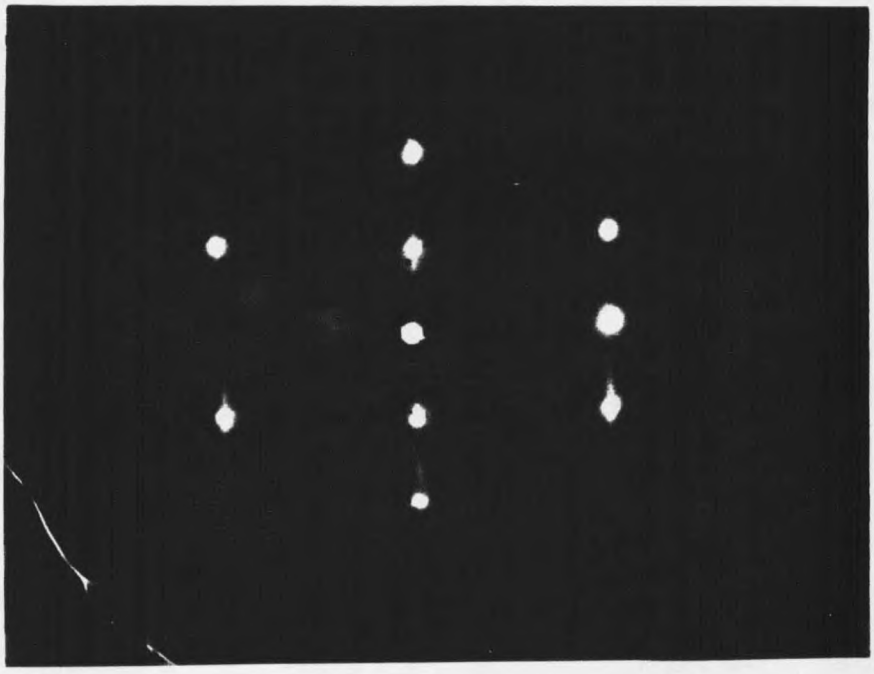

b

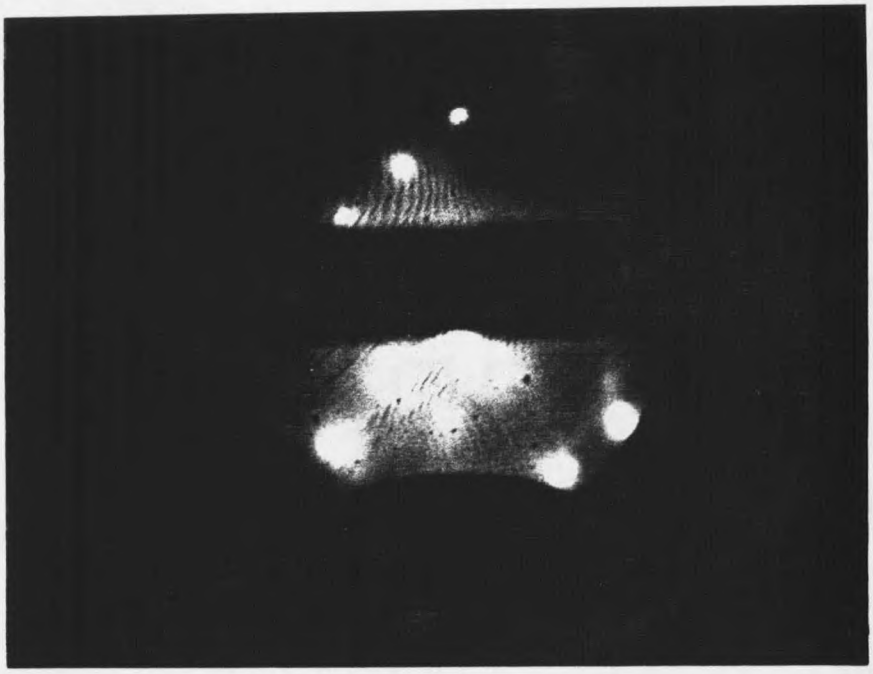

Figure 25. LEED patterns a and b, obtained on clean and Ti-covered (with subsequent heating, see text) $TiO_2(110)$ surfaces.

No LEED pattern was observed after 4.5 monolayers of titanium had been deposited on the TiO_2(110) surface. A weak, diffuse pattern appeared after heating the sample to temperatures above 920 K for less than 1 minute. The LEED spots became sharper after a short (<1 minute) high temperature treatment at temperatures around 1320 K and formed a (1x1)-pattern which is shown in picture b (E_p = 51 eV, exposure time: 1 sec., aperture: 1.8).

Further heating was avoided in order to keep the bulk defect concentration of the yellowish sample low (see chapter 5).

Results From Measurements Of Conductivity And Work Function Changes

The figures to be presented in this subchapter show a representative selection of results obtained from $\Delta\sigma$ (Figures 26-37) and $\Delta\phi$ (Figure 38-40) experiments carried out on a yellowish TiO_2(110) sample in the PHI 545A vacuum chamber described in chapter 3.

Measurements of surface-conductivity and work-function changes performed on bluish samples yielded -apart from higher bulk conductivities - similar $\Delta\sigma$ and $\Delta\phi$ results.

The two curves presented in Figure 26 demonstrate the effect of thin evaporated titanium films as well as argon-ion bombardment on the surface conductivity σ_s of the TiO_2(110) sample. The experiments were run at T = 303 K in a residual gas atmosphere of 1.5×10^{-9} mbar, and the surface conductivity changes $\Delta\sigma_s$ were calculated by multiplying the measured bulk conductivity changes $\Delta\sigma_b$ by the sample thickness d (= 0.65 mm), as explained elsewhere [79]. The curves were calculated by fitting exponential functions to the experimentally obtained data points (indicated by dots).

The solid line (A) illustrates increases in the surface conductivity (referred to the stoichiometric surface) upon the deposition of small amounts of titanium measured in monolayer (ML) coverages .

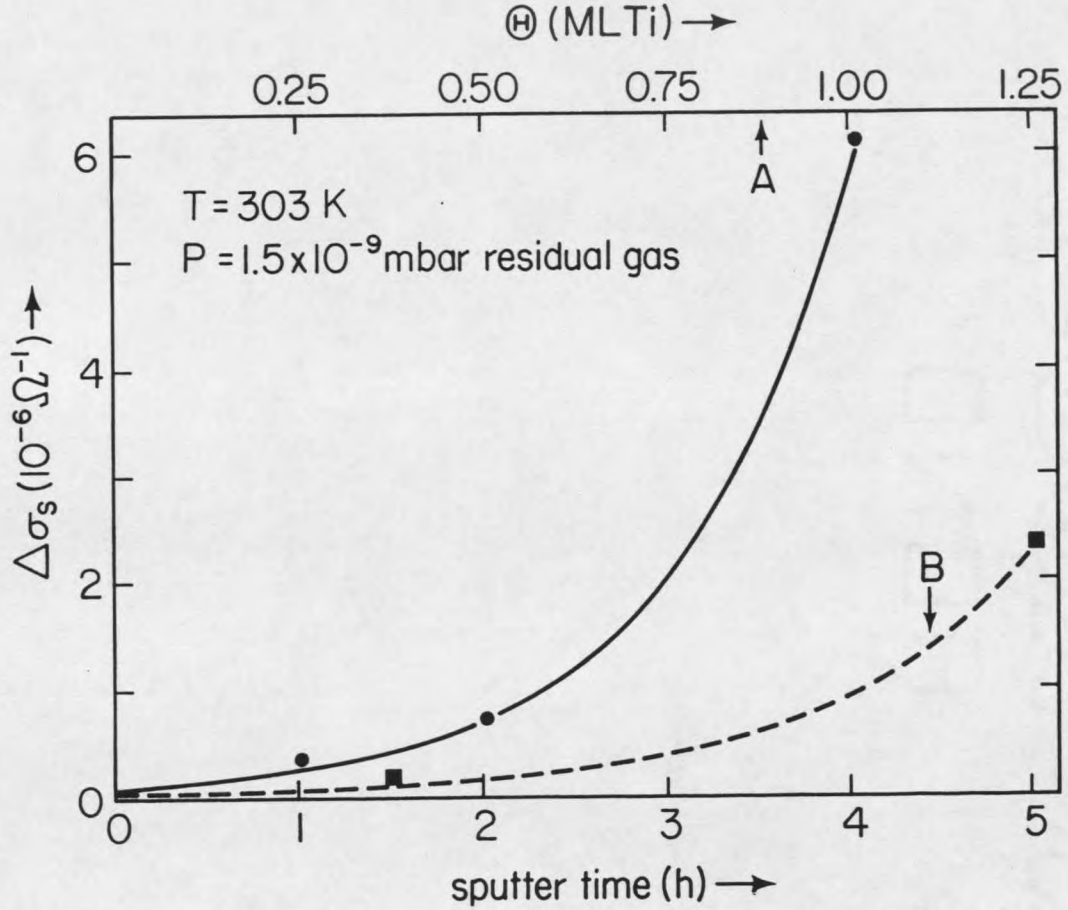

Figure 26. Surface-conductivity changes $\Delta\sigma_s$ of $TiO_2(110)$ upon evaporation of Ti (solid curve A), as well as argon-ion bombardment (dashed curve B). Further explanations are given in the text.

The dashed curve (B) represents results obtained immediately after several hours (h) of argon-ion bombardment (E_p = 1000 eV, I_{em} = 11 mA, I_{targ} = 1 μA) and also shows increases in the surface conductivity. These results will be discussed in the next chapter.

The effect of a 1-minute oxygen exposure at an O_2-pressure of 6.7×10^{-6} mbar on the surface conductivity of the stoichiometric TiO_2(110) surface is shown in Figure 27. The two solid lines obtained from smoothing the data points (indicated by dots) show pronounced conductivity decreases for two different sample temperatures (348 and 423 K). The decrease in the surface conductivity appears to be much more enhanced at elevated temperatures. A possible explanation for this phenomenon will be given in the discussion in chapter 5.

The data points in Figure 28 were recorded during 1-minute exposures of molecular hydrogen at a H_2-pressure of 2.0×10^{-5} mbar and reflect conductivity increases at three different temperatures (303, 348 and 423 K). In this case, however, the conductivty changes are more pronounced at lower temperatures and, in general, are one order of magnitude smaller than those measured during oxygen exposures.

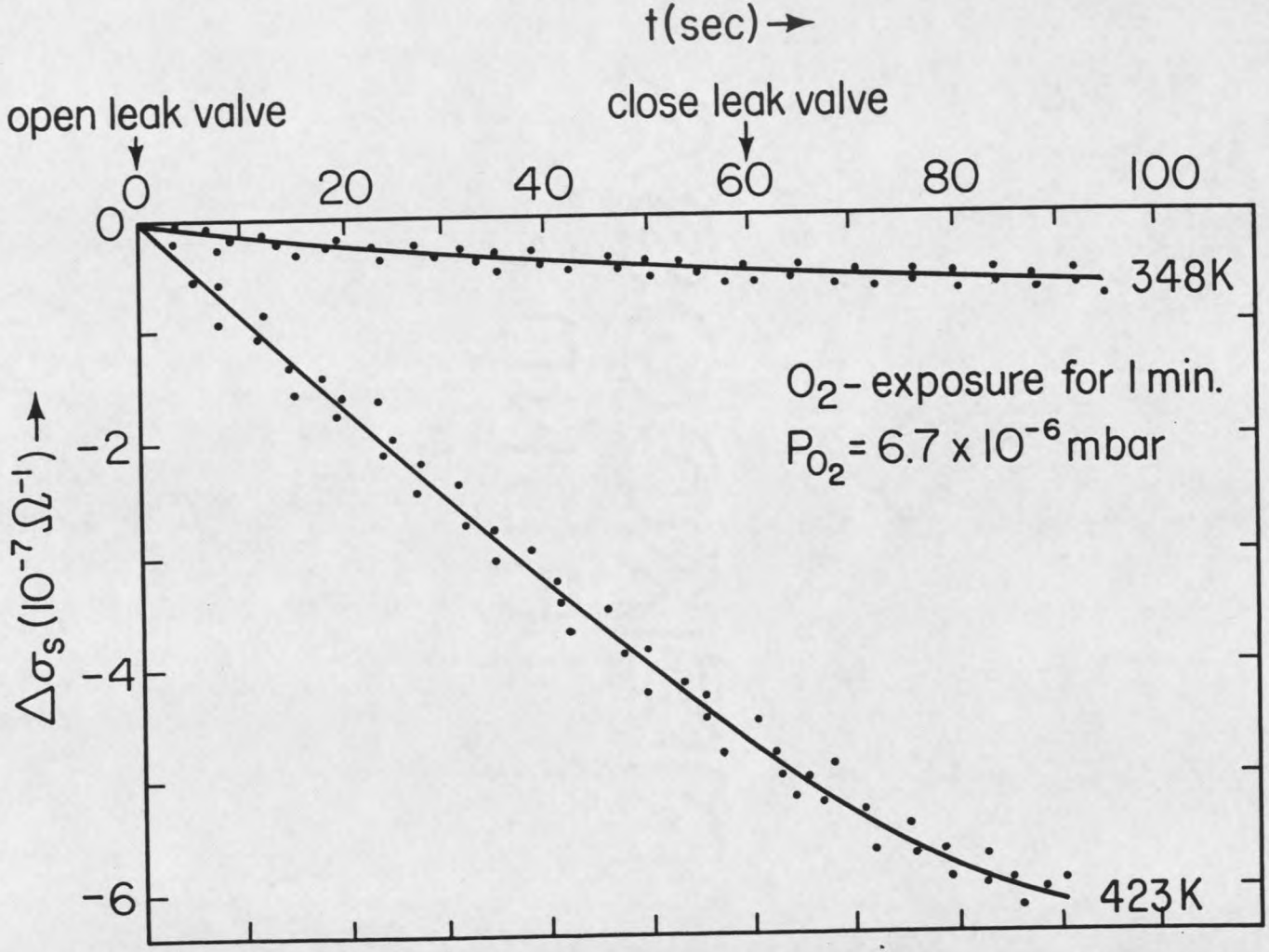

Figure 27. Time-dependent surface-conductivity changes of $TiO_2(110)$ upon oxygen exposure at two different sample temperatures.

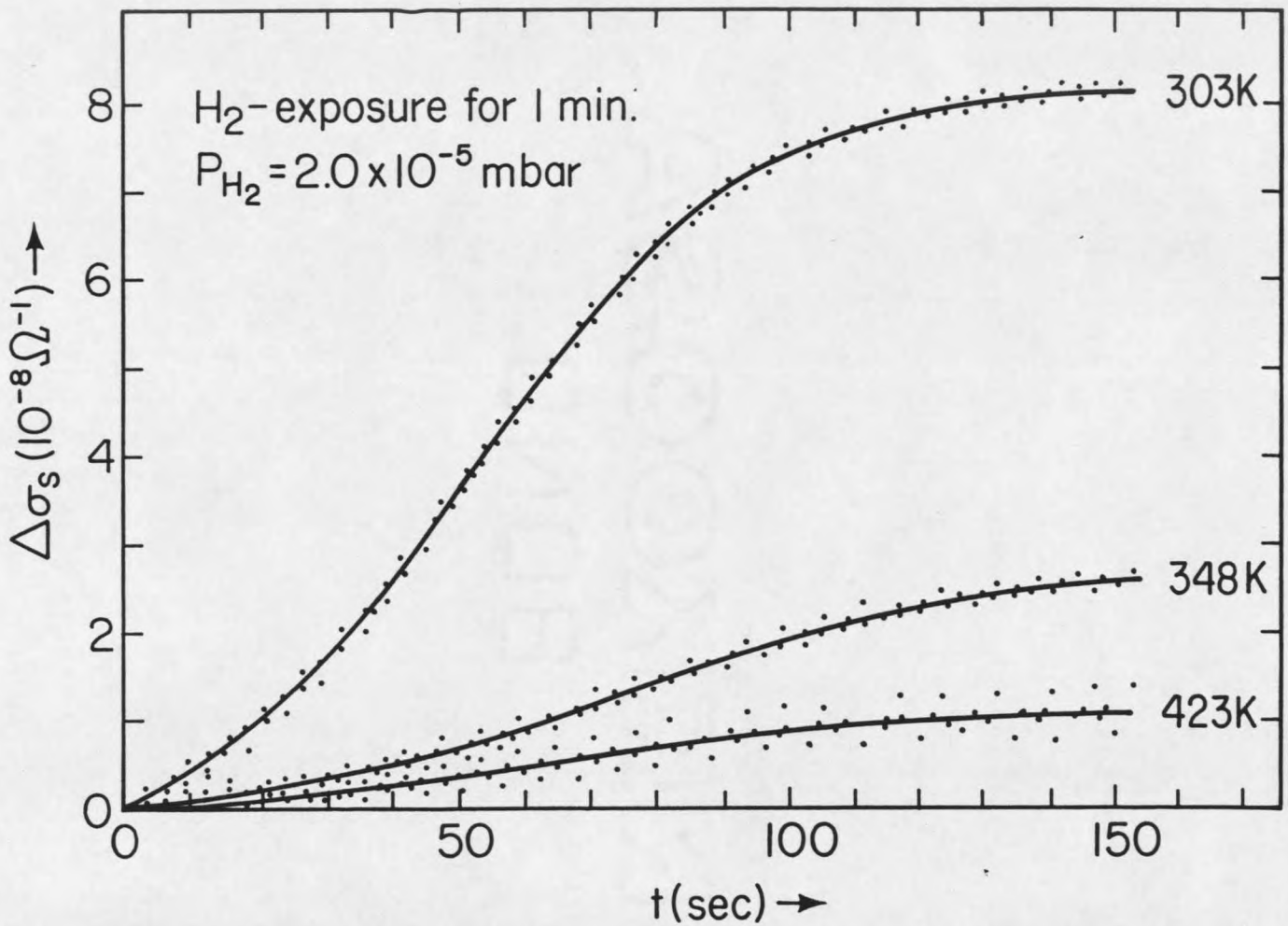

Figure 28. Surface-conductivity changes of $TiO_2(110)$ upon exposure to molecular hydrogen at three different sample temperatures.

The following Figure 29 presents results obtained from surface conductivity measurements done during 2-minute exposures of carbon monoxide at a CO-pressure of 2.0×10^{-5} mbar. It was observed that the conductivity changes increased with temperature. The changes were found to be negative for temperatures less or equal to 323 K, and positive for temperatures greater or equal to 333 K, i.e. a sign change occurs between 323 and 333 K. Again, the conductivity changes recorded here, in general, are one order of magnitude smaller than those obtained during oxygen exposures.

The effect of small amounts of titanium, evaporated onto the $TiO_2(110)$ surface on the conductivity change during a 1-minute O_2 exposure ($P_{O2} = 6.7 \times 10^{-6}$ mbar, T = 348 K) is shown in Figure 30. The solid curves illustrate that submonolayer amounts (0.25 and 0.50 ML) of evaporated titanium enhance the decrease in the surface conductivity of the sample: the higher the titanium coverage, the more pronounced the surface conductivity changes during O_2 exposure.

In Figure 31, it can be seen, however, that higher titanium coverages (1.0, 1.5 and 2.0 ML) reduce the conductivity changes that occur during oxygen exposure. For 1.5- and 2.0-monolayer coverages the conductivity decreases are even smaller than those measured on the stoichiometric surface (0 ML).

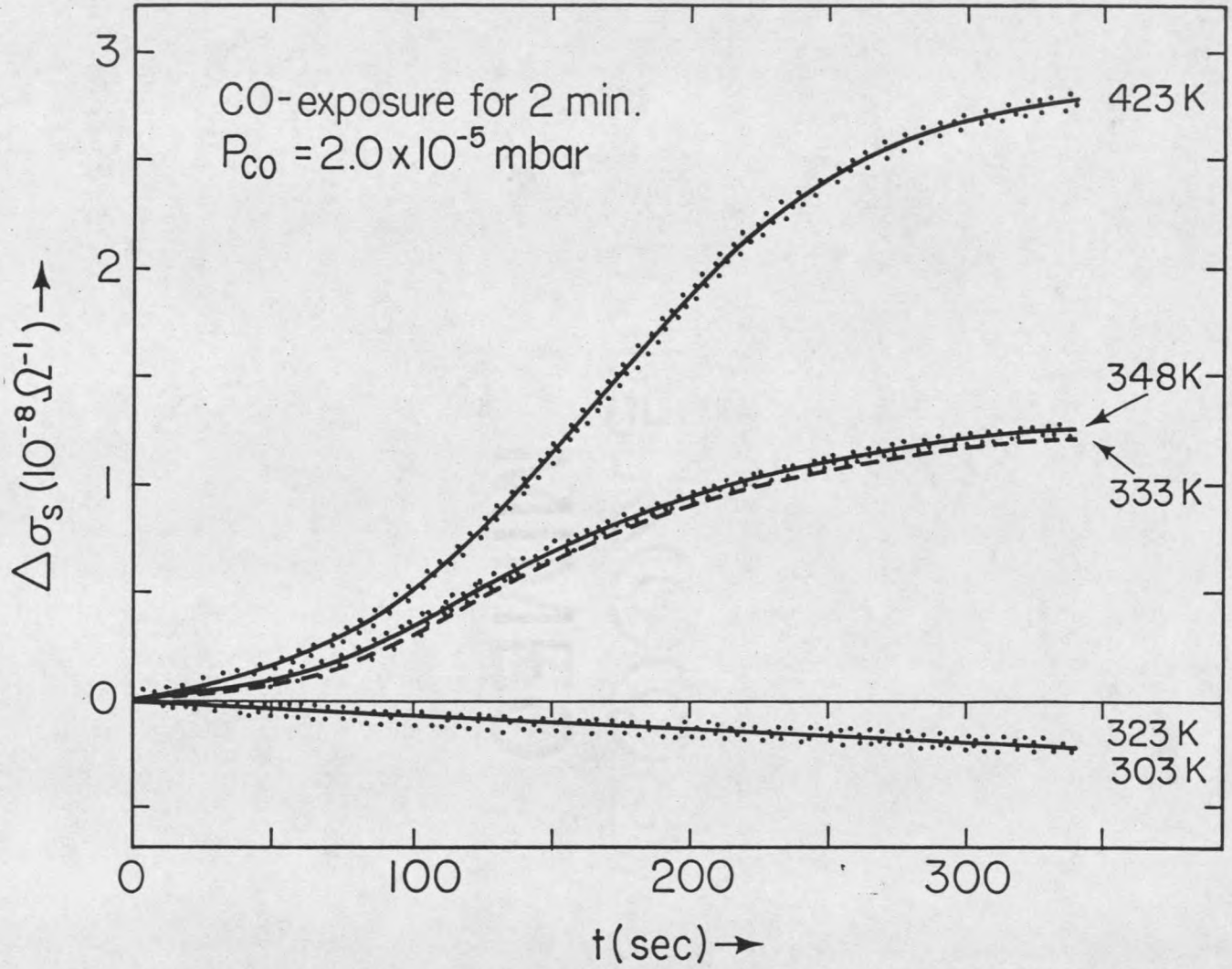

Figure 29. Surface-conductivity changes of TiO_2(110) upon CO exposure at five different sample temperatures.

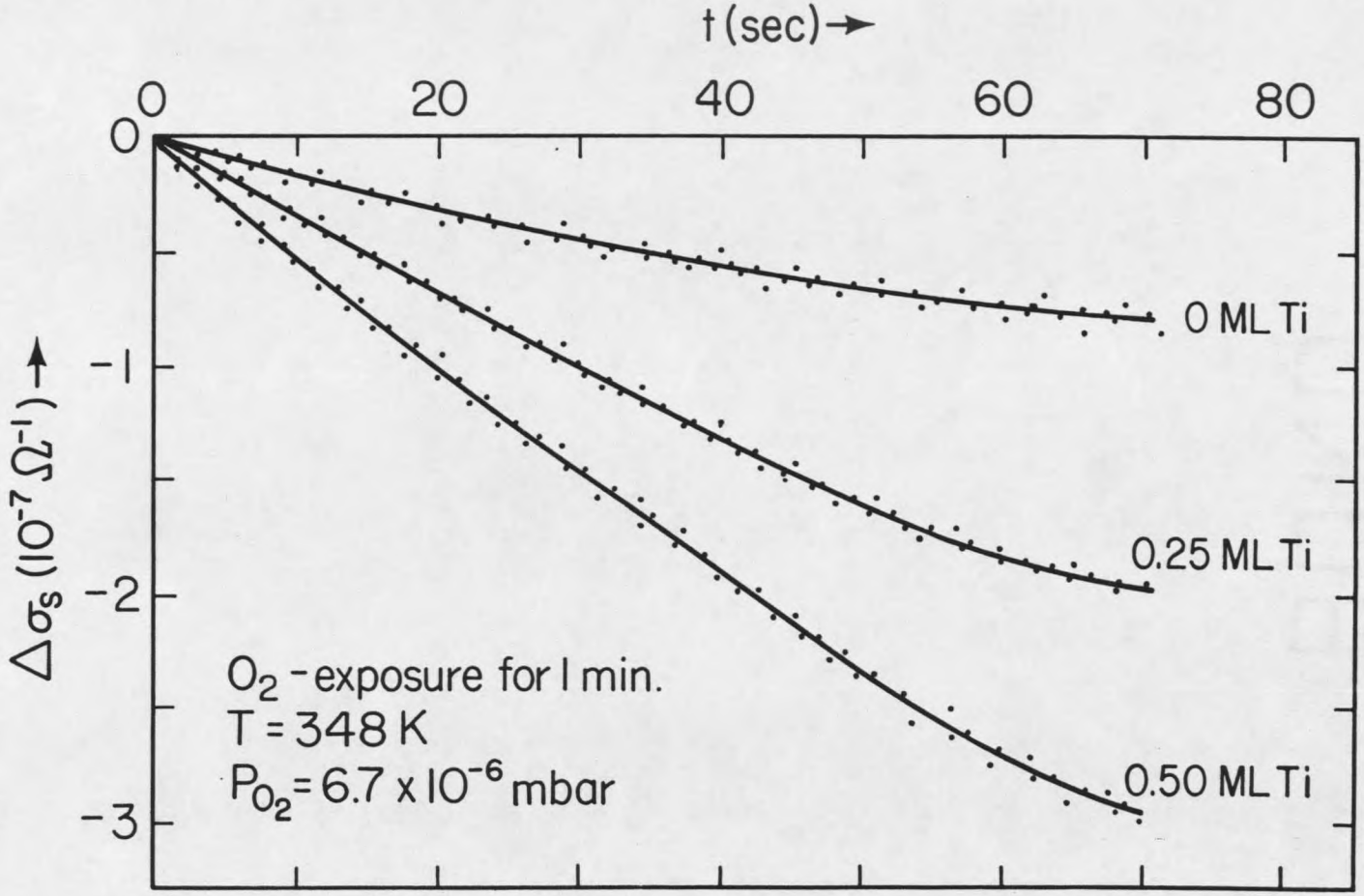

Figure 30. Surface-conductivity changes of clean and Ti-covered $TiO_2(110)$ upon oxygen exposure at 348 K. The Ti coverages range from 0.25 to 0.50 monolayers.

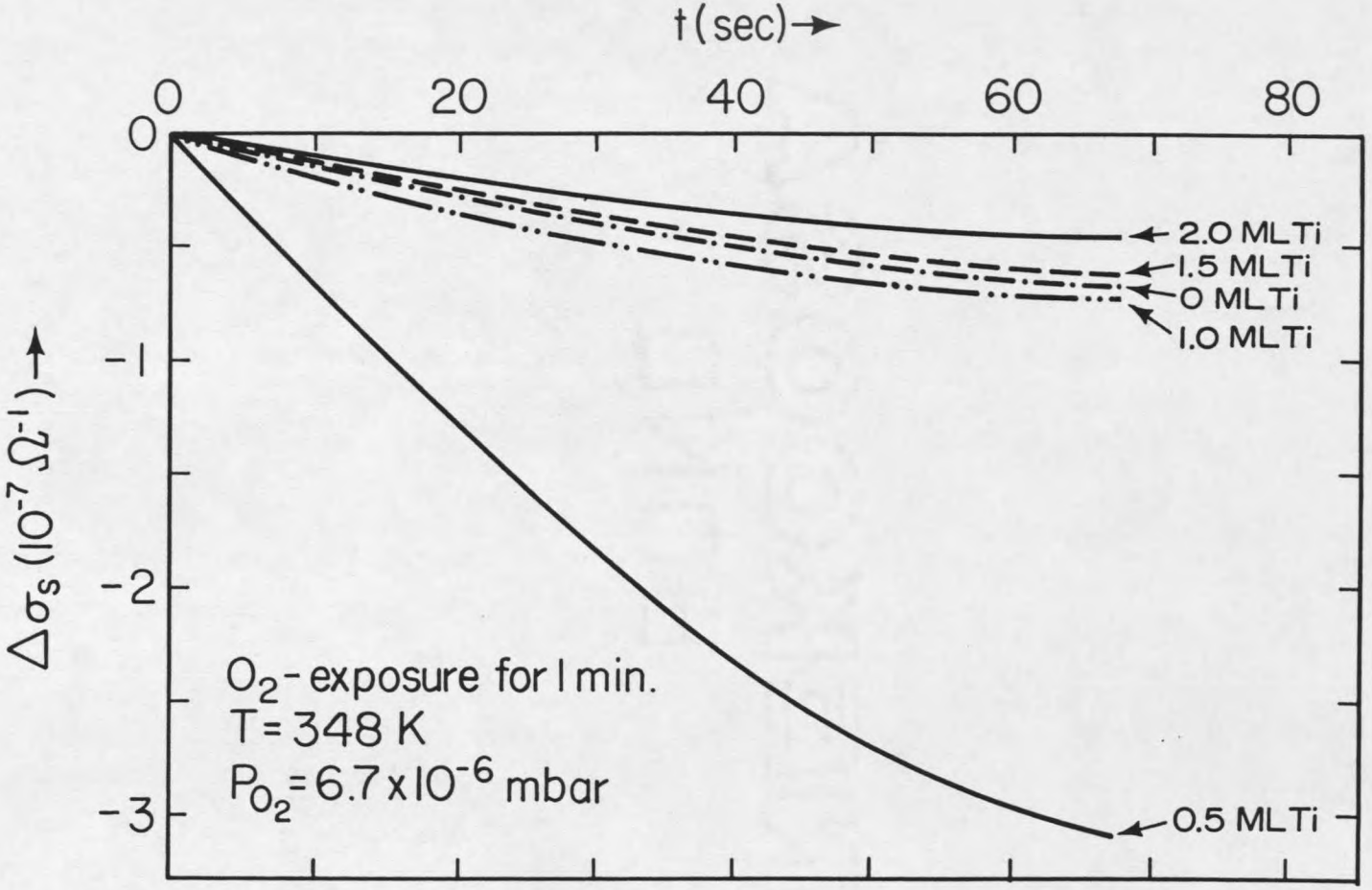

Figure 31. Surface-conductivity changes of clean and Ti-covered $TiO_2(110)$ upon oxygen exposure at 348 K. The Ti coverages range from 0.5 to 2.0 monolayers. The curves obtained for 0 and 0.5 monolayer coverages are identical to corresponding curves of Figure 30.

Figure 32 summarizes the results presented in Figures 30 and 31. The maximum values $\Delta\sigma_{s,max}$ of the conductivity changes (corresponding to the last data points recorded during the measuring times) were referred to the maximum change at zero titanium coverage [yielding $\Delta(\Delta\sigma_{s,max})$ values] and then plotted versus the titanium coverage The data points obtained in this manner were subsequently connected through solid lines. According to this diagram, the conductivity changes (with respect to the change at the clean surface) first decrease with increasing titanium coverage, and then - after passing through a minimum value around 0.5 monolayers - increase, until a sign change occurs between 1.0 and 1.5 monolayers. Only small increases $\Delta(\Delta\sigma_{s,max})$ were measured for titanium coverages between 1.0 and 2.0 monolayers.

The data presented in Figure 33 were obtained for similar experimental conditions as in Figure 30, but for a sample temperature of 423 K and slightly different titanium coverages (0, 0.2, 0.4 and 0.6 ML). We again observe enhanced conductivity decreases on titanium-covered surfaces, if these are exposed to oxygen.

The curves shown in Figure 34 demonstrate how heavy argon ion bombardment (E_p = 1000 eV, I_{em} = 11 mA, I_{targ} = 1 μA) affects the surface-conductivity changes during a 1-minute oxygen exposure (P_{O2} = 6.7x10^{-6} mbar, T = 303 K).

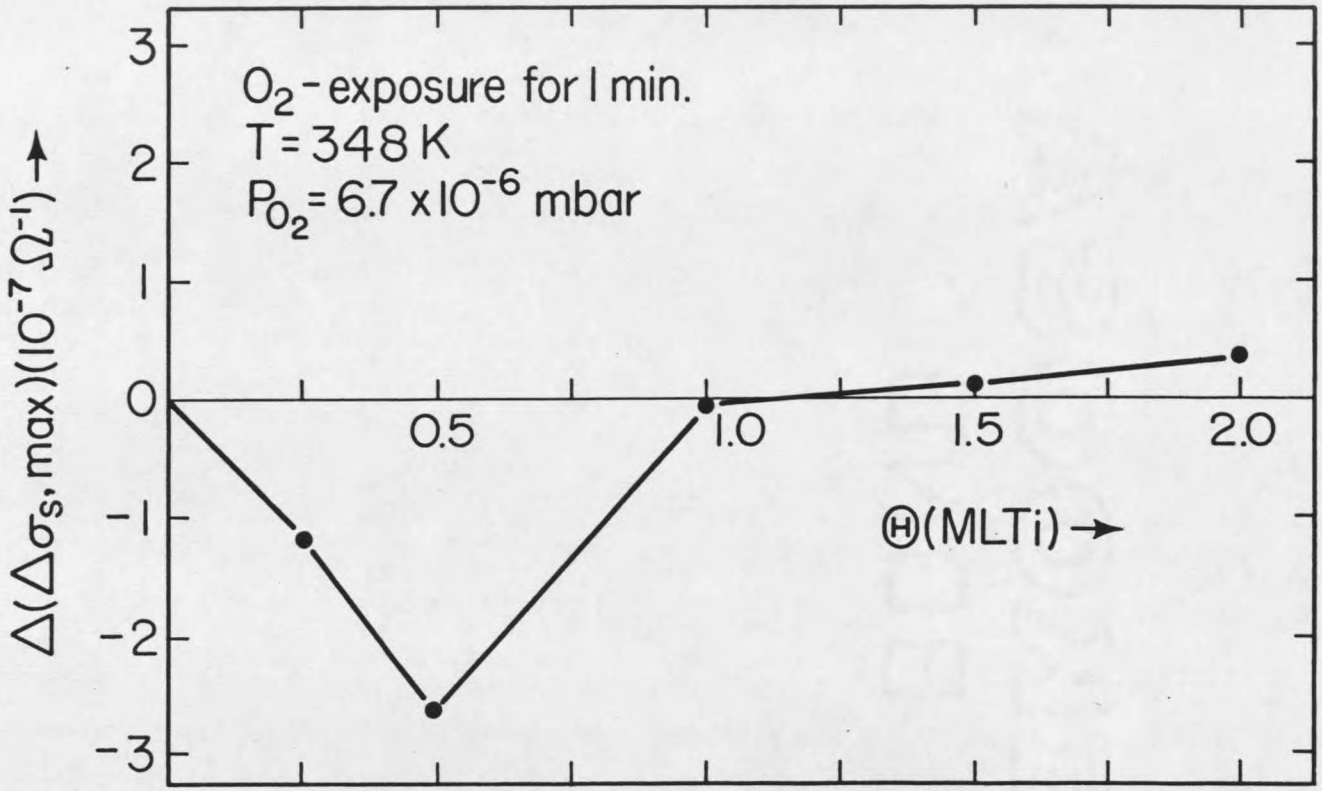

Figure 32. Maximum surface-conductivity changes $\Delta(\Delta\sigma_{s,max})$ plotted versus Ti coverage. These changes are referred to maximum conductivity changes (see text) obtained on ideal surfaces and were calculated from the curves shown in Figures 30 and 31.

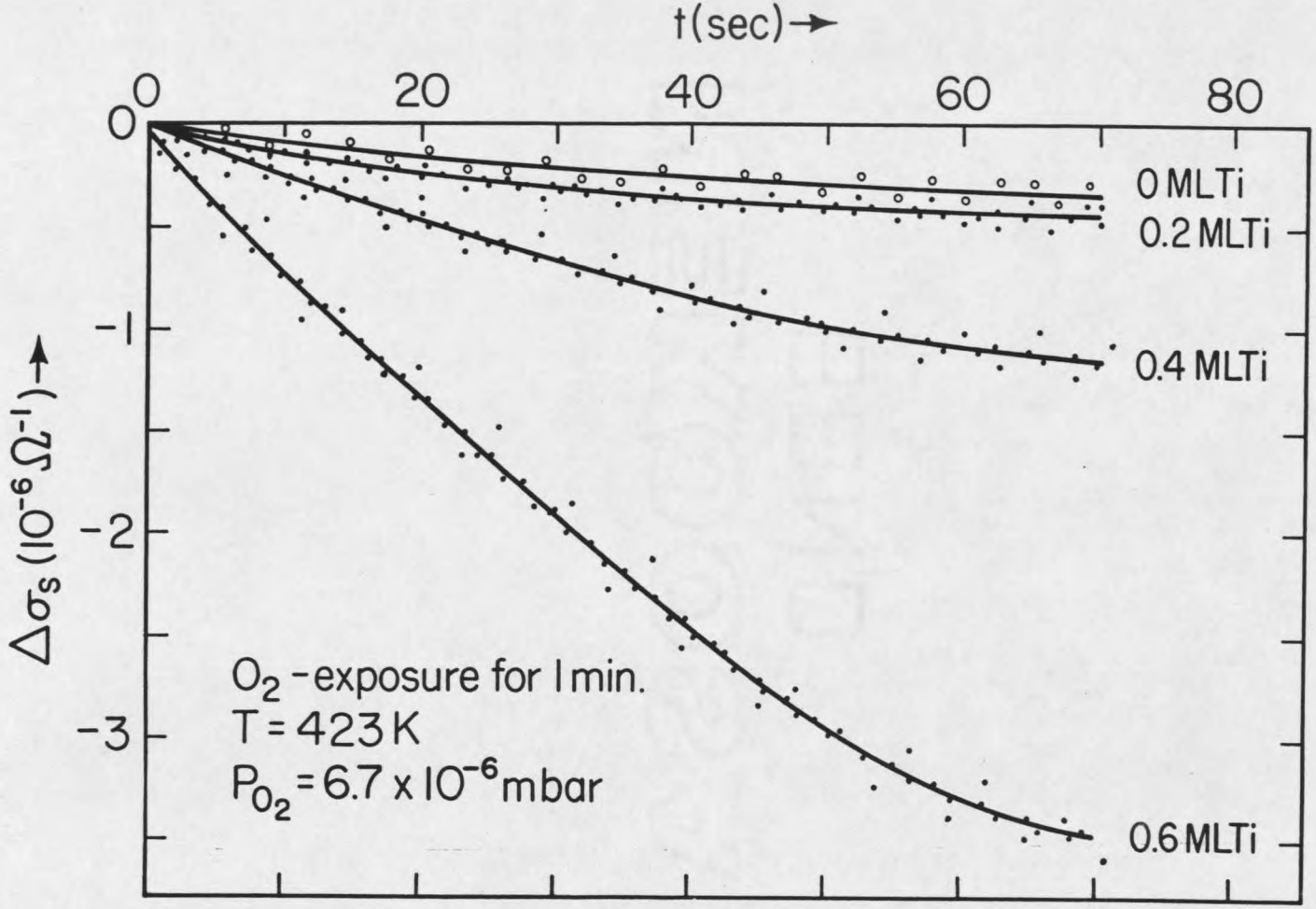

Figure 33. Surface-conductivity changes of clean and Ti-covered TiO_2(110) upon oxygen exposure at 423 K.

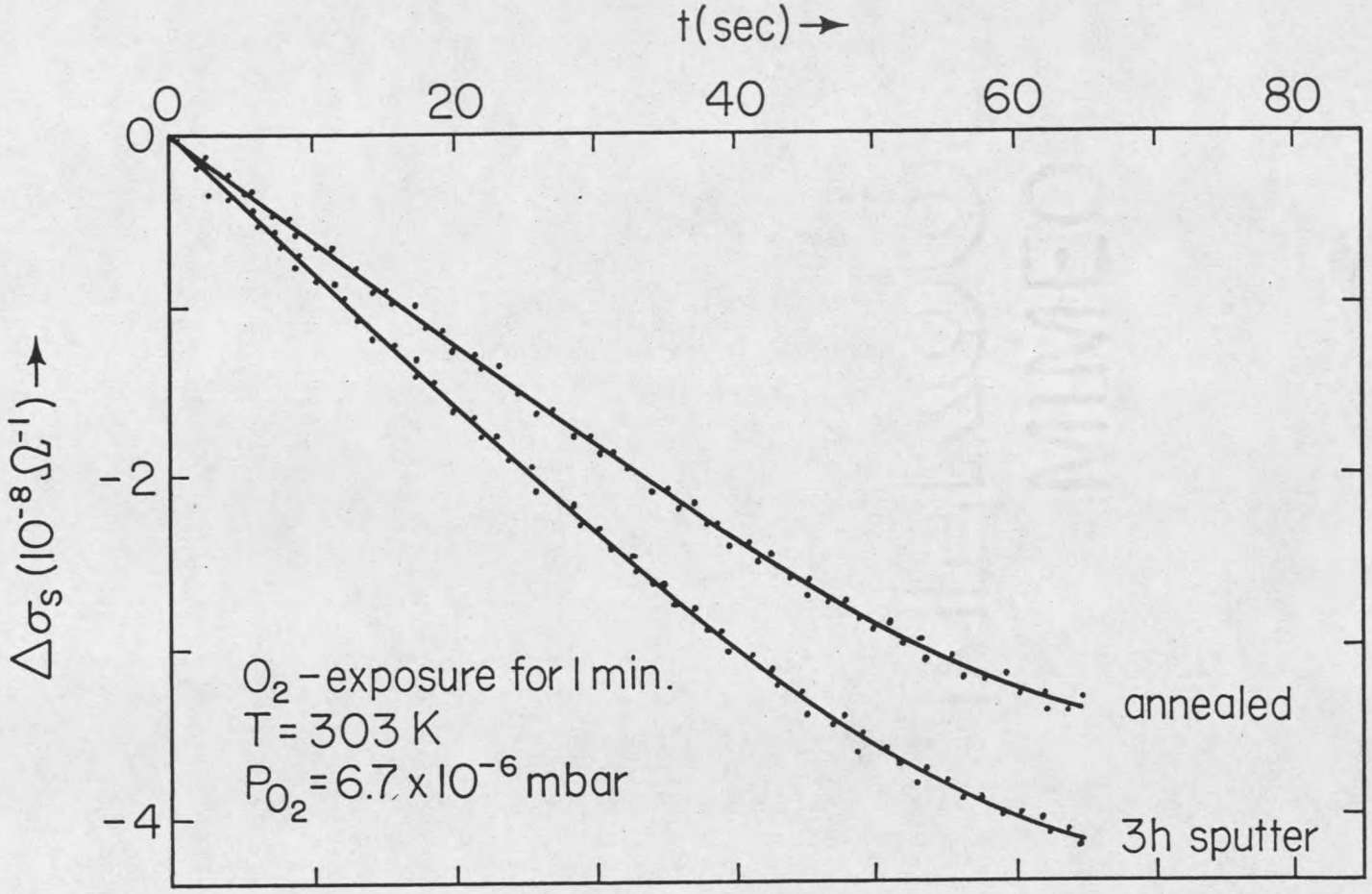

Figure 34. Surface-conductivity changes of annealed and heavily ion-bombarded TiO_2(110) upon oxygen exposure at 303 K.

The solid line labelled "annealed" was obtained on a stoichiometric $TiO_2(110)$ surface, whereas the data points leading to the curve "3 h sputter" were recorded on a $TiO_2(110)$ surface that had been sputtered for 3 hours. Similarly to surfaces covered with submonolayer amounts of titanium, we again observe an enhanced conductivity decrease on a non-stoichiometric surface, when the latter is exposed to oxygen.

The results presented in Figure 35 show that monolayer amounts (1 ML) of titanium deposited on a $TiO_2(110)$ surface reduce the conductivity increase measured during the exposure of molecular hydrogen. The curve labelled "0 ML Ti" represents results obtained on a stoichiometric surface and shows pronounced conductivity increases during a 1-minute exposure of molecular hydrogen (P_{H2} = 2.0x10^{-5} mbar, T = 303 K). The solid line labelled "1 ML Ti" results from the same kind of experiment carried out on a titanium-covered (1 ML) $TiO_2(110)$ surface and shows much-less-pronounced increases in the surface conductivity.

The following two Figures 36 and 37 represent $\Delta\sigma_s$ experiments performed during 2-minute exposures of carbon monoxide (P_{CO} = 2.0x10^{-5} mbar, T = 303 K in Figure 36 and T = 348 K in Figure 37).

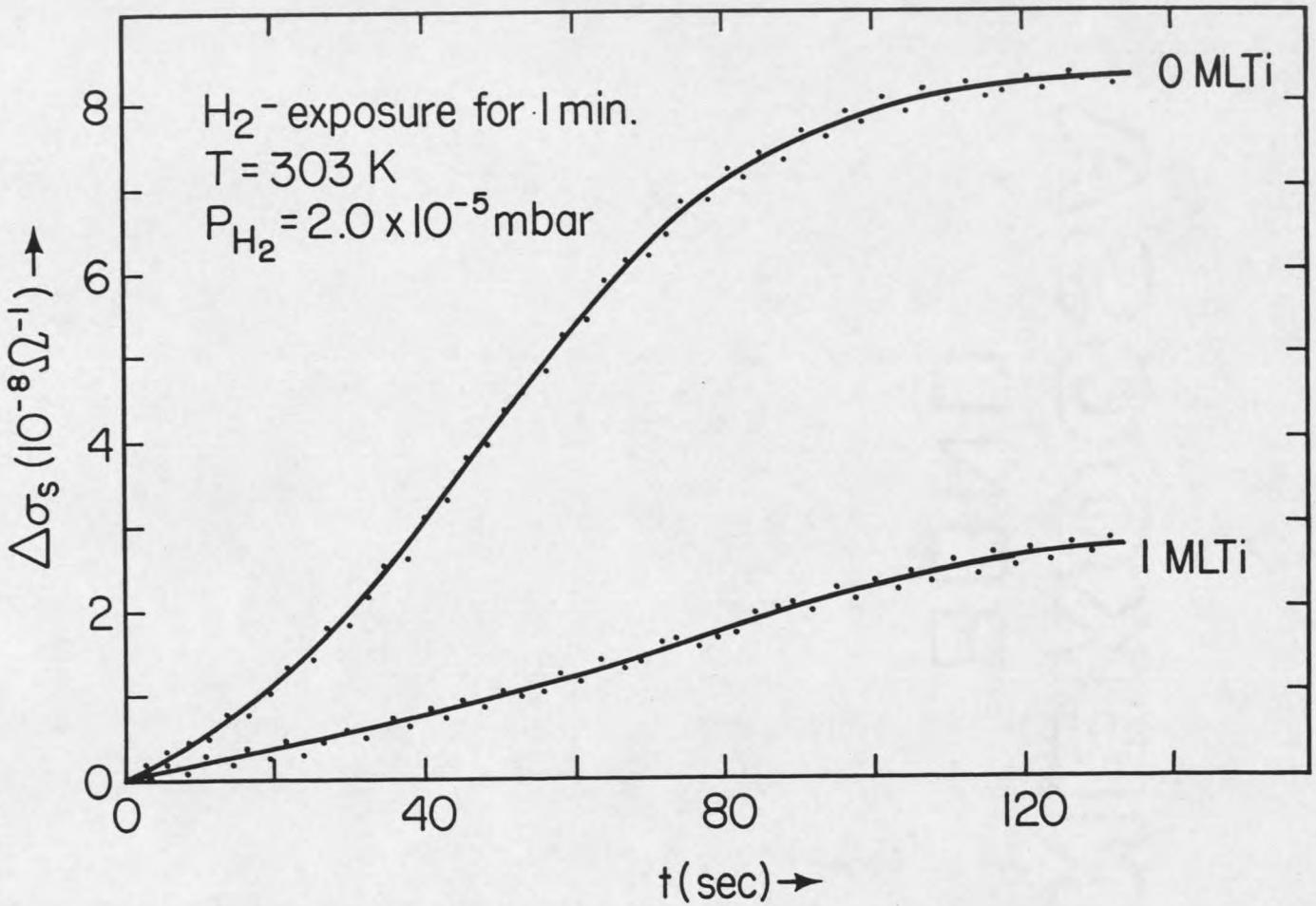

Figure 35. Surface-conductivity changes of clean and Ti-covered TiO_2(110) upon exposure to molecular hydrogen at 303 K.

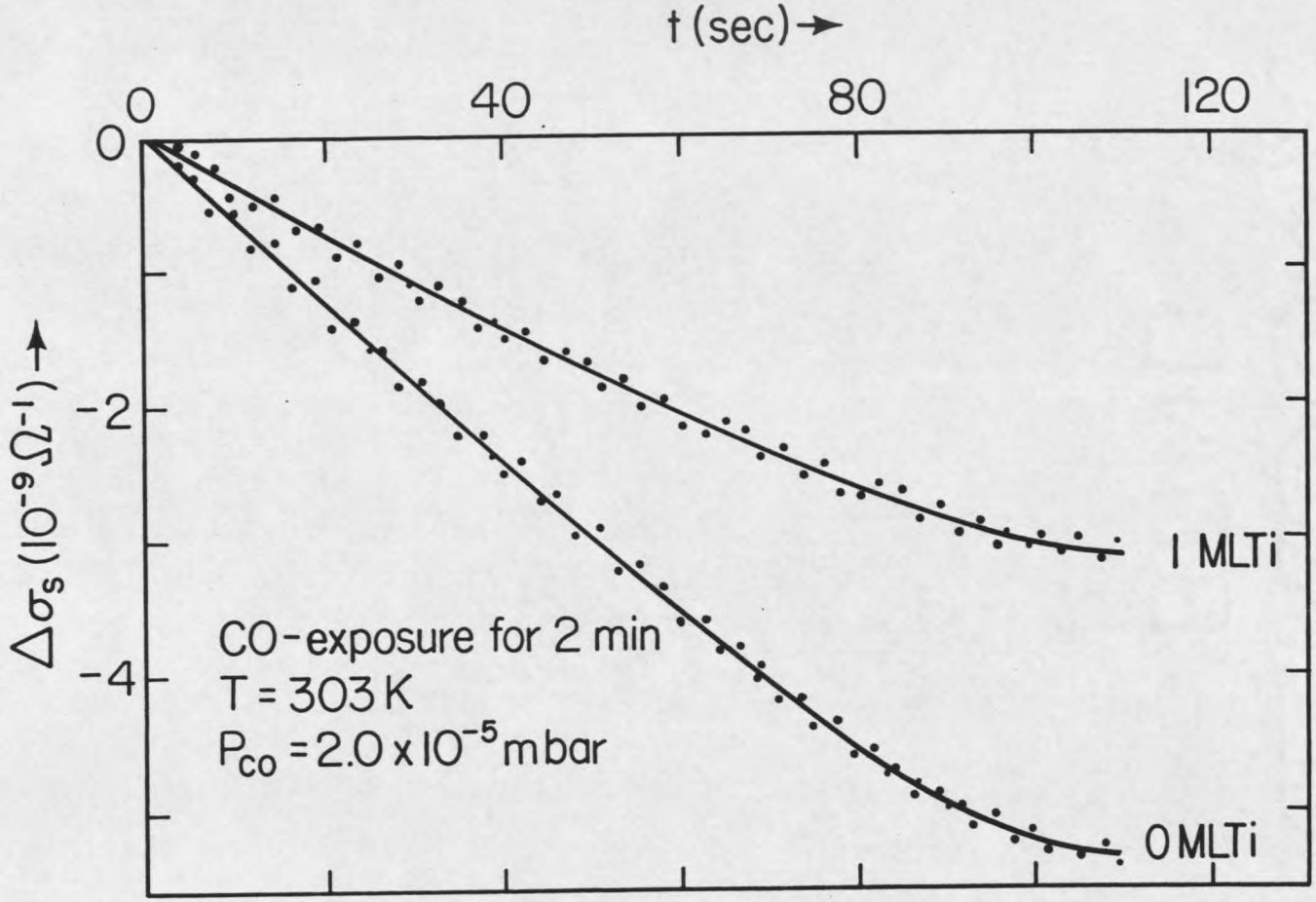

Figure 36. Surface-conductivity changes of clean and Ti-covered TiO_2(110) upon CO exposure at 303 K.

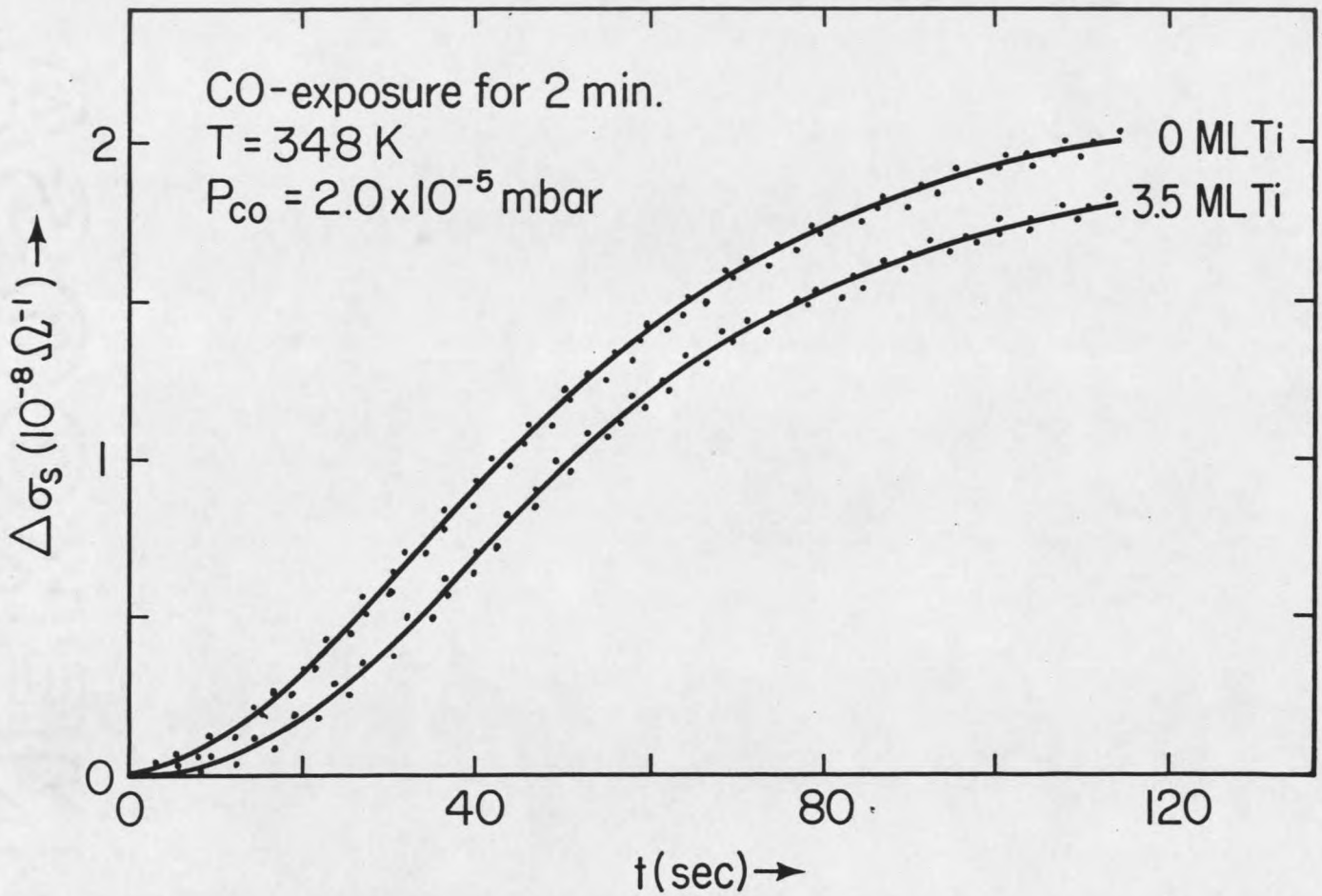

Figure 37. Surface-conductivity changes of clean and Ti-covered TiO_2(110) upon CO exposure at 348 K.

The figures indicate that - independently of the sample temperature - monolayer (1 ML in Figure 36) and multilayer (3.5 ML in Figure 37) amounts of titanium deposited on the surface lead to less-pronounced changes in the surface conductivity.

In further experiments - not represented by figures - it was found that several hours of heavy argon-ion bombardment (E_p = 1000 eV, Iem = 11 mA, Itarg = 1 μA) also reduces the conductivity changes measured at different temperatures during H_2- as well as CO-exposures.

A 1 hour ion bombardment, e.g., causes 42 % smaller conductivity changes with respect to the stoichiometric surface upon CO adsorption at 303 K and P_{CO} = $2x10^{-5}$ mbar. The conductivity increases found during H_2 exposure at 348 K and P_{H2} = $2x10^{-5}$ mbar were reduced by 17.5 % after 2 hours of argon-ion bombardment. These phenomena will be discussed in the next chapter.

The following three figures present results obtained from measurements of work function changes ($\Delta\phi$) performed at 303 K on differently treated $TiO_2(110)$ surfaces during oxygen, hydrogen and carbon monoxide exposures. In general, the experiments were started 4 minutes before the gas exposures in order to get an average initial CPD value.

As soon as the sample was exposed to one of the gases mentioned above, the CPD values changed rapidly and

stabilized within seconds, i.e. remained constant until the end of the experiment, which usually took about 10 minutes.

The curves shown in Figure 38 reflect $\Delta\phi$ measurements done during 1-minute oxygen exposures at an oxygen partial pressure of 6.7×10^{-6} mbar. The bottom curve labelled "annealed" represents results obtained on a stoichiometric $TiO_2(110)$ surface. The two curves above were recorded on titanium-covered (0.5, 1.0 and 2.0 ML) surfaces, whereas the uppermost curve results from measurements performed on a heavily ion-bombarded (t = 2 h, E_p = 1000eV, I_{em} = 11 mA, I_{targ} = 1 μA) $TiO_2(110)$ surface. The results show that the work function of a $TiO_2(110)$ sample always increases during oxygen exposures. The increases are more pronounced on titanium-covered and heavily sputtered surfaces.

The graphs in Figure 39 present work function changes recorded during 1-minute exposures of molecular hydrogen at a hydrogen partial pressure of 6.7×10^{-6} mbar. The stoichiometric ("annealed") $TiO_2(110)$ surface exhibits a pronounced decrease in its work function, when exposed to hydrogen. But as soon as the coverage of titanium deposited on the surface reaches 0.5 monolayers, work function increases are observed. These become more pronounced with increasing layer thickness (1 ML). Strong work function increases are also observed on ion-bombarded (t = 1 h, E_p = 1000 eV, I_{em} = 11 mA, I_{targ} = 1 μA) surfaces represented by the uppermost curve.

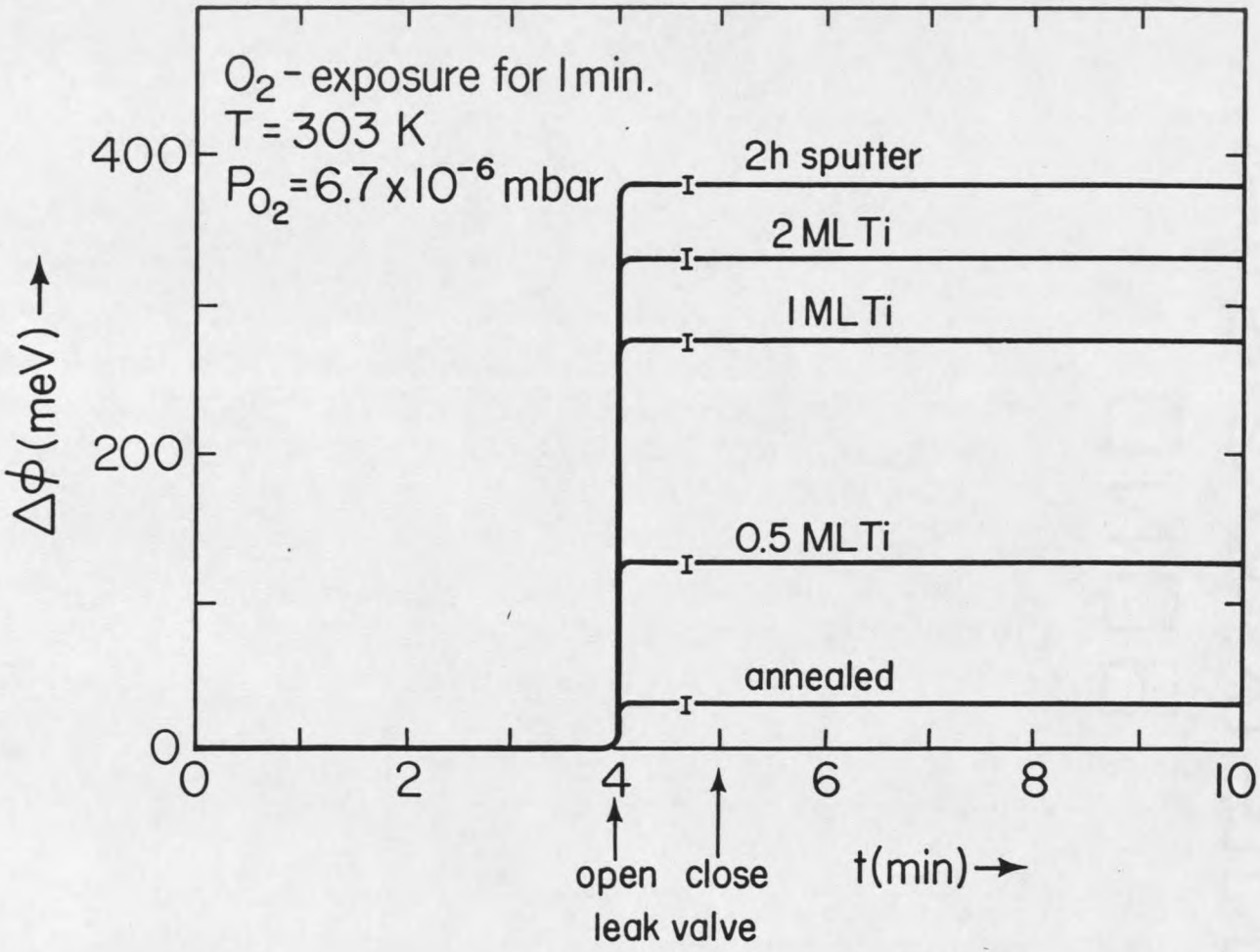

Figure 38. Work-function changes $\Delta\phi$ of annealed, Ti-covered and ion-bombarded TiO_2(110) upon oxygen exposure at 303 K.

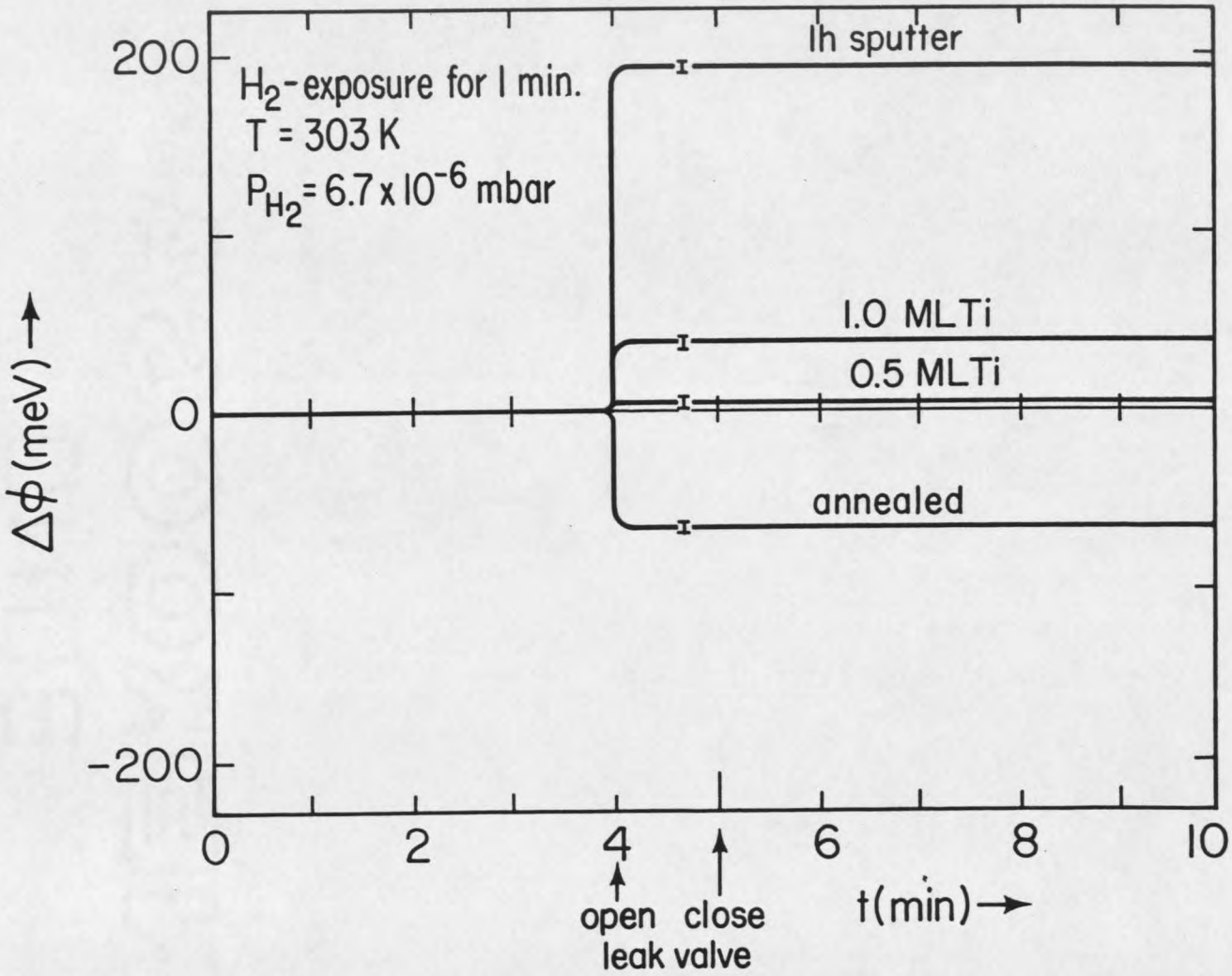

Figure 39. Work-function changes $\Delta\phi$ of annealed, Ti-covered and sputtered TiO_2(110) upon exposure to molecular hydrogen at 303 K.

The curves presented in Figure 40 were derived from measurements performed during 2-minute carbon monoxide exposures at a CO partial pressure of 2.0×10^{-5} mbar. Similar to the results shown in Figure 39, the stoichiometric ("annealed") $TiO_2(110)$ surface exhibits strong work function decreases, when exposed to carbon monoxide. Monolayer amounts (1 ML) of titanium evaporated onto the surface cause less-pronounced work function decreases, whereas multilayer titanium coverages (3.5 ML) result in work function increases. Heavily sputtered (t = 3 h, E_p = 1000 eV, I_{em} = 11 mA, I_{targ} = 1 μA) surfaces also show strong work function increases, when exposed to carbon monoxide, as illustrated by the uppermost curve.

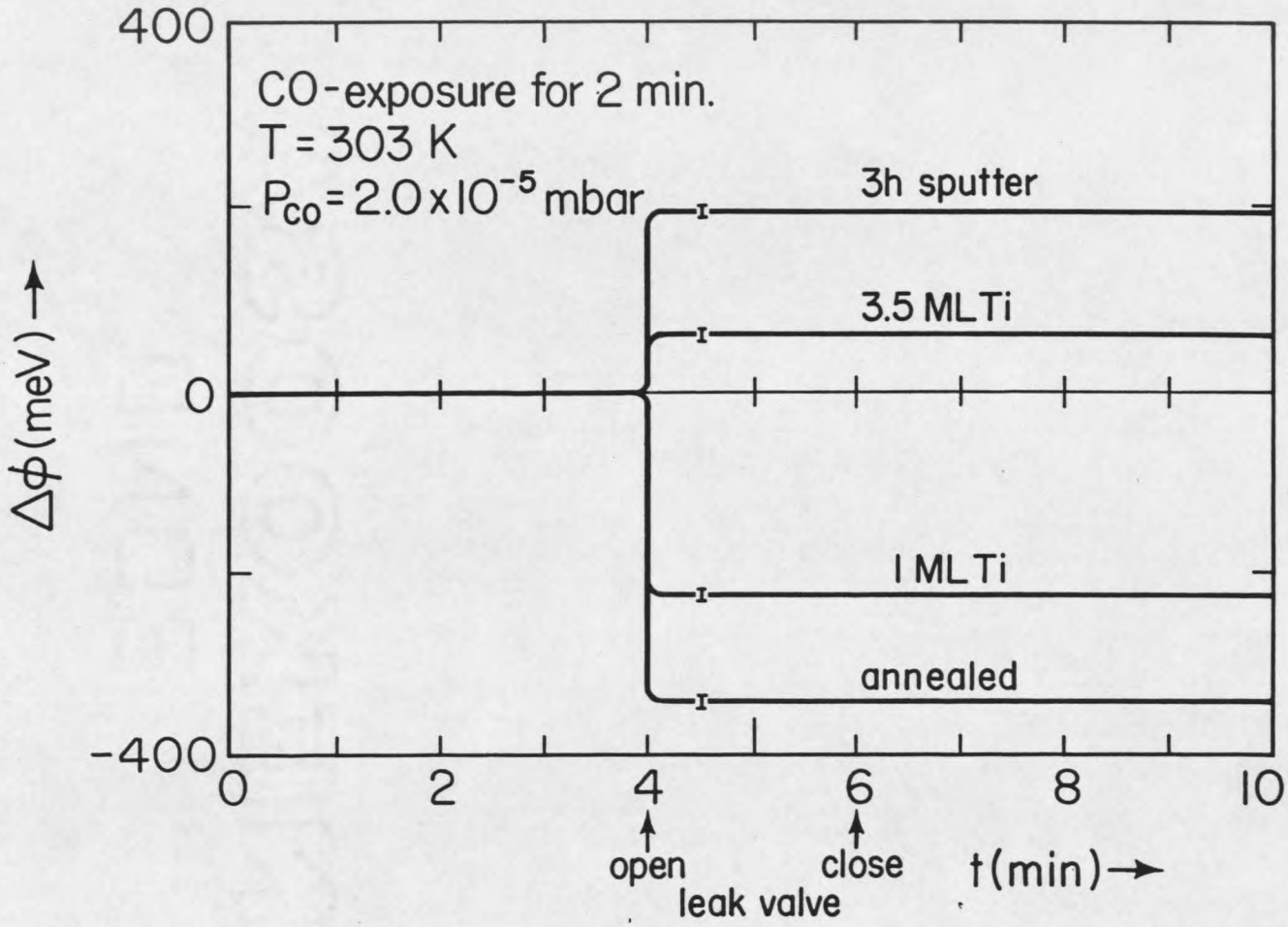

Figure 40. Work-function changes $\Delta\phi$ of annealed, Ti-covered and ion-bombarded TiO_2(110) upon CO exposure at 303 K.

CHAPTER 5

DISCUSSION

In the following chapter, the experimental results presented above will be analyzed and discussed in more detail.

In the first part of the discussion, it will be shown how some important physical bulk properties, such as bulk electronic densities, bulk Fermi level positions, Debye lengths and energetic bulk defect levels, can be derived from bulk conductivity measurements.

The second part of this chapter will present a theoretical analysis of electron-spectroscopic results and a discussion of the changes in the surface electronic structure of TiO_2 samples upon the formation of surface defects.

In the third and fourth parts, the adsorption of gases on stoichiometric and defective TiO_2(110) surfaces, respectively, will be discussed in terms of a charge transfer model. This model will also be applied to explain the transfer of charges from chemisorbed submonolayer amounts of titanium to the TiO_2 substrate.

The last part of this chapter will present a model that describes the diffusion of defects in the bulk of

TiO_2. Within the framework of this model, diffusion coefficients and diffusion profiles will be calculated and discussed.

Bulk Conductivity and Bulk Defects

The majority charge carriers in n-type rutile are electrons that mainly arise from the thermal depopulation of defect (oxygen vacancy)-induced donor levels in the band gap (see chapter 2). Thermally-excited electronic valence-to-conduction-band transitions are negligible at low temperatures due to the fairly large gap energy of 3.05 eV. Also, acceptor-type band gap states, which are induced by oxygen interstitials and cause p-type conduction, can be neglected for oxygen partial pressures less than 1 mbar (see chapter 2). The bulk conductivity σ_b can thus be written in a simple form:

$$\sigma_b = e\,\mu_b\,\, nb \tag{25}$$

Here, $e = 1.6021 \times 10^{-19}$ C (elementary charge), and μ_b is the temperature-dependent bulk Hall mobility for conduction-band electrons, and n_b is the temperature-dependent bulk density of conduction-band electrons.

The bulk density of conduction-band electrons, n_b, can be computed in the following way [130,138]:

$$n_b = 2 \int_{E_C}^{\infty} dE\; D_C(E)\; f(E) \tag{26}$$

E_C is the energy at the lower conduction-band edge, and

$$f(E) = \{1+\exp[(E-E_F)/k_BT]\}^{-1} \qquad (27)$$

is the Fermi function with E_F being the Fermi energy, T the temperature and $k_B = 8.6173 \times 10^{-5}$ eV K^{-1} Boltzmann's constant. $D_C(E)$ is the energy-dependent density of conduction-band levels per unit energy, and - in the case of parabolic bands [138] - given by:

$$D_C(E) = 2\pi(2m_{eff}/h^2)^{3/2} \times (E-E_C)^{1/2} \qquad (28)$$

with $m_{eff} \simeq 25\ m_e$ being the effective mass of conduction-band electrons (see chapter 2), $m_e = 9.1091 \times 10^{-31}$ Kg the electronic rest mass, and $h = 4.1357 \times 10^{-15}$ eVsec Planck's constant. The two different electronic spin orientations are considered by the factor 2 in Equation 26.

In practice, the semiconductor bulk of TiO_2 is usually nondegenerate [138], i.e.

$$E_C - E_F > 3k_BT$$

$$E_F - E_V > 3k_BT$$

(E_V is the energy at the upper valence-band edge).

The Fermi function given in Equation 27 can thus be approximated by an exponential Boltzmann function, which

facilitates the integration of Equation 26. With the help of Equation 28 - assuming parabolic conduction bands - we obtain:

$$n_b = N_C \exp[(E_F - E_C)/k_B T] \qquad (29)$$

with $N_C = 2(2\pi m_{eff} k_B T/h^2)^{3/2}$.

With known bulk Hall mobility data μ_b (see chapter 2), experimentally obtained bulk conductivities σ_b and the help of Equations 25 and 29 we can now determine the bulk electronic densities n_b and the positions of the bulk Fermi level E_F relative to the lower conduction band edge E_C.

The bulk conductivity σ_b of a yellowish TiO_2(110) sample (see chapter 3) was measured for sample temperatures ranging from 300 to 600 K. The resulting bulk electronic densities and Fermi-level positions are plotted in Figure 41. Also shown is the effective Debye length L_D to be discussed later. For n-type semiconductors with negligible bulk hole concentration [100], this bulk property is given by:

$$L_D = [\epsilon \epsilon_0 k_B T/(e^2 n_b)]^{1/2} \qquad (30)$$

$\epsilon_0 = 1.4185 \times 10^{-32}$ C2/(eVcm) is the electric-field constant and ϵ the temperature-dependent dielectric constant of rutile (see chapter 2).

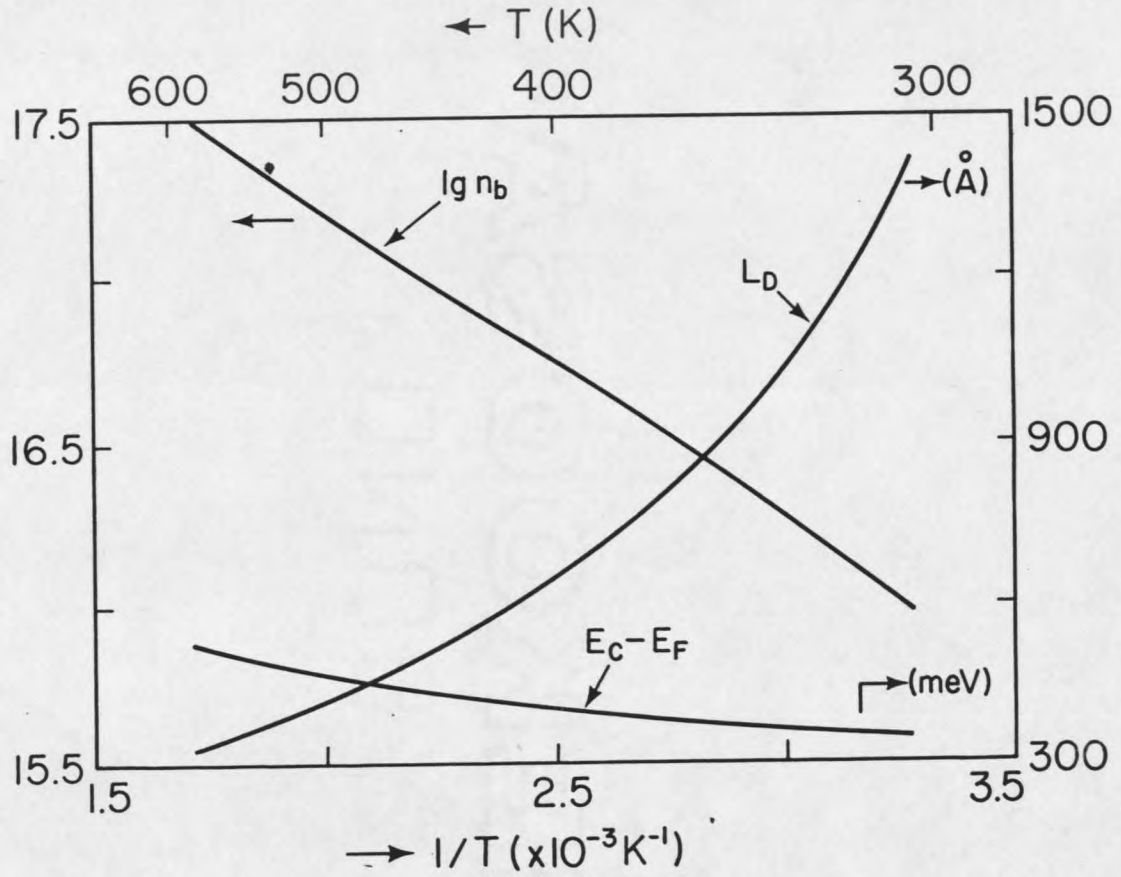

Figure 41. Bulk densities of conduction-band electrons, n_b, bulk Fermi level positions, E_C-E_F, and effective Debye lengths, L_D, plotted as a function of inverse temperature. These quantities were calculated from temperature-dependent bulk conductivities and bulk Hall mobilities of TiO_2.

The most important defect in TiO_2 is the oxygen vacancy (see chapter 2) associated with two Ti^{3+} ions. For two electrons trapped at the defect, the ground-state configuration may be characterized by $2Ti^{3+}\ V_O^0$, paramagnetic first ionization stage by $2Ti^{3+}\ V_O^+$ and the completely ionized defect by $2Ti^{3+}\ V_O^{2+}$. For simplification, the label "$2Ti^{3+}$" will be omitted in the following.

In a simple model, the ionization of a donor-type oxygen vacancy can be described quantitatively by applying the law of mass action [79]:

$$V_O^0 \text{ <=====> } V_O^+ + e^- \qquad (31)$$

$$V_O^+ \text{ <=====> } V_O^{2+} + e^- \qquad (32)$$

The first and second ionization potentials can formally be attributed to two band-gap donor levels E_{D1} and E_{D2}. The occupancy of these donor levels is determined by the Fermi function and the corresponding degeneracy factors:

$$\frac{N_{D0}}{N_{D0} + N_{D1}} = \frac{1}{1 + 2\ \exp[(E_{D1}-E_F)/k_BT]} \qquad (33)$$

$$\frac{N_{D1}}{N_{D1} + N_{D2}} = \frac{1}{1 + 0.5\ \exp[(E_{D2}-E_F)/k_BT]} \qquad (34)$$

N_{D0}, N_{D1} and N_{D2} are the bulk densities of completely occupied, singly and doubly ionized donors having degeneracies of 1, 2 and 1, respectively.

With the help of Equations 33 and 34 as well as 29 we can calculate the two equilibrium constants K_{D1} and K_{D2} attributed to Equations 31 and 32.

$$K_{D1} = N_{D1}\, n_b/N_{D0} = 2\, N_C \exp[(E_{D1}-E_C)/k_BT] \qquad (35)$$

$$K_{D2} = N_{D2}\, n_b/N_{D1} = 0.5\, N_C \exp[(E_{D2}-E_C)/k_BT] \qquad (36)$$

The condition of electroneutrality requires:

$$n_b = N_{D1} + 2\, N_{D2} \qquad (37)$$

The total bulk defect (donor-type oxygen vacancy) density is given by:

$$N_D = N_{D0} + N_{D1} + N_{D2} \qquad (38)$$

From Equations 35-38 we get:

$$n_b = N_D\, K_{D1}\, \frac{2\, K_{D2} + n_b}{n_b^2 + n_b\, K_{D1} + K_{D1}\, K_{D2}} \qquad (39)$$

The unknown parameters N_D, E_{D1} and E_{D2} can be calculated by fitting the experimentally obtained, temperature-dependent bulk electronic densities n_b (see Figure 41) to Equation 39. This was done for the sample described above by applying both the Gauss-Marquardt procedure [139] and the Simplex Algorithm [140]. The results are:

$$N_D = 1.14 \times 10^{17} \text{ cm}^{-3}$$

$$E_C - E_{D1} = 0.421 \text{ eV}$$

$$E_C - E_{D2} = 0.470 \text{ eV} \qquad (40)$$

At room temperature, both donor levels are located below the Fermi level (see Figure 41) and hence are only partially ionized (see further discussion in the last part of this chapter).

Surface Structure Including Surface Defects

The formation of $Ti^{\delta+}$ ($\delta<4$) species at the TiO_2(110) surface upon the deposition of foreign titanium atoms can be studied by means of XPS, XAES, AES, ELS and EELS.

In the Ti2p core-level spectra presented in Figure 7, additional emissions are observed on the low-binding-energy sides of the parent peaks. These features become more intense and broader with increasing titanium coverage and can be attributed to less-ionic titanium at the surface, because core electrons are less strongly bound in less-positively-charged ions. The $Ti2p_{3/2}$ core-level positions of Ti^{3+}, Ti^{2+} and metallic titanium are indicated by correspondingly-labelled dashed vertical lines and have been measured for Ti_2O_3 [141], TiO [142] and titanium metal [120]. According to these results, the deposition of submonolayer amounts (0.7 ML Ti in curve b) of titanium leads to the formation of mainly Ti^{3+} ions at the TiO_2(110) surface, i.e. charge transfer occurs from the foreign Ti atoms to the TiO_2 substrate.

Increasing titanium coverage, however, reduces the number of elementary charges transferred per additional foreign titanium atom as can be seen in curve c. Here, the additional core-level feature already shows a significant contribution from Ti^{2+} ions. The titanium coverage

corresponding to this curve was determined to be 1.1 monolayers (see also chapter 4).

Further deposition of titanium led to curves d and e (2.0 and 4.5 ML Ti) demonstrating the formation of an overlayer of titanium.

The sequence of evaporation experiments explained above strongly suggests that a defect-like structure involving Ti3+ species can be created at TiO_2(110) surface by depositing submonolayer amounts of titanium on the latter. In the low-coverage regime, each foreign titanium atom apparently chemisorbs as Ti3+ due to an energetically-favored charge transfer from the evaporated species to the TiO_2 substrate.

In the following, a quantitative XPS line-shape analysis of one of the Ti2p core-level spectra shown in Figure 7 will be presented. The theoretical background of this kind of analysis will be explained in more detail in Appendix A.

The X-ray-induced photoelectrons emerging from a sample lose kinetic energy in mainly two processes that lead to additional emissions on the low-kinetic-energy sides (high-binding-energy sides) of core-level peaks. One of these loss features is associated with single, extrinsic surface-and bulk-plasmon excitations of the photoelectrons. The second one, which occurs mainly in metals, is due to

intrinsic shake-up or final-state effects caused by emerging photoelectrons (see e.g. references 143,144 and Appendix A).

In Figures 42 and 43, the XPS core-level line shapes and positions of the Ti2p levels of stoichiometric titanium dioxide as well as metallic titanium are shown on the same energy scale, with intensities normalized to the $Ti2p_{3/2}$ core-level emission of stoichiometric TiO_2. Both the $Ti2p_{1/2}$ and $Ti2p_{3/2}$ levels of Ti exhibit a striking asymmetry at low kinetic energies (Figure 42). This asymmetry is characteristic of XPS core-level spectra obtained on metals, due to the fact that emerging photoelectrons lose kinetic energy by creating electron-hole pairs in the Fermi sea of the metal. This effect is independent of the shape of the sample and is thus called "intrinsic" as mentioned above. It is much less pronounced in semiconductors and negligible in insulators, because of large energy gaps between valence and conduction bands. The core-level asymmetries indeed are much smaller in TiO_2 as shown in Figure 43.

With the use of the Simplex Algorithm [140] mentioned above the two experimentally obtained XPS line shapes presented in Figures 42 and 43 (solid lines) were each fitted to a sum of five Gaussians after a simple linear background had been subtracted. At least five Gausssians were necessary to adequately fit the curve with background.

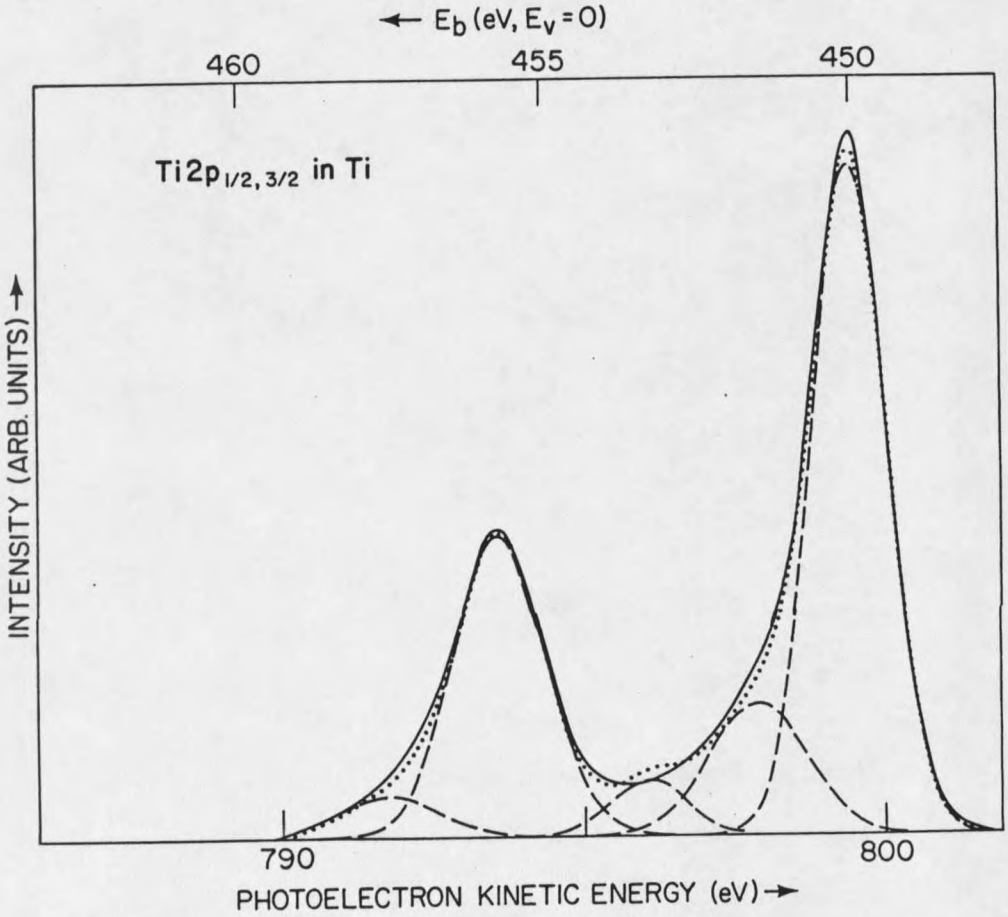

Figure 42. Ti2p core-level spectrum (solid line) of metallic Ti. The dashed curves represent Gaussians fitted to the XPS line shapes. The dotted curve was obtained by adding the Gaussians and represents the theoretical line shape. Further details are discussed in the text.

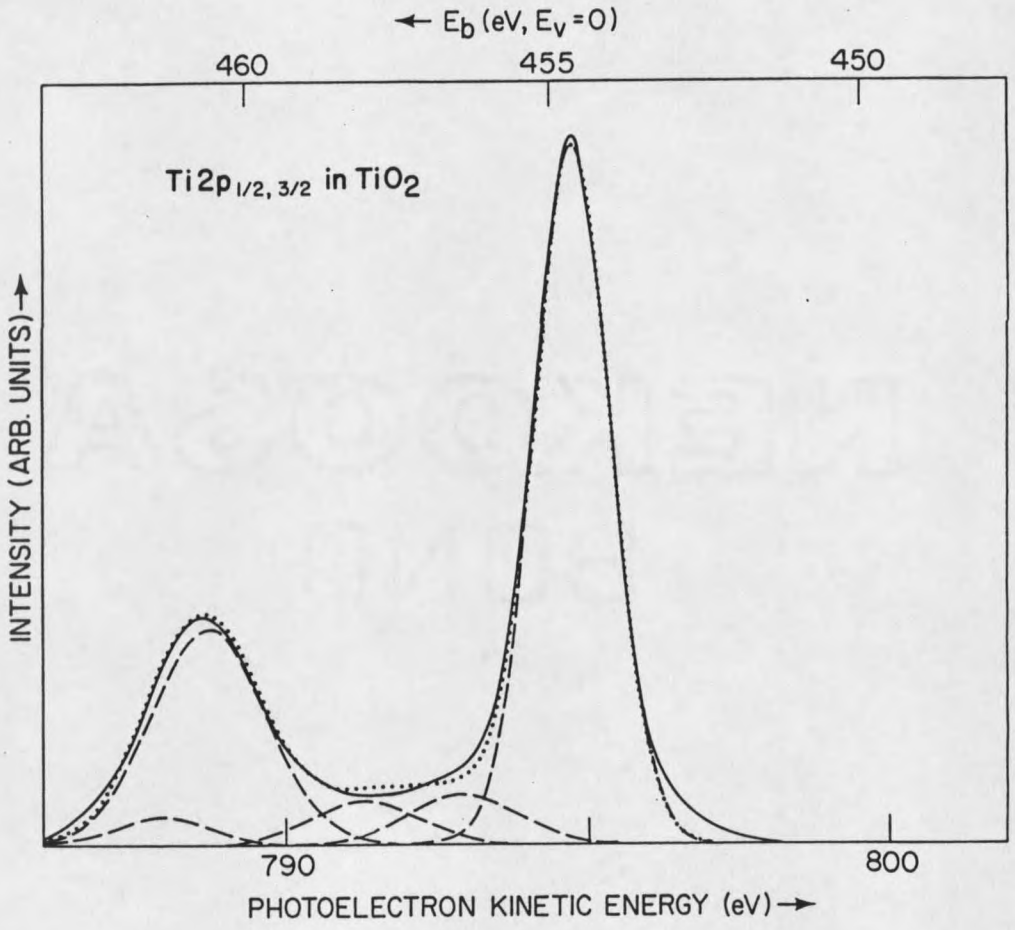

Figure 43. Ti2p core-level spectrum (solid line) of TiO_2. The dashed and dotted curves were obtained in a similar way as in Figure 42.

These Gaussians are indicated by dashed lines, their sums, i.e. the theoretically obtained line shapes, by dotted lines. The peak positions (at maximum intensity) E_0, amplitudes A, half widths E (FWHM), integrals I and per cent contributions (%) of the individual integrals to the total integral of the theoretically obtained line shapes are listed in Tables 1 and 2. The peak numbers increase with increasing photoelectron kinetic energy of the corresponding peak maxima.

Table 1. Gaussians fitted to a Ti2p spectrum of Ti.

Peak	E_0 (eV)	A (cps)*	ΔE (eV)	I (eV cps)	%
1	791.30	86.26	1.98	181.90	3.9
2	793.25	649.66	1.87	1294.60	28.3
3	795.84	119.71	1.48	188.00	4.1
4	797.74	285.47	1.93	586.40	12.8
5	799.37	1453.59	1.51	2328.90	50.9

*cps = counts per second

Table 2. Gaussians fitted to a Ti2p spectrum of TiO_2.

Peak	E_0 (eV)	A (cps)	ΔE (eV)	I (eV cps)	%
1	787.91	72.18	1.58	121.40	2.7
2	788.65	560.81	2.06	1230.00	27.0
3	791.08	113.21	1.83	220.80	4.8
4	792.61	133.10	1.87	265.40	5.8
5	794.33	1824.79	1.40	2720.20	59.7

Peaks 1 ,3 and 4 in either spectrum can mathematically be attributed to the loss features mentioned above and

make it possible to formally subtract the latter from the measured XPS line shape. Information about the physical properties of these features, however, cannot be derived from the Gaussians because of the absence of an underlying model.

Figure 44 presents a representative Gaussian fit of curve c shown in Figure 7. Before fitting the Ti2p spectrum to eight Gaussians, a linear background and the theoretically obtained peaks 1, 3 and 4 of Table 2 were subtracted from the experimentally obtained spectrum in order to eliminate at least part of the loss features.

The choice of eight Gaussians was made because each core-level feature, namely $Ti2p_{1/2}$ and $Ti2p_{3/2}$, is believed to have contributions from Ti^{4+}, Ti^{3+}, Ti^{2+} and Ti^{1+} ions, as suggested by curve c in Figure 7. The parameters of these eight Gaussians are listed in Table 3.

Table 3. Gaussians fitted to Ti2p spectrum c.

Peak	E_0 (eV)	A (cps)	ΔE (eV)	I (eV cps)	%
1	788.64	551.74	2.20	1294.00	12.6
2	790.19	297.10	1.60	507.40	4.9
3	791.82	409.12	1.83	795.40	7.8
4	792.43	238.36	2.28	578.90	5.6
5	794.30	1560.83	2.02	3357.30	32.7
6	796.20	788.75	2.57	2159.60	21.1
7	797.60	460.53	2.01	982.90	9.6
8	798.70	345.81	1.58	582.10	5.7

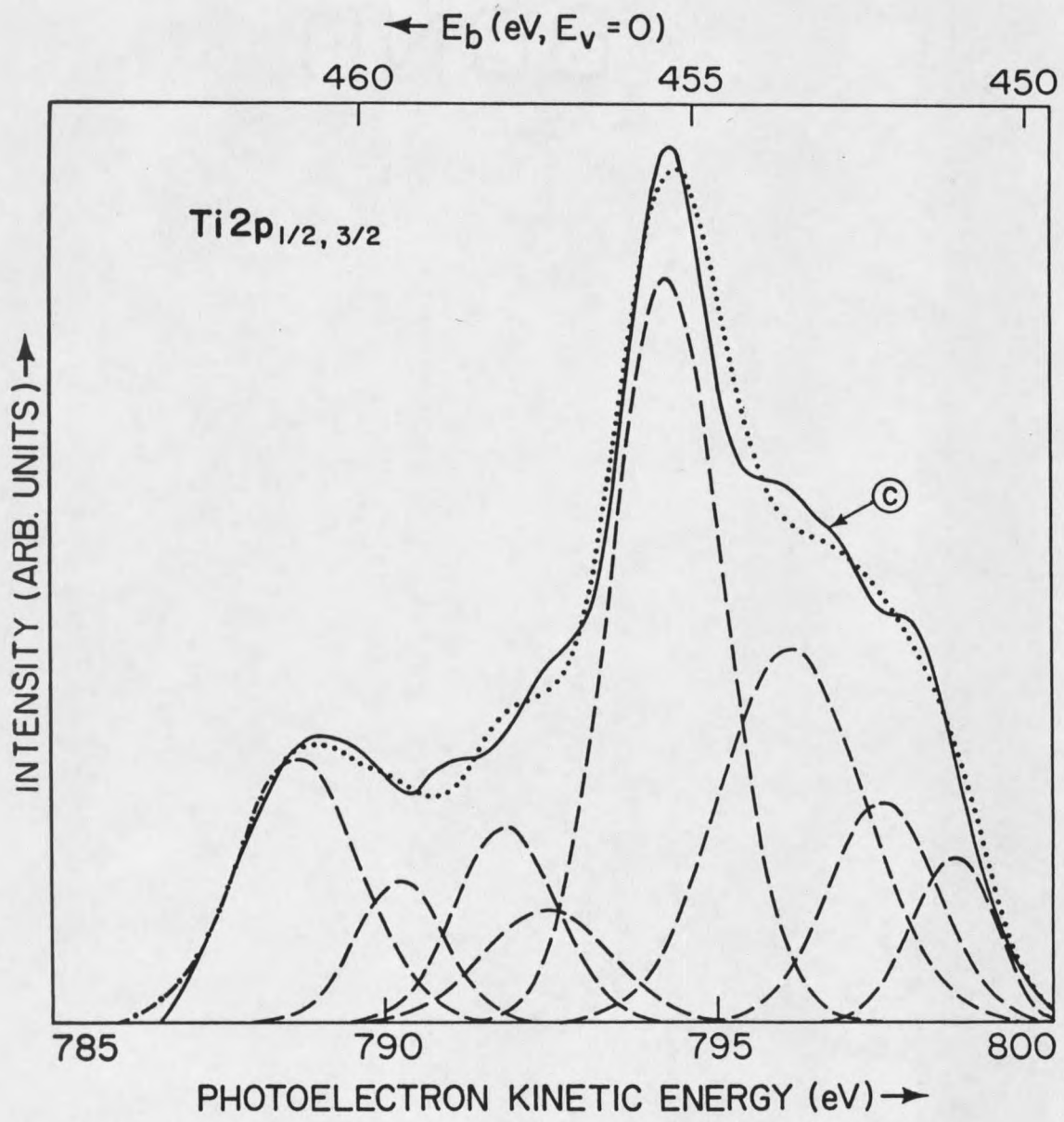

Figure 44. Ti2p core-level spectrum c (solid line) of Figure 7, fitted by eight Gaussians (dashed lines). All Gaussian parameters were varied during the line-shape analysis (see text).

The sum of peaks 5 to 8 gives a mathematically and physically satisfactory fit of the $Ti2p_{3/2}$ emission as indicated by the dotted line. These peaks thus represent the contributions of the different bulk and surface titanium ions to the $Ti2p_{3/2}$ core-level feature. From Table 3 it can be seen that the per cent contributions of Ti^{4+} and Ti^{3+} ions are dominant.

The remaining Gaussians 1 to 4 yield a mathematical fit of the $Ti2p_{1/2}$ emission and thus formally represent the $Ti2p_{1/2}$ core-level peaks of the different titanium ions. Their positions, relative amplitudes and half widths, however, differ from the physically expected ones [120,141,142]. Using peaks 5 to 8 as reference peaks, as well as known and estimated values for the Ti2p spin-orbit splittings in different titanium ions, four (physically more realistic) $Ti2p_{1/2}$ Gaussians were constructed. These are plotted in Figure 45 together with peaks 5 to 8 from Figure 44, and apparently don't yield a good mathematical fit of the $Ti2p_{1/2}$ emission.

Gaussians are believed to yield reasonable mathematical and physical fits of core-level spectra obtained on purely insulating or semiconducting samples due to negligible XPS peak asymmetries. The more metallic the material becomes, however, the more pronounced these asymmetries will be.

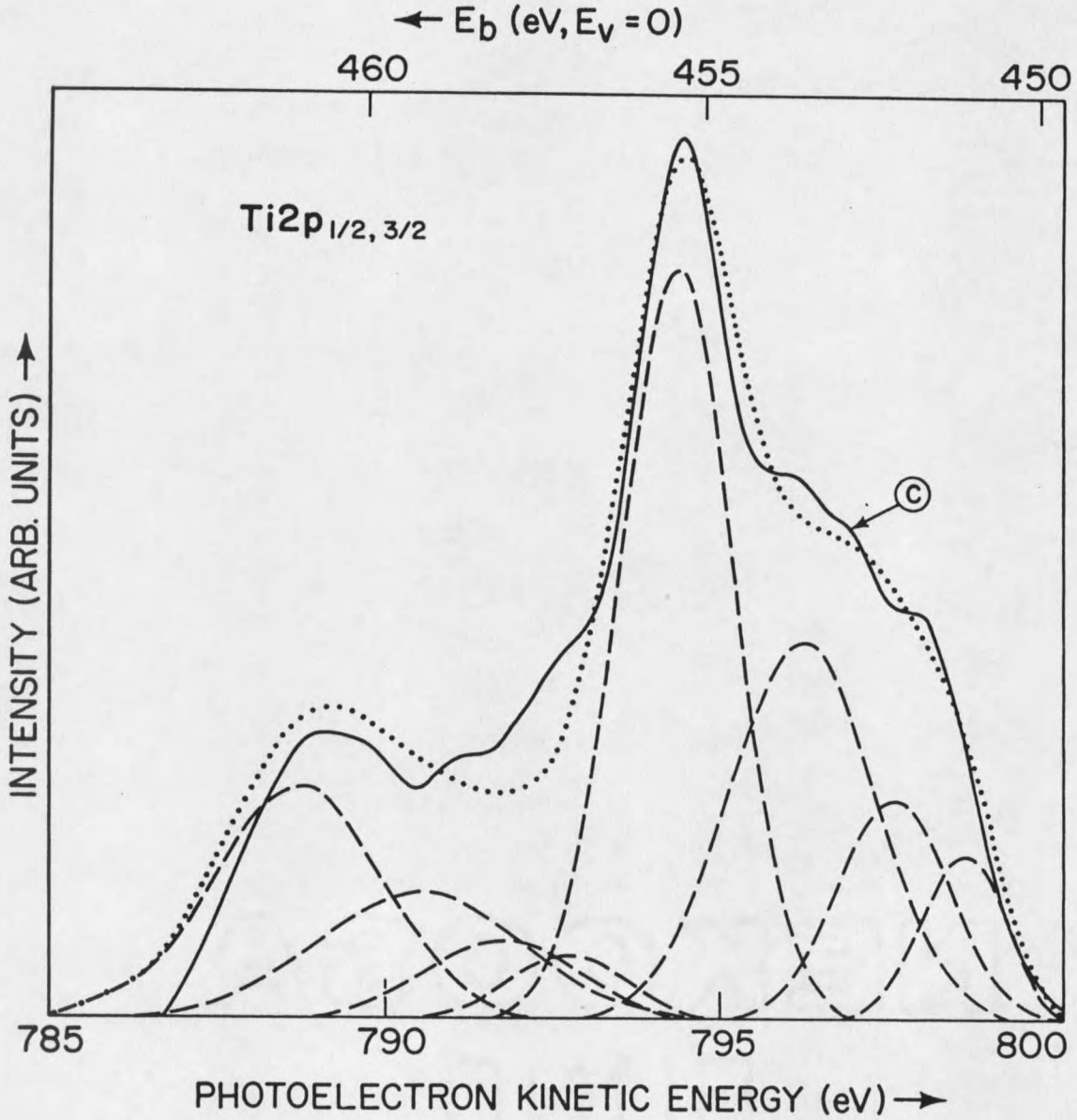

Figure 45. Ti2p core-level spectrum c of Figure 7, fitted by eight Gaussians. Here, the Gaussian parameters of the $Ti2p_{1/2}$ peaks were estimated from the parameters of corresponding $Ti2p_{3/2}$ peaks. Further explanations are given in the text.

The Ti^{3+}, Ti^{2+} and Ti^{1+} ions discussed above cause occupied Ti3d states in the TiO_2 band gap resulting in an exponential increase of the surface conductivity (see Figure 26). This indicates an enhanced metallicity at the titanium-covered surface. For this reason, it was also tried to fit eight asymmetric, Gauss-broadened Doniach-Sunjić functions [144] to curve c (only linear background subtracted) of Figure 7.

These functions account for the intrinsic shake-up excitations and will be discussed in Appendix A. Besides peak position and amplitude (= proportionality constant that includes all energy-independent prefactors, see Equation 103 in Appendix A), other physical properties such as the line width γ (due to the finite lifetime of the core-hole), the so-called Anderson singularity (asymmetry) index α as well as the analyzer broadening and core-hole-induced phonon broadening ΔE_{ph} had to be fitted to the experimentally obtained line shape. Assuming a constant Gaussian broadening of 0.8 eV due to the analyzer and the X-ray source, we obtained the results listed in Table 4 and plotted in Figure 46.

The asymmetries of peaks 1 and 5 are small, as expected because these peaks represent the $Ti2p_{1/2}$ and $Ti2p_{3/2}$ core levels of Ti^{4+} ions respectively. The asymmetry, however, increases with decreasing titanium oxidation number.

Table 4. Gauss-broadened Doniach-Sunjic functions fitted to Ti2p curve c.

Peak	E_0 (eV)	A (cps)	γ (eV)	α	E_{ph} (eV)	I (eV cps)	%
1	788.62	148.74	1.32	0.05	0.22	352.99	6.1
2	789.46	108.15	1.41	0.17	0.22	300.13	5.2
3	791.40	171.02	1.36	0.17	0.22	494.10	8.6
4	792.50	187.02	1.00	0.25	0.22	563.24	9.8
5	794.30	785.47	0.90	0.04	0.22	1640.74	28.5
6	796.25	392.75	1.00	0.17	0.22	1023.56	17.8
7	797.80	298.96	1.00	0.17	0.22	779.16	13.5
8	798.75	198.71	1.00	0.25	0.22	606.06	10.5

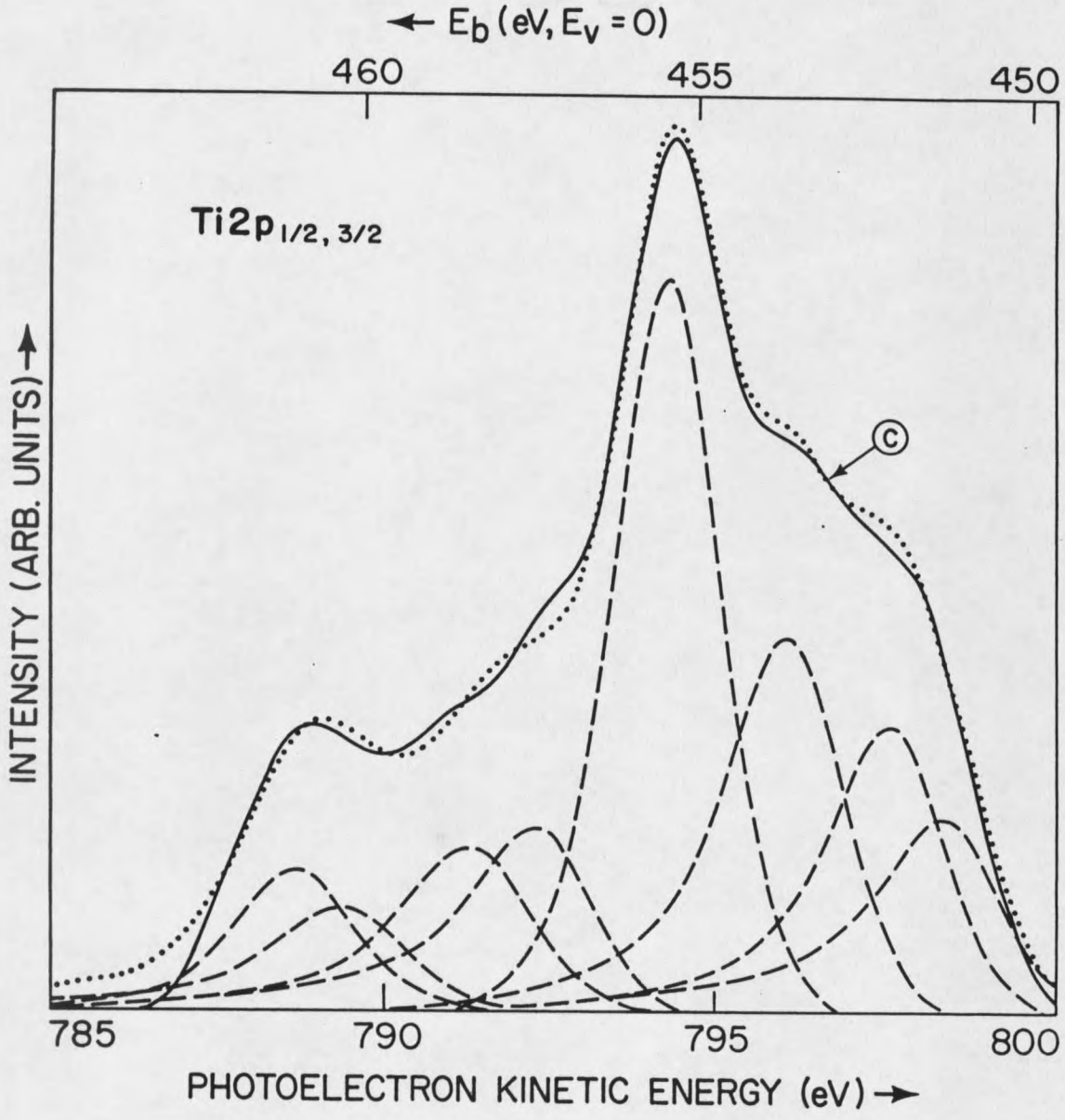

Figure 46. Ti2p core-level spectrum c of Figure 7, fitted by eight Doniach-Sunjic functions (dashed lines). All parameters were varied during the line-shape analysis.

Mainly for this reason, the relative contributions of peaks 7 and 8 to the $Ti2p_{3/2}$ emission are greater than those obtained for Gausssians. Again, positions and relative amplitudes of the Doniach-Sunjić functions representing the corresponding $Ti2p_{1/2}$ core levels don't agree with the physically expected ones. Physically more realistic $Ti2p_{1/2}$ peaks are shown in Figure 47. Their positions and amplitudes were calculated from corresponding $Ti2p_{3/2}$ positions and amplitudes and by assuming the same asymmetry indices for corresponding $Ti2p_{1/2}$ and $Ti2p_{3/2}$ peaks.

In Figure 48, the kinetic energies of the $Ti2p_{3/2}$ peak maxima are plotted versus titanium oxidation number. The crosses (x) indicate experimental data points obtained for Ti^{4+} in TiO_2 (this thesis), Ti^{3+} in Ti_2O_3 [141], Ti^{2+} in TiO [142] and for neutral Ti atoms in metallic titanium [120]. The triangles (Δ) indicate the $Ti2p_{3/2}$ positions calculated from a Gaussian fit of curve c in Figure 44 (see Table 3). A solid line was drawn through the centers of these triangles in order to illustrate the functional dependence of the $Ti2p_{3/2}$-peak shift on the titanium oxidation number. The dots (•) represent results obtained from a Doniach-Sunjic-type fit of curve c (see Figure 46 and Table 4). Figure 48 shows resonable agreement between theoretically and experimentally obtained $Ti2p_{3/2}$-peak positions.

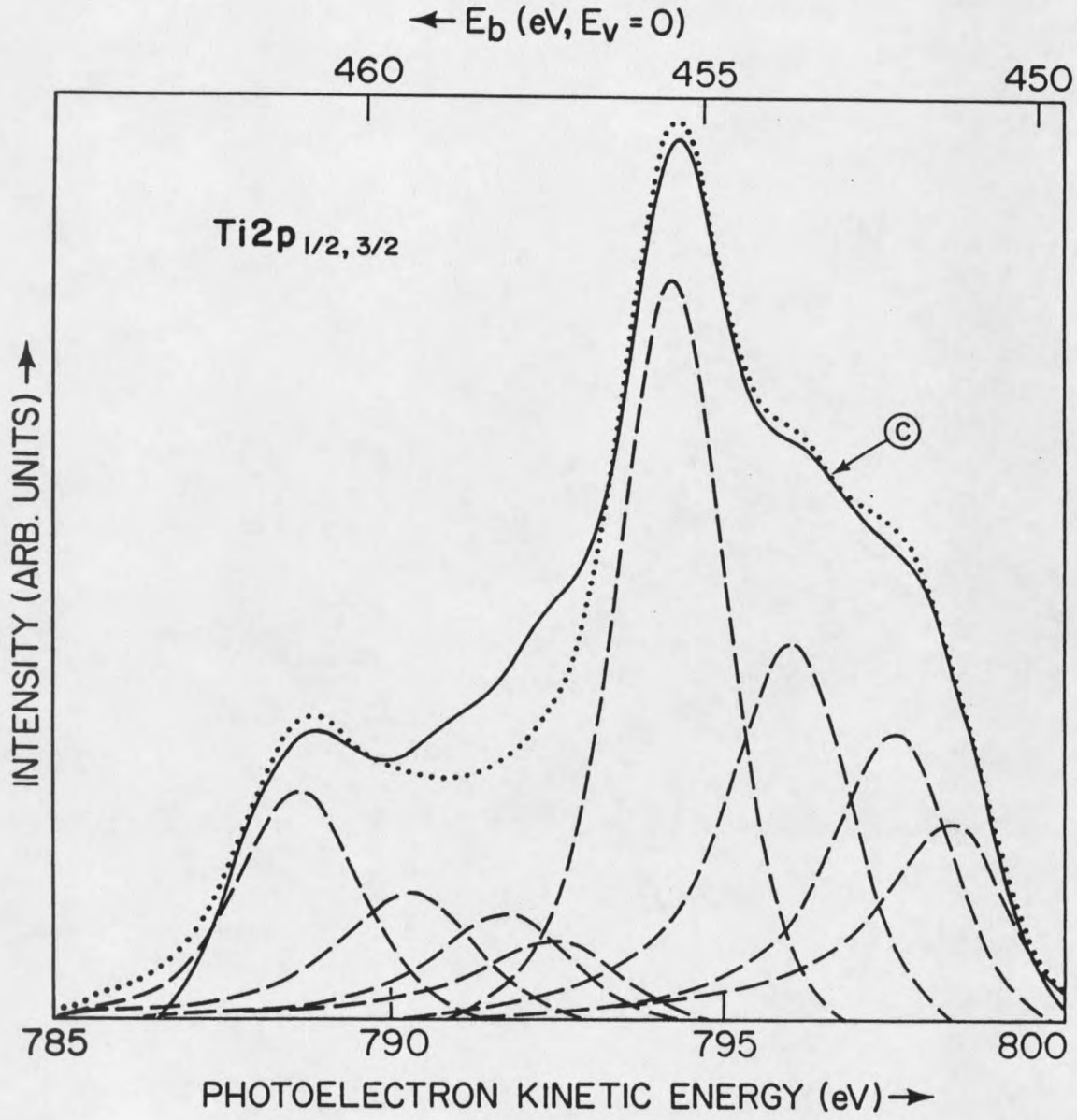

Figure 47. Ti2p core-level spectrum c of Figure 7, fitted by eight Doniach-Sunjic functions. Similar to Figure 45, the $Ti2p_{1/2}$-peak parameters were estimated from the parameters of corresponding $Ti2p_{3/2}$ peaks.

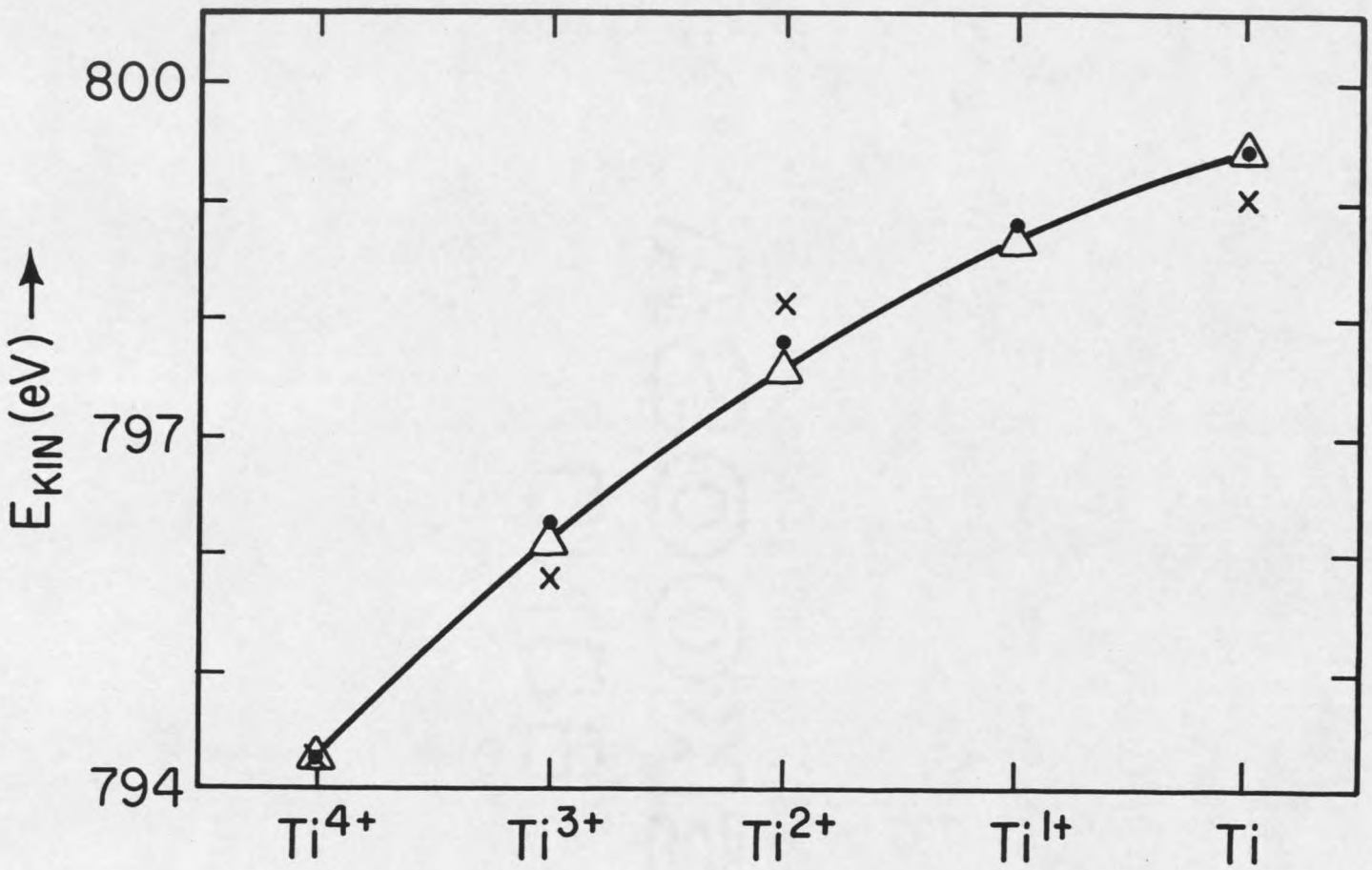

Figure 48. $Ti2p_{3/2}$-peak positions plotted as a function of Ti oxidation number. The crosses (x) indicate experimental data points (see text), the triangles (Δ) represent results obtained from a Gaussian fit of curve c in Figure 44. The dots (•) indicate results of a Doniach-Sunjić-type fit of curve c in Figure 46.

The experimental curves in Figure 8 (see also chapter 4) demonstrate the effect of heavy argon-ion bombardment on the Ti2p core-levels. Similarly to the results obtained on titanium-covered surfaces, additional emissions on the low-binding-energy sides of $Ti2p_{1/2}$ and $Ti2p_{3/2}$ can be observed indicating the presence of differently charged titanium species at the surface. Argon-ion bombardment leads to pronounced surface-atom disorder and probably causes the removal of oxygen atoms with subsequent charge transfer from the vacancy to the titanium sites.

The 01s core-level peak exhibits characteristic shifts towards higher binding energy upon the deposition of titanium. This effect is illustrated in Figure 9. An asymmetric broadening of the 01s core-level on the high-binding-energy side (curve a) has already been observed by Sham and Lazarus [88], who performed angle-dependent XPS measurements on clean and hydrated TiO_2(001) samples (see also chapter 2). On clean (scraped) samples, they observed the growth of a new feature on the high-binding-energy side of the 01s core-level with increasing photoelectron take-off angle (measured with respect to the surface normal). They assigned this feature to oxide ions terminating the surface. Even at zero take-off angle, this feature caused an asymmetry in the 01s core-level line shape, quite similar to the one observed in curve a of Figure 9 (take-off angle = 0°). We can thus

assume that the O1s-peak broadening observed in curve a of Figure 9 is due to the presence of surface oxide ions.

In general, XPS core-level binding energy shifts ΔE_b arise from four main contributions [159]:

$$\Delta E_b = \Delta E_{chem} + \Delta E_{Mad} + \Delta(-eV_s) + \Delta E_{relax} \qquad (41)$$

where ΔE_{chem} is the chemical shift depending on the charge of the ion under study. ΔE_{Mad} is the change in the Madelung potential energy depending on the ionic environment and $\Delta(-eV_s)$ denotes changes in the band bending (see below). The term ΔE_{relax} represents changes in the final-state relaxation energy which is partially added to the photoelectron kinetic energy upon reoccupation of the core hole.

Figure 49 presents a Gaussian fit of curve a of Figure 9. This curve was obtained on a clean stoichiometric TiO_2(110) surface (see chapter 4) and exhibits an asymmetry on its high-binding-energy side. A linear background was subtracted first and then three Gaussians were tentatively fitted to the line shape, two representing the asymmetric tail. The Gaussian parameters are listed in Table 5.

Table 5. Gaussians fitted to 01s spectrum a.

Peak	E_0 (eV)	A (cps)	ΔE (eV)	I (eV cps)	%
1	720.17	108.96	0.94	108.90	2.4
2	721.21	252.82	1.24	332.80	7.4
3	722.84	2487.98	1.53	4054.40	90.2

Peak 3 represents bulk oxygen ions, whereas peak 2 can be assigned to surface oxygen ions which are less negatively charged due to one missing Ti^{4+} neighbor (see Figures 1 and 2). In the average, each surface oxygen ion thus lacks of 2/3 of an electron compared to bulk oxygen, resulting in a chemical shift towards higher core-level binding energies.

Peak 1 originates from extrinsic many-body effects (see Appendix A) accompanying the emitted photoelectrons. Its position and intensity depends on the kind of background subtraction used.

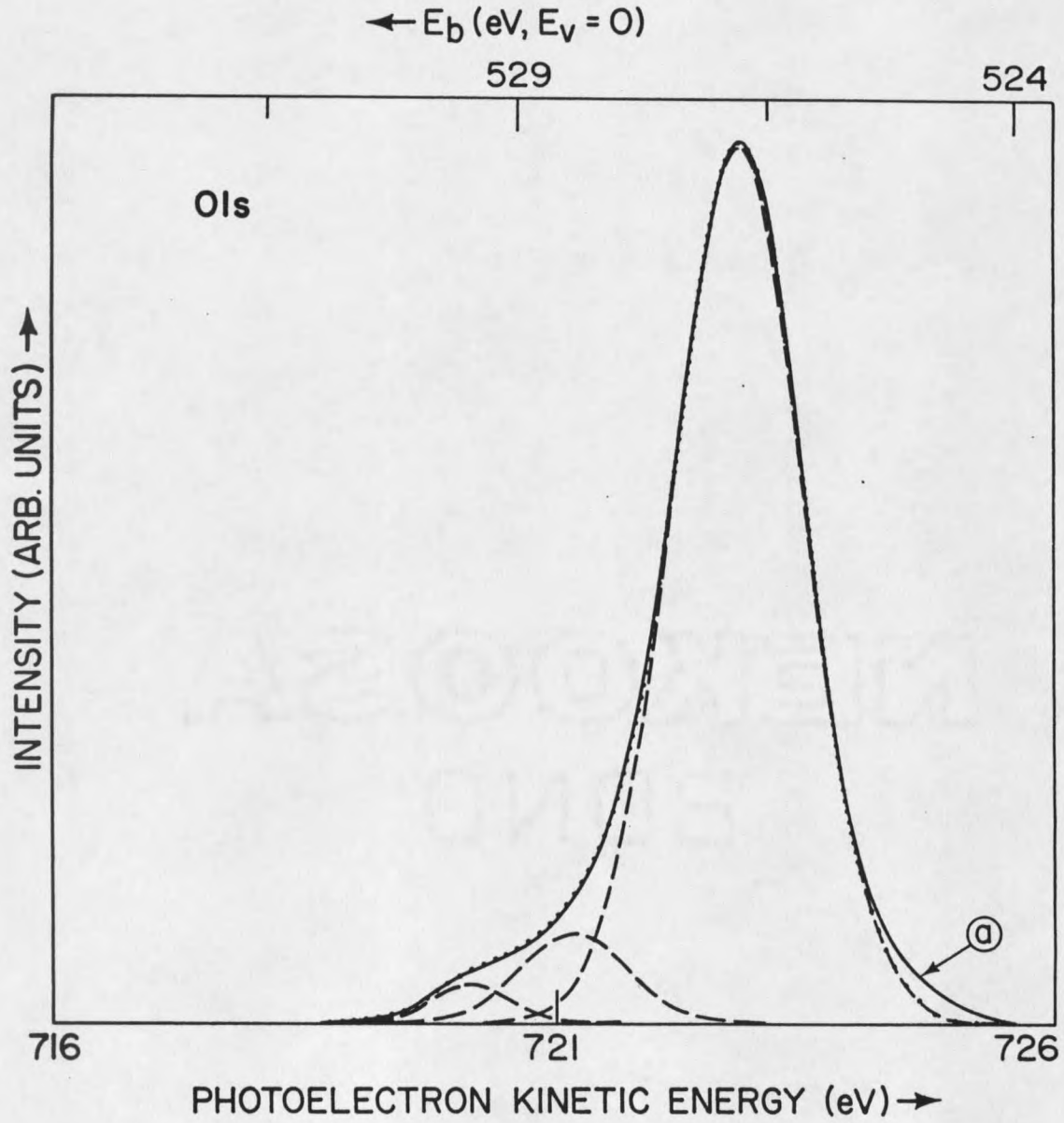

Figure 49. O1s core-level spectrum a (solid line) of Figure 9, fitted by three Gaussians (dashed lines), indicating the presence of bulk- and surface-oxygen species (see text). All Gaussian parameters were varied during the line-shape analysis.

Figure 50 shows a similar fit of curve c of Figure 9. This curve was obtained after the deposition of 1.1 monolayers of titanium . Again, a linear background was subtracted, before the three-Gaussian fit was calculated for a constant bulk O1s peak position. The Gaussian parameters are listed in Table 6.

Table 6. Gaussians fitted to O1s spectrum c (peak 1 fixed).

Peak	E_0 (eV)	A (cps)	ΔE (eV)	I (eV cps)	%
1	720.53	157.44	3.50	587.20	11.8
2	721.95	460.52	1.68	823.60	16.5
3	722.84	2229.26	1.51	3571.80	71.7

Figure 51 presents a slightly different Gaussian fit of curve c. The parameters are listed in Table 7. In this case, the bulk O1s position was varied, too, resulting in a shift of this peak towards higher binding energies. Simultaneously, peak 2 shifts towards lower binding energies and exhibits a lower intensity than the corresponding peak in Figure 50.

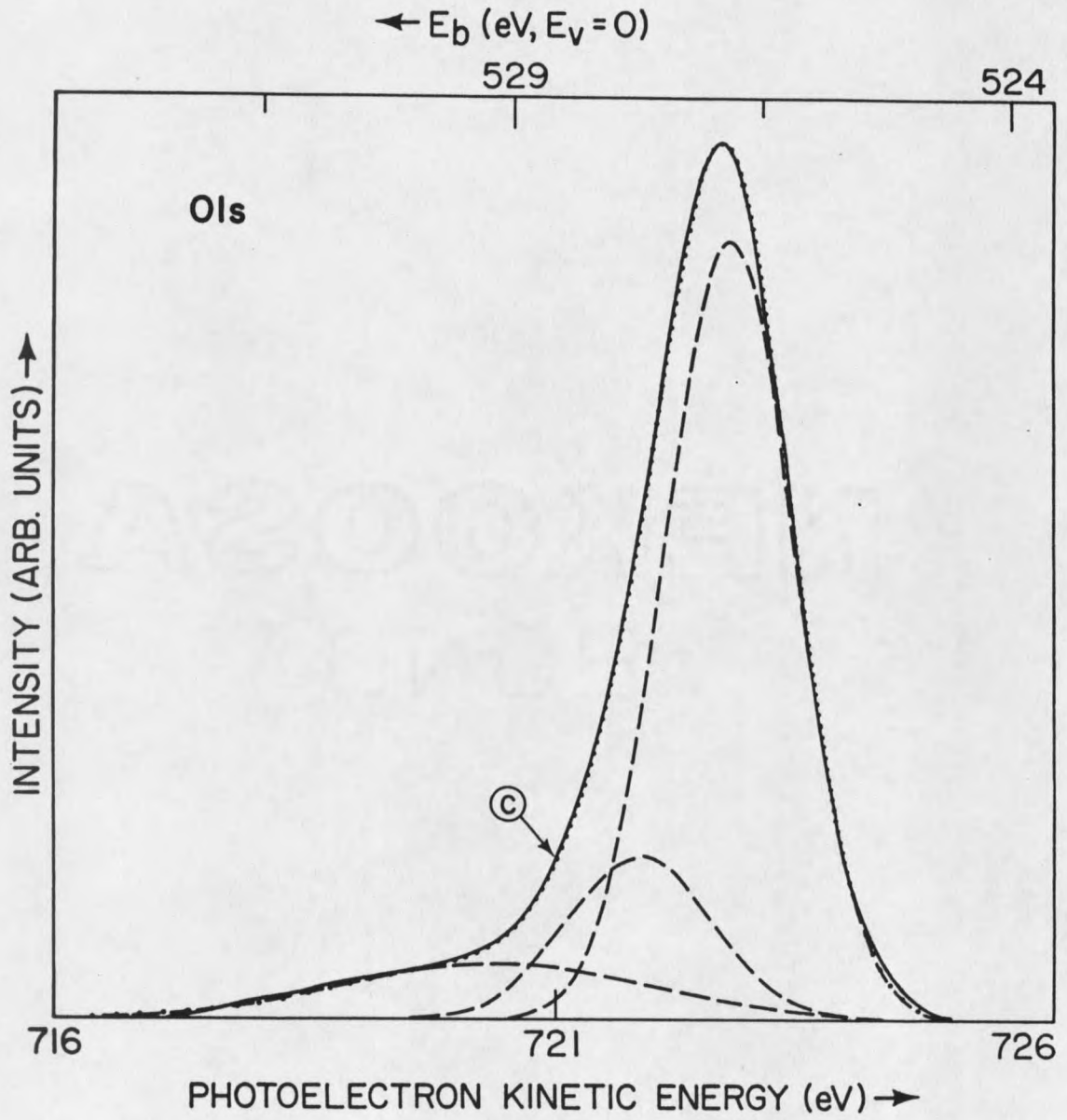

Figure 50. O1s core-level spectrum c of Figure 9, fitted by three Gaussians. The energetic position of the most intense Gaussian, representing the bulk emission, was set equal to the corresponding peak position shown in Figure 49.

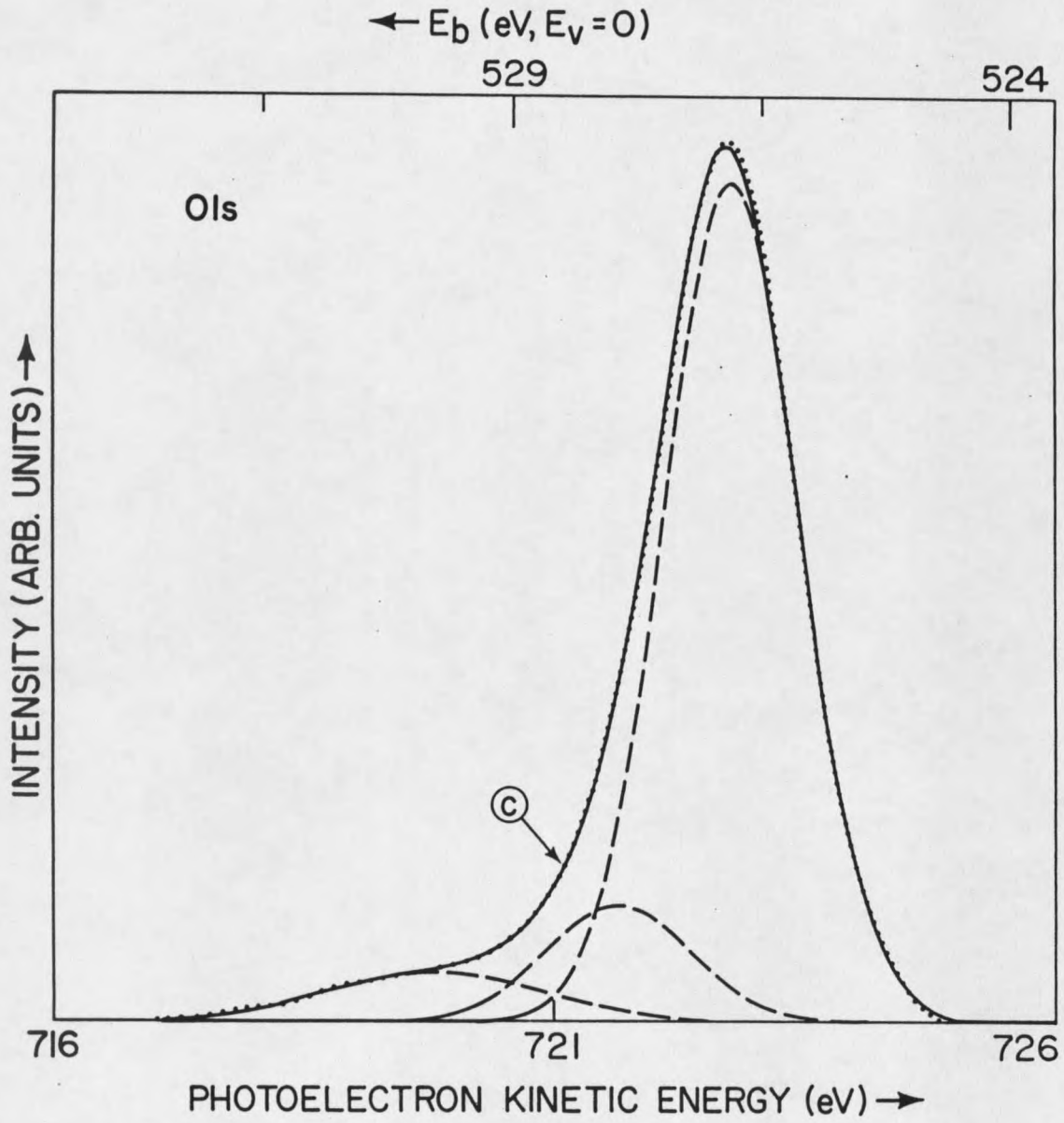

Figure 51. O1s core-level spectrum c of Figure 9, fitted by three Gaussian. In contrast to Figure 50, all Gaussian parameters were varied during the peak analysis (see text).

This phenomenon may be explained by a titanium-induced band bending and formation of bulk-like oxygen ions due to the presence of titanium species at the oxygen-rich (110) surface (see Figure 2).

Table 7. Gaussians fitted to 01s spectrum c (peak 1 free).

Peak	E_0 (eV)	A (cps)	ΔE (eV)	I (eV cps)	%
1	719.83	138.79	2.61	385.00	7.7
2	721.65	328.27	1.69	591.00	11.8
3	722.79	2392.98	1.58	4015.70	80.5

The presence of titanium species at the surface leads to a charge transfer from these species to surface oxygen ions. This causes a shift of the surface-derived peak 2 towards the 01s bulk peak as can be observed in Figure 51.

The negative band bending accompanying the accumulation layer at the titanium-covered surface causes 01s peak shifts towards higher binding energies. This effect is demonstrated in Figure 52. The solid line represents the experimentally observed 01s binding energy shifts. The hatched area was determined from shifts in the upper valence-band edge E_V upon the deposition of titanium (see Figure 11) and thus indicates the range of experimentally observed band bendings (for corresponding titanium coverages).

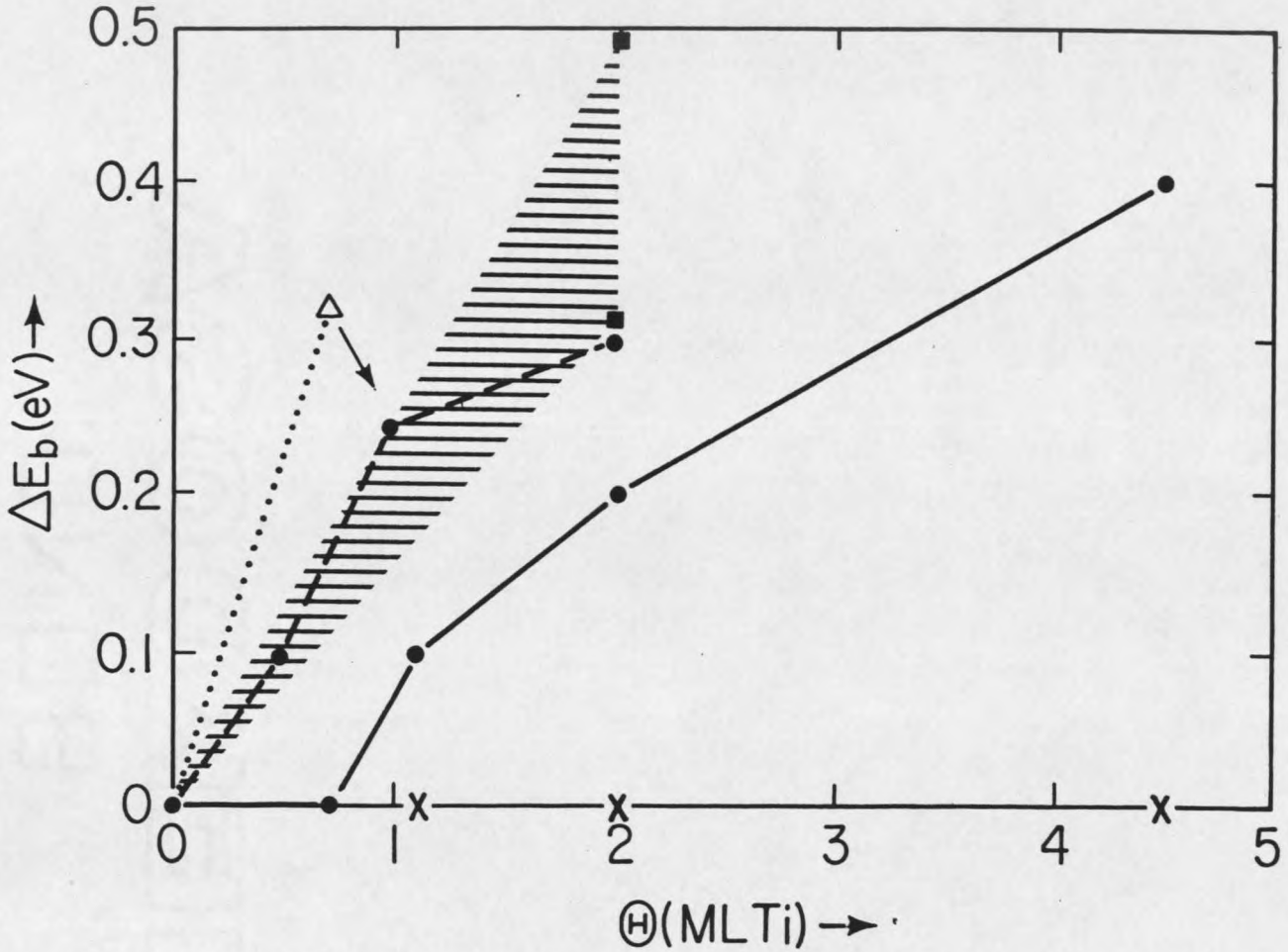

Figure 52. Binding-energy shifts of O1s (solid line, see Figure 9), Ti3p (triangle Δ and dotted line, see Figure 10), $Ti2p_{3/2}$ (crosses x, see Figure 7) and the TiO_2 valence band (squares ■ and hatched area, see Figure 11), as well as work-function changes (dashed line, see Figure 38), plotted as a function of Ti coverage.

The triangle (Δ) indicates the Ti3p core-level shift observed for a titanium coverage of 0.7 ML (see curve b in Figure 10), whereas the crosses (x) represent the $Ti2p_{3/2}$ shifts for different titanium coverages (see Figure 7).

The fact that no shifts in the $Ti2p_{3/2}$ core-level, but pronounced O1s and valence-band shifts are observed may indicate that the presence of a space-charge layer doesn't necessarily lead to equal changes of all core-level binding energies.

The band bending is determined by a mean electrostatic potential which strongly influences the binding energies of delocalized valence-band states and can be measured in $\Delta\phi$ experiments. The localized core levels, such as O1s, $Ti2p_{3/2}$ and Ti3p, however, are more affected by spatially varying local electric fields, leading to different binding energy changes. In addition, the $Ti2p_{3/2}$ core-level position of Ti^{4+} ions is also influenced by $Ti2p_{1/2}$ emissions arising from less positively charged titanium species.

Table 8 lists expected values for the different ΔE_b contributions that cause titanium and oxygen core-level shifts in the bulk-to-surface (b -> s) transition as well as in transitions between differently charged ions.

It was assumed that less-ionic species (at constant interionic distances) cause a decrease in the Madelung potential energy. Furthermore, the final-state relaxation

effect is believed to increase with increasing number of electrons in the vicinity of the ionic species.

Table 8. ΔE_b contributions

ΔE_i	$Ti^{b->s}$	$O^{b->s}$	$Ti^{(4->4-x)+}$	$O^{(2->2-x)-}$
ΔE_{chem}	<0	>0	<0	>0
ΔE_{Mad}	<0	<0	<0	<0
$\Delta(-eV_s)$	$\Delta(-eV_s)$	$\Delta(-eV_s)$	$\Delta(-eV_s)$	$\Delta(-eV_s)$
ΔE_{relax}	>0	>0	<0	>0

The dashed curve in Figure 52 was calculated from work function changes measured upon exposing titanium-covered surfaces to oxygen (see Figure 38). The results plotted in this curve are referred to the work-function increase obtained on a clean TiO_2(110) surface (curve labelled "annealed" in Figure 38) and hence demonstrate the effect of partial annealing of titanium-covered surfaces on the TiO_2 work function. Assuming that corresponding work-function decreases would be observed upon the deposition of titanium (not measurable with the Kelvin-probe set-up) we compare the results of the dashed curve to the XPS core-level and valence-band shifts (Figure 52). The dashed curve is found entirely within the hatched area, indicating that most of the work-function change expected upon the deposition of titanium is probably due to band bending.

The experimentally observed O1s shifts (solid curve) are smaller than the measured work-function changes and band bendings. This may be due to errors involved in the determination of XPS binding-energy changes as well as small contributions from electron-affinity changes accompanied by titanium-induced dipole moments (see below).

Applying the general formalism for determining concentrations of elements from XPS data (see Appendix A) and taking numerical values for total cross sections and inelastic mean free paths from the literature, we determined a Ti-to-O ratio of 0.43 for stoichiometric surfaces (corresponding to curve a in Figures 7 and 9). For defective surfaces the ratio increased and, as an example, a value of approximately 0.50 was observed for heavily ion-bombarded surfaces [80]. These values are smaller than expected theoretically for stoichiometric and defective surfaces. Deviations in the order of 15 % are most probably caused by inaccurate values for cross sections, which had to be taken from free-atom results [80,145-147] and which are expected to depend on the effective ionic charge. Also, the background subtraction and the assumption of constant spectrometer sensitivity for both the $Ti2p_{3/2}$ and O1s core-levels may induce systematic errors. The relative increase, however, of the Ti-to-O ratio during defect formation could be determined with an accuracy of about 1 % [80].

In Figure 10, additional emissions are observed on the low-binding energy side of the Ti3p core-level peak after the deposition of successive amounts of titanium on TiO_2(110). Due to the higher photoelectron kinetic energies, however, the surface sensitivity of these features is less pronounced [136]. A small Ti3p core-level shift towards higher binding energies is observed in curve b. The magnitude of this shift is indicated as a triangle (Δ) in Figure 52.

The Ti3p core-level peak representing the stoichiometric surface (curve a) is derived from contributions of the $Ti3p_{1/2}$ and $Ti3p_{3/2}$ states. The spin-orbit splitting for energy quantum number 3, however, is much smaller than the one observed for Ti2p states (see Figure 7). By simply applying Bohr's model to metallic titanium, a spin-orbit splitting of 7.96 eV (exp.: 6.15 eV [120]) was estimated for Ti2p states, whereas a splitting of only 0.70 eV was calculated for Ti3p states. This is mainly due to the fact that the energetic separation between spin-1/2 and spin-3/2 states is - according to Bohr's semiclassical model - inversely proportional to the sixth power of the energy quantum number. The experimentally observed spin-orbit splitting for Ti2p states in TiO_2 is 5.70 eV (see Figure 7 and reference 120). This result indicates that the experimentally expected splitting of Ti3p states in TiO_2 will be even less than

0.70 eV. Due to the limited spectrometer resolution (see chapter 3) the $Ti3p_{1/2}$ and $Ti3p_{3/2}$ states couldn't be resolved and instead, only one broad peak was observed on stoichiometric $TiO_2(110)$ (see curve a in Figure 10).

The presence of two non-resolved core-level states as well as pronounced background noise prevented an accurate theoretical line-shape analysis.

The changes in the valence-band structure upon deposition of successive amounts of titanium on $TiO_2(110)$ are shown in Figure 11. The observation of a new emission in the TiO_2 band-gap region (above the upper valence-band edge E_V of stoichiometric TiO_2) as well as the depopulation of upper O2p-derived valence-band states is consistent with the assumption of occupied Ti3d states characteristic for defective surfaces (see chapter 2). Curve e was recorded on a $TiO_2(110)$ surface covered with a metallic titanium overlayer (4.5 ML) and thus shows contributions from both Ti and TiO_2 valence bands.

The horizontal and sloping lines in spectra a-e indicate two different ways of determining the upper valence-band edge of the TiO_2 substrate. The uncertainties involved are mainly due to the different backgrounds and lead to pronounced errors in the determination of band bendings as demonstrated by the hatched area in Figure 52.

The two squares (□) represent the two different values obtained for the valence-band shift (i.e. band bending) of curve d in Figure 11.

Due to a high background-noise level and low valence-band cross sections (see chapter 4), no band-gap features were observed on sputtered surfaces or surfaces covered by very small amounts of titanium.

Figures 12 and 13 illustrate the rapid growth of a second peak in the TiLMV Auger line upon deposition of titanium or ion bombardment, respectively. As was already pointed out in chapter 2, this (comparatively surface-sensitive) peak is a local probe for surface defects and can be attributed to an intra-atomic Auger transition involving occupied Ti3d states.

Due to pronounced background noise no attempts were made to fit theoretical functions to the observed Auger line shapes. The dotted lines in Figures 12 and 13, however, schematically indicate the background levels as well as the two different contributions arising from TiO_2 and Ti.

In an earlier study [80] involving a simple Auger-line-shape analysis, we determined shapes and positions of the Ti3d-derived band-gap state measured on ion-bombarded TiO_2(110) surfaces by means of UPS (see chapter 2). In a first approximation, we assumed constant transition probabilities and the Auger peak TiLMV of

stoichiometric surfaces to be given by a convolution product of our experimentally observed $Ti2p_{3/2}$, Ti3p and valence-band features. We then used the defect-induced excess features in the Ti3p and $Ti2p_{3/2}$ peaks, assumed a Gaussian band-gap (defect) state and varied its position and halfwidth to fit the experimentally observed TiLMV feature. Even this simple model made possible to explain and characterize defect states in the band gap. These were determined to be located 0.3 eV below the conduction-band edge and with a halfwidth of 0.5 eV [80].

The surface optical Fuchs-Kliewer phonons observed on $TiO_2(110)$ surfaces during EELS studies (see Figures 14, 15 and reference 81) can be identified by comparing bulk data [148,149] and a theoretical treatment [82] with typical results summarized in Table 9.

The observed surface optical-phonon modes are singly-excited surface modes $\tilde{\nu}_1$, $\tilde{\nu}_2$ and $\tilde{\nu}_3$ as well as combination and multiple excitations of these fundamental modes. The frequencies $\tilde{\nu}_1$ and $\tilde{\nu}_2$ have also been observed by Kesmodel et al. [82] in an EELS study on $TiO_2(100)$.

Table 9. Surface- and Bulk-Optical-Phonon Loss Energies for Rutile TiO_2.

Loss energy (meV)	Surface data Mode assignment	Theory[a]	Bulk data IR-active	IR data[b]	INS data[c]
54	$\tilde{\nu}_1$	52.8-56.4	$\Gamma_5^{\pm}$ (LO)	56.8	53.2
95	$\tilde{\nu}_2$	93.8-98.8	Γ_1^{-} (LO)	100.5	100.6
46	$\tilde{\nu}_3$	46.2-46.3	Γ_5^{+} (TO)	22.7	23.4
149	$\tilde{\nu}_1 + \tilde{\nu}_2$				
141	$\tilde{\nu}_3 + \tilde{\nu}_2$				
190	$2\tilde{\nu}_2$				
244	$\tilde{\nu}_1 + 2\tilde{\nu}_2$				
285	$3\tilde{\nu}_2$				
339	$\tilde{\nu}_1 + 3\tilde{\nu}_2$				
380	$4\tilde{\nu}_2$				

In our study [81] with better instrumental resolution and signal-to-noise ratio we could also observe the $\tilde{\nu}_3$ mode. It could be determined even more sensitively from the gain feature due to the relative enhancement of lower loss energies according to the Boltzmann distribution (see Figure 15 and Appendix B), which results in a better separation of $\tilde{\nu}_3$ and $\tilde{\nu}_1$ features in the gain spectrum. For $\tilde{\nu}_2$ in particular we have been able to also observe higher-order multiple losses which show the expected Poisson distribution of intensities (see Appendix B).

At primary energies above E_p = 11 eV, the different sample pretreatments (see chapter 4) led to identical values of $\tilde{\nu}_1$, $\tilde{\nu}_2$, and $\tilde{\nu}_3$, as listed in Table 9. At lower primary energies we observed characteristic shifts of surface optical phonons at stoichiometric surfaces towards higher loss energies [81]. For all three frequencies we found a shift of approximately 2 meV in the fundamental mode at E_p = 6.4 eV, whereas the multiple losses $2\tilde{\nu}_2$, $3\tilde{\nu}_2$, and $4\tilde{\nu}_2$ showed shifts of 2.5, 3, and 3.5 meV for $5.5\ \text{eV} \leq E_p \leq 7.0\ \text{eV}$.

The physical origin of this shift is not quite clear at present. Reduced amplitudes and shifts towards lower loss energies upon defect formation at the surface may qualitatively be understood by damping of the collective vibational modes in the presence of defect-induced conduction electrons with the frequency of phonons at a

defective surface

$$\omega_D = (\omega_s^2 - \kappa^2)^{1/2} \qquad (42)$$

for a frequency on the stoichiometric surface ω_s, with $\kappa = \beta/2m_{eff}$, where β is the damping constant, and $m_{eff} = 25m_e$ is the effective mass of TiO_2 conduction band electrons (see chapter 2). As an example, from the above-mentioned frequency shift in $\tilde{\nu}_2$ at $E_p = 6.4$ eV we calculate $\beta = 2.1 \times 10^{-16}$ Kg sec^{-1} and $\hbar\kappa = 19.6$ meV for samples with high concentration of defects.

At stoichiometric surfaces, these defects are annealed and defect-free (sub)surface regions are produced which extend about 1000 Å into the bulk [79]. The dependence of the surface-phonon shift and damping on the primary energy may also be explained by the primary-energy dependence of the Fuchs-Kliewer phonon amplitudes in subsurface layers. The efective amplitude as a function of distance from the surface is given by $\exp(-Q_{\parallel}|z|)$ with the inverse electron momentum transfer parallel to the surface (see references 99, 150 and Appendix B):

$$Q_{\parallel}^{-1} = |\vec{k}_0| \hbar\omega_s \sin\theta / 2E_p \qquad (43)$$

Here, $\vec{k}_0$ and E_p are the wave vector and the energy of the incoming electron, respectively, and Θ is the scattering angle. For $\tilde{\nu}_2$ we estimate values of $Q_{\parallel}^{-1}$ between 925 and 1934 Å for E_p between 6.4 and 28 eV. Geometric and

electronic perturbations in the first few monolayers extend little if compared with $Q_{\parallel}^{-1}$ and the region which contributes to the time-dependent electric field at $E_p > 11$ eV. As a consequence, surface disorder or defects do not affect the observed optical-phonon frequencies at higher primary energies, whereas deviations between ideal and defective surfaces are expected for $Q_{\parallel}^{-1} < 1000$ Å.

The experimentally determined value h is, within experimental error, identical with the corresponding plasmon frequency of free carriers in these samples of 18 meV. The latter value was estimated from the concentration of free electrons of 1×10^{19} cm^{-3} and their effective mass. These plasmons couple with Fuchs-Kliewer phonons and cause the above-mentioned damping. Owing to the line width of our instrument and the large "background" near the elastic peak resulting from Fuchs-Kliewer phonons we could not resolve plasmon excitations at low energies.

Figure 16 demonstrates how 4.5 monolayers of titanium deposited on TiO_2(110) affect the Fuchs-Kliewer phonon intensities. The observed screening caused by the conducting overlayer has also been reported by Dubois et al. [137] who performed experimental and theoretical EELS studies on silver-covered Te-doped GaAs(100) surfaces. They observed an intense surface optical phonon at 36.2 meV and a weaker plasmon-phonon coupled mode at 12-13 meV. Both modes were completely screened by a 3-Å-thick uniform

overlayer of silver in good agreement with their theoretical predictions.

In their model, they derived an expression for the inelastic electron-scattering cross section in the dipole regime involving the frequency-dependent dielectric constants of both the GaAs substrate and the silver overlayer regarded as a thin dielectric layer. Further mathematical details will be given in Appendix B.

The dashed and dotted lines in Figures 53 and 54 represent difference spectra calculated from the loss features shown in Figures 18 and 20 by subtracting the solid curves (corresponding to stoichiometric surfaces) in these figures from corresponding dashed and dotted curves.

The difference spectra show broad defect-induced loss features between 0.35 and 2 eV loss energies. These features can be attributed to electronic transitions from occupied Ti3d-derived band-gap states to empty Ti3d states in the conduction band of TiO_2. These d-d transitions have already been observed in our earlier studies [80,81] and by Henrich et al. [56] (see chapter 2).

Figure 55 shows the TiO_2 valence- and conduction-band structures according to the results given in reference 2. It will be used to explain the origin of the loss features b and c presented in Figures 22 and 23.

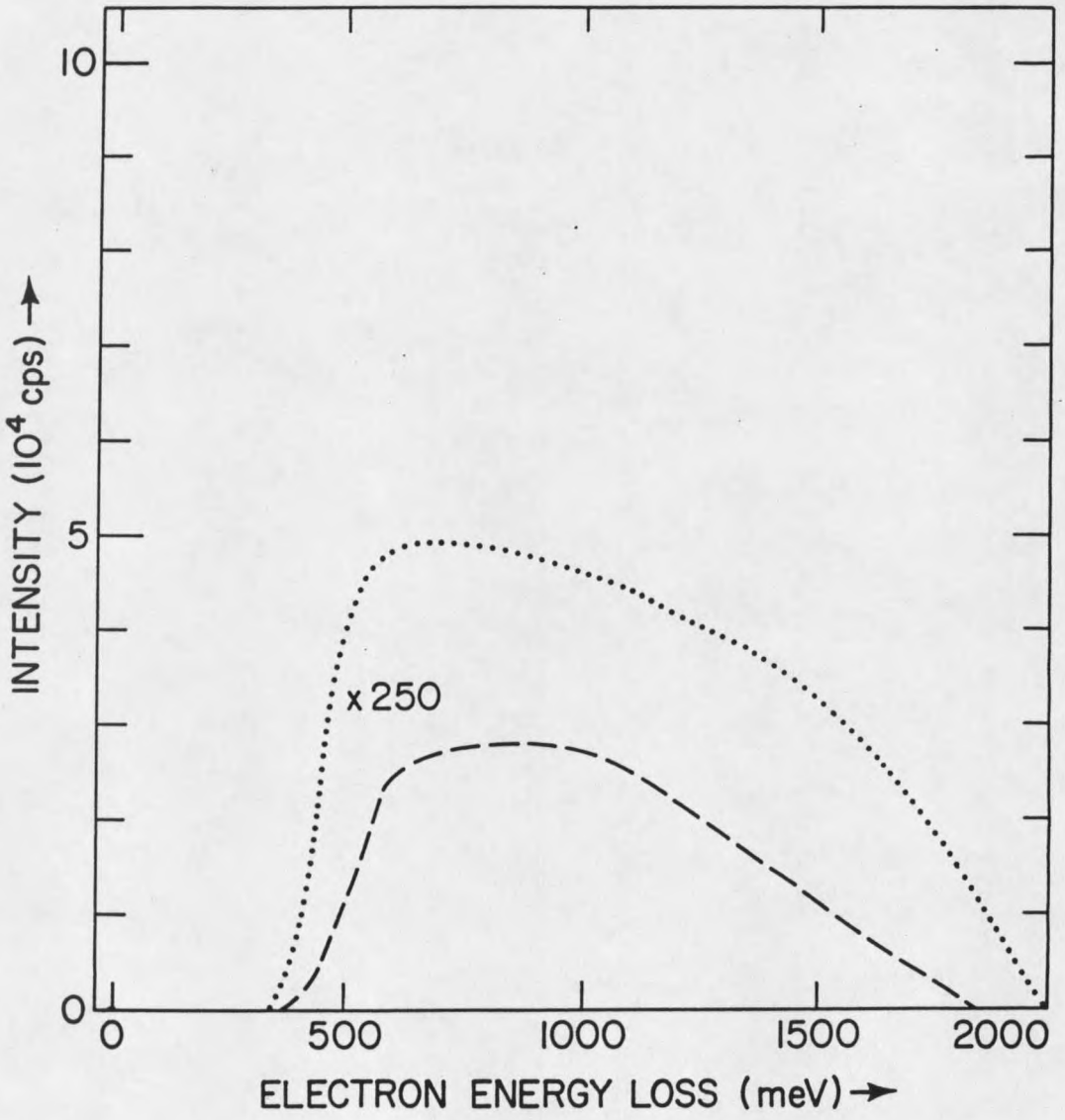

Figure 53. EELS difference spectra of TiO_2(110), calculated from the curves in Figure 18 (see text).

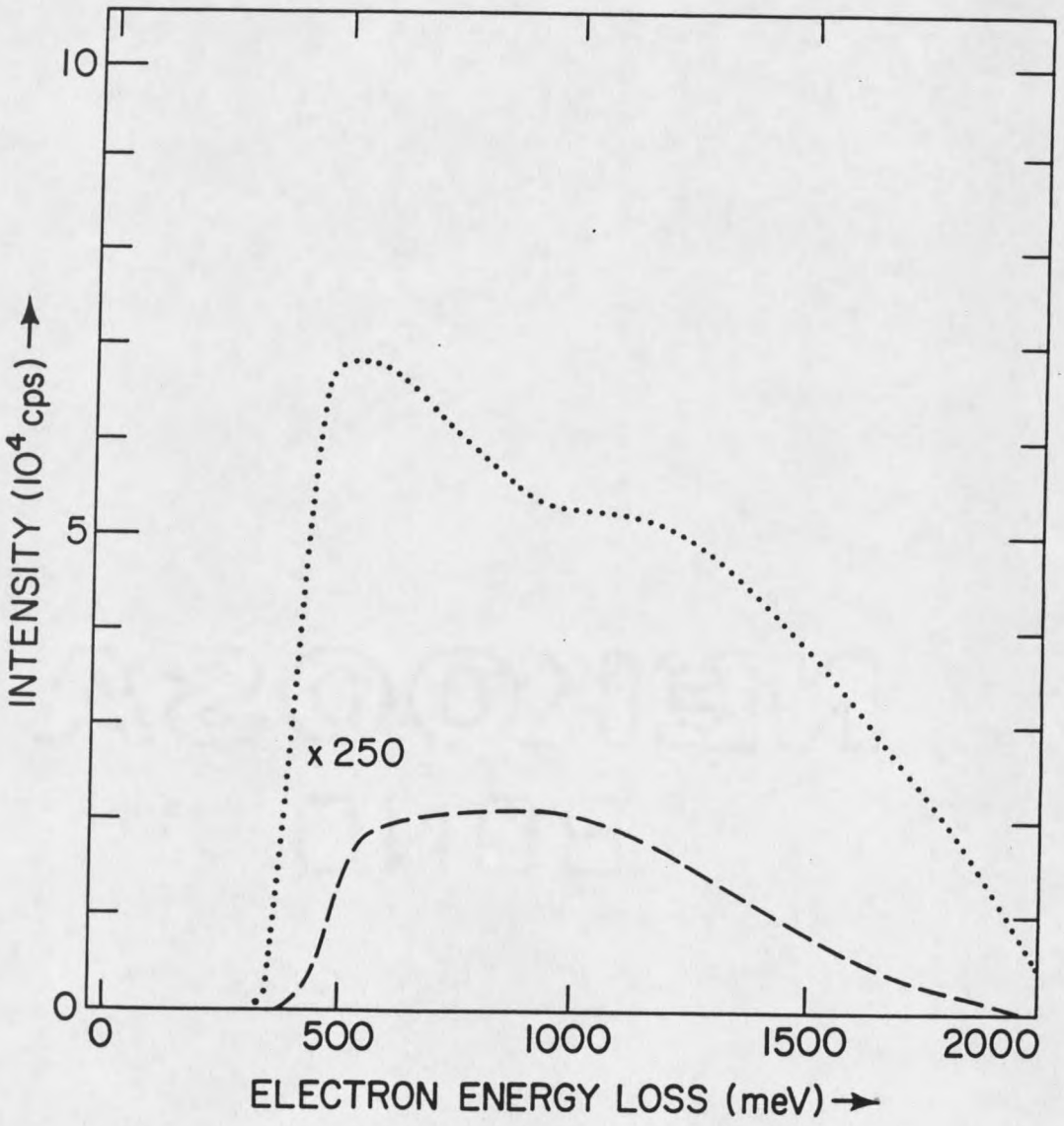

Figure 54. EELS difference spectra of TiO_2(110), calculated from the curves in Figure 20 (see text).

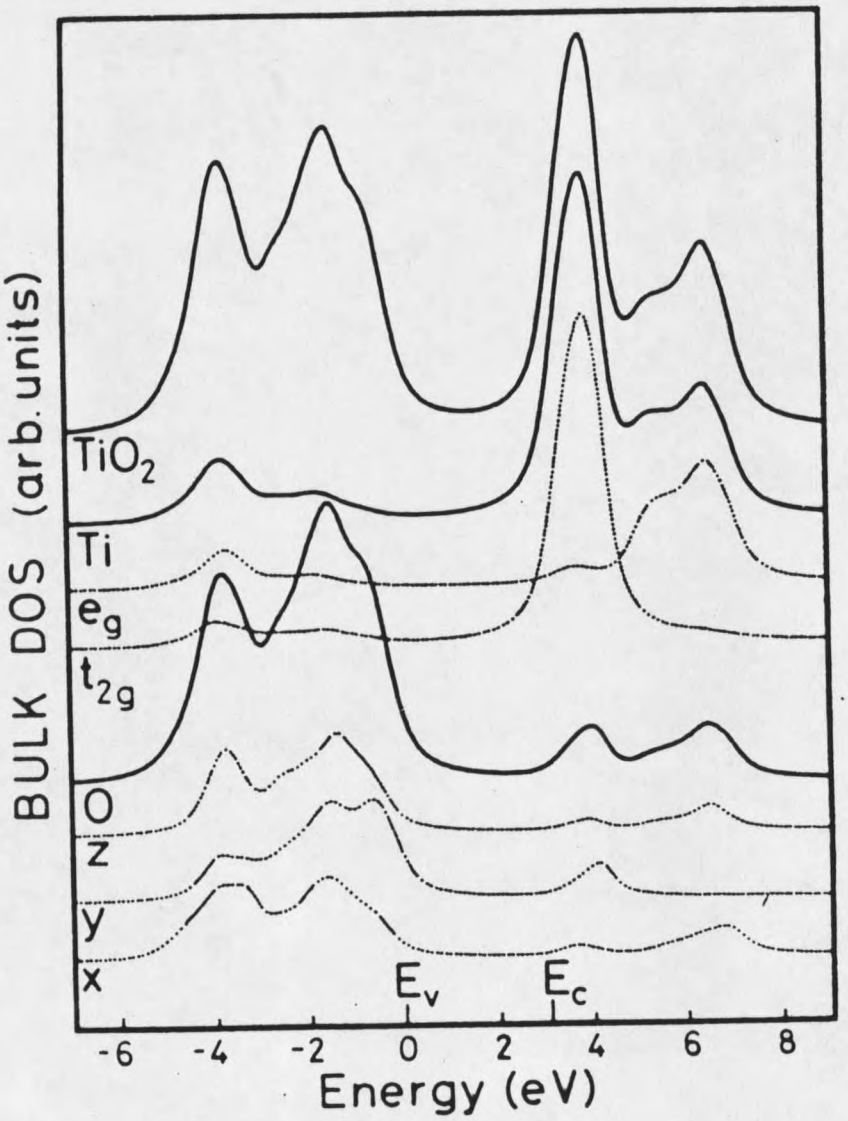

Figure 55. Bulk density of states (DOS) of TiO_2, together with partial oxygen (O) and titanium (Ti) densities of states. O DOS's are decomposed into $O_{z,y,x}$ orbital contributions and Ti partial DOS's are decomposed into subbands of e_g and t_{2g} symmetry (see reference 2).

The upper part of the valence band and the lower part of the conduction band have t_{2g} symmetry and are derived from weak $pd\pi$ interactions between Ti and O ions in the TiO_2 bulk. The lower valence and the upper conduction subbands are of e_g symmetry and originate from strong $pd\sigma$ interactions.

As was pointed out in our earlier studies [80], loss feature b apparently is due to an electronic transition from the upper part of the valence band to the lower part of the conduction band (see also Figure 3) which are separated by 5.5 eV (= loss energy of feature b). This explains the attenuation of feature b during argon-ion bombardment, because defect formation results in partial depopulation of the O2p-derived states that form the upper part of the valence band (see chapter 2 and Figure 11).

Kurtz et al. [151] suggested a similar interpretation of their ELS results obtained on differently treated TiO_2 and Ti_2O_3 samples.

The feature c at a loss energy of 10.2 eV is also sensitive to the formation of defects as shown in Figures 22 and 23. Furthermore, the intensity of this feature was found to be enhanced on samples with a high bulk-defect concentration (opaque part of the sample, see chapters 3 and 4). With the help of the theoretical curves presented in Figure 55 this loss feature can be assigned to an electronic transition from the lower part of the valence

band to the upper part of the conduction band, i.e. transitions bwtween merely Ti-derived states (see curve labelled "Ti") or between merely O-derived states (see curve labelled "O") as well as cross transitions involving both Ti- and O-derived states.

Kurtz et al. [151] also observed this loss feature on oxygen-exposed Ti_2O_3 (thus having a TiO_2 overlayer) and on vacuum-fractured TiO_2, but not on freshly cleaved Ti_2O_3. Hence, they interpreted this feature as being characteristic for Ti^{4+} species and due to a O2p => Ti3d charge-transfer excitation. This interpretation, however, doesn't explain the enhanced intensity of feature c on opaque (high bulk defect concentration) TiO_2 samples as shown in Figure 23.

Loss feature d is not sensitive to the formation of surface defects and was attributed to a O2p => O3s transition by Kurtz et al. [151].

The features e-h of higher loss energies shown in Figure 24 are derived from electronic transitions that also involve lower-lying oxygen (O2s) and titanium (Ti3p, Ti3s) core-levels. Features e, f and h may be due to O2s => O2p, Ti3p => Ti3d and Ti3s => O2p transitions, respectively, whereas the highly intense feature g is probably derived from a transition involving the Ti3p core-level and higher-lying, unoccupied titanium or oxygen levels that

don't contribute to the valence and conduction bands. The physical origin of features i and j is not well understood at present.

The LEED patterns presented in Figure 25 have been used to roughly estimate surface interatomic distances of differently treated TiO_2(110) surfaces (see chapter 4) by applying the formalism explained in chapter 3.

For the annealed surface represented by pattern a the spacings in the (1x1)-structure were calculated to be c = 2.83 Å and a = 4.35 Å (compare to the values given in Figure 1).

The analysis of the more diffuse pattern b turned out to be more difficult, because of the big sample rod (see chapters 3 and 4). The temperature treatments after the evaporation of 4.5 monolayers of titanium apparently led to a (1x1)-structure whose direct-lattice constants were estimated to be c = 2.86 Å and a = 4.40 Å. These results indicate that the original (1x1)-structure of a TiO_2(110) surface can probably be retrieved by further temperature treatments, suggesting that either titanium diffuses into the TiO_2 bulk or the titanium overlayer is oxidized to TiO_2 by bulk oxygen at high temperatures (compare to results obtained on oxidized Ti(0001) metal surfaces [68]).

Adsorption on Stoichiometric Surfaces

The Surface Space-Charge Region

A space-charge region near the surface of a (semi) conducting solid may be produced by an electric field, outside the solid, established by an external source or by the proximity of another solid with a different work function. Alternatively, the space-charge region may result from the presence of a localized (adsorbate-induced) charged layer at the surface proper, due usually to surface states [100].

The majority (maj) and/or minority (min) charge-carrier (electrons and holes) densities in the space-charge region near a semiconductor surface (s) differ from the bulk (b) values, and hence we may encounter three different kinds of space-charge layers [100]:

$$maj_s > maj_b : \text{accumulation layer}$$

$$maj_s < maj_b \text{ and } \begin{cases} min_s < maj_b : \text{depletion layer} \\ min_s > maj_b : \text{inversion layer} \end{cases}$$

Although electrons in a single crystal are free to move about, they are not able to leave the crystal surface easily. This implies that their energy is lower inside the solid than outside. The work required to remove an electron at the Fermi level to a point in free space just outside the solid is defined as the work function ϕ of the solid

(see also chapter 3). In semiconductors, it is found useful to define a second quantity, the electron affinity χ, as the work required to remove an electron from the bottom edge of the conduction band at the surface to a point in free space just outside the semiconductor. The corresponding changes in potential as one moves from the solid into free space are very steep since they arise from short-range binding forces exerted by the crystal lattice on the electron (typically, 10^8 V/cm over an interatomic spacing). Such potential steps are sometimes referred to as micropotentials, to stress their microscopic character [100].

The electrostatic field established by the accumulated space-charge is usually much weaker than the crystal field, so that the macropotential from which it is derived leaves the micropotential associated with ϕ and χ practically unaffected. Thus the macropotential is superimposed on the short-range micropotential, and the energy-band edges assume the shape of the macropotential [100]. The lower conduction-band edge E_C in the space-charge region, e.g., can now be expressed in terms of its bulk value $E_{C,b}$ and the macropotential V:

$$E_C = E_{C,b} - eV \qquad (44)$$

The term -eV is commonly referred to as band bending.

The potential W is defined as follows:

$$eW = E_F - E_I \tag{45}$$

Here, E_I denotes the Fermi-level energy of the intrinsic (no defect-induced band-gap states) semiconductor and is given by:

$$E_I = \frac{1}{2}(E_V + E_C) - \frac{1}{2} k_B T \ln\left(\frac{N_C}{N_V}\right)$$

or

$$= \frac{1}{2}(E_V + E_C) - \frac{3}{4} k_B T \ln\left(\frac{m_{eff,C}}{m_{eff,V}}\right) \tag{46}$$

E_V, E_C are the energies at the upper (lower) valence (conduction) band edges, N_C is defined in Equation 29 and N_V is a similar expression for valence-band holes, $m_{eff,C}$ and $m_{eff,V}$ are the effective masses of conduction band electrons and valence band holes [130].

According to Equation 46, the intrinsic Fermi level also assumes the shape of the macropotential and is thus parallel to the conduction- and valence-band edges, in contrast to the constant Fermi-level energy E_F.

The macropotential or potential barrier V can be defined as follows:

$$V = W - W_b \tag{47}$$

W_b is the bulk value of W. The reduced (dimensionless)

potentials u and v are given by:

$$u = \frac{e\,W}{k_B T} \qquad v = \frac{e\,V}{k_B T} \tag{48}$$

In the case of nondegenerate semiconductors (see above), we can express the conduction-band electron density n and the valence-band hole density p in the space-charge region with the help of Equation 29 (and a similar equation for p_b) by adding -eV to the argument of the exponential term therein:

$$n = n_b \exp(v) = n_I \exp(u)$$

and

$$p = p_b \exp(-v) = n_I \exp(-u) \tag{49}$$

with

$$n_I = (N_C N_V)^{1/2} \exp[-E_g/(2k_B T)] = n_b = p_b \tag{50}$$

for intrinsic semiconductors [130].

$E_g = E_C - E_V$ is the band-gap energy.

The bulk value of u is thus given by:

$$u_b = \ln(n_b/n_I) \tag{51}$$

and can be determined from experimental (see above) n_b and theoretical n_I data.

In the presence of donor-type defects (see above), we can write the excess charge density ρ -resulting from the space-charge region - as follows:

$$\rho = -e\{[n-n_b] - [N_{D1}(v)-N_{D1}] - 2\,[N_{D2}(v)-N_{D2}] - [p-p_b]\} \quad (52)$$

with
$$N_{D0}(v) = \frac{N_D}{1 + A\exp(-v) + A\,B\exp(-2v)}$$

and
$$N_{D1}(v) = \frac{N_D}{1 + \exp(v)/A + B\exp(-v)}$$

and
$$N_{D2}(v) = \frac{N_D}{1 + \exp(v)/B + \exp(2v)/(A\,B)} \quad (53)$$

where
$$A = 2\exp[(E_{D1}-E_F)/(k_BT)]$$
$$B = 0.5\exp[(E_{D2}-E_F)/(k_BT)]$$

as was derived from Equations 33, 34 and 38 by adding -eV to corresponding energy terms. For the first time, the term for $N_{D0}(v)$ is not neglected as has been done in earlier studies [13,79]. The temperature-dependent quantities A and B can be determined from measured and calculated E_C-E_F and E_C-E_{D1}/E_C-E_{D2} data, respectively (see above).

The barrier height can now be calculated by solving Poisson's equation:

$$\frac{d^2V}{dz^2} = -\frac{\rho}{\epsilon\epsilon_0} \quad (54)$$

Here, z is the spatial coordinate perpendicular to the surface (z=0 at the surface, and z>0 in the bulk). is the dielectric constant in the space-charge region and is ϵ

assumed to be equal to the bulk dielectric constant [100].

Equations 48, 49, 52 and 54 lead to:

$$\frac{d^2v}{dz^2} = \frac{1}{L_D^2}\left\{\frac{\sinh(u_b+v)}{\cosh(u_b)} - \tanh(u_b) - \frac{1}{n_b+p_b}\left[N_{D1}(v)-N_{D1}+2(N_{D2}(v)-N_{D2})\right]\right\} \quad (55)$$

where $L_D = \{\epsilon\epsilon_0 k_B T/[e^2(n_b+p_b)]\}^{1/2}$

is the effective Debye length as given in Equation 30, with negligible bulk hole concentration ($p_b \sim 0$).

Equation 55 can be integrated once, yielding:

$$\frac{dv}{dz} = \mp\frac{Fd}{L_D} \quad \begin{matrix} - \text{ for } v>0 \\ + \text{ for } v<0 \end{matrix} \quad (56)$$

with

$$Fd = 2^{1/2}\left\{\frac{\cosh(u_b+v)}{\cosh(u_b)} - v\tanh(u_b) - 1 - \frac{N_D}{n_b+p_b}\left[\ln\left(\frac{(AB+A+1)\exp(2v)}{AB+A\exp(v)+\exp(2v)}\right) - v\,\frac{A(2B+1)}{AB+A+1}\right]\right\}^{1/2} \quad (57)$$

The shape of the bands in the space-charge region is then calculated by numerically integrating the above equation.

The space-charge density Q_{sc} is defined as the total net charge accumulated in the space-charge region per unit

surface area [100] and is calculated as follows:

$$Q_{sc} = \int_0^\infty dz\, \rho\,[v(z)] \qquad (58)$$

From Equations 54-58 we get:

$$Q_{sc} = \mp e(n_b+p_b)\, L_D\, F_s^d \qquad (59)$$

with $F_s^d = Fd(z=0)$.

The excess surface-carriers densities ΔN and ΔP are defined as the number (per unit surface area) of mobile electrons ΔN and holes ΔP in the space-charge layer with respect to their numbers at flat bands (bulk values, $z\to\infty$ and $v\to 0$). We get:

$$\Delta N = \int_0^\infty dz\ (n-n_b) \quad \text{and} \quad \Delta P = \int_0^\infty dz\ (p-p_b) \qquad (60)$$

From the above equations we derive:

$$\Delta N = n_b L_D \int_{v_s}^{0} dv\ \frac{\exp(v)-1}{\mp F^d} \quad \text{and} \quad \Delta P = p_b L_D \int_{v_s}^{0} dv\ \frac{\exp(-v)-1}{\mp F^d} \qquad (61)$$

with $v_s = v(z=0)$.

In a simple scattering model in which the surface acts as a completely diffuse (random) scatterer, Many et al. [100] derived expressions for electron mobilities μ_s in accumulation and depletion layers:

$$\frac{\mu_s}{\mu_b} = \begin{cases} [1+rF_s^d(1+v_s)^{1/2}/v_s]^{-1} & \text{for accumulation layers} \\ 1-\lambda n_b[\exp(v_s)-1]/\Delta N & \text{for depletion layers} \end{cases} \quad (62)$$

with $\lambda = \mu_b[m_{eff,c}k_BT/(2\pi e^2)]^{1/2}$ and $r = \lambda/L_D$.

For the TiO_2 sample investigated in this thesis, the electronic mean free path λ is less than 1 Å and L_D is of the order of 1000 Å at room temperature (see Figure 41). This means that the surface mobilities μ_s are roughly equal to the bulk mobility μ_b.

Furthermore, the bulk hole concentration p_b in these samples is negligible and doesn't have to be accounted for in the above-presented space-charge formalism. From the relation

$$n_b p_b = N_C N_V \exp[-E_g/(k_BT)] \quad \text{(see reference 130)}$$

and experimental values for n_b and E_g (see above) we estimate p_b to be of the order of 10^{-27} cm^{-3} close to room temperature.

In the case of TiO_2, the chemisorption-induced part of the surface-conductivity change, $\Delta\sigma_s^{chem}$, is thus given by:

$$\Delta\sigma_s^{chem} = e\mu_s \Delta N \quad (63)$$

Here, we neglected conduction in surface states (see chapter 2).

Chemisorption-induced changes $\Delta\sigma_s^{chem}$ can be derived from measured $\Delta\sigma_\square^{chem}$ data by multiplying the latter ones by the sample thickness d. This hold for van-der-Pauw bulk conductivity changes obtained on thin samples [79,100,104].

Partial charges δ are formally attributed to adsorption complexes and given by the surface charge Q_{ss} per unit area (which is trapped during chemisorption divided by the surface concentration of adsorbed particles $n_{ad,s}$ and the elementary charge e [79,108]:

$$\delta = \frac{Q_{ss}}{e\, n_{ad,s}} \tag{64}$$

The electroneutrality condition requires:

$$Q_{ss} + Q_{sc} = 0 \tag{65}$$

Changes in concentration of free electrons upon chemisorption are formally described by the formation of donor- or acceptor-type extrinsic defects, These defects introduce electronic states in the band gap (originally empty in ideal $TiO_2(110)$. They may be characterized by an energy E_{ss}^{eff} (of, in general, unknown degeneracy), which is related to the partial charge via Fermi statistics [79]:

$$f(E_{ss}^{eff}-E_F) = \{1+\exp[(E_{ss}^{eff}-E_F)/(k_BT)]\}^{-1}$$

$$= \begin{cases} -\delta & \text{for acceptors} \\ 1-\delta & \text{for donors} \end{cases} \tag{66}$$

Dipole moments attributed to adsorption complexes are introduced to formally explain the discrepancy between the theoretically expected band bending $-eV_s$ and the experimentally determined changes in work function $\Delta\phi$:

$$\Delta\phi = -eV_s + \Delta\chi \qquad (67)$$

In the low-coverage range with negligible dipole-dipole interaction, the electron-affinity change $\Delta\chi$ is assumed to arise from the dipole-induced potential difference [13,79]

$$\Delta V_{dipole} = \Delta\chi/e \qquad (68)$$

which is related to the normal component $_{ad}$ of the adsorbate-induced dipole moment (orientation of z-axis as above):

$$\Delta V_{dipole} = \frac{n_{ad,s}\,\mu_{ad}}{\epsilon_s\,\epsilon_0} \qquad (69)$$

with ϵ_s being the surface dielectric constant. Values for $-eV_s$, $\Delta\chi$ and μ_{ad} can thus be obtained from simultaneous $\Delta\sigma_s$, $\Delta\phi$ and TDS (yielding $n_{ad,s}$) experiments.

In the case of degenerate semiconductors (see above), the space-charge formalism described above has to be modified, because now the Fermi function in Equation 27 may not be replaced by a simple Boltzmann function. Thus the integral in Equation 26 has to be solved numerically, which

complicates the subsequent procedures that lead to the space-charge properties explained above.

Typical theoretical results for $\Delta\sigma_s$, Q_{sc} and μ_s obtained for a nondegenerate $TiO_2(110)$ sample at 305 K are plotted versus band bending in Figure 56.

Chemisorption of Titanium

Chemisorption of evaporated titanium on $TiO_2(110)$ has been observed for submonolayer coverages as discussed above.

The increase of the $TiO_2(110)$ surface conductivity accompanying the charge transfer is represented by the solid line in Figure 26. The solid and dashed lines were obtained by fitting the expression

$$\Delta\sigma_s = a \exp(b\Theta)$$

with $a = 1.414 \times 10^{-6}\,\Omega^{-1}$ / $b = 4.152$ ML^{-1} (solid line),

$a = 4.227 \times 10^{-7}\,\Omega^{-1}$ / $b = 0.885$ h^{-1} (dashed line),

and $\Theta = n_{ad,s}/n_{ad,smax}$ being the relative Ti coverage to the corresponding data points indicated by dots.

From the surface conductivity changes observed during the deposition of 0.25, 0.5 and 1.0 monolayers of titanium on $TiO_2(110)$, corresponding partial charges and band bendings were calculated using the formalism derived above for degenerate semiconductors, with a maximum coverage of $n_{ad,smax} = 2.08 \times 10^{15}$ cm^{-2}, estimated from Figure 1.

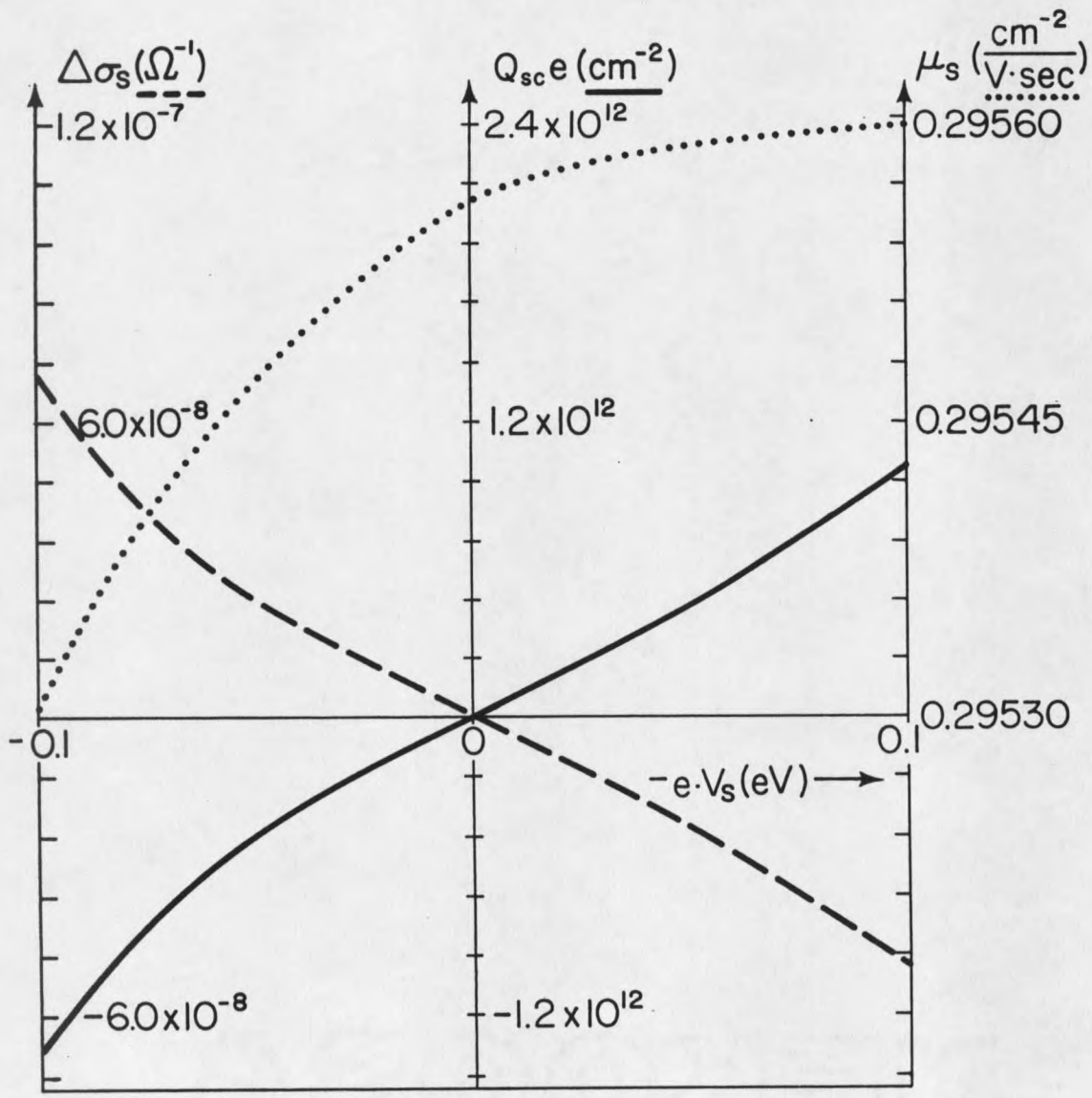

Figure 56. Space-charge densities Q_{sc} (solid line), excess (surface) conductivities $\Delta\sigma_s$ (dashed line) and surface Hall mobilities μ_s (dotted line) of TiO_2(110), plotted as a function of band bending $-eV_s$.

The results are plotted as solid lines in Figure 57 and indicate the formation of an accumulation layer (negative band bendings) near the $TiO_2(110)$ surface upon the deposition of titanium. The positive partial charge residing on each foreign titanium species expectedly drops between 0.25 and 0.50 ML, but then inceases up to a coverage of 1.0 ML. This phenomenon is possibly due to a "short-circuit" caused by the conducting titanium overlayer as well as an increased electron mobility in this layer. It cannot be described within the framework of the space-charge/charge-transfer model.

With the known energetic separation between the lower bulk conduction-band edge and the Fermi level of $E_{C,b}-E_F = 0.337$ eV (T = 303 K), it was also possible to determine the Ti-coverage-dependent quantities $E_{ss}^{eff}-E_F$, $E_{C,s}-E_{ss}^{eff}$ and $E_{C,s}-E_F$ with $E_{C,s}$ being the lower conduction-band edge at the surface. These space-charge properties are also shown in Figure 57 as dashed, dotted and dot-dashed lines, respectively.

The dot-dashed curve representing $E_{C,s}-E_F$ has a zero between 0.5 and 0.75 ML Ti, i.e. due to the strong band bending the lower conduction-band edge reaches the Fermi level, resulting in a two-dimensional electron gas, which apparently causes the pronounced increase in surface conductivity observed in Figure 26.

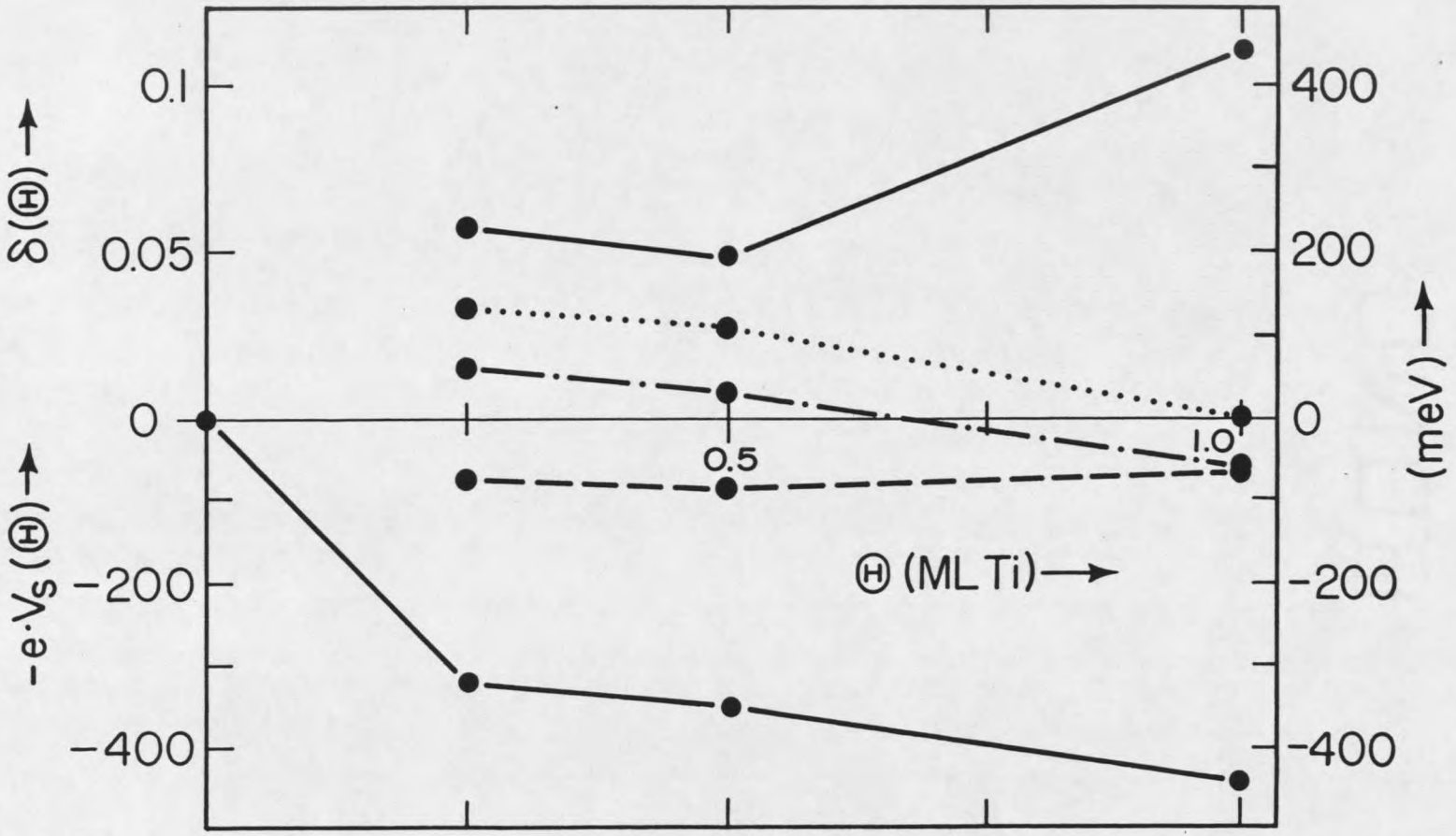

Figure 57. Partial charges δ (upper solid line), band bendings $-eV_S$ (lower solid line) as well as energetic separations $E_{ss}^{eff}-E_F$ (dashed line), $E_{C,s}-E_{ss}^{eff}$ (dotted line) and $E_{C,s}-E_F$ (dot-dashed line), plotted versus Ti coverage (see text).

The distance between the conduction-band edge $E_{C,s}$ and the adsorbate-induced surface state E_{ss}^{eff} also decreases. This phenomenon causes correlation effects between the surface state and conduction-band states and leads to charge transfer from the conduction band back to the titanium species. The resulting negative partial charges on the foreign titanium atoms may explain the core-level shift of the Ti2p3/2 peak with respect to the expected position in metallic titanium (see curve e in Figure 7).

With the use of the band bending (Figure 57) and (Figure 38) results expectedly small (see above) titanium-induced dipole moments of 0.121, 0.053 and 0.019 Debye were calculated for titanium coverages of 0.25, 0.50 and 1.0 ML. The low values indicate that the adsorbed titanium species interact with two surface oxygen ions (see Figure 2) and cause a small upward shift in the positions of these ions. This relaxation effect reduces the adsorbate-induced dipole moments.

It is believed that the foreign titanium atoms adsorb in such a way that the TiO_2 bulk lattice is continued in z-direction, perpendicular to the (110) surface. This can be demonstrated with the help of the geometric model in Figure 1.

Oxygen Adsorption

The adsorption of oxygen at an oxygen partial pressure of 6.7×10^{-6} mbar and temperatures of 348 and 423 K was monitiored by $\Delta\sigma_s$ and $\Delta\phi$ measurements as explained in chapter 4.

The surface conductivity decreases shown in Figure 27 as well as the work-function increase shown in Figure 38 ("annealed") suggest acceptor-type chemisorption of oxygen molecules leading to $O_{2,chem}^{-}$ species at the $TiO_2(110)$ surface. The transfer of electrons from the TiO_2 conduction band to the adsorbate leads to a decrease in the surface conductivity as well as an overlayer of negative charges localized at the chemisorbed oxygen species. This negatively charged overlayer causes a depletion layer near the surface and thus increases the work function of the TiO_2 substrate.

The enhancement of the surface conductivity changes at higher temperature (see Figure 27) indicates that also bulk diffusion of oxygen and subsequent bulk-defect annealing strongly contributes to these changes. This phenomenon will be discussed in more detail in the last part of this chapter.

From earlier studies on oxygen adsorption on metal-oxide-semiconductor surfaces [79,108] we know that oxygen chemisorbs as $O_{2,chem}^{-}$ with $\delta = -1$ (see chapter 2), i.e. the acceptor-type surface state will always be found

far below the Fermi level [106]. These results, in connection with measured $\Delta\sigma_s$ values and the space-charge formalism, make possible the determination of oxygen coverages and initial sticking coefficients, as well as oxygen-induced dipole moments.

In order to separate the two $\Delta\sigma_s$ contributions from chemisorption and bulk diffusion, we assume that the initial time-derivative of $\Delta\sigma_s$ is solely determined by O_2 chemisorption:

$$\left.\frac{d\Delta\sigma_s}{dt}\right|_{t=0} = \left.\frac{d\Delta\sigma_s^{chem}}{dt}\right|_{t=0} \qquad (70)$$

From the above-presented space-charge theory we know:

$$\Delta\sigma_s^{chem} = e\mu_s\, n_b\, L_D \int_{v_s}^{0} dv\, \frac{\exp(v)-1}{\pm F^d} \quad \text{(see Equation 63)}$$

and hence:

$$\frac{d\Delta\sigma_s^{chem}}{dt} = \frac{e\,\mu_s\, n_b\, L_D}{\pm F_s^d}\,[1-\exp(v_s)]\,\frac{dv_s}{dt} \qquad (71)$$

Using the approximations $dt \sim \Delta t \sim 5$ secs. (assuming rapid changes, see also Figure 38) and $dv_s \sim \Delta v_s \sim v_s$, we get:

$$\left.\frac{d\Delta\sigma_s^{chem}}{dt}\right|_{t=0} \sim \frac{e\,\mu_s\, L_D\, n_b\,[1-\exp(v_s)]\, v_s}{\pm F_s^d\,\Delta t} \qquad (72)$$

With the experimentally determined value

$$\left.\frac{d\Delta\sigma_s^{chem}}{dt}\right|_{t=0} \sim -1.6\times10^{-9}\,\Omega^{-1}\,sec^{-1}$$

as well as μ_s-, n_b-, L_D- and F_s^d-data at room temperature, and Equation 48 we calculate the barrier height (band bending) at the surface to be:

$$-eV_s = 39.4 \text{ meV} \qquad (73)$$

From Equations 59, 64 and 65 with $\delta = -1$ we then derive the absolute oxygen room-temperature coverage $n_{ad,s}$ at an oxygen partial pressure of 6.7×10^{-6} mbar:

$$n_{ad,s} = 2.66\times10^{11} \text{ cm}^{-2}$$

or $$\Theta(O_2) = 1.8\times10^{-4} \qquad (74)$$

with $$n_{ad,smax} = 1.48\times10^{15} \text{ cm}^{-2} \text{ [13]}.$$

This result is in good agreement with experimentally (TDS) obtained oxygen coverages on TiO_2(110) samples [79].

From Equations 63 and 73 we also calculate:

$$\Delta\sigma_s^{chem} = -4.436\times10^{-9}\,\Omega^{-1} \qquad (75)$$

From the experimentally determined maximum (after 75 secs.) surface-conductivity change at room temperature and $p_{O2} = 6.7\times10^{-6}$ mbar of

$$\Delta\sigma_{s,max} = -1.812\times10^{-7}\,\Omega^{-1} \qquad (76)$$

we determine the maximum $\Delta\sigma_s$ contribution from bulk oxygen diffusion to be:

$$\Delta\sigma s,\overset{diff}{max} = -1.768\times10^{-7}\,\Omega^{-1} \qquad (77)$$

because $$\Delta\sigma s,max = \Delta\sigma_s^{chem} + \Delta\sigma s,\overset{diff}{max}. \qquad (78)$$

Thus only 2.5 % of the measured surface-conductivity change is due to oxygen chemisorption, whereas 97.5 % are caused by bulk oxygen diffusion and subsequent bulk-defect annealing.

In connection with the measured work-function increase (see Figure 38) of

$$\Delta\phi = 35 \text{ meV} \qquad (79)$$

and Equation 67, the calculated band bending (see above) leads to an electron-affinity change of

$$\Delta\chi = -4.4 \text{ meV} \qquad (80)$$

resulting in an oxygen-induced dipole moment whose normal component (see Equations 68 and 69) is calculated to be (apart from the unknown surface dielectric constant ϵ_s):

$$\mu ad/\epsilon_s = -4.39 \text{ Debye} \qquad (81)$$

with 1 e $\mathring{A}$ = 4.802 Debye.

The oxygen sticking coefficient S_{O2} is defined by the following equation:

$$\frac{dn_{ad,s}}{dt} = R = S_{O2}\, Z_{O2} \qquad (82)$$

where $$Z_{O2} = p_{O2}\,(2\pi m_{O2} k_B T)^{-1/2}$$

is the collision number for oxygen molecules of mass m_{O2} at temperature T at an oxygen partial pressure p_{O2}. This is the number of oxygen molecules striking a unit surface area per unit time. At room temperature, with $p_{O2} = 6.7\times10^{-6}$ mbar we get:

$$Z_{O2} = 1.778\times10^{15}\ \text{cm}^{-2}\ \text{sec}^{-1} \qquad (83)$$

From Equations 64, 65 and 82 with $\delta = -1$ we derive:

$$S_{O2} = \frac{1}{Z_{O2}\, e}\ \frac{dQ_{sc}}{d(-eV_s)}\ \frac{d(-eV_s)}{dt} \qquad (84)$$

With the help of the space-charge formalism and the approximation $d(-eV_s) \sim \Delta(-eV_s)$ and $dt \sim \Delta t \sim 5$ secs. we calculate the initial sticking coefficient

$$S_{O2}(t=0) = 8.11\times10^{-5} \qquad (85)$$

This result confirms the general fact that gases don't stick well at metal-oxide semiconductor surfaces [79,108].

Hydrogen Adsorption

The adsorption of hydrogen on stoichiometric TiO_2(110) surfaces was also studied by means of $\Delta\sigma$ and $\Delta\phi$ measurements. The results are shown in Figures 28 and 39.

Surface-conductivity increases at different temperatures as well as the work-function decreases at room temperature indicate donor-type adsorption of hydrogen species.

The interaction of hydrogen with the oxygen-rich (110) surface leads to the formation of surface OH groups with subsequent charge transfer to the TiO_2 substrate. The resulting band bending explains the observed conductivity and work-function changes.

The surface-conductivity changes measured during hydrogen adsorption are small compared to those obtained during oxygen adsorption (compare to Figure 27), and they decrease with increasing temperature. These observations lead to the assumption that the main contribution of $\Delta\sigma_s$ arises from hydrogen chemisorption, whereas small $\Delta\sigma_s$ increases are due to bulk diffusion of hydrogen forming donor-type defects, i.e. bulk OH-bonds with hydrogen atoms bridging two oxygen atoms [79].

The solubility of hydrogen in TiO_2 apparently decreases with increasing temperature, because of less-pronounced conductivity changes observed at elevated temperatures.

Due to the unavailability of data from desorption techniques such as TDS, the determination of hydrogen coverages, partial charges and surface dipole moments was not possible.

Carbon Monoxide Adsorption

Studies of surface-conductivity and work-function changes on annealed $TiO_2(110)$ during CO adsorption are represented by Figures 29 and 40.

The surface-conductivity decreases at 303 and 323 K indicate acceptor-type chemisorption, which is probably due to the formation of CO_2^{δ} complexes at the surface. The adsorbing CO molecules react with surface oxygen ions, the resulting CO_2 molecule accepts - in the thermodynamical average - a negative partial charge δ from the TiO_2 conduction band leading to a decrease in the surface conductivity.

The observed work-function decrease during CO exposure leads to the assumption of a large negative electron-affinity change, which compensates for the expected positive band bending at the surface and is due to the formation of surface dipoles.

From this point of view, the C-O bond axis of an adsorbing CO molecule (the C-atom interacting with surface oxygen)is not perpendicular to the surface, because the high electronegativity of oxygen would result in a

negatively charged top layer accompanied by an increase in work function. It is thus believed that the C-O bond axis is almost parallel to the surface, resulting in a negative normal component of the adsorbate-induced net-dipole moment.

Adsorption on Defective Surfaces

Oxygen Adsorption

$\Delta\sigma$ and $\Delta\phi$ results obtained on a defective $TiO_2(110)$ surface during oxygen adsorption are shown in Figures 30-34 and 38.

The observed surface-conductivity decreases are more pronounced on ion-bombarded (Figure 34) and titanium-covered (Figures 30 and 33) surfaces up to 0.6-monolayer coverages, if compared to results obtained on ideal surfaces. This phenomenon may be explained by the presence of another mechanism.

In addition to oxygen chemisorption and bulk oxygen diffusion, the charge transfer involved in surface-defect annealing contributes to the overall surface-conductivity changes measured on defective $TiO_2(110)$ surfaces during oxygen exposure. This effect increases with increasing temperature (see Figure 33), because surface-defect annealing is more pronounced at elevated temperatures (see previous chapters).

This mechanism is also reflected in the enhanced work-function increases observed on defective samples (see Figure 38). The originally lower - if compared to stoichiometric surfaces - work function of defective surfaces (due to the presence of positively charged titanium species at the surface) is drastically increased

upon surface-defect annealing, which is accompanied by a charge transfer from surface titanium to adsorbing oxygen species.

The magnitude of the surface-conductivity changes dropped between titanium coverages of 0.5 and 2.0 monolayers at 348 K, as shown in Figures 31 and 32. This phenomenon is not well understood at present. Hypothetically, it may be assumed that a complete overlayer of titanium reduces the O_2-bulk-diffusion effect and hence the measured conductivity changes.

Hydrogen Adsorption

The adsorption of hydrogen on defective (titanium-covered) surfaces results in less-pronounced surface-conductivity increases, if compared to corresponding results obtained on ideal surfaces. This is illustrated by the curves shown in Figure 35 and may be explained by two competing mechanisms:

1) donor-type adsorption and formation of donor-type OH complexes at the surface and in the bulk (see above).
2) acceptor-type adsorption leading to Ti^{4+}-H-complexes at the surface (see chapter 2).

This concept of competing effects arising from donor- and acceptor-type adsorption of hydrogen is strongly supported

by $\Delta\phi$ results obtained on TiO_2(110) surfaces with different defect concentrations (see Figure 39).

At titanium coverages of about 0.5 monolayers, extremely small work-function changes were observed, suggesting equal concentrations of positively and negatively charged surface hydrogen species.

Acceptor-type chemisorption dominates for higher titanium coverages or after heavy argon-ion bombardment, indicating a dominant concentration of Ti^{4+}-H^- species at the surface.

Our earlier EELS studies [81] showed that atomic hydrogen preferentially adsorbs on defective TiO_2(110) surfaces and leads to O-H stretch vibrations at a loss energy of 455 meV (see chapter 2). The Ti^{4+}-H- species expected on defective surfaces (see above), however, could not be detected in EELS, mainly because of a Ti-H vibrational-loss energy of 260 meV. In this energy range, a large background from contributions of multiple $\tilde{\nu}_2$ excitations was observed [81].

For a quite similar reason, the substrate-OH vibration couldn't be observed, either. We therefore calculated its value in a simple classical model. In this calculation, we assumed that O-H force constants β(O-H) known from the literature for free O-H radicals [$h\omega$(O-H) = 458 meV] to a first approximation do not change in the O-H adsorption complex. We also assumed that the mass of the surface

cations at the adsorption site is large if compared to the mass of oxygen and calculated two eigenfrequencies from:

$$\omega(OH)_{ad} = \frac{1}{2}\left[\frac{\beta}{m_H} + \frac{\beta + K}{m_O}\right] \pm \left[\frac{1}{4}\left(\frac{\beta}{m_H} + \frac{\beta + K}{m_O}\right)^2 - \frac{\beta K}{m_H m_O}\right]^{1/2} \quad (86)$$

with K as the force constant of the substrate-OH vibration.

Assuming $\omega(OH)_{ad} << \omega(O\text{-}H)_{free}$ we found:

$$[\omega(OH)_{ad}]^2 = [\omega(O\text{-}H)_{free}]^2 - [\omega(O\text{-}H)_{ad}]^2. \quad (87)$$

With the experimental value for $\omega(O\text{-}H)_{ad}$ we calculated $h\omega(OH)_{ad}$ = 52 meV. This value is comparable to substrate-OH vibrational loss energies measured on other samples such as platinum (see explanations given in reference 81).

Carbon Monoxide Adsorption

The interaction of CO molecules with defective TiO_2(110) surfaces was studied by means of $\Delta\sigma$ and $\Delta\phi$ measurements. Typical results are shown in Figures 36, 37 and 40.

The measured surface-conductivity decreases at 303 K (Figure 36) are less pronounced than those obtained on annealed surfaces. This indicates that fewer CO chemisorption sites - namely surface oxygen ions - are

available on defective surfaces, due to the strong interaction between $Ti^{\delta+}$ species and surface oxygen.

At highly defective surfaces, the work function increases upon CO exposure at 303 K. This observation suggests that the bonding geometry of chemisorbed CO complexes changes in the presence of a large amount of surface titanium species. The C-O bond axis is not parallel to the surface any more, resulting in a strong positive dipole barrier which causes a work-function increase.

At elevated temperatures and high titanium coverages (Figure 37), the conductivity increases are comparable to the values obtained on annealed samples. The CO_2 molecules created at the surface desorb into the gas phase, leaving additional point defects at the surface.

At elevated temperatures, surface titanium species either diffuse into the bulk or are annealed by bulk oxygen diffusing to the surface (see below). This explains the observation of almost equal conductivity changes on annealed and defective surfaces.

The following Table 10 presents a survey of partial charges δ and dipole moments μ_{ad} experimenatally obtained (or expected) for O_2, H_2 and CO chemisorption on stoichiometric (st) and defective (d) $TiO_2(110)$ surfaces.

Table 10. Partial Charges and Dipole Moments μ_{ad} (Debye).

Gas	δ^{st}	μ_{ad}^{st}/ϵ_s	δ^{d}	μ_{ad}^{d}/ϵ_s
O_2	-1*	-4.39	-1*	>-4.39
H_2	0.01*	-12*	<0.01	>-12
CO	0.006*	-5*	<0.006	>-5

*see references 13 and 79.

Diffusion of Defects

The diffusion of oxygen into the TiO_2 bulk and the diffusion of defects (oxygen vacancies) can be described by the well-known diffusion equation (Fick's second law [152]), because due to the large effective Debye length (essentially flat bands, see above) the surface and subsurface defect concentration won't differ much from the bulk defect concentration:

$$\frac{\partial \Delta c(z,t)}{\partial t} = D \frac{\partial^2 \Delta c(z,t)}{\partial z^2} \qquad (88)$$

D is the diffusion coefficient, t the time and z the spatial coordinate perpendicular to the sample (z=0 at the surface and z>0 in the bulk). $\Delta c(z,t)$ denotes the space- and time-dependent change in the defect concentration caused by defect annealing due to diffusion of oxygen into the bulk. Thus $\Delta c(z,t) = 0$ corresponds to a highly defective crystal of bulk defect concentration N_D, whereas $\Delta c(z,t) = \Delta c_E$ corresponds to a sample with an extremely low oxygen-vacancy concentration (annealed sample).

For a TiO_2 sample in an oxygen atmosphere of constant pressure (T=const) providing an equilibrium oxygen concentration at the $TiO_2(110)$ surface we can write:

$$\Delta c(0,t) = \Delta c_E \quad \text{and} \quad \Delta c(z>0,0) = 0 \qquad (89)$$

These are the boundary conditions necessary for solving the above partial differential equation (88), which can be accomplished with the help of standard mathematical techniques (e.g. Laplace transformation and subsequent contour integration).

A particular solution of Equation 88 - considering Equation 89 - is given by:

$$\Delta c(z,t) = \Delta c_E \{1-\mathrm{erf}[z(4Dt)^{-1/2}]\} \qquad (90)$$

with $\mathrm{erf}(x) = 2\pi^{-1/2}\int_0^x dt\ \exp(-t^2)$, the error function.

The average defect-concentration change $\Delta c'(t)$ in the sample of thickness d is defined in the following equation:

$$\Delta c'(t) = d^{-1}\int_0^d dz\ \Delta c(z,t) \qquad (91)$$

$$= \Delta c_E \{1-\mathrm{erf}[d(4Dt)^{-1/2}]+[4Dt/(\pi d^2)]^{1/2}\ [1-\exp(-d^2/(4Dt))]\}$$

Another quantity of interest is the time-dependent "center-of-mass" of bulk defects:

$$\bar{z}(t) = \frac{\int_0^d dz\ z\ \Delta c(z,t)}{\int_0^d dz\ \Delta c(z,t)} \qquad (92)$$

From Equations 90 and 92 we calculate:

$$\bar{z}(t) = \frac{d}{2}\,\frac{f_1(t)}{f_2(t)} \qquad (93)$$

with $$f_1(t) = 1-[1-2Dt/d^2]\ \mathrm{erf}[d(4Dt)^{-1/2}] - [4Dt/(\pi d^2)]^{1/2}\ \exp[-d^2/(4Dt)]$$

and $$f_2(t) = 1-\mathrm{erf}[d(4Dt)^{-1/2}] + [4Dt/(\pi d^2)]^{1/2}\ \{1-\exp[-d^2/(4Dt)]\}.$$

From Equation 93 we get:

$\bar{z}(t\to\infty) \to d/2$ and $\bar{z}(t\to 0) \to (\pi Dt/4)^{1/2} \to 0$.

In the following, the spatially-averaged changes in the defect concentration $\Delta c'(t)$ given in Equation 91 will be related to the experimentally obtained bulk-conductivity changes $\Delta\sigma_b(t)$, measured at T = 348 K upon oxygen exposure ($p_{O2} = 6.7\times10^{-6}$ mbar). But beforehand, we have to determine the (temperature-dependent) number $n(e^-)$ of conduction-band electrons associated with one point defect.

Both donor levels E_{D1} and E_{D2} (see above) contribute to the conductivity according to their position with respect to the Fermi level. With the use of Fermi statistics, we find:

$$n(e-) = 2-f(E_{D1}-E_F)-f(E_{D2}-E_F) \qquad (94)$$

where f(E) is the Fermi function given above. With the

calculated E_{D1}, E_{D2} and E_F values at T = 348 K we get:

$$n(e^-) = 0.15 \qquad (95)$$

Thus each oxygen vacancy gives 0.15 electrons to the TiO_2 conduction band at T = 348 K. This result can be verified by comparing the bulk density of conduction-band electrons $n_b = 2.31 \times 10^{16}$ cm^{-3} at T = 348 K to the bulk-defect concentration $N_D = 1.14 \times 10^{17}$ cm^{-3} (see above):

$$n_b \simeq 0.15\ N_D = 1.71 \times 10^{16} \text{ cm}^{-3}.$$

The Fermi function as well as the two donor levels E_{D1} and E_{D2} are plotted in Figure 58 at three different temperatures. The solid lines were obtained for 348 K [n(e$^-$)=0.15], the dashed lines for 300 K [n(e$^-$)=0.05] and the dotted lines for 600 K [n(e$^-$)=1.61]. The figure illustrates that both donor levels are only partially ionized at low temperatures, whereas both of them are nearly depopulated at 600 K [n(e$^-$)=1.61].

We can now compare $\Delta\sigma_b(t)$ measured at 348 K to $\Delta c'(t)$:

$$\Delta\sigma_b(t) \simeq \frac{\sigma_0}{N_D}\, n(e^-)\, \Delta c'(t) \qquad (96)$$

with $\sigma_0 = \sigma_b(t=0)$

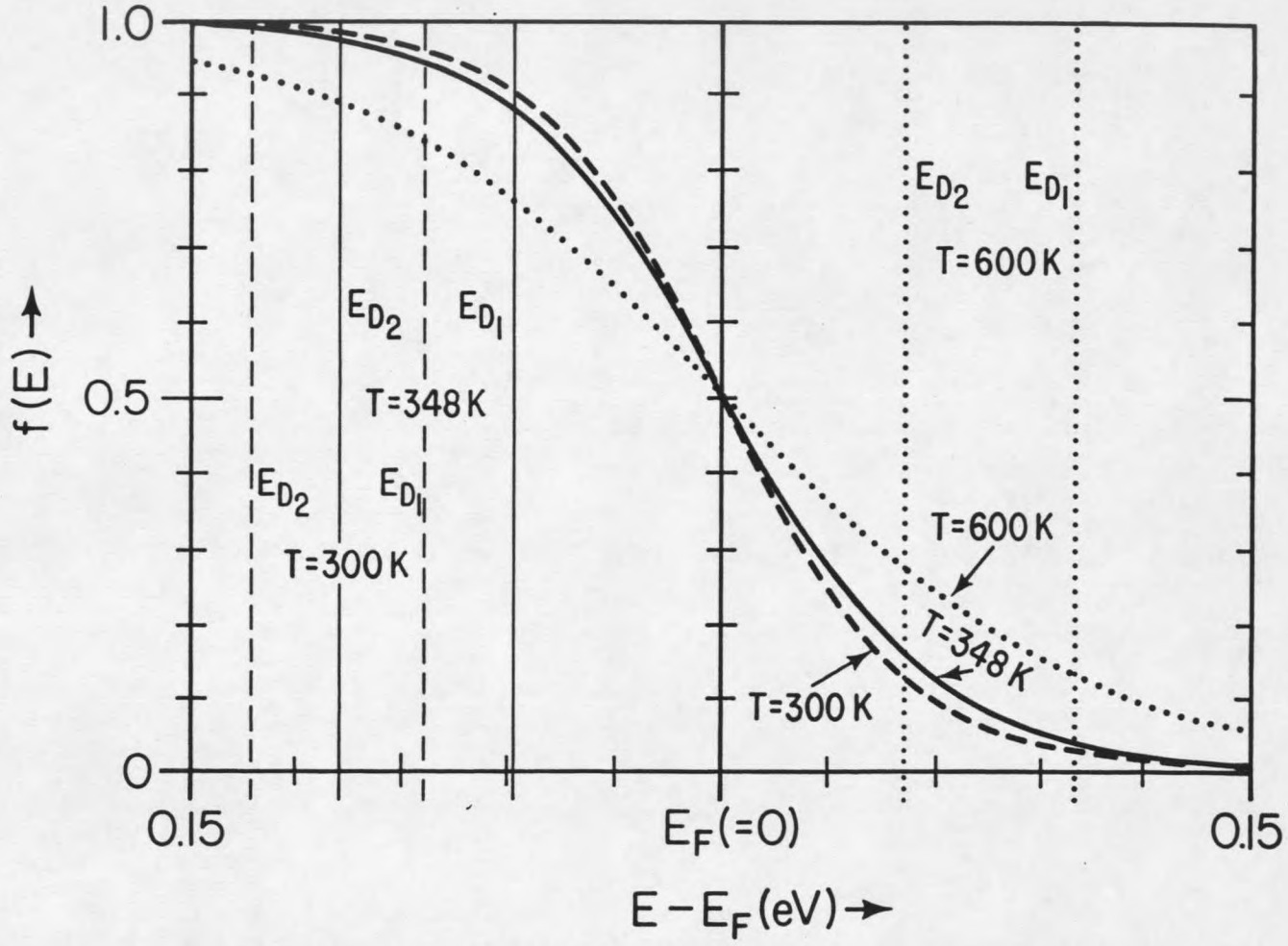

Figure 58. Fermi function plotted for three different temperatures as a function of energy. Also shown are the corresponding energetic positions (referred to E_F) of donor levels E_{D1} and E_{D2}.

The diffusion coefficient D as well as the maximum change Δc_E in the defect concentration (corresponding to the equilibrium value after annealing) is determined by fitting Equation 96 to the experimentally obtained $\Delta\sigma_b(t)$ values. With the use of the Simplex Algorithm we get:

$$D = 2.77\times10^{-7}\ cm^2sec^{-1} \quad \text{and} \quad \Delta c_E = -1.85\times10^{17}\ cm^{-3} \qquad (97)$$

And indeed, $|\Delta c_E| \simeq N_D$, the original bulk defect concentration.

The shapes of the functions z(t) and Δc't) are plotted in Figure 59. Here, the bottom horizontal axis represents the highly defective sample, the upper axis the annealed sample with $\bar{z}(t=\infty) = d/2$.

Diffusion profiles $\Delta c(z,t)/\Delta c_E$ for different times (10 to 1,000,000 secs.) are shown in Figure 60. Again, the lower horizontal axis at $\Delta c(z,t)/\Delta c_E = 0$ represents a high bulk defect concentration, whereas the upper axis with $\Delta c(z,t)/\Delta c_E = 1$ corresponds to a stoichiometric sample.

The diffusion coefficient calculated above disagrees with results obtained by Haul et al. during isotope-exchange experiments with ^{18}O-labelled oxygen (see chapter 2). From their extrapolated data an oxygen diffusion coefficient of $8.38\times10^{-42}\ cm^2sec^{-1}$ is calculated for T = 348 K. Extrapolation of results measured in the temperature range between 980 and 1570 K, however, underestimates typical low-temperature and surface effects.

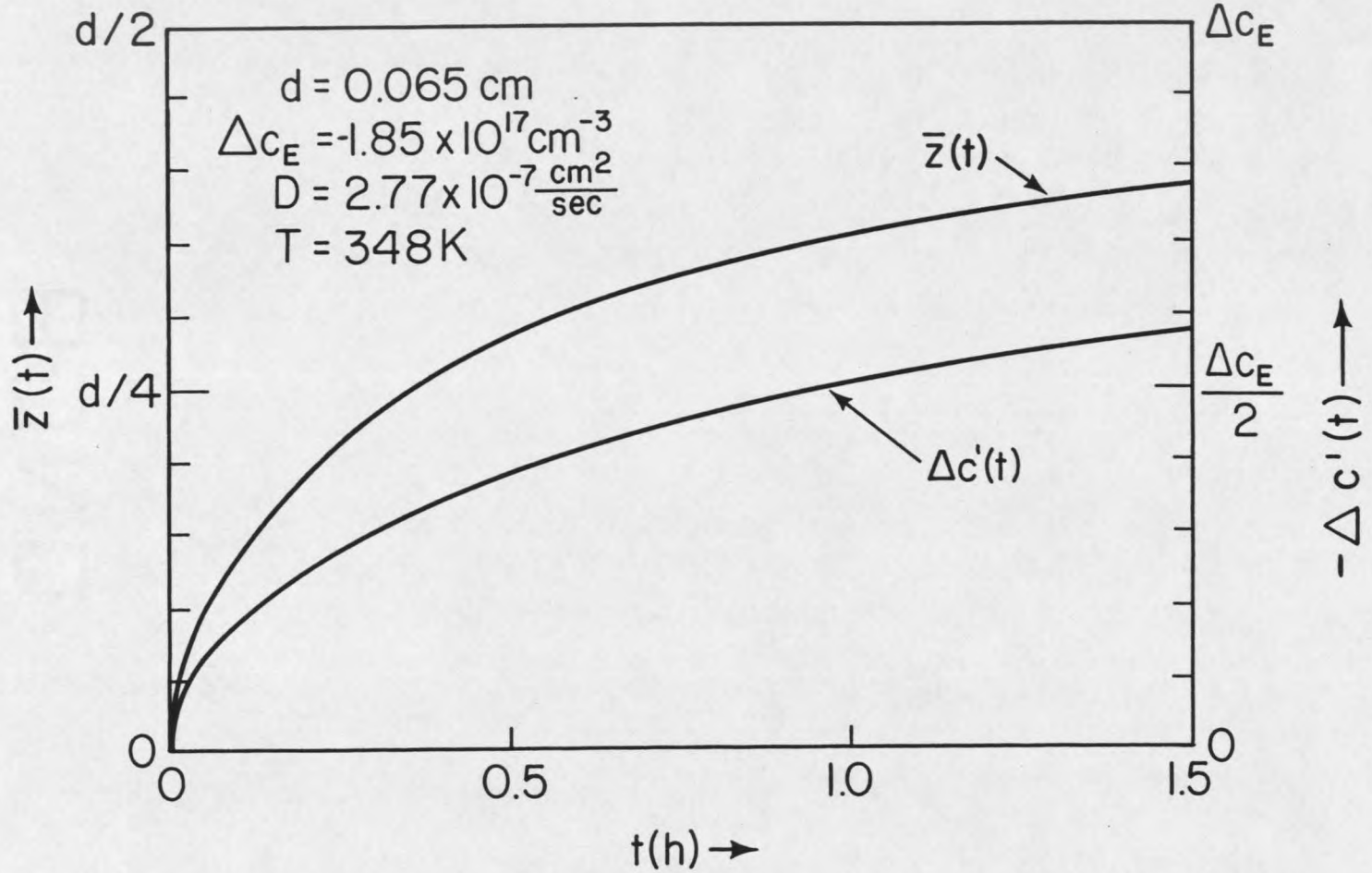

Figure 59. Average bulk-defect-concentration changes, $\Delta c'$, and "center-of-mass" of bulk defects, $\bar{z}$, plotted as a function of time. This figure illustrates bulk-defect annealing and is explained in more detail in the text.

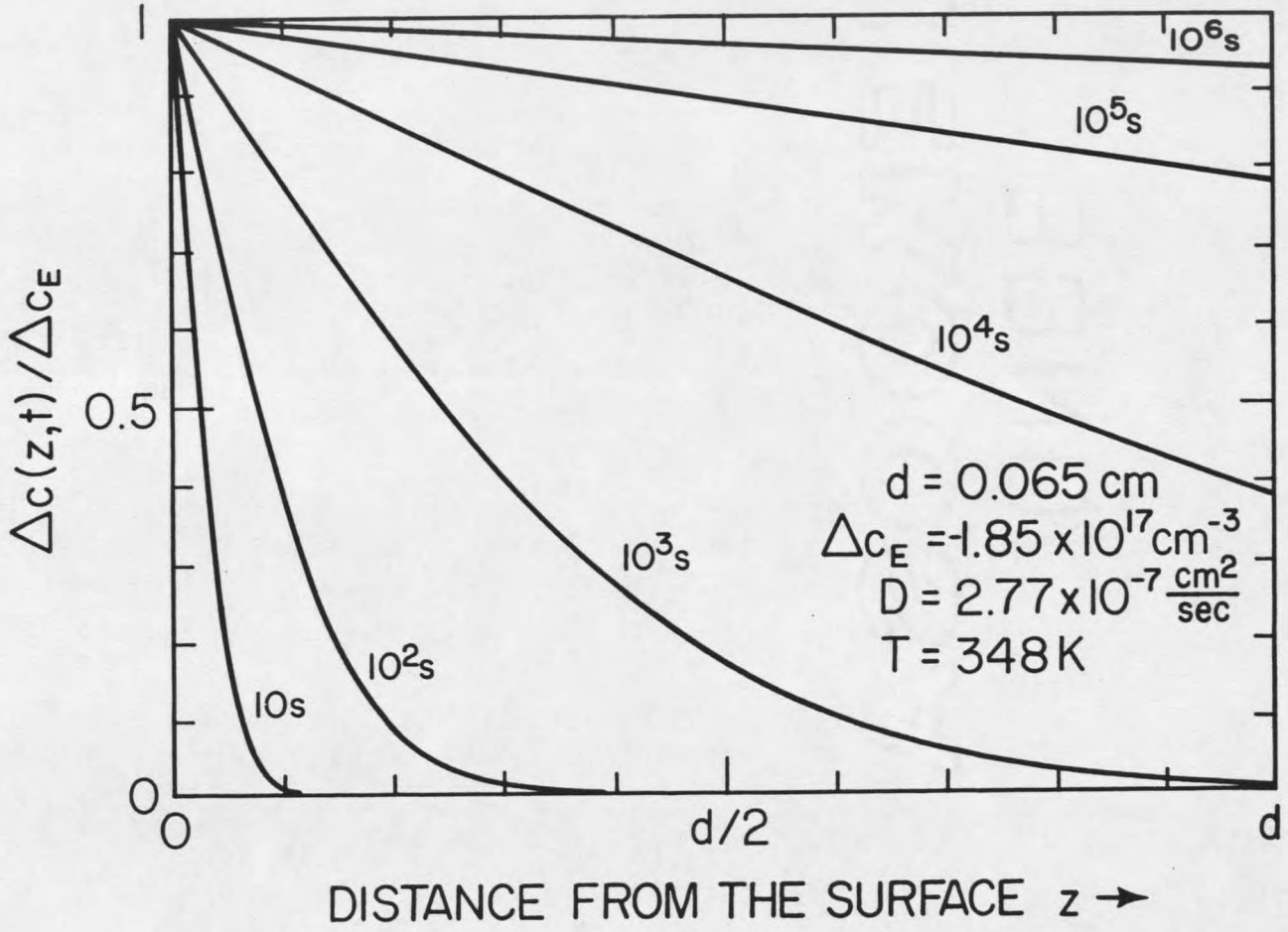

Figure 60. Diffusion profiles, $\Delta c/\Delta c_E$, of bulk defects at different times.

Room-temperature chemisorption of oxygen, e.g., with subsequent charge transfer leads to electrochemical potential gradients at the surface. The resulting attractive forces between positively charged bulk-oxygen vacancies and negatively charged oxygen chemisorption complexes enhances the diffusion of bulk defects (electromigration of defects).

Furthermore, inhomogeneous distribution of charged bulk defects accompanied by locally varying band energies as well as lattice distortions near the surface (amorphous structure in subsurface regions) may lower the diffusion activation energy.

In addition, published results of investigations of bulk defects in rutile TiO_2 are contradictory (see chapter 2). Some results favor the oxygen vacancy ($2Ti^{3+}$ V_O) as the dominant defect [11,17,161] while others [23-25,168,169] favor a titanium interstitial (Ti_I^{3+}), and yet others favor a combination of the two [21,36,162].

Paramagnetic Resonance results on reduced rutile indicate the presence of Ti3+ ions on normal and interstitial sites [21,26] as well as centers with unexplained spectra [21].

Internal friction results [28,29,160] cannot be explained on the basis of oxygen vacancies at all, but can be explained on the basis of associated Ti^{3+} interstitial pairs [21].

Kevane [161] considered oxygen vacancies and their effects on electrical conduction in some metal oxides through an exact solution of the equilibrium relations between oxygen partial pressure in the ambient gas and concentrations of oxygen vacancies and conduction electrons in the oxide.

From conductivity as well as Infrared and Optical Absorption studies Cronemeyer [11,17] concluded that the dominant defect in rutile is an oxygen vacancy.

Dominik et al. [21] observed three distinct dielectric relaxation processes in rutile. They assigned one process to an oxygen vacancy, another one to an interstitial Ti^{3+} ion.

In this circumstance, the nature of the diffusing element (titanium or oxygen) involved in bulk defect diffusion is not clear at present. The results presented in this thesis do not distinguish between titanium interstitials and oxygen vacancies as dominant defects, because the measurable electrical properties arising from both kinds of defects are identical. Also annealing of surface defects monitored by XPS (see above) can be discussed in two ways:

1) bulk oxygen diffuses to the surface at elevated temperatures and anneals surface defects, resulting in a new oxide overlayer.

2) titanium species at the surface diffuse into the bulk at elevated temperatures, leaving an almost ideal surface.

LEED studies (see above) are not suitable for characterizing the type of surface defect, either. Diffuse spots observed after the deposition of titanium (see chapter 4) became more intense upon heating, suggesting diffusion of titanium into the bulk or diffusion of oxygen to the surface (with subsequent surface-defect annealing).

High-temperature treatments of defective $TiO_2(110)$ surfaces were done at different temperatures T (870, 1070 and 1220 K). Assuming that the corresponding annealing times τ ($\sim$ 15, 2 and 1 min.) [τ = time for reobtaining a sharp LEED pattern] are approximately given by

$$\tau = \tau_0 \exp[\Delta E/(k_B T)],$$

an activation energy of $\Delta E \simeq 2$ eV was estimated for the annealing process. This activation energy is greater than the activation energy for Ti diffusion (1.04 eV, see chapter 2), but less than the activation energy measured for O diffusion (2.65 eV, see chapter 2).

In order to simplify the data analysis and interpretation the defect structure of TiO_2 has been discussed in this thesis on the basis of oxygen vacancies.

Further isotope-exchange experiments to study the defect diffusion in TiO_2 are desirable. They might give an unequivocal explanation of the nature of the dominant defect in rutile.

CHAPTER 6

SUMMARY AND OUTLOOK

In this thesis, electronic bulk- and surface-defect structures of TiO_2 samples and the interaction of different gases with stoichiometric and defective $TiO_2(110)$ surfaces were investigated extensively by various experimental techniques.

Bulk conductivity measurements as a function of sample temperature and the assumption of donor-type oxygen vacancies as main bulk defects led to the determination of a bulk-defect concentration of 1.14×10^{17} cm-3 as well as two donor-level positions 0.421 and 0.470 eV below the lower conduction-band edge.

With the use of surface-sensitive probes, such as XPS, XAES, AES, EELS and ELS as well as measurements of surface-conductivity changes $\Delta\sigma_s$, the formation of surface-defect-related Ti3+ species was monitored during high-temperature treatment, argon-ion bombardment and deposition of submonolayer amounts of titanium on the surface.

The presence of surface defects led to broadenings and/or additional peaks in the Ti2p-, Ti3p-, O1s-core-levels and TiLMV Auger transition as well as

changes in the valence-band structure accompanied by a weak band-gap-state emission. Electronic transitions from this band-gap state to the TiO_2 conduction band were observed in ELS.

Relative concentrations and core-level binding energies of differently charged surface titanium species were determined by fitting symmetric Gaussians as well as asymmetric Doniach-Sunjić functions to experimentally obtained XPS core-level spectra. Good agreement was found between theoretically and experimentally determined Ti2p-core-level-binding energies in titanium ions at TiO_2(110) and different titanium oxides, respectively. Ti^{4+} ions representing stoichiometric surfaces and defect-related Ti3+ species were found to give the dominant contributions to the titanium core-level spectra.

The formation of surface defects was accompanied by an increase in the surface conductivity of TiO_2(110). Submonolayer amounts of titanium deposited on this surface resulted in titanium partial charges of $\delta = 0.057$ and $= 0.047$ at titanium coverages of 0.25 and 0.50 monolayers as well as adsorbate-induced surface states between 0.410 and 0.415 eV below the lower conduction-band edge.

The interaction of gases with stoichiometric and defective TiO_2(110) surfaces were studied by means of measurements of conductivity $\Delta\sigma_s$ and work-function $\Delta\phi$ changes.

Oxygen chemisorption with $\delta = -1$ on stoichiometric surfaces led to negative $\Delta\sigma_s$ values and, in connection with a space-charge-layer model, to calculated room-temperature values for the relative oxygen coverage, the initial sticking coefficient and the oxygen-induced surface dipole moment of 1.8×10^{-4}, 8.11×10^{-5} and $4.39\,\epsilon_s$ Debye. From initial time-derivatives of surface-conductivity changes it was derived that only 2.5 % of the measured conductivity changes were due to oxygen chemisorption, whereas the remaining part arose from bulk-defect annealing.

On defective surfaces between 0 and 0.6 ML titanium coverages at 348 and 423 K, the surface-conductivity changes upon O_2 exposure were enhanced if compared to the results obtained on stoichiometric surfaces.

In a simple diffusion model applied to the diffusion of bulk oxygen a diffusion constant of 2.77×10^{-7} cm2 sec^{-1} at T = 348 K was calculated by fitting the experimentally determined $\Delta\sigma_b$-data to theoretical changes in the oxygen vacancy concentrations derived from Fick's second law. Also, a maximum defect-concentration change, corresponding to the annealed (stoichiometric) sample in thermodynamic

equilibrium, of -1.85×10^{17} cm^{-3} was calculated, in good agreement with the above-given bulk-defect concentration.

Positive work-function changes were observed on stoichiometric and defective surfaces upon oxygen chemisorption. The changes were more pronounced on defective surfaces.

From the $\Delta\sigma_s$- and $\Delta\phi$-data it was concluded that defect-related Ti^{3+} species at the (110) surface strongly interact with adsorbing oxygen, leading to the annealing of these species accompanied by pronounced $\Delta\sigma_s$-decreases and $\Delta\phi$-increases.

Positive $\Delta\sigma_s$ and negative $\Delta\phi$ changes were observed on stoichiometric surfaces upon hydrogen exposure, suggesting donor-type chemisorption of hyrdogen species and the formation of OH groups at these surfaces.

Work-function increases, however, and less-pronounced $\Delta\sigma_s$ increases were found on slightly defective surfaces, confirming the earlier assumption of the presence of Ti^{4+}-H^- species at defective TiO_2 surfaces.

The chemisorption of CO molecules at stoichiometric surfaces led to negative $\Delta\phi$ and $\Delta\sigma_s$ values below 323 K as well as positive $\Delta\sigma_s$ changes above 333 K. The phenomena were explained by the formation of CO_2 molecules at the surface, accompanied by strong adsorbate-induced dipole moments as well as an increase in the surface-defect concentration. At elevated temperatures, the CO_2 molecules

desorb into the gas phase and surface defects diffuse into the bulk, thus increasing the conductivity.

At highly defective surfaces, work-function increases and less-pronounced $\Delta\sigma_s$ decreases at low temperatures were recorded. These results indicate that fewer CO chemisorption sites - namely surface oxygen ions - are available on defective surfaces, due to the strong interaction between Ti3+ species and surface oxygen. Furthermore, the observation of work-function increases suggests changes in the bonding geometry of chemisorbed CO complexes in the presence of a high concentration of surface titanium species.

Due to the unavailability of equipment, coverages, adsorption rates, sticking coefficients, isosteric heats of adsorption, desorption energies and temperatures of adsorbing and desorbing gases couldn't be determined experimentally. These properties, however, are of great interest, because they lead, e.g., to the determination of partial charges and surface dipole moments. With the help of Thermal Desorption Spectroscopy (TDS) or other desorption techniques, these parameters will be determined in future studies.

Furthermore, angle-resolved photoemission experiments on TiO_2 surfaces will be performed to probe surface electronic band structures including defect-derived bands

in the band gap. Angle-resolved XPS studies will make possible the separate study of surface and bulk species.

Further isotope-exchange experiments may explain the physical origin of the dominant defect in rutile TiO_2.

Additional studies on the catalytic activity of differently treated (stoichiometric, defective, or covered by foreign atoms) TiO_2 surfaces and the design of new TiO_2 gas sensors will be of further interest.

REFERENCES CITED

REFERENCES CITED

1. Z. K. Jarcebski, in: Oxide Semiconductors, Pergamon Press, Oxford-New York (1973) 212.

2. S. Munnix, M. Schmeits: Phys. Rev. B30 (1984) 2202.

3. E. A. Grant: Rev. Mod. Phys. 31 (1959) 646.

4. A. von Hippel, J. Kalnajs, W. B. Westphal: J. Phys. Chem. Solids 23 (1962) 779.

5. J. O. Dimmock, R. G. Wheeler: Phys. Rev. 127 (1962) 391.

6. J. G. Gay, W. A. Albers, F. J. Arlinghaus: J. Phys. Chem. Solids 29 (1968) 1449.

7. M. Tinkham: Group Theory and Quantum Mechanics, McGraw-Hill, New York (1964).

8. S. Ellialtioglu, T. Wolfram, V. E. Henrich: Solid State Commun. 29 (1978) 321.

9. G. A. Samara, P.S. Peercy: Phys. Rev. B27 (1973) 1131.

10. D. Tsur, M. Blau, M. Wegner: J. Phys. C7 (1974) 1257.

11. D. C. Cronemeyer: Phys. Rev. 87 (1952) 876.

12. L. E. Hollander jr., P. L. Castro: J. Appl. Phys. 33 (1962) 3421.

13. R. Feierabend: Doctoral Thesis, Universitaet Hannover, Hannover/West Germany (1982).

14. P. G. Wahlbeck, P. W. Gilles: J. Am. Ceram. Soc. 49 (1966) 181.

15. Y. W. Chung, W. J. Lo, G. A. Somorjai: Surf. Sci. 64 (1977) 588.

16. R. G. Breckenridge, W. R. Hosler: Phys. Rev. 91 (1953) 793.

17. D. C. Cronemeyer: Phys. Rev. 113 (1959) 1222.

18. J. H. Becker, W. R. Hosler: Phys. Rev. 137 (1965) A1872.

19. G. B. Acket, J. Volger: Phys. Lett. 8 (1964) 244.

20. L. E. Hollander, P. L. Castro: J. Appl. Phys. 33 (1962) 3421.

21. L. A. K. Dominik, R. K. MacCrone: Phys. Rev. 163 (1967) 756.

22. E. Iguchi, K. Yajima: J. Phys. Soc. Japan 32 (1972) 1415.

23. J. Yahia: Phys. Rev. 130 (1963) 1711.

24. R. D. Carnahan, J. D. Brittain: J. Am. Ceram. Soc. 48 (1965) 365.

25. D. S. Tannhauser: Solid State Commun. 1 (1963) 223.

26. P. F. Chester: J. Appl. Phys. Suppl. 32 (1961) 2233.

27. T. R. Sandin, P. H. Keesom: Phys. Rev. 177 (1969) 1370.

28. R. D. Carnahan, J. D. Brittain: J. Appl. Phys. 34 (1963) 3095.

29. J. B. Wachtman jr., L. R. Doyle: Phys. Rev. 135 (1964) A276.

30. K. Hauffe, J. Hupfeld, T. Wetterling: Z. Phys. Chem. (N. F.) 103 (1976) 115.

31. R. R. Hasiguti, K. Minami, H. Yonemitsu: J. Phys. Soc. Japan 16 (1961) 2223.

32. W. Jakubowski: Acta Phys. Polon. 33 (1968) 465.

33. M. E. Straumanis, T. E. Ejima, W. J. James: Acta Cryst. 14 (1961) 493.

34. S. Andersson et al.: Acta Chem. Scand. 11 (1957) 1641.

35. P. Kofstad: J. Less-Common Metals 13 (1967) 635.

36. P. Kofstad: J. Phys. Chem. Solids 23 (1962) 1579.

37. K. S. Forland: Acta Chem. Scand. 18 (1964) 1267.

38. R. Haul, G. Duembgen: J. Phys. Chem. Solids 26 (1965) 1.

39. W. R. Turber, J. H. Mante: Phys. Rev. 139 (1965) A1655.

40. G. A. Acket, J. Volger: Physica 32 (1966) 1680.

41. H. P. R. Frederikse: J. Appl. Phys. Suppl. 32 (1961) 2211.

42. V. N. Bogomolov, V. P. Zhuze: Soviet Physics-Solid State 5 (1964) 2404 [F. Tverd. Tela 5 (1963) 3285].

43. V. N. Bogomolov et al.: F. Tverd. Tela 11 (1969) 3214.

44. T. Goto, T. Okada: J. Phys. Soc. Japan 25 (1968) 289.

45. J. B. Goodenough: Prog. Solid State Chem. 5 (1972) 145.

46. H. B. Whitehurst et al.: J. Phys. Chem. Solids 28 (1967) 861.

47. J. A. van Raalte: J. Appl. Phys. 36 (1965) 3365.

48. J. H. Becker, W. R. Hosler: J. Phys. Soc. Japan Suppl. 18 (1963) 152.

49. V. N. Bogomolov, P. M. Szavkunov: F. Tverd. Tela 5 (1963) 2027.

50. R. A. Parker: Phys. Rev. 124 (1961) 1719.

51. E. Iguchi, H. Sawatar, R. J. D. Tilley: Phys. Stat. Sol. (B) 101 (1980) 333.

52. B. H. Soffer: J. Chem. Phys. 35 (1961) 940.

53. J. W. DeFord, O. W. Johnson: J. Appl. Phys. 44 (1973) 3001.

54. O. W. Johnson, S.-H. Paek, J. W. DeFord: J. Appl. Phys. 46 (1975) 1026.

55. Y. Chen, R. Gonzalez, K. L. Tsang: Phys. Rev. Lett. 53 (1984) 1077.

56. V. E. Henrich, G. Dresselhaus, H. J. Zeiger: Phys. Rev. Lett. 36 (1976) 1335.

57. V. E. Henrich, G. Dresselhaus, H. J. Zeiger: Solid State Comm. 24 (1977) 623.

58. V. E. Henrich: Prog. Surf. Sci. 9 (1979) 143.

59. W. J. Lo, Y. W. Chung, G. A. Somorjai: Surf. Sci. 71 (1978) 199.

60. M. L. Knotek, J. E. Houston: Phys. Rev. B15 (1977) 4580.

61. M. L. Knotek, P. J. Feibelman: Phys. Rev. Lett. 40 (1978) 964.

62. M. L. Knotek: Surf. Sci. 101 (1980) 334.

63. M. L. Knotek: Surf. Sci. 91 (1980) L17.

64. M. L. Knotek, V. O. Jones, V. Rehn: Phys. Rev. Lett. 43 (1979) 300.

65. V. E. Henrich, R. L. Kurtz: Phys. Rev. B23 (1981) 6280.

66. E. Bertel, R. Stockbauer, T. E. Madey: Phys. Rev. B27 (1983) 1939.

67. E. Bertel, R. Stockbauer, R. L. Kurtz, T. E. Madey, D. E. Ramaker: Surf. Sci. 152/153 (1985) 776.

68. E. Bertel, R. Stockbauer, T. E. Madey: Surf. Sci. 141 (1984) 355.

69. H. S. Jarrett: Phys. Rev. Lett. 54 (1985) 217.

70. H. Yamada, Y. Yamamoto: Surf. Sci. 134 (1983) 71.

71. T. Nakayama: Surf. Sci. 133 (1983) 101.

72. L. E. Firment: Surf. Sci. 116 (1982) 205.

73. Z. Sroubek, J. Zavadil, K. Zdánsky: J. Vac. Sci. Technol. 19 (1981) 80.

74. W. E. Wall, M. W. Ribarsky, J. R. Stevenson: J. Appl. Phys. 51 (1980) 661.

75. R. D. Iyengar et al.: J. Am. Chem. Soc.88 (1966) 5055.

76. S. Nishigaki: Surf. Sci. 125 (1983) 762.

77. G. D. Davis, M. Natan, K. A. Anderson: Appl. Surf. Sci. 15 (1983) 321.

78. M. Murata, K. Wakino: J. Electr. Spectr. Rel. Phenom. 6 (1975) 459.

79. W. Goepel, G. Rocker, R. Feierabend: Phys. Rev. B28 (1983) 3427.

80. W. Goepel, J. A. Anderson, D. Frankel, M. Jaehnig, K. Phillips, J. A. Schaefer, G. Rocker: Surf. Sci. 139 (1984) 333.

81. G. Rocker, J. A. Schaefer, W. Goepel: Phys. Rev. B30 (1984) 3704.

82. L. L. Kesmodel, J. A. Gates, Y. W. Chung: Phys. Rev. B23 (1981) 489.

83. S. Munnix, M. Schmeits: Surf. Sci. 126 (1983) 20.

84. S. Munnix, M. Schmeits: Phys. Rev. B28 (1983) 7342.

85. S. Munnix, M. Schmeits: Phys. Rev. B31 (1985) 3369.

86. R. V. Kasowski, R. H. Tait: Phys. Rev. B20 (1979) 5168.

87. C. C. Kao, S. C. Tsai, M. K. Bahl, Y. W. Chung, W. J. Lo: Surf. Sci. 95 (1980) 1.

88. T. K. Sham, M. S. Lazarus: Chem. Phys. Lett. 68 (1979) 426.

89. C. D. Jaeger, A. J. Bard: J. Phys. Chem. 83 (1979) 3146.

90. V. Guruswamy, J. O. M. Bockris: Solar Energy Mat. 1 (1979) 441.

91. N. van Hieu, D. Lichtman: Surf. Sci. 103 (1981) 535.

92. V. M. Bermudez, M. A. Hoffbauer: Phys. Rev. B30 (1984) 1125.

93. J. Cunningham, J. P. J. Tobin: Surf. Sci. 108 (1981) L465.

94. H. W. Gundlach, K. E. Heusler: Z. Phys. Chem. (N. F.) 119 (1980) 213.

95. M. L. Knotek: Electrochem. Soc., Extended Abstracts, Philadelphia, May 1977.

96. W. Siripaia, M. Tomkiewicz: Phys. Rev. Lett. 50 (1983) 443.

97. M. Scrocco: Chem. Phys. Lett. 61 (1979) 453.

98. R. Fuchs, K. L. Kliewer: Phys. Rev. 140 (1965) A2076.

99. H. Lueth: Festkoerperprobleme 21 (1981) 117 [Ad. Sol. State Phys. 23 (1982) 117].

100. A. Many, Y. Goldstein, N. B. Grover: Semiconductor Surfaces, North-Holland, Amsterdam (1971).

101. W. Goepel, in: Festkoerperprobleme 20 (1980)

102. T. Wolfram, S. Ellialtioglu: Appl. Phys. 13 (1977) 21.

103. V. E. Henrich, R. L. Kurtz: J. Vac. Sci. Technol. 18 (1981) 416.

104. M. Henzler: Surf. Phys. of Materials 1 (1975) 241.

105. V. E. Henrich, G. Dresselhaus, H. J. Zeiger: J. Vac. Sci. Technol. 15 (1978) 534.

106. J. Hupfeld: Doctoral Thesis, Universitaet Goettingen, Goettingen/West Germany (1975).

107. W. Goepel: J. Vac. Sci. Technol. 16 (1979) 1229.

108. W. Goepel, G. Rocker: J. Vac. Sci. Technol. 21 (1982) 389.

109. I. S. Sazanova et al.: Kinetica i Kataliz 11 (1970) 447.

110. P. C. Gravelle et al.: J. C. S. Faraday I. 52 (1971) 140.

111. C. J. Engelder, E. L. Miller: J. Physik. Chem. 36 (1932) 1345.

112. D. Y. Cha, G. Parravano: J. Cat. 11 (1968) 228.

113. N. Yamamoto, S. Tonomura, H. Tsubomura: J. Electrochem. Soc. 129 (1982) 444.

114. A. J. Bard: J. Photochem. 10 (1979) 59.

115. G. N. Schrauzer, T. D. Guth: J. Am. Chem. Soc. 99 (1977) 7189.

116. I. Izumi, F. R. F. Fan, A. J. Bard: J. Phys. Chem. 85 (1981) 218.

117. A. Jujishima, K. Honda: Nature [London] 238 (1972) 37.

118. Basic Research Opportunities for Lasting Fuel Gas Supplies Report from Workshop at Texas A&B University (1981), edited by C. A. Rodenberger et al. [Gas Research Institute, Chicago (1982)].

119. Solar Energy Conversion: Solid State Physics Aspects, Vol.31 of Topics in Applied Physics, edited by B. O. Seraphim, Springer-Verlag, Berlin (1981).

120. Handbook of X-ray Photoelectron Spectroscopy, by C. D. Wagner, W. M. Riggs, L. E. Davis, J. F. Moulder, G. E. Muelenberg (Ed.), published by: Perkin-Elmer Corporation, Physical Electronics Division, Eden Prairie, Minnesota.

121. H. Froitzheim, in: Electron Spectroscopy for Surface Analysis, edited by H. Ibach, Springer-Verlag, Berlin, New York (1977).

122. H. Ibach, D. L. Mills: Electron Energy Loss Spectroscopy and Surface Vibrations, Academic Press (1982).

123. M. Henzler, J. Clabes: Jpn. J. Appl. Phys. Suppl. 2/2 (1974) 389.

124. M. Henzler, in: Topics in Current Physics 4, edited by H. Ibach, Springer-Verlag, Berlin (1977).

125. M. Henzler, F. W. Wulfert: Proc. XIII. Intern. Conf. Phys. Semicond., Rome (1976).

126. M. Henzler: Surf. Sci. 22 (1970) 12.

127. M. Henzler: Appl. Phys. 9 (1976) 11.

128. L. J. van der Pauw: Philips Res. Rep. 13 (1958) 1.

129. L. J. van der Pauw: Philips Tech. Rev. 20 (1958) 220.

130. N. W. Ashcroft, N. D. Mermin: Solid State Physics, Saunders College, Philadelphia (1976).

131. R. C. Riviere: Sol. State Surf. Sci. 1 (1969) 180.

132. A. G. Knapp: Surf. Sci. 34 (1973) 289.

133. P. P. Craig, V. Radoka: Rev. Sci. Instr. 41 (1970) 258.

134. J. S. W. de Boer et al.: Rev. Sci. Instr. 44 (1973) 1003.

135. Applications of Piezoelectric Quartz Crystal Microbalances, edited by C. Lu, A. W. Czanderna, Vol. 7 of Methods amd Phenomena: Their Applications in Science and Technology, Elsevier, Amsterdam, Oxford, New York, Tokyo (1984).

136. M. P. Seah, W. A. Dench: Surface and Interface Analysis 1 (1979)1.

137. L. H. Dubois, G. P. Schwartz, R. E. Camley, D. L. Mills: Phys. Rev. B29 (1984) 3208.

138. R. Seiwatz, M. Green: J. Appl. Phys. 29 (1958) 1034.

139. P. R. Bevington: Data Red. and Error Anal. Phys. Sci., McGraw-Hill, New York (1969).

140. M. S. Caceci, W. P. Cacheris: Byte (May 1984)340.

141. N. Beatham, A. F. Orchard, G. Thornton: J. Phys. Chem. Solids 42 (1981) 1051.

142. H. F. Franzen, M. X. Umaña, J. R. McCreary, R. J. Thorn: J. Sol. State Chem. 18 (1976) 363.

143. C. J. Powell, P. E. Larson: Appl. Surf. Sci. 1 (1978) 186.

144. S. Doniach, M. Sunjić: J. Phys. C3 (1970) 285.

145. F. H. Scofield: J. Electron Spectrosc. Related Phenomena 8 (1976) 129.

146. J. Cazaux: Appl. Surf. Sci. 10 (1982) 124.

147. R. F. Reilman, A. Msezane, S. T. Manson: J. Electron Spectrosc. Related Phenomena 8 (1976) 389.

148. D. M. Eagles: J. Phys. Chem. Solids 25 (1964) 1243.

149. J. G. Traylor, H. G. Smith, R. M. Nicklow, M. K. Wilkinson: Phys. Rev. B3 (1971) 3457.

150. L. H. Dubois, G. P. Schwartz: Phys. Rev. B26 (1982) 794.

151. R. L. Kurtz, V. E. Henrich: Phys. Rev. B25 (1982) 3563.

152. W. Jost: Diffusion, Steinkopff-Verlag, Darmstadt/West Germany (1957).

153. Electron Spectroscopy: Theory, Techniques and Applications 2, Academic Press (1978).

154. Topics in Applied Physics 26: Photoemission in Solids I, Springer-Verlag (1978).

155. Electron Spectroscopy for Surface Analysis, edited by H. Ibach, Springer-Verlag (1977).

156. Characterization of Solid Surfaces, edited by P. F. Kane, G. B. Larrabee, Plenum Press (1974).

157. Handbook of Auger Electron Spectroscopy, by L. E. Davis, N. C. MacDonald, P. W. Palmberg, G. E. Riach, R. E. Weber, published by: Perkin-Elmer Corporation, Physical Electronics Division, Eden Prairie, Minnesota.

158. M. Klaua, G. Oertel, in: Festkoerperanalyse mit Elektronen, Ionen und Roentgenstrahlen, Vieweg (1980).

159. J. W. Davenport, R. E. Watson, M. L. Peolman, T. K. Sham: Solid State Commun. 40 (1981) 999.

160. R. D. Carnahan, J. O. Brittain: J. Appl. Phys. 37 (1966) 1808.

161. C. J. Kevane: Phys. Rev. 133 (1964) A1431.

162. R. D. Shannon, J. Appl. Phys. 35 (1964) 3414.

163. P. H. Citrin, G. K. Wertheim: Phys. Rev. B16 (1977) 4256.

164. P. Nozières, C. T. de Dominicis: Phys. Rev. 178 (1969) 1097.

165. M. H. L. Pryce, in: Phonons in Perfect Lattices with Point Imperfections, edited by R. W. H. Stevenson, Oliver and Boyd, Edinburgh/Scotland (1966) 403.

166. P. Weightman: Rep. Prog. Phys. 45 (1982) 753.

167. M. Green, V. E. Cosslett: Brit. J. Appl. Phys. (J. Phys. D) 1, Ser. 2 (1968) 425.

168. T. Hurlen: Acta Chem. Scand. 13 (1959) 365.

169. R. N. Blumenthal et al.: J. Electrochem. Soc. 114 (1967) 172.

170. G. J. Schulz: Rev. Mod. Phys. 45 (1973) 423.

APPENDICES

APPENDIX A

XPS LINE SHAPES AND CORE-LEVEL INTENSITY MEASUREMENTS

XPS Line Shapes

When a core electron is suddenly removed from an atom in a metal, the response of the remaining electrons and nuclei is quite different from that observed in a system made up of a single atom with one electron, like atomic hydrogen, or even one with many electrons, like argon. Although understandably attractive and of great utility, simple one-electron models cannot give insight into such phenomena in many-body systems [163].

Nozières and de Dominicis [164] explained the experimentally observed skew line shape of metal core levels as the result of Kondo-like many-electron interactions of the metallic conduction electrons with the accompanying deep hole in the final state. Subsequent theoretical and experimental studies performed by Doniach and Sunjić [144] and Citrin et al. [163], respectively, improved this model by also considering a Lorentzian lifetime broadening, as well as Gaussian broadenings due to the spectrometer and electron-phonon coupling.

The kinetic energy ϵ_k of a X-ray-induced photoelectron is a direct measurement of the energy E_h of the hole state (measured relative to the Fermi level) left behind in the metal:

$$\epsilon_k = \hbar\omega + E_g - E_h - \phi \qquad (98)$$

where $\hbar\omega$ is the X-ray energy, E_g the initial ground state energy of the metal, and ϕ is the work function. Thus the maximum photoelectron energy ϵ_{max} corresponds to the ground state of the hole+metal-system, while photoelectrons emitted below the maximum correspond to events in which the hole+Fermi-sea-system is left in an excited state.

Excited states with energies very close to (a fraction of an electronvolt) the ground state are those in which the Fermi sea is excited by the creation of low-energy conduction electron-hole pairs (i.e. charge-density fluctuations). It turns out that since the energy for creating pairs goes continously to zero as the momentum transfer to the pair, an infrared catastrophe occurs in which it is very favorable to produce a large number of very-low-energy pairs. Thus the photoemission cross section $d\sigma/d\epsilon$ is changed from a δ-function (for δ-function ingoing X-ray spectrum) in the absence of pair formation to a singular (though integrable) curve tailing off on the low-energy side of ϵ_{max} (see dashed curve A in Figure 61) [144].

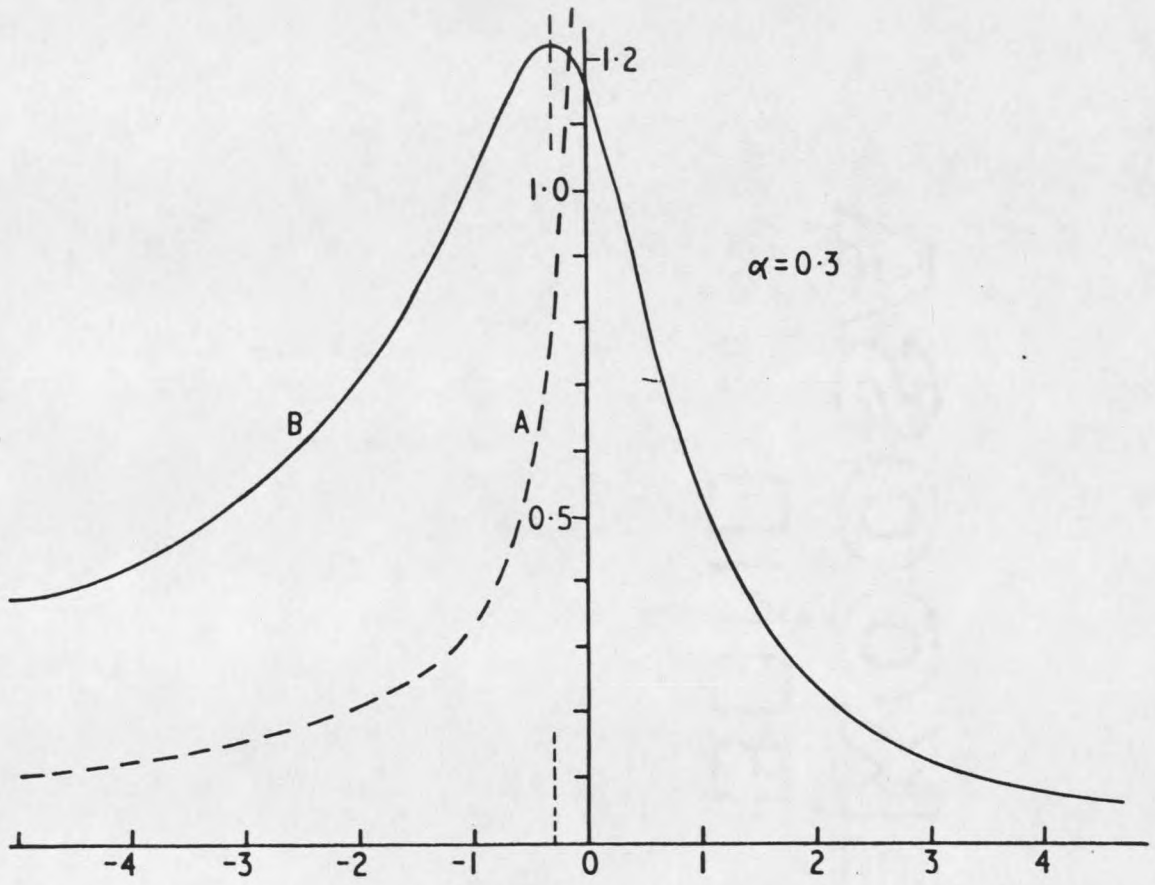

Figure 61. Theoretical XPS line shapes (see reference 144) with (solid line B) and without (dashed line A) lifetime broadening (see text).

In practice, this event will be rounded out by lifetime effects (see solid curve B in Figure 61). However, in the photoemission, the resulting tailing of the line shape has to be distinguished from events in which the escaping electron loses energy to the Fermi sea. We can, conceptually, distinguish two types of such energy loss: energy loss to the bulk metal (e.g. plasmon emission), and energy loss to surface states of the metal (e.g. surface plasmons).

We may assume that the probability of bulk energy loss by the escaping photoelectron is a function of thickness of the metallic target, and goes to zero as the film thickness goes to zero. This will not apply to surface energy loss, but presumably the probability of this process will decrease with increasing photon energy.

In contrast, the excitation of the Fermi sea accompanying the final hole state are an intrinsic property of the metal, so they should not depend either on film thickness (above a few atomic layers) or on incident photon energy [144].

The photoemission scattering cross section can be written - to lowest order in the X-ray field and by neglecting all interactions of the escaping electrons with the other electrons in the metal - as follows [144]:

$$\frac{d\sigma}{d\epsilon_k} \sim \mathrm{Re}\left\{\frac{1}{\pi}\int_0^\infty dt\ \langle b(t)b^+(0)\rangle \exp\left[\frac{i}{\hbar}(\hbar\omega-\epsilon_k)t\right]\right. \qquad (99)$$

This cross section is thus given as the Fourier transform of the hole-hole correlation function: b^+ is the hole creation operator and

$$b^+(t) = \exp(iHt/\hbar)b^+\exp(-iHt/\hbar).$$

Nozières and de Dominicis (ND) [164] derived an asymptotic formula for this correlation function, valid for long times, i.e. energy transfers

$$\epsilon = \epsilon_k - \epsilon_{max} << D$$

where D is the conduction band width. For s-wave scattering at the core hole of binding energy $_0$ they found:

$$\langle b(t)b^+(t)\rangle = \frac{\exp(-i\epsilon_0 t/\hbar)}{(iDt/h)^\alpha} \qquad (100)$$

Here, $\alpha = (\delta/\pi)^2$ is the Anderson singularity index and δ the phase shift for scattering of conduction electrons from the hole potential.

Equations 99 and 100 yield (with $\hbar\omega \simeq \epsilon_0 + \epsilon_{max}$):

$$\frac{d\sigma^{ND}}{d\epsilon} \sim \frac{\Theta(-\epsilon)}{D^{\alpha}\,\Gamma(\alpha)\,|\epsilon|^{1-\alpha}} \qquad (101)$$

where Γ is the gamma function and $\Theta(x>0) = 1$, $\Theta(x<0) = 0$. This cross section is plotted versus energy transfer as curve A in Figure 61.

For a general potential, Nozières and de Dominicis showed that α is given by:

$$\alpha = \sum_{l=0}^{\infty} (2l+1)\,(\delta_l/\pi)^2 > 0 \qquad (102)$$

Here, δ_l is the phase shift of the l-th partial wave [164]. Friedel's sum rule [163] limits α to values no greater than 0.5.

The above singular line shape will in practice be modified by the finite lifetime of decay of the hole states due to electron capture. The detailed theory of the resulting time-dependence would require a higher order treatment of the interaction with the X-ray field. Doniach and Sunjić (DS) [144] accounted for this effect by multiplying the right side of Equation 100 by an exponential lifetime factor $\exp(-\gamma t/h)$, with 2γ being the full width at half (peak) maximum (FWHM). This new correlation function led to the following modified scattering cross section:

$$\frac{d\sigma^{DS}}{d\epsilon} \sim \frac{1}{D^{\alpha}} \frac{\Gamma(1-\alpha)}{[\epsilon^2+\gamma^2]^{(1-\alpha)/2}} \cos\left[\frac{\pi\alpha}{2} + (1-\alpha)\arctan\left(\frac{\epsilon}{\gamma}\right)\right] \quad (103)$$

Here, ϵ is measured relative to the maximum energy ϵ_{max} in the absence of lifetime broadening (see Figure 61, curve B).

Sudden creation of a core hole causes the initial-state wave functions to contract, producing excited eigenstates of the ion. The contracted positive ion couples to the surrounding nuclei and excites phonons. The eigenstates of this ion are thus thought of as being "shaken-up" from the initial state according to the Franck-Condon principle. In this language, phonons are vibrational analogs of electronic satellites of the final-state system.

For vibrational transitions in the sudden approximation, the distribution of the closely spaced states is strictly Poisson [165]. In the classical limit, i.e., when the mean number $\bar{n}$ of such states is very large, the distribution becomes Gaussian and the strength of the (relaxed) adiabatic transition is therefore very weak. [163].

The presence of phonons thus leads to an additional broadening of the XPS line shapes predicted by Doniach and Sunjić. It can be accounted for by convoluting the

expression in Equation 103 with a Gaussian whose half-width is given by the phonon broadening.

Another effect that was considered when fitting experimental XPS spectra to theoretical line shapes (see chapter 5) is the influence of the X-ray source and the spectrometer. The transfer function of the latter one can often be approximated by a Gaussian [163] which also has to be convoluted with the Doniach-Sunjić function given in Equation 103.

Hence the experimentally observed XPS line shapes discussed in chapter 5 were fitted to Doniach-Sunjić functions, twice convoluted with different Gaussians (equivalent to one convolution product containing one "effective" Gaussian).

In the fitting procedures discussed in chapter 5, bulk- and surface-plasmon contributions were subtracted as a linear background. These are often also approximated by a Shirley background (proportional to the total peak integral) or Lorentzians of variable height and width [153,163]. Further details concerning XPS background analysis are given in references 153, 154 and 166.

Core-Level Intensity Measurements

The total X-ray core-level intensity $I(E^i_{kin,nl})$ - i.e. the measured current (counts per second) - of photoelectrons of kinetic energy E^i_{kin} excited from the

energy level nl of species i (with concentration N_i) in the sample may be written as follows [143,146,147]:

$$I(E^i_{kin},nl) = \phi(h\nu)\ N_i\ \frac{d\sigma_i(nl,h\nu)}{d\Omega}\Delta\Omega\ \lambda_{eff}(E^i_{kin})$$

$$x\ F(E^i_{kin},E_a)\ T(E^i_{kin},E_a)\ D(E)\ \frac{\Delta E}{2\gamma} \qquad (104)$$

Here, $\phi(h\nu) = \Delta\omega\kappa I_p\ n_{e->x}\ /(4\pi)$ is the number of characteristic X-ray photons of energy h per second irradiating an effective surface area A.

$\Delta\omega$ is the solid angle within which the effective area A can be viewed from the X-ray source.

$n_{e->x}$ is the number of photons of energy $h\nu$ created per incident electron.

I_p is the primary electron beam current (electrons per second) on the anode.

κ is an attenuation factor determined by filters interposed between the X-ray source and the sample.

According to Green et al. [167], we have:

$n_{e->x} = M\ (U_0-1)^{1.63}$ for K, L and M shells, where $U_0 = E_0/E_x$, with E_0/e being the voltage applied between cathode and anode. E_x is the ionization energy of

the X shell.

Using the results obtained by Green et al. for K-shell X-rays, we derived the following approximation formula for M:

$$M = M_0 \, E_k^{1.63} \exp(-Z/Z_0)$$

where Z is the atomic number and

$Z_0 \simeq 12$, $M_0 \simeq 2.52 \times 10^{-4}$ (keV)$^{-1.63}$.

$\frac{d\sigma_i(nl,h\nu)}{d\Omega} = \frac{\sigma_i(nl,h\nu)}{4\pi}[1 - \frac{\beta_i(nl,h\nu)}{2} P_2(\cos\theta)]$ is the angular distribution of photoelectrons ionized by unpolarized light impinging on a (nl)-subshell [147]. $\sigma_i(nl,h\nu)$ is the total cross section for photoionization of a (nl)-subshell electron of species i with photon current $\phi(h\nu)$. It has been calculated relativistically for K_α lines of Mg and Al in the single-potential Hartree-Slater atomic model by Scofield [145]. The results are believed to be reliable as long as the X-ray energy is at least by 500 eV greater than the electron binding energy for the level (nl). The dipole approximation for photoionization used by Scofield starts to break down for X-rays in the keV-range. For photoelectrons of speed v, corrections (Δ) to $\sigma_i(nl,h\nu)$ go as v^2/c^2

while corrections (Δ) to the angular distribution go as v/c [147].

Examples: h = 1.0 keV ===> $\Delta(\sigma_i) \simeq 0.4$ %, and

$\Delta(d\sigma_i/d\Omega) \simeq 6$ %.

h = 2.5 keV ===> $\Delta(\sigma_i) \simeq 1.0$ %, and

$\Delta(d\sigma_i/d\Omega) \simeq 10$ %.

$\beta_i(nl,h\nu)$ is an asymmetry factor calculated by Reilman et al. [147].

θ is the angle between the directions sample - X-ray source and sample - analyzer.

$P_2(x) = (3x^2-1)/2$ is a Legendre polynomial. Note: The β_i-dependent term in $d\sigma_i/d\Omega$ drops out for $\theta = 54\ 44'08''$.

$\Delta\Omega$ is the solid angle of acceptance of the analyzer.

$\lambda_{eff}(E^i_{kin}) = \lambda(E^i_{kin})\cos\alpha$ is the attenuation length of electrons with kinetic energy E^i_{kin} in species i.

$\lambda(E^i_{kin})$ is the inelastic mean free path (IMFP) of electrons with kinetic energy E^i_{kin} in species i. Seah and Dench [136] analyzed experimentally obtained IMFP's of electrons in elements, organic and inorganic compounds, as well as adsorbed gases. They derived approximation formulas relating the IMFP's to the electron kinetic energies. For organic compounds, e.g., they found:

$$\lambda(E^i_{kin}) = A(E^i_{kin})^{-2} + B(aE^i_{kin})^{1/2}.$$

Here, A = 2170 ML(eV)^2 and B = 0.72 ML/(nm eV)$^{1/2}$. The letter "a" represents the monolayer (ML) thickness of the organic compound (see chapter 3). The above equation predicts a minimum value for λ, which, however, couldn't be located exactly due to insufficient experimental results in the kinetic energy range from 10 to 100 eV [136].

α is the angle between the surface normal and the surface - analyzer direction.

$F(E^i_{kin},E_a)$ is an electron-optical factor that has to be included, if electrons are decelerated from their initial energy E^i_{kin} to some energy E_a before entering the energy analyzer.

$T(E^i_{kin},E_a)$ is the transmission function of the analyzer.

D(E) is the counting efficiency of the electron (with energy E) detector.

ΔE is the analyzer energy window.

2γ is the photoelectron line width.

The ratio $\Delta E/2\gamma$ has to be replaced by 1 in Equation 104, if $\Delta E >> 2\gamma$.

Equation 104 makes possible the determination of concentrations N_i from experimentally obtained intensities $I(E^i_{kin},nl)$. This, however, requires detailed knowledge of

analyzer and X-ray source characteristics. In chapter 5 we therefore calculated relative titanium-to-oxygen concentrations and assumed that most of the above-listed parameters, such as ϕ,$\Delta\Omega$,F, T, D and $\Delta E/2\gamma$, wouldn't change significantly between photoelectron kinetic energies from 720 eV (01s-core level) to 795 eV ($Ti2p_{3/2}$-core level).

Further details concerning quantitative XPS-data analysis are discussed in the references cited above.

APPENDIX B

ELECTRON ENERGY LOSS SPECTROSCOPY (EELS) AND SURFACE OPTICAL PHONONS

Basic Theory of EELS

During the past two decades physicists and chemists have explored both the nature of the outermost atomic layers of solids and the manner in which atoms and molecules bind to the surface. Many common probes of solids (photons, neutrons), however, penetrate many atomic layers into the material so that information descriptive of the near vicinity of the surface appears as a small feature superimposed on a large signal from the bulk of the material.

Particles that sample only the outermost layer or two (electrons, atoms) have limited penetration, because they strongly interact with the atoms of the material. Electrons with energy in the range of a few electron volts sample only a few atomic layers. As they approach or exit from the crystal, they interact with the vibrational modes of the crystal surface, or possibly with other elementary excitations (e.g. adsorbate vibrations) localized there. The energy spectrum of electrons back-reflected from the surface is thus a rich source of information on its dymamics [122].

High Resolution Electron-Energy-Loss Spectroscopy [(HR)EELS] makes possible the study of the vibrational

motion of atoms and molecules on and near the surface by the analysis of the energy spectrum of low-energy electrons backscattered from it.

An electron incident on the crystal with energy E_i may excite a quantized vibrational mode with energy $\hbar\omega_0$ before being backscattered into the vacuum. It thus emerges with energy $E_s = E_i - \hbar\omega_0$, so an analysis of the energy spectrum of the backscattered electrons provides direct information on the vibrational frequencies of the substrate, or on those of atoms and molecules adsorbed on the surface.

The method is sensitive to the surface because, with the incident kinetic energy E_i chosen suitably, the electron penetrates, at most, two or three atomic layers into the crystal. The backscattered electrons thus carry information on only the near vicinity of the surface [122].

In an electron-energy-loss study of surface vibrations, the sample is placed in ultrahigh vacuum. A highly monoenergetic beam of electrons with low kinetic energies is directed toward the surface, and the energy spectrum and angular distribution of electrons backscattered from the surface are measured. The experimental problem is to achieve high resolution through production of a very monoenergetic and well-collimated electron beam, along with sensitive detectors. This must be done without degrading the signal below the detectable level.

At present, the best resolution that may be obtained is 30 cm-1 (3.7 meV), although to detect weak signals it is sometimes necessary to operate at lower resolution. The resolution achieved in electron-energy-loss spectroscopy is thus substantially less than is customarily encountered in optical spectroscopies, though it is adequate for the study of both the vibrational modes of adsorbed molecules, and of the substrate [122].

The discussion of the inelastic electron scattering process requires one to address the nature of the interaction between the incoming electron and the vibrating atoms of the solid. In general, this is a complex problem, since the electron strongly interacts with the substrate, and any attempt to describe this coupling in simple terms necessarily leads to a schematic and limited picture. Nonetheless, it proves useful to distinguish between three limiting cases, though one recognizes that there are no sharp and precisely defined boundaries between them [122]:

Dipole Scattering

As an atom on a surface or in a molecule vibrates, it modulates the electric dipole moment of its environment in a time-dependent fashion. An electron in the vacuum above the crystal senses a long-range electric field of dipolar character, and this produces small-angle scatterings substantially more intense than the scattering observed at

large deflection angles. One observes a number of inelastics sharply peaked about the specular direction, when dipole scattering is present. The principal features of this mechanism will be outlined in simple terms below.

Intermediate Negative-Ion Resonances

Negative-ion resonances are frequently observed in elastic collisions between electrons and molecules in the gas phase [170]. On a surface, the lifetime of such resonances is rather short when a chemisorbed molecule is coupled to the subtrate-electron states. Negative-ion resonances for molecules adsorbed on surfaces have not been observed yet, except in a few experiments [122].

Impact Scattering

For small defection angles, with dipole scattering dominant, it is possible to obtain a simple and useful form for the scattering cross section without resort to a microscopic description of the electron-substrate interaction (see below). At large deflection angles, it is necessary to turn to a fully microscopic picture to theoretically describe the cross section. This large-deflection-angle regime, outside the dipolar region, is often referred to as the impact scattering regime.

Interaction Potential

Suppose we consider the scattering of an electron from a small molecule. Let the position $\vec{R}_1$ of each nucleus be

written $\vec{R}_l = \vec{R}_l^{(0)} + \vec{u}_l$, where $\vec{R}_l^{(0)}$ is a vector to the equilibrium position of nucleus l, and $\vec{u}_l$ is the amplitude of the vibrational motion about its equilibrium position.

Suppose the electron interacts with the molecule through a superposition of two-body potentials (neglecting the fact that charge flows within the molecule, as the nuclei shift away from their equilibrium position):

$$V(\vec{x}) = \sum_l V_l(\vec{x}-\vec{R}_l) \tag{105}$$

If by $V^{(1)}(\vec{Q})$ we denote the contribution to $V(\vec{Q})$ - the Fourier transform of $V(\vec{x})$ - of first order in the nuclear displacements $\vec{u}_l$, we have:

$$V(1)(\vec{Q}) = i \sum_l V_l(\vec{Q}) \exp[i\, \vec{Q}\cdot\vec{R}_l^{(0)}]\ \vec{Q}\cdot\vec{u}_l \tag{106}$$

Here, $\vec{Q} = \vec{K}(i) - \vec{K}(s)$ is the change in wave vector of the electron. If we consider very small angle scatterings, where $|\vec{Q}|\, d_0 << 1$ with d_0 a measure of the size of the molecule, we then get:

$$\lim_{|\vec{Q}|\to 0} V^{(1)}(\vec{Q}) = i\, 4\pi e\, \vec{Q}\cdot\vec{p}/Q^2$$

Here, $\vec{p} = \sum_l e\, Z_l\, \vec{u}_l$ is the oscillating portion of the electric dipole moment of the molecule, and Z_l is the net charge surrounding the nucleus located at $\vec{R}_l^{(0)}$.

From this argument, we can see that in the limit of very small wave vector transfers, the cross section for inelastic scattering of the electron from the vibrational motion of the molecule is controlled by only one parameter, the component $\vec{p}$ of the electric dipole moment which oscillates at the frequency ω_0 of the normal mode responsible for the scattering.

Oscillating electric-dipole moments in crystals, however, are not only produced by the vibrational motions of nuclei, but also by other excitations such as fluctuations in the electronic degrees of freedom. Examples are fluctuations in the free carriers in metals or doped semiconductors, and interband transitions in insulators [122].

From Equation 106, we can see that when $|\vec{Q}|d_0$ is not small, the calculation of the electron scattering cross section requires detailed and microscopic knowledge of the nature of the electron-molecule interaction, as well as the geometry. This is the impact scattering regime, where the cross section for inelastic scattering cannot be expressed simply in terms of a small number of phenomenological parameters. Further details discussing this particular regime are given in reference 122.

The Dipole-Scattering Cross Section

The small-angle-dipole-scattering theory applied to a two-layer system consisting of a semi-infinite substrate

with complex dielectric constant $\epsilon_b(\omega)$ and a surface layer of thickness d with dielectric constant $\epsilon_s(\omega)$ yields a scattering efficiency S per unit solid angle $d\Omega(\hat{K}_s)$ per unit (loss) energy $d\hbar\omega$. This quantity is denoted by $d^2S/d\Omega(\hat{K}_s)d\hbar\omega$ and has been calculated for small angular deviations of the scattered electron from the specular direction. Furthermore, retardation effects have been ignored. It has been assumed that information about the charge fluctation at a point $\vec{x}'$ is transmitted instantly to the point $\vec{x}$ where the electron is located. The theory yields [122]:

$$\frac{d^2S}{d\Omega(\hat{K}_s)d\hbar\omega} = \frac{2\,|R_i|^2}{\pi^2\, a_0\, K_i\, E_i\, \cos\Theta_i} \times (1-2\theta_E)^{1/2}$$

$$\times \frac{[(\theta_E \sin\Theta_i - \theta\cos\Theta_i\cos\phi)^2+\theta^2\sin^2\phi]^{1/2}}{[\theta^2+\theta_E^2]^2}$$

$$\times [1+n(\omega)]\ \mathrm{Im}\{\frac{-1}{1+\tilde{\epsilon}(Q_{\parallel},\omega)}\} \qquad (107)$$

Here, $|R_i|^2$ is the intensity of the specularly reflected, elastic beam normalized to the incident intensity. K_i, E_i and Θ_i are the magnitudes of the wave vector, the energy and the angle (measured with respect to the crystal normal) of the incident electron, respectively. The angle between the wave vector $\vec{K}(s)$ of the scattered electron, and that of the specular beam is denoted by θ ($<<$ 1 here), while ϕ

measures the azimuthal orientation of $\vec{K}(s)$, as one "looks down" the specular beam [122]. Furthermore, $\theta_E = \hbar\omega/(2E_i)$, $n(\omega) = \{\exp[\hbar\omega/(k_B T)]-1\}^{-1}$ and

$$\tilde{\epsilon}(Q_{\parallel},\omega) = \epsilon_s(\omega) \times \frac{1 + \Delta(\omega)\exp(-2Q_{\parallel}d)}{1 - \Delta(\omega)\exp(-2Q_{\parallel}d)} \qquad (108)$$

with $\Delta(\omega) = [\epsilon_b(\omega)-\epsilon_s(\omega)]/[\epsilon_b(\omega)+\epsilon_s(\omega)]$, a_0 is the Bohr radius and $Q_{\parallel}$ the magnitude of the change in wave vector parallel to the surface (see above).

In the limit $Q_{\parallel}d \ll 1$, which is well satisfied for $\theta \simeq \theta_E$ in typical electron energy loss studies of adsorbate layers, the expression in Equation 107 may be decomposed into two terms. The first, $d^2S_b/d(\hat{K}_s)dh$, describes electron scattering by electric field fluctuations in the vacuum above the crystal produced by excitations in the bulk. The second term, $d^2S_s/d\Omega(\hat{K}_s)d\hbar\omega$, is proportional to the layer thickness d (see above) and descirbes scattering by electric fields produced by fluctuations within the surface layer. We have [122]:

$$\frac{d^2S}{d\Omega(\hat{K}_s)d\hbar\omega} = \frac{d^2S_b}{d\Omega(\hat{K}_s)d\hbar\omega} + \frac{d^2S_s}{d\Omega(\hat{K}_s)d\hbar\omega} \qquad (109)$$

The first term on the right side of the above equation can be obtained by simply replacing $\tilde{\epsilon}(Q_{\parallel},\omega)$ by $\epsilon_b(\omega)$ in Equation 107. The second term is calculated by multiplying the expression on the right side of Equation 107 by the

thickness d. Furthermore, the contents of the braces has to be replaced by

$$\frac{-1}{\epsilon_s(\omega)} \times \frac{\epsilon_b^2(\omega)-\epsilon_s^2(\omega)}{[\epsilon_b(\omega)+1]^2}$$

In an actual experiment, it is not $d^2S/d\Omega(\hat{K}_s)d\hbar\omega$ that is measured, but rather this quantity integrated over the solid angle subtended by the entrance slit of the analyzer. We suppose this to be circular, centered on the specular direction, and that it catches all electrons scattered into the angular range $0 < \theta < \theta_c$. With the polar axis of a spherical coordinate system aligned along the specular direction [$d\Omega(\hat{K}_s) = \theta\, d\theta d\phi$] we then get the following expression for the differential cross section for inelastic scattering of electrons from bulk excitations [122]:

$$\frac{dS_b}{d\hbar\omega} = \frac{4\,|R_i|^2\,(1-2\theta_E)^{1/2}}{\pi^2\, a_0\, K_i\, \cos\Theta_i} \times \frac{1+n(\omega)}{\hbar\omega}$$

$$\times\, \mathrm{Im}\left\{\frac{-1}{1+\epsilon_b(\omega)}\right\} \times F_b(\hat{\theta}_c) \qquad (110)$$

The function

$$F_b(\hat{\theta}_c) = \int_0^{2\pi} d\phi \int_0^{\hat{\theta}_c} d\hat{\theta}\hat{\theta} \cdot \frac{[(\sin\Theta_i - \hat{\theta}\cos\Theta_i\cos\phi)^2+\hat{\theta}^2\sin^2\phi]^{1/2}}{[1+\hat{\theta}^2]^2}$$

describes the number of inelastically scattered electrons collected by a spectrometer that picks up all electrons

with scattering angles $0 < \theta < \theta_c$. Here, $\hat{\theta} = \theta/\theta_E$ is a reduced scattering angle.

Surface Optical Phonons

When electrons are scattered from the surface of an ionic insulator, a surface mode is usually found. This is the surface optical phonon with frequency ω_s that lies between that ω_{TO} of the bulk long-wavelength transverse optical phonon, and the frequency ω_{LO} of the bulk longitudinal optical phonon. We may describe the contribution to the EELS cross section from this mode with the help of Equation 110.

For a cubic material with one infrared active bulk transverse optical (TO) phonon, the dielectric function may be written [122]:

$$\epsilon_b(\omega) = \epsilon_\infty + \frac{4\pi\, n\, e^{*2}}{M_r} \frac{1}{\omega_{TO}^2 - \omega^2 - i\omega\gamma(\omega)} \qquad (111)$$

Here, n is the number of unit cells per unit volume, e^* the Born or transverse effective charge, and M_r the reduced mass of the unit cell. If $\epsilon(0) = \epsilon_\infty + 4\pi n e^{*2}/(M_r\omega_{TO}^2)$ is the static dielectric constant of the material, then the loss function $\mathrm{Im}\{-1/[1+\epsilon_b(\omega)]\}$ has a peak at the frequency

$$\omega_s = \omega_{TO}\left[\frac{\epsilon(0)+1}{\epsilon_\infty+1}\right]^{1/2} \qquad (112)$$

providing the damping function $\gamma(\omega)$ is sufficiently small. The frequency ω_s necessarily lies above ω_{TO}, but below the longitudinal optical phonon frequency

$$\omega_{LO} = \omega_{TO} \left[\epsilon(0)/\epsilon_\infty\right]^{1/2} \quad \text{(see reference 122).}$$

In the limit of small damping, we can approximate the loss function as follows [122]:

$$\mathrm{Im}\left\{\frac{-1}{1+\epsilon_b(\omega)}\right\} = \frac{\pi}{2} \times \frac{\epsilon(0)-\epsilon_\infty}{[\epsilon(0)+1]\,[\epsilon_\infty+1]} \times \left[\delta(\hbar\omega_s-\hbar\omega)-\delta(\hbar\omega_s+\hbar\omega)\right] \tag{113}$$

Here, we allow for the possibility of inelastic scattering with phonon absorption, as well as that with phonon emission. Then the probability, normalized to that for specular reflection, for an electron to scatter from the surface with emission of a surface optical phonon is given by:

$$\frac{S_b^{(tot+)}}{|R_i|^2} = \frac{2}{\pi} \times \frac{1+\bar{n}_s}{a_0 K_i \cos\Theta_i} \times \frac{\epsilon(0)-\epsilon_\infty}{\epsilon(0)+1} \times \frac{F_b(\hat{\theta}_c)}{1+\epsilon_\infty} \tag{114}$$

Here, $n_s = \{\exp[\hbar\omega_s/(k_B T)]-1\}^{-1}$ and $\epsilon_E \ll 1$ (see Equation 110). Similarly, the probability for scattering with phonon absorption is:

$$\frac{S_b^{(tot-)}}{|R_i|^2} = \frac{2}{\pi} \times \frac{n_s}{a_0 K_i \cos\Theta_i} \times \frac{\epsilon(0)-\epsilon_\infty}{\epsilon(0)+1} \times \frac{F_b(\hat{\theta}_c)}{1+\epsilon_\infty} \tag{115}$$

According to the above equations, the loss and gain intensities to be observed vary with $(\cos\Theta_i)^{-1}$ and $E_i^{-1/2}$ (the factor K_i in the denominators is proportional to $E_i^{1/2}$). Furthermore, the ratio of the energy gain scattering to energy loss is, for one-phonon events, predicted to be equal to $\exp[-\hbar\omega_s/(k_B T)]$. These predictions of the theory have been verified experimentally on various samples in the past [122].

The theory presented above may also be applied to surface plasmons and interband electronic transitions with appropriate choices of $\epsilon_b(\omega)$ and $\epsilon_s(\omega)$. Further details are given in reference 122.

It can be seen that for either emission of a plasmon or a surface optical phonon at the absolute zero of temperature the scattering probability integrated over the solid angle and normalized to that of the specular beam is given by:

$$\Gamma = \frac{\pi}{a_0 K_i \cos\Theta_i} \times \frac{\epsilon(0)-\epsilon_\infty}{\epsilon(0)+\epsilon_\infty} \times \frac{1}{1+\epsilon_\infty} \qquad (116)$$

The formula applies to a metal upon letting the static dielectric constant $\epsilon(0)$ become infinite [122].

Suppose we let $S_n^{(+)}$ be the total probability that the electron excites n quanta as it passes by the surface, losing the energy $n\hbar\omega_s$ in the process. We then have, for scattering from thermal excitations:

$$S_n^{(+)} = \Gamma_n |R_i|^2 \qquad (117)$$

In the limit of zero temperature, Γ_n is given by a Poisson distribution:

$$\Gamma_n = (\Gamma^n/n!)\exp(-\Gamma) \qquad (118)$$

The Poisson distribution of surface-optical phonon intensities has been observed in earlier EELS studies, e.g. on TiO_2 samples (see chapters 2 and 5).

Within the framework of the theory presented above, the surface mode of a semi-infinite dielectric was derived simply by examining the positions of the poles of the appropriate electron-energy-loss expression (see above). For an ionic crystal, where the frequency-dependent dielectric function is given by Equation 111, this mode may be derived equally well within the so-called lattice-dynamical theory, as was first done by Fuchs and Kliewer [98]. For this reason, the surface optical phonons are often referred to as "Fuchs-Kliewer" phonons.

Within the lattice dynamical framework, the surface optical modes are described by a macroscopic theory. The equation of motion of the different ionic sublattices is derived from classical electrodynamical theory and yields the transverse and longitudinal frequencies $_{TO}$ and $_{LO}$, as

well as Equation 112. Further mathematical and physical details are given in references 98 and 122.

The surface optical (Fuchs-Kliewer) phonons are accompanied by a long-range electric field [99,122]:

$$E_x = E_0 \sin(Q_{||} x - t) \exp(-Q_{||}|z|)$$
$$E_z = E_0 \cos(Q_{||} x - t) \exp(-Q_{||}|z|) \operatorname{sgn}(z) \qquad (119)$$

Here, the x-axis is parallel to the surface and the z-axis parallel to the surface mormal, i.e. the crystal fills the halfspace with $z<0$.

From the above equation we see that the character of the phonons is mixed: transverse-longitudinal, and that the electric field decays into the crystal and into the vacuum with a penetration depth of the inverse magnitude of the wave vector transfer $1/Q_{||}$. For small changes in the wave vector $\vec{Q}_{||} \to 0$ (see above), the electric field due to the phonons thus penetrates deeply into the crystal.

Screening of Surface Optical Phonons

Dubois et al. [137] discovered that the surface optical phonon (36.2 meV loss energy) of a (100) Te-doped GaAS sample was completely screened by a 3-A-thick uniform overlayer of silver (monolayer thickness of silver: 2.57 A, see chapter 3). Their experiment only measured small-angle

deviations (± 1) from the specular direction, and thus the dipolar scattering theory was applied to the Ag/GaAs system.

The GaAs substrate can be viewed as a dielectric [137] with frequency-dependent dielectric constant given by:

$$\epsilon_b(\omega) = \epsilon_\infty^{(b)} + \frac{[\epsilon_0^{(b)} - \epsilon_\infty^{(b)}]\,\omega_{TO}^2}{\omega_{TO}^2 - \omega^2 - i\omega\Gamma} \qquad (120)$$

Here, ω_{TO} is the transverse-optical phonon frequency of the material. This is overlaid by a silver film, regarded as a thin dielectric layer of thickness d described by a dielectric constant

$$\epsilon_s(\omega) = \epsilon_\infty^{(s)} - \frac{\omega_p^2}{\omega(\omega + i\gamma)} \qquad (121)$$

with ω_p as the conduction-electron plasma frequency. Γ and γ are phonon and plasmon damping constants, respectively.

The inelastic electron-scattering cross section is now calculated from Equations 107 and 108 by integrating over an appropriate solid angle as described above.

The theoretical results showed decreasing surface-optical phonon intensities with increasing silver coverage, in good agreement with preceding experiments [137]. The observed features can be explained as follows.

In the absence of phonon and plasmon damping ($\Gamma = \gamma = 0$), the condition $1 + \tilde{\epsilon}(Q_{\parallel}, \omega) = 0$ (pole of the loss function, see

Equation 107) yields:

$$\frac{\epsilon_s(\omega)+1}{\epsilon_s(\omega)-1} \times \frac{\epsilon_s(\omega)+\epsilon_b(\omega)}{\epsilon_s(\omega)-\epsilon_b(\omega)} = \exp(-2Q_{\parallel}d) \qquad (122)$$

We are interested in the regime where $Q_{\parallel}d<<1$, and $\omega<<\omega_p$, so $|\epsilon_s(\omega)| \simeq |-\omega_p^2/\omega^2| >> 1$. Then the above equation can be written as follows:

$$1 + \frac{2}{\epsilon_s(\omega)} \times [1+\epsilon_b(\omega)] = 1 - 2Q_{\parallel}d \qquad (123)$$

This equation leads to the dispersion relations

$$\omega_{\pm}^2(Q_{\parallel}) = \frac{1}{2}[\omega_s^2+\omega^2(Q_{\parallel})] \pm \frac{1}{2}\{[\omega_s^2-\omega^2(Q_{\parallel})]^2 + 4(\omega_s^2-\omega_{TO}^2)\omega^2(Q_{\parallel})\}^{1/2} \qquad (124)$$

with

$$\omega_s^2 = \omega_{TO}^2 \times \frac{\epsilon_0^{(b)}+1}{\epsilon_\infty^{(b)}+1} \qquad (125)$$

as the surface-optical phonon frequency for a GaAs-vacuum interface, and

$$\omega^2(Q_{\parallel}) = \frac{\omega_p^2 Q_{\parallel} d}{1+\epsilon_\infty^{(b)}} \qquad (126)$$

is the dispersion relation of the low-frequency surface

mode of the conduction electrons in a thin metal film with vacuum above, and substrate with frequency-independent dielectric constant $\epsilon_{\infty}^{(b)}$ below.

An important parameter [137] is the wave vector Q_0 for which the low-frequency collective mode of the film crosses the GaAs surface-optical phonon frequency. This is determined by setting $\omega_s = \omega(Q_0)$, and hence we get:

$$Q_0 = \frac{1}{d} \times \frac{\omega_{TO}^2}{\omega_p^2} \times (1+\epsilon_0^{(b)} \qquad (127)$$

With the help of Equation 124 it can easily be shown that

$$\omega_{-}^2(Q_{\parallel} \to 0) \dashrightarrow \omega^2(Q_{\parallel})$$
$$\omega_{+}^2(Q_{\parallel} \to 0) \dashrightarrow \omega_s^2$$

and
$$\omega_{-}^2(Q_{\parallel} >> Q_0) \simeq \omega_{TO}^2$$
$$\omega_{+}^2(Q_{\parallel} >> Q_0) \simeq \omega^2(Q_{\parallel}),$$

since $\omega_s \simeq \omega_{TO}$ for GaAs.

As $Q_{\parallel} \to 0$, the ω_+ branch approaches ω_s which shows that for $Q_{\parallel} << Q_0$, the GaAs surface optical phonon is not effected by the presence of the Ag film. It thus produces electric fields with strength unaffected by the overlayer. When $Q_{\parallel} >> Q_0$, in essence the GaAs surface mode is driven down in frequency to ω_{TO}. But any oscillation of the lattice of an ionic crystal will fail to generate a macroscopic electric field, if the oscillation frequency is ω_{TO}. This is true

independent of the spatial variation of the lattice motion, because the macroscopic field $\vec{E}(\vec{x})$ generated by lattice displacements $\vec{u}(\vec{x})$ is given by (see references 122 and 137, as well as Equation 111 with = 0):

$$e^{*}\vec{E}(\vec{x}) = M_r(\omega_{TO}^2-\omega^2)\vec{u}(\vec{x}) \qquad (128)$$

Thus the crucial issue is whether $Q_c>Q_0$, or $Q_c<Q_0$, where Q_c is the maximum wave vector accepted by the spectrometer. If $Q_c<Q_0$, the feature near ω_s or ω_{TO} is produced by scattering off the ω_+ branch. These modes generate an electric field comparable in strength to that associated with the bare GaAs surface, and the surface optical phonon is observed at full strength in the loss spectrum.

On the other hand, if $Q_c>>Q_0$, nearly all electrons collected by the spectrometer have suffered momentum transfers very large compared to Q_0, and in this region of phase space, we have no collective modes near ω_s or ω_{TO} which generate a macroscopic field, the loss peak is absent or weak [137].

By setting Q_c equal to Q_0, a critical film thickness d_c can be defined as follows (see Equation 127):

$$d_c = \frac{1}{Q_c} \times \frac{\omega_{TO}^2}{\omega_p^2} \times [1+\epsilon_0^{(b)}] \qquad (129)$$

Then, if $d>>d_c$, the GaAs surface optical phonon is

suppressed by the Ag film, while if $d<d_c$, it is present with substantial strength.

With $Q_c \simeq 10^6$ cm^{-1}, $h\omega_{TO} \simeq 33$ meV, $h\omega_p \simeq 3.5$ eV, and $\epsilon_0^{(b)} \simeq 13$, we get $d_c \simeq 0.1$ Å, i.e one monolayer of Ag is quite sufficient to suppress the scattering from GaAs surface optical phonons [137].

In the case of a titanium-covered TiO_2(110) surface, similar features have been observed. The surface-optical phonon intensities dropped significantly upon the deposition of small amounts of titanium (see chapters 4 and 5). From Equation 43 and the data presented in chapters 2 and 4 ($E_i=E_p=27.1$ eV, $\Theta_i=60^\circ$, $h\omega_s=95$ meV, etc.), as well as $h\omega_p$(Ti) $\simeq$ 12.5 eV, we calculate $Q_c \simeq 4\times10^5$ cm^{-1} and d_c(Ti) $\simeq$ 0.1 Å. The low value indicates that even submonolayer coverages of titanium significantly screen the very strong Fuchs-Kliewer modes on TiO_2(110) surfaces.